University of Bath

UNIVERSITY OF
BATH

PHD

Studies of Perovskite Solar Cells

Pering, Sam

Award date:
2019

Awarding institution:
University of Bath

Link to publication

Alternative formats
If you require this document in an alternative format, please contact:
openaccess@bath.ac.uk

Studies of Perovskite Solar Cells

Samuel Robert Pering

A thesis submitted for the degree of Doctor of Philosophy

University of Bath

Department of Chemistry

May 2019

Abstract

Solar cell technology is rapidly establishing itself as a viable option for large-scale power generation. Currently the most popular technology for this is based on Silicon-solar cell technology, which is also known as first generation photovoltaics. Hybrid inorganic-organic perovskite materials based on methylammonium lead iodide are an emerging technology. In the 10 years since their discovery efficiencies have risen from 3 % to 23 %, and as such are on the verge of commercialisation. Yet there are still some unsolved problems. One such problem is the lack of stability, caused by a susceptibility to degradation by water, heat and even light. Using mixed-cation perovskites has been shown to improve the short-term performance and long-term stability of perovskite solar cells. In this work a new and stable alternative cation to methylammonium is proposed, azetidinium. Azetidinium lead iodide exhibits a unique 2.5-Dimensional structure when used on its own, and improves efficiency and stability when used in conjunction with methylammonium. Following this the effect of cation-mixing is assessed in more detail. A wide-ranging study using 8-different cationic additives was performed to analyse their effect on iodide diffusion in methylammonium lead iodide. The distortion caused, expanding perovskite lattice size, increases the barrier for iodide diffusion, and with the largest cationic additives bulk iodide diffusion is no longer observed on the timescale of the experiment. This is then extended to formamidinium-based perovskites and the record efficiency triple-cation perovskite. In this case the cationic additives reduce the activation energy for iodide diffusion, and this is attributed to the distortion to smaller lattice sizes.

Acknowledgements

Firstly I would like to thank Petra for all her support and advice over the past three and a half years. Also all group members for discussion and help along the way. Dom and Pete for keeping me entertained during the quieter moments and instrument downtime. I would also like to acknowledge everyone who I collaborated with, both at the university and elsewhere. Particularly Dibya who provided a large amount of computational assistance with projects.

I would like to thank the University of Bath for funding, providing a good research environment and excellent campus to work in. The Department of Chemistry has been my home for the past 8 years, and as such I would like to thank everyone in there for making it a great place for research.

I would also like to acknowledge my brother Tom, for his help at every stage of my career so far. Finally thank you to Vicky for your support throughout the process.

Declaration of work done in conjunction with others

Various parts of this work have been part of collaborative efforts. Computational measurements on Azetidinium Lead Iodide were performed by Federico Brivio and Dibya Ghosh. Raman from the same chapter was measured by Ralf Niemann. Single-crystal XRD measurements were taken by Peter Kubiak and Andrew Johnson. Solar cells were made and measured with Joel Troughton at SPECIFIC in Swansea.

For chapter 7, computational measurements were made by Dibya Ghosh. Complementary muon work referred to in the text and published as part of the same work was done by Dominic Ferdani, at ISIS.

Contents

Table of Figures

Chapter 2

Chapter 3

Chapter 5

Chapter 6

Chapter 8

List of frequently used abbreviations:

Ac: Acetamidinium

AC: Alternating Current

AFM: Atomic Force Microscopy

AM: Air Mass

Am: Ammonium

Az: Azetidinium

AzPI: Azetidinium Lead Iodide

C_{geo}: Geometric Capacitance

DM: Dimethylammonium

DMF: Dimethyl formamide

DMSO: Dimethyl sulfoxide

DSSC: Dye-Sensitised Solar Cell

E_a: Activation Energy

EIS: Electrochemical Impedance Spectroscopy

EQE: External Quantum Efficiency

ETM: Electron Transport Material

eV: electron Volts

FA: Formamidinium

FAI: Formamidinium iodide

FAPI: Formamidinium lead iodide, CH(NH2)2PbI3

FF: Fill Factor

FTO: Fluorine-doped Tin Oxide

GA: Guanidinium

HTM: Hole Transport Material

Inverted: A cell which has the structure: TCO-HTM-PVSK-ETM-Metal

J_{mp}: Current at max power point

J_{SC}: Short-circuit current density

JV: Current-voltage

MA: Methylammonium

MAI: Methylammonium iodide

MAPBr: Methylammonium lead bromide, CH3NH3PbBr3

MAPI: Methylammonium lead iodide, CH3NH3PbI3

MO: Molecular Orbital

PCBM: [6,6]-phenyl C71-butyric acid methyl ester

PEDOT:PSS: poly(3,4-ethylenedioxythiophene) polystyrene sulfonate

PSC: Perovskite Solar Cell(s)

PV: Photovoltaic

PVSK: Perovskite

PXRD: Powder X-ray diffraction

R_{recomb}: Recombination resistance

SCXRD: Single-crystal X-ray diffraction

Spiro-OMeTAD: 2,2',7,7'-tetrakis(N,N'-di-p-methoxyphenylamine)-9,9'-spirobifluorene

Standard: A cell which has the structure: TCO-ETM-PVSK-HTM-Metal

TCO: Transparent Conducting Oxide

Triple-Cation: Cells that contain Cs, MA and FA

UV/Vis: Ultraviolet/Visible

V_{mp}: Voltage at max power point

V_{OC}: Open-circuit Voltage

XRD: X-ray diffraction

Z: Impedance

τ: Time constant

ω_{max}: The maximum frequency value for a circuit feature

1: Broader Context

The photovoltaic effect, in which light energy is converted to electrical energy, was discovered in the mid-19th century, at a time when the rapid expansion of global industry was being powered by coal and oil. These resources were at the time plentiful, however their non-sustainable nature was identified by Arrhenius who established the link between CO_2 emissions and climate change. Photovoltaic technology was not well established until the space race when a constant source of power was required for satellites and space stations. Since then, and due to the growing field of climate science, research into alternative sources of power that are both renewable and do little damage to the environment has exploded in popularity. Solar, wind, hydroelectric and geothermal energy are four examples of the most popular renewable sources of energy. Their prevalence depends largely on the country they are in – for example wind energy in Europe and solar in Australia. Hydroelectric has been in large usage in Costa Rica, and has enabled them to meet their energy requirements using solely renewable sources for over 30 days.

A further benefit of solar energy is that it allows for the decentralisation of energy generation, *i.e.* solar panels can be mounted on homes to promote energy independence. The problem remains however with the storage of the created energy for use at night-time. Large-scale lithium-ion batteries have been created for this purpose, but the increasing scarcity of lithium supplies do not make this a sustainable option. Sustainability is also an issue in the solar cells themselves; most commercialised technology involves monocrystalline silicon, or materials including rare elements such as tellurium or indium – hence the need for photovoltaic technology from more abundant and renewable sources.

2: Literature Review

2.1. First Generation Solar Cells

A photovoltaic device uses a semiconductor to convert light energy into electrical energy. Absorption of photons equal to or greater than the characteristic band gap for the semiconductor excites electrons from the valence band (the highest occupied energy level) to the conduction band (the lowest unoccupied energy level), which can then be used to do work (discussed in more detail Chapter 3.2-3.3). The first such device was created in 1873 using only selenium coated in gold to generate a current.[1] However due to the discovery of vast oil deposits removing the need for renewables research, it wasn't until the space race of the 1950's that solar cell technology as we know it started – using silicon to create a cell of roughly 6 percent efficiency.[2] Silicon solar cells were used to extend the life of satellite operations as the batteries used at the time were very expensive. It was recognised that the efficiencies of these cells were limited by undesirable recombination of electrons and holes before charge collection, series resistances from connecting the cell to the external circuit and reflection of a significant proportion of light; problems still affecting solar cell performance today.[3]

Silicon is still the overwhelming favourite for photovoltaic (PV) power generation, with a market share of 95 %; the relative abundance of silicon being a large factor in its favour.[4] Silicon can however not function as a PV material on its own. In order for charge to be collected, a gradient needs to be built into the device along which electrons can flow. Asymmetry is built into devices by selectively doping different parts of the material, either with electron donors (to form an *n*-type material) or hole donors (*p*-type). When *n*-type and *p*-type materials are connected, a *p-n* junction is formed, which provides the necessary field to allow for photovoltaic activity (Chapter 3.3). In silicon solar cells, the *p-n* junction was designed to be as close to the surface as possible, for electrons and holes to have the greatest probability of being separated before recombination. Silicon solar cells also require a thick absorber layer, as the material's absorption coefficient is low. The low absorption coefficient is due to the band gap of silicon being indirect; which means that the maximum of the valence band and the minimum of the conduction band do not overlap. As a result the momentum of the electron needs to change upon excitation, requiring a phonon of correct momentum from the crystal. The requirement for photon and phonon to be concurrent

reduces the probability for carrier generation, thus the lower absorption coefficient. Another problem in Silicon solar cells is high series resistances, to fix this grid-like structures were set up to minimise the length an electron had to travel to be collected by the circuit, reducing the resistance. The third problem, of the reflective surface of silicon, could be solved by either adding an anti-reflective coating or etching the surface of the silicon. [5–8]

Crystallinity also plays a large part in the performance of silicon solar cells – the presence of defects can lead to extra energy levels within the band gap that can facilitate unwanted recombination and reduce the number of charge carriers collected. Thus the highest efficiencies can be obtained for monocrystalline silicon cells. Commercial efficiencies of over 25 % have been reported,[9,10] close to the calculated efficiency limit for silicon solar cells of 29.4 %.[11] The indirect nature of its band gap allows for long carrier lifetimes, increasing the probability of charge separation.

2.2. Second Generation Solar Cells

In efforts to drive price per watt down, alternative materials for photovoltaic applications were researched. Second generation solar cells use thin film inorganic technologies; these materials have direct band gaps (as opposed to silicon), which means that their absorption coefficient is larger, hence thinner absorber layers can be used, aiming to reduce the cost of production. Cadmium telluride (CdTe) had been identified as a material with a suitable band gap for photovoltaic applications, at 1.5 eV.[12] As CdTe is a *p*-type semiconductor, *n*-type cadmium sulphide (CdS) is added to form a *p-n* junction.[13] CdTe photovoltaics are the most widespread thin film technology, with a market share of 5%, and a maximum efficiency CdTe cell of over 22 %.[14]

CdTe is classed as a *II-VI* semiconductor, referring to the group in the periodic table that each constituent element comes from. The most efficient thin film technology is currently a *III-V* semiconductor consisting of gallium and arsenic. Gallium arsenide (GaAs) cells can reach efficiencies of up to 28 %.[15] However, like silicon, single crystal devices are most efficient – multicrystalline GaAs solar cells are significantly less so at 18 %.[16] Although during the early space age GaAs cells could not match silicon cells for efficiency, as their power generation improved they were favoured for extra-terrestrial applications due to their increased hardness.[17]

Another photovoltaic material recognised in the early fifties was copper indium selenide (CIS).[18] With a narrow band gap of 1.0 eV, the efficiency of these cells was limited until the inclusion of gallium, turning CIS into CIGS, could engineer the band gap to lie between 1.0 and 1.7 eV – enabling more of the solar spectrum to be absorbed.[19] The current efficiency record for CIGS is 21.7 %,[14] and as with most second generation photovoltaics the main barrier to widespread commercial use is the cost of the materials required, demonstrated in the table below.

Table 2.2.1. The cost of photovoltaics: looking at the availability and price of materials required for second generation solar cells (cost taken for 1 kg of the at least 99.9% pure element, Alfa Aesar 2019)

Element	Earth abundance (ppm)	Cost (£/kg)
Silicon	277000	600
Gallium	19	1400
Arsenic	1.8	1400
Copper	60	70
Indium	0.25	5000
Selenium	0.05	240

One way to combat the costs is by using thinner films – in the case of silicon solar cells, the use of amorphous silicon means much less material is required. Although amorphous silicon cells have an efficiency limit of only 15 %,[20] they lend themselves to a wide variety of cell architectures and potential substrates, expanding avenues of research and lowering costs of production.[21] The current efficiency record for these cells is 10 % - although the voltage is marginally higher than that of crystalline silicon solar cells, the relative thickness of the film means that the current produced is under half that of its crystalline counterpart due to low hole-mobility.[3,10]

2.3. Emerging Photovoltaics

Another method used to reduce the production cost of photovoltaic materials is to use cheaper materials, as is the case in the next generation copper, zinc, tin and sulphur (CZTS) cell that replaces the expensive and rare indium, gallium and selenium in CIGS with cheaper and more abundant elements. An added advantage of this material is that the components are less toxic. Although CZTS cells can only reach half the efficiency of their less sustainable CIGS analogue,[22] the inclusion of Se into the absorber layer can boost the efficiency to over 12 % - however if too many impurities are introduced this can reduce their performance.[23,24] High temperatures are required to make these cells, which currently limits their commercial potential.[25,26]

For large-scale production of solar cells, the device fabrication needs to be easy, and cheap. Organic solar cells are a potential technology that can be made using simple methods.[27] Two advances have enabled organic solar cells to reach competitive efficiencies; the first is the development of conducting polymers.[28] The latest organic cells use a donor-acceptor system of organic molecules, typically a conducting polymer such as poly(3-hexylthiophene-2,5-diyl) (P3HT) as the donor, as the delocalised π-electrons are ideal for photoexcitation.[29] A fullerene based small molecule is then used as the acceptor molecule, usually [6,6]-phenyl C_{60}-butyric acid methyl ester ($PC_{60}BM$); performance can be improved by using the larger fullerene $PC_{71}BM$.[30] Similarly by also switching the polymer for one with a more suitable band gap, poly [[2,6′-4,8-di(5-ethylhexylthienyl)-benzo[1,2-*b*;3,3-*b*]dithiophene][3-fluoro-2[(2-ethylhexyl)carbonyl]thieno[3,4-*b*]thiophenediyl]] (PTB7-Th), efficiencies of over 10 % can be realised.[31,32] Examples of these molecules/polymers are pictured below in Figure 2.3.1.
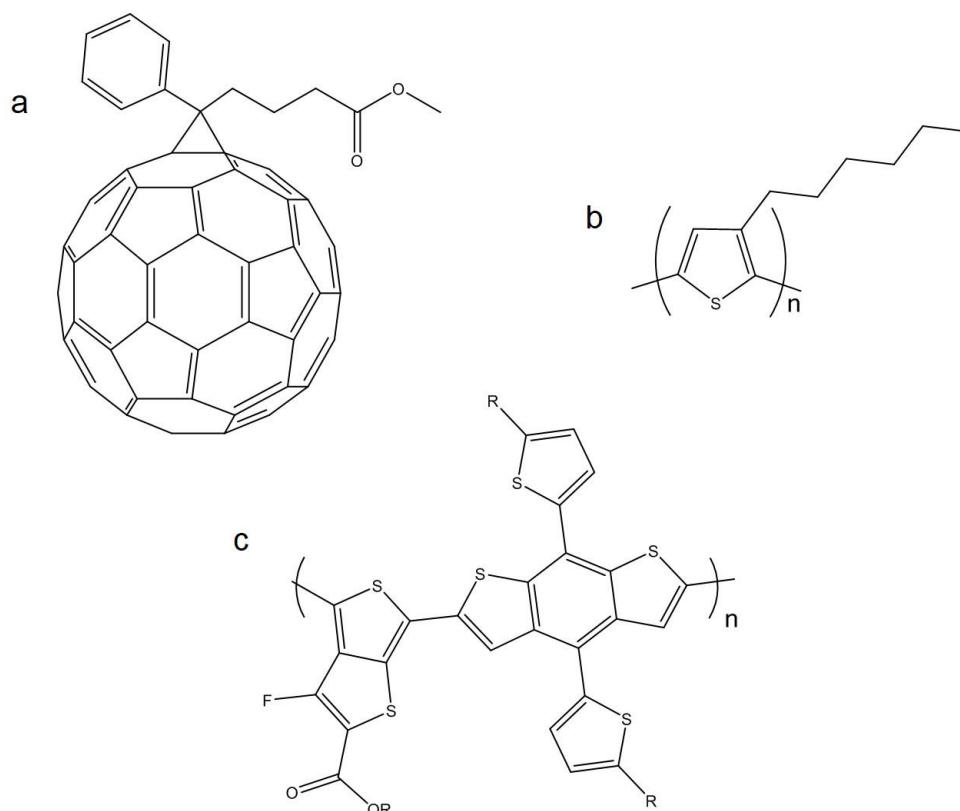
Figure 2.3.1. *Molecules and polymers used in Organic Solar Cells: a) PC$_n$BM, b) P3HT and*
c) PTB7-Th

The second of these is the use of bulk heterojunction structures. In a bulk
heterojunction (illustrated in Figure 2.3.2) the device architecture ensures that no
matter where a carrier pair is generated, the donor/acceptor components of the device
and the interfaces are within the standard diffusion length of the carriers.[27]
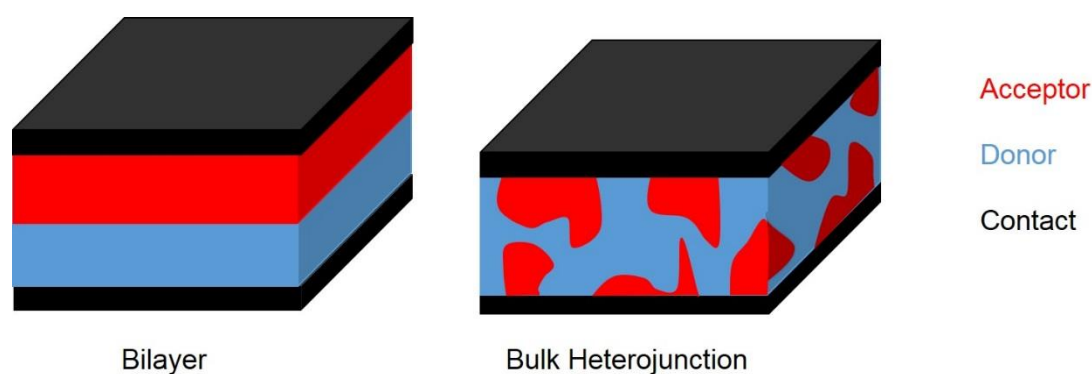
Figure 2.3.2. *A Comparison of the bilayer and bulk heterojunction device architectures*

In order to reach the highest efficiencies in organic solar cells, additives are also
required as sensitisers; either polymers, nanoparticles, dyes or small molecules,

forming ternary organic solar cells.[33] Small molecule based organic solar cells are the current efficiency record holders, with efficiencies of over 15 %.[34]

Finding suitable materials for solar cell applications involves careful consideration of the bandgap used as it determines the range of wavelengths of light that the material will absorb.[35] In CIGS and CZTS cells, additive engineering can alter the band gap to tune for improved carrier generation and photovoltaic performance. Another way is to use an absorber where the band gap depends upon its size; a quantum dot – particles that are small enough that energy levels become finite.[36] Quantum dot solar cells have the potential to exceed the Shockley-Queisser limit at a particular bandgap. The Shockley Queisser limit is the thermodynamic limit to solar cell efficiency, where the vast majority of loss is due to thermal relaxation of carriers excited by photons with energy greater than that of the band gap (Chapter 3.3). Whereas if a quantum dot absorbs a photon of energy greater than the bandgap, a second carrier pair can be generated through transferring the excess energy to a ground state electron in a process called impact ionisation.[37–39] Similar to silicon cells, quantum dot cells have high current density yet low voltage, caused by the polydispersity of the quantum dots leading to different energy levels across the absorber layer.[40] Currently this is limiting quantum dot solar cells to 10-11 % efficiency.[41,42]

The concept of Dye-Sensitised Solar Cells (DSSC) was conceived in an attempt to simulate photosynthesis.[43,44] The modern DSSC was invented in 1991, consisting of dye-coated TiO_2 nanoparticles immobilised on a transparent conducting oxide (TCO), fluorine doped tin oxide (SnO_2:F, FTO) – with a liquid redox electrolyte for the regeneration of the dye.[45] Impressively the first mesoporous dye cells were over 7 % efficient. Interest was generated due to the scalable manufacturing methods,[46] however a barrier to commercialisation is that the most common dyes use the expensive element ruthenium.[47] Alternatives have been synthesised using copper or organic based dyes,[33,48,49] with zinc-porphyrin dyes producing the highest efficiency dye cells at 13 %.[50] Other problems that face DSSC are their stability, exacerbated by the use of a liquid electrolyte which is difficult to contain. To solve this solid-state DSSC can be made, and can currently reach similar efficiencies to their liquid based counterparts.[51] It is through attempts to generate solid-state DSSC with improved absorber qualities that some perovskites were first identified as potential semiconductors for photovoltaics, and this led to their rapid rise as a distinct class of solar cells.[52]

2.4. Perovskite Solar Cells

2.4.1. The Perovskite

"Perovskite" refers to the parent structure of the material, based on the crystal structure of the mineral $CaTiO_3$. The general formula for this family of compounds is ABX_3, where A is a monovalent cation, B a divalent cation and X is a monovalent anion. The structure itself, illustrated in Figure 2.4.1.1, consists of BX_6 octahedra with interstitial A cations.
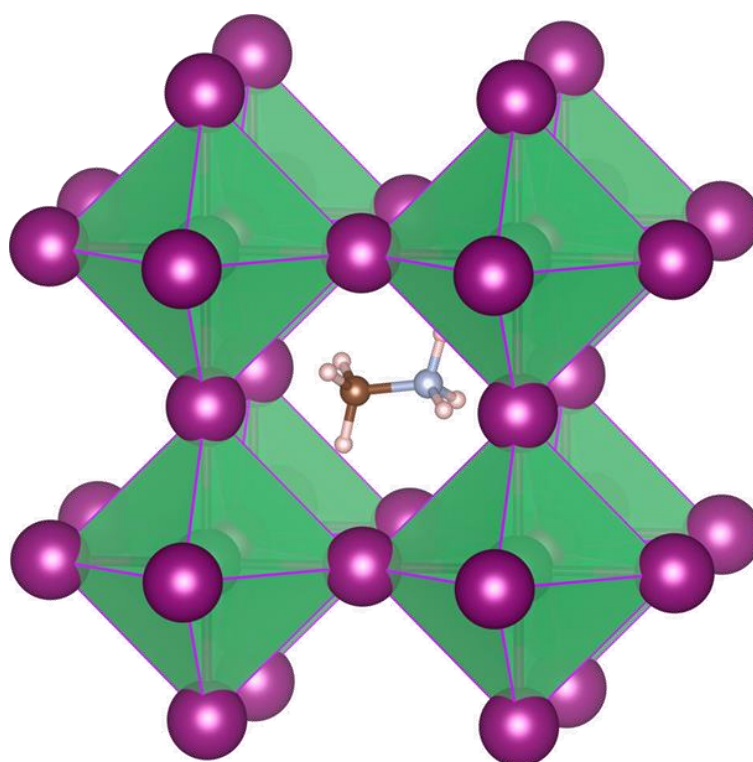
Figure 2.4.1.1. *The ABX_3 perovskite structure,* [53]

Whether or not a cubic perovskite is formed depends on the relative size of each of the constituent ions (and the temperature).[54] The Goldschmidt tolerance factor is a parameter to assess whether a given set of ions will readily form a 3-dimensional perovskite[55]:

$$t = \frac{r_A + r_X}{\sqrt{2}(r_B r_X)} \tag{2.1}$$

where r_A, r_B and r_X relate to the ionic radii of the corresponding ions from the ABX_3 formula. Equation 2.1 has recently been modified to compensate for the effect of the halide 'X' ions on contracting the radius of the inorganic 'B' cation.[56] Altering this

slightly allows for a greater radius range in the components used to make a crystalline perovskite, all of which (that have been used to create a solar cell) are tabulated in Table 2.4.1.1. For perovskite solar cells the first and most widely studied of these is methylammonium lead iodide, $CH_3NH_3PbI_3$ (MAPI), hence the name of this family of photovoltaic materials is often more generally referred to as hybrid organic-inorganic halide perovskites.[52] MAPI has a band gap of 1.5 eV – slightly higher than that of the ideal absorber band gap, which was determined to be 1.34 eV.[35,57] The current highest efficiency achieved by pure MAPI perovskite cells is over 19 %.[58] During the early development of Perovskite Solar Cells (PSC), MAPI had started with an efficiency of 3.8 %.[52] Attempts to improve the performance of the fledgling technology centred on altering the band gap. The easiest way to modify the band gap is by tuning the halide concentration; by substituting iodide for bromide in varying proportions, the band gap can be tuned from 1.5 eV to 2.3 eV.[59–61] With its 2.3 eV band gap, CH_3NH_3PbBr (MAPBr) could potentially reach a higher open-circuit voltage (V_{OC}) than MAPI – however 2.3 eV corresponds to an absorption onset wavelength of around 540 nm, meaning that half of the solar spectrum is being wasted and as such the top efficiencies for MAPBr cells are 8 %.[62] A useful side effect is that it allows for colour variation of the solar cells – important for applications like building integrated photovoltaics, where black is not always the desired colour.[59] Using chloride anions in the X position further increases the band gap above 2.5 eV, producing a white film which is not useful for photovoltaic applications.[63,64] Small amounts of chloride anions can however be used in mixed-anion setups to improve the performance of both MAPI and MAPBr perovskites – due to the size disparity chloride has a better fit with MAPBr.[65–67] Pseudohalides such as thiocyanate (SCN^-)[68] and fluoroborate (BF_4^-)[69] have also been substituted into PSCs, although only as additives to improve performance (the use of additives will be discussed in more detail later). Computational studies have suggested that PF_6^- could also be used to form a cubic perovskite, however at the time of writing this has not been tested experimentally.[70]

Table 2.4.1.1. A list of A, B and X cations and anions that have been used for Perovskite Solar Cells. Those marked with a * have only been used as additives and do not form 3D perovskites on their own

A^+	B^{2+}	X^-
Methylammonium [52]	Lead [52]	Iodide [52]
Formamidinium [71]	Tin [72]	Chloride [65]
Caesium [73]	Antimony [74]	Bromide [75]
Guanidinium* [76]	Bismuth*[77]	Thiocyanate [78]
Hydrazinium* [79]	Titanium*[80]	Fluoroborate [69]
Azetidinium* (Chapter 5)[81]		
Imidazolium*[82]		
n-butylammonium* [83]		
Ammonium*[84]		
Benzylammonium*[84]		
Rubidium*[85]		

Computational studies have proposed a wide range of potential elements/compounds for use in PSCs. By using an approach based on the perovskite tolerance factor, the resulting speculative perovskites can be further narrowed down by attempting to computationally derive the band gap.[56,70,86–88] This has enabled practical studies to focus on compounds that are likely to exhibit at least some photovoltaic activity.

Formamidinium (FA), with an ionic radius of 253 pm (compared to 217 pm for methylammonium), is the most common alternative for the A-site cation. It forms a 3D perovskite with a 1.43 eV bandgap, allowing for a greater absorption of the solar spectrum.[71] FAPI however requires higher processing temperatures, as the phase transition from the inactive yellow phase to the active black phase occurs at 140 °C (which is not stable at room temperature), as opposed to 100 °C for MAPI.[89,90] Caesium (Cs),[91] guanidinium (GA),[92] hydrazinium (HA)[79] and azetidinium (Az) ([81], the topic of Chapter 5) have all been used as the sole A-cation with Pb and I, however

due to their size do not form a stable 3D perovskite limiting the efficiency, and thus are more commonly used as additives in a MAPI based parent structure. The ionic radius of caesium lends itself more readily to $CsPbBr_3$ perovskites, reaching efficiencies of over 6 %. [93–95]

Mixing the A-site cations is another route to band gap engineering, most notably in the case of FA.[96] The highest efficiencies can be achieved by using a stoichiometric majority of FA compared to MA, reducing the annealing temperature required (with respect to FAPI) and producing solar cells with an efficiency of over 18 %.[97] Formamidinium and methylammonium are also completely phase-miscible – meaning that no matter what the ratio of FA to MA, the resulting perovskite will always form a solid solution.[96] It is even the case that a MAPI perovskite can be converted to FAPI through cation exchange as a reversible process.[98] This is the only combination of cations (at the time of writing) that is known to form a solid solution at all molar ratios, all the others mentioned above and in table 2.4.1.1 undergo phase separation at certain substitution ratios. Phase separation is likely caused by the fact that the others do not form 3D perovskites (with lead and iodine) due to their ionic radius, thus as the concentration gets high enough it forms a separate, non-3D phase within the MAPI structure. Nevertheless, the performance of MAPI has been shown to improve on the addition of small amounts of most cationic additives, credited largely to improvements in open-circuit voltage[76] or film morphology.[79,84] The effect of small amounts of cationic additives on MAPI is studied in Chapter 7.

With the wide potential of the ABX_3 structure, the combinations are not limited to mixing at just one of the sites. Mixed-cation and mixed-anion systems have been used to great effect, and these result in the perovskite solar cells with the current highest efficiencies. $Cs_{0.05}((FA_{0.83}MA_{0.17})Pb(I_{0.83}Br_{0.17})_3)$ and the quad cation version including Rb can reach efficiencies of over 22 %.[99,100]

The effect of substitution causes distortion of the MAPI lattice.[101,102] If the substitution ratio is high enough this leads to the previously mentioned phase separation – however it does not necessarily have a negative impact, if the non-3D phase is suitably crystalline. 2D perovskites are formed by larger cations such as *n*-butylammonium (*n*-Bu), in which single sheets of PbI_6 octahedra are separated by layers of the organic cation. This is represented pictorially in Figure 2.4.1.2.

They can be identified by a peak in the XRD pattern at low 2θ values of 5-6 °, as this reflection originates from the gaps between 3D layers – this spacing is larger than that of the 3D layer, which typically appears at 2θ values of around 13-14 °.[103]
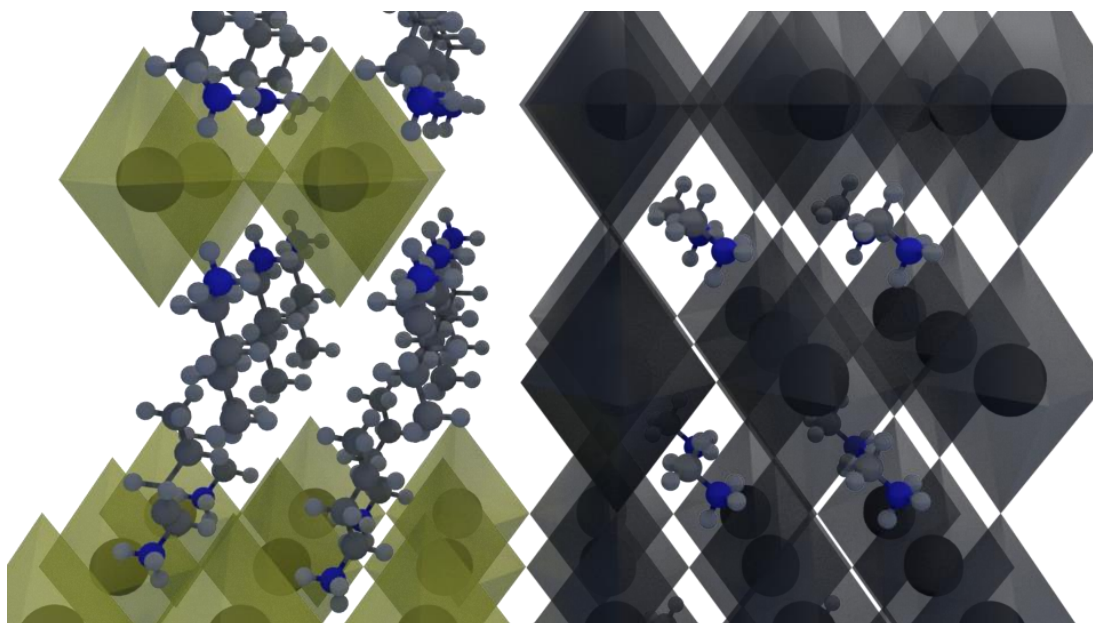
Figure 2.4.1.2. A pictorial representation of 2D (left) and 3D (right) perovskites

2D perovskites have advantages and disadvantages – the most notable disadvantage being that an interrupted lead iodide structure does not allow for efficient charge transfer.[83] This can be overcome by hot-casting the material so that the inorganic plane runs vertically between the contacts, enabling charge transfer through the layers that is not blocked by the organic buffer layers. Changing the orientation of the perovskite can improve the efficiency from 4.73 % to 11.6 %.[104] The advantage of 2D perovskites is that the use of large hydrophobic cations can boost the moisture resistance of the cell, which means that PSC made using 2D materials maintain a greater proportion of their photovoltaic performance over time.[83]

If the molar proportions are controlled correctly, 2D elements can be introduced into 3D perovskites, combining the efficiency of the 3D PSC and the stability of the 2D. Phenylethylammonium (PEA), shown in Figure 2.4.1.3, shares a similar structure to *n*-Bu and 5-AVA, *i.e.* a long organic tail that can occupy the space between the lead iodide sheets. Like *n*-Bu, substitution of MA for PEA causes horizontal buffer layers of PEA cations, inhibiting effective charge transfer and reducing the efficiency of MAPI to 4.73 %.[105] Once again, special processing methods can lead to the vertical alignment of the sheets. Adding thiocyanate (SCN) to the precursor solution can

achieve this, and boost the efficiency to 11 %.[106] The *n* value is a parameter used to describe the 3D:2D ratio; which roughly translates to efficiency:stability – using a large *n* value of 60, a 15.36 % efficient cell can be produced.[107] PEAPI has also been used as a 2D capping layer for the triple-cation perovskite, which improves stability whilst still keeping the efficiency above 20 %.[108]
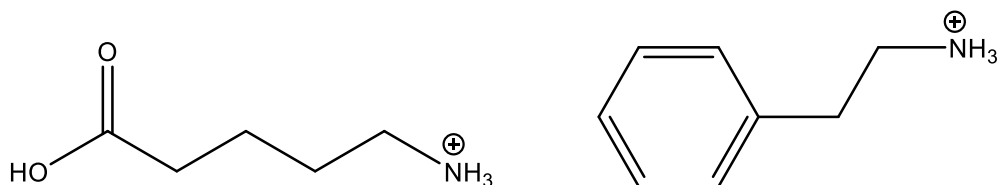
Figure 2.4.1.3. *The chemical structure of 5-Ammonium valeric acid (5-AVA) (left) and phenylethylammonium (PEA) (right)*

Using the molecule 5-ammonium valeric acid (5-AVA, Figure 2.4.1.3), an 11 % efficient solar cell was able to maintain its performance over the course of a year.[109] At the time of writing these perovskites and methods have not been around for long enough for longer timescales of stability to be investigated. Although the stability for these cations is high, charge transfer is inhibited by the large spaces between the 3D perovskite layers. By using a shorter chain diamine-based cation the 3D layers can be brought closer together, improving the efficiency whilst maintaining a high (albeit not as high) stability.[110]

B-site replacement or substitution has also been examined, though to a lesser extent. The next element up in group IV of the periodic table, tin, has been the first choice as a replacement for lead. $MASnI_3$ and $FASnI_3$ have suitable band gaps of 1.28 eV and 1.4 eV, however efficiencies have not been able to exceed 7 %.[111–113] Due to the increased propensity of Sn to oxidise from Sn^{2+} to Sn^{4+}, tin-based PSC are much less stable than their lead analogues.[114] Stability issues can be partially overcome using mixed-metal perovskites. A 50:50 ratio of Sn:Pb can boost the efficiency to 13.6 %.[115] Antimony and bismuth have also been identified as potentially being suitable metals for lead-free PSC.[116] Using MA as the A-site cation, for antimony the band gap has been deemed to be unsuitably high at 2.17 eV,[117] and for bismuth it is slightly lower at 2.04 eV – but at the time of writing no cells have been made using these yet.[116] If Cs is used instead of MA, bismuth based PSC can reach efficiencies of just over 1 %.[118]

Bismuth and antimony can be combined with a metal of +1 valence to form double perovskites, a compound with the general formula $A_2BB'X_6$. Computational studies

have suggested that copper, silver and gold would be appropriate.[119] $Cs_2BiAgBr_6$ is touted as a more stable alternative to MAPI, yet its band gap of 1.85 eV is significantly higher than the optimum (1.34 eV) – so there is still a large portion of the solar spectrum left unabsorbed by this compound.[77,120] The resulting PCE for $Cs_2BiAgBr_6$ is 1.44 %.[121] Titanium can also be used as the B-site metal in double perovskites, improving stabilised efficiencies to over 3%.

In summary, the flexibility of the ABX_3 structure allows for manipulation of the cell properties by either varying the primary cations/anions or through the use of additives. Therefore the search for new potential ions for PSC is of great importance. Many ions have been identified through computational studies that have not yet been used. Some, like aziridinium,[122] are unlikely to be used as the strain on the cation makes them difficult to use in practice due to instability. Others such as dysprosium and samarium (for the B-site), are simply too rare and expensive.[56] With a focus on high efficiencies, some cations like acetamidinium and tetramethylammonium are unlikely to form high-efficiency PSC on their own due to their size, however may be useful as in mixed cation devices.[123] A recent shift in research focus from breaking efficiency records to breaking stability records may result in some of the less conventional ions (*i.e.* ones that will not form a highly efficient PSC on their own) being employed.

2.4.2. Cell structure

Perovskite solar cells were originally developed from dye-sensitised solar cells, therefore the first PSC inherited the structure of DSSC, which involved a mesoporous TiO_2 scaffold, along with planar TiO_2 coated glass.[124] The majority of hybrid organic-inorganic perovskites are ambipolar, which means they exhibit both *n* and *p* type characteristics, and can therefore reach relatively high efficiencies on their own, without the need for any other layers.[125] The efficiency can be improved by the usage of hole/electron selective layers. These contact layers can improve the separation of charge carriers in PSC by facilitating or blocking the intended carrier.[126] As discussed in the previous section, the band gap of the perovskite material is easily manipulated, therefore careful selection of the materials used for the contact layers (also called blocking layers or transport materials) is essential.

Photovoltaic carrier generation promotes an electron to the conduction band and results in a hole in the valence band – this is where the basis of contact layer selection

begins. An example of a band level diagram for a cell with a TiO_2 electron transport material (ETM, electron selective contact) and the small organic molecule 2,2',7,7'-tetrakis(N,N'-di-*p*-methoxyphenylamine)-9,9'-spirobifluorene (Spiro-OMeTAD) as the hole transport material (HTM) is shown below.[127] The energy levels for each material are measured based on a clean surface in a vacuum; when used in devices the effects of band bending and impurities can lead to significant variation in the actual values. As a rough guide for contact layer selection they can be useful, because if the difference in energy levels is too great it increases the probability of recombination at defect energy states that lie between them.
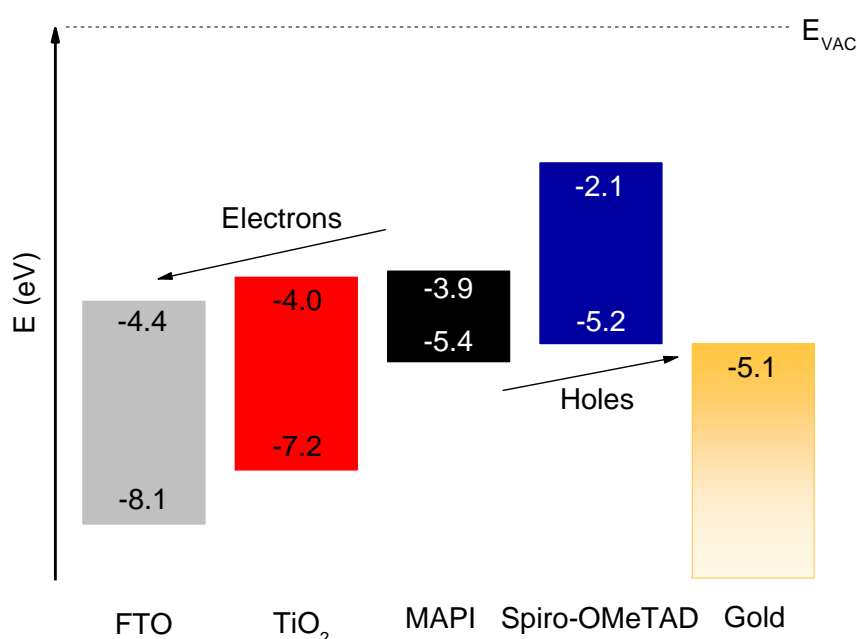
Figure 2.4.2.1. *Energy level diagram for a standard structure PSC relative to the energy of the vacuum level*

Mesoporous structures currently hold the efficiency and stability records for PSC.[99,109] Efforts were made to remove the mesoporous layer as it required an additional high temperature processing step, thus making the energy payback time for the cell longer.[128] ZnO is an alternative ETM that only requires processing at 150 °C as opposed to 500 °C for TiO_2 – efficiencies of PSC using ZnO are over 15 %.[129] Using SnO as the ETM can improve the efficiency of MAPI cells to 18 %, the improvement was attributed to better band alignment with the perovskite absorber layer than the TiO_2 and ZnO.[130] Chemical bath deposition (CBD) is also used for the deposition of ETM materials, which reduces the required processing temperatures below 100 °C - opening the possibility for PSC to be made on flexible substrates.[131] CdS has been

deposited by CBD and when tested as an ETM can produce cells with 10.3 % efficiency, which while scalable introduces the expensive and toxic element cadmium into the device.[132] Furthermore it is less efficient than SnO deposited in the same manner.[133] Although complicating the fabrication process, passivating the surface of the ETM can prevent surface recombination and improve the stability of the cell.[134] Very thin films of fullerene based molecules such as Phenyl C_{61}-Butyric acid methyl ester (PCBM) or Al_2O_3 (less than 5 nm thick) coated on the surface of an *n*-type oxide layer can boost the open-circuit voltage of the cell, with a mixture of PCBM and Poly methyl methacrylate (PMMA) increasing the V_{OC} of the triple cation perovskite to 1.18 V.[135,136] A scaffold layer of Al_2O_3 can also be deposited within the perovskite precursor, allowing for lower temperature deposition of the mesoporous layer.[137]

All the aforementioned devices use the same HTM, the small molecule Spiro-OMeTAD (Figure 2.4.2.2.). An artefact of DSSC,[138] Spiro-OMeTAD is the most commonly used HTM. As with mesoporous TiO_2 it is used in the highest efficiency and stability cells.[99,109] However to be used, Spiro-OMeTAD requires doping from cobalt or lithium salts to improve the conductivity – which has been linked to degradation of the perovskite layer.[139,140] Stability issues, combined with the price of Spiro-OMeTAD (291 £/g as of April 2019 (Merck)) has led to a search for alternative HTM materials.
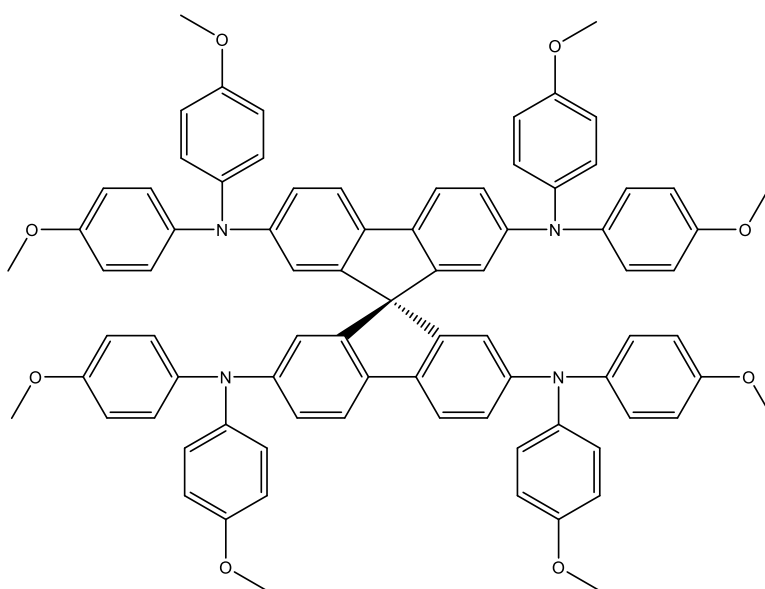
Figure 2.4.2.2. The chemical structure of Spiro-OMeTAD

Other examples of organic hole transport materials are poly-tri arylamine (PTAA) and poly 3-hexylthiophene (P3HT), which can be used to make devices with similar

efficiencies to Spiro-OMeTAD based cells.[141–143] These are however still prohibitively expensive for upscaling production, at 1800 £/g and 380 £/g (Merck) respectively. CuI is an attractive alternative as it is around 0.2% of the cost of a Spiro-OMeTAD layer.[144] The valence band edge is not as well aligned to MAPI as Spiro, leading to both voltage and current losses, limiting the efficiency to 7 %.[145] By using an interlayer of the better aligned poly(3,4-ethylenedioxythiophene) polystyrene sulfonate (PEDOT:PSS) the band edge mismatch can be overcome and the cell PCE more than doubled.[146] PEDOT:PSS can also be used as the sole HTM to produce high-efficiency cells, although its use requires an overhaul of the cell structure.[147] PEDOT:PSS is dispersed in water – if deposited on top of MAPI it would dissolve the perovskite.[148]

To avoid dissolution of the perovskite an 'inverted' structure is used, in which the HTM is deposited first. The inverted structure has proven advantageous as all the layers can be deposited at lower temperatures.[149] Perovskite crystallisation on PEDOT:PSS films leads to a film with fewer pinholes and can produce PSC of up to 18 % with high reproducibility.[150] Yet the long term stability of these devices is hindered by the instability of the PEDOT:PSS layer.[151,152] Inverted PSC made using PTAA are also relatively unstable, but this can be improved with the addition of an MoS_2 layer on top of it to form a binary HTM system, extending the period within which the cell retains 80% of its efficiency from 171 hours to 568.[153] Further advantages of inorganic HTM layers are that they are often cheaper and more easily processable – to this end NiO_x was introduced as a more stable HTM for inverted cells in 2014, with starting efficiencies of 7 %.[154] Although cheap and solution processable, NiO_x still requires a high temperature annealing step.[155] The band edge of NiO_x aligns fairly well with MAPI (Figure 2.4.2.3) and can reach efficiencies of 16% - this can be improved to 19 % for the triple cation perovskite by doping the NiO_x with magnesium, lithium, and more oxygen.[156]
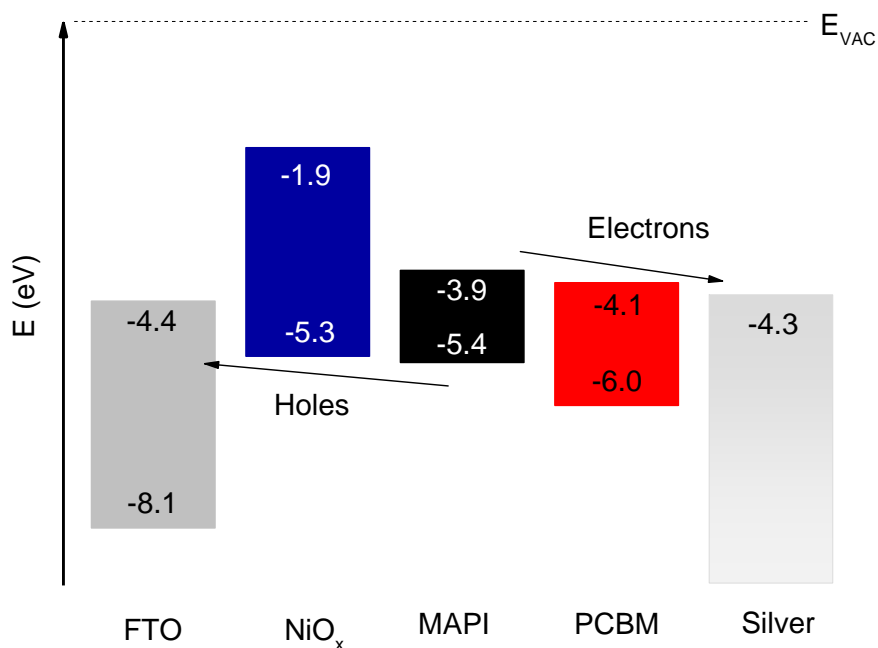
Figure 2.4.2.3. *Energy level diagram for an inverted structure PSC relative to the energy of the vacuum level*

The doping of the nickel oxide layer to improve band alignment is not limited to magnesium and lithium; copper, silver, and yttrium have also been used, resulting in improved efficiencies through an increase of the fill factor.[157–159] As with the standard cell architecture, the bottom transport layer in the inverted cell can also be passivated. In the case of NiO_x, a KCl treatment has been suggested to reduce recombination at the interface enabling an increase in the open-circuit voltage to 1.15 V.[160] CuSCN is an example of an HTM that has been used in both standard and inverted PSC. Deposition of perovskite films on the CuSCN layer leads to an improved perovskite morphology and thus cells exhibit better performance than the standard architecture analogues.[161,162]

The most commonly used ETM for inverted PSC is PCBM, a fixture since 2013.[163] Either the C_{60} or C_{71} variant can be employed, with the latter giving marginally better performance.[164–166] The effect of an alkyl chain on the ester has also been probed (in PCBM it is simply a methyl group). Tian *et al.* explored the use of a 2-ethylhexyl group on the ester and discovered that it not only improved performance but also long-term stability.[167] There are few inorganic alternatives for the ETM as a top contact due to the difficulty of depositing the materials on top of the perovskite layer. SnO_x and Al-doped ZnO (AZO) have been used, however these still require a fullerene

derivative layer.[168] These inorganic layers can act as interlayers between the fullerene and the metal electrode and also enhance the long term performance of the cell.[169] To overcome the requirement for the fullerene ETM layer, nanocrystals of the inorganic material can be used, as these can be deposited from solvents that will not damage the perovskite layer.[170] Both SnO_x and CeO_2 have been used in this manner, reaching efficiencies of 12 and 16 % respectively. [170,171]

The final layer to consider is the metal contact, usually the expensive metals silver or gold. Multiple metals can also be used to improve band-edge alignment, for example electrodes based on a thin layer of Ca followed by a thicker layer of Al.[150] By drop-casting the perovskite layer through a porous carbon film the need for an HTM and a metal electrode is eliminated.[172] Carbon based PSC usually use both a planar and mesoporous TiO_2 layer as the ETM,[173] which can then be followed by a second mesoporous layer of ZrO_2 before the carbon and the perovskite.[174] The efficiency of carbon cells using MAPI is lower than that of the planar or inverted architectures, yet they tend to maintain a greater proportion of their efficiency for a longer time.[172–175] $Cs_{0.05}(FA_{0.83}MA_{0.17})PbI_{0.83}Br_{0.17}$, the perovskite that produces the highest efficiencies in the other cell architectures also provides a performance boost to PSC using a carbon electrode. With additional layers of Al_2O_3 and NiO (as opposed to ZrO_2) an efficiency of 17 % for a carbon PSC has been recorded, maintaining 90% of its initial efficiency after 1000 hours.[176] Figure 2.4.2.4 shows an illustration of the four main architectures for a perovskite solar cell: planar, mesoporous, inverted and carbon based.
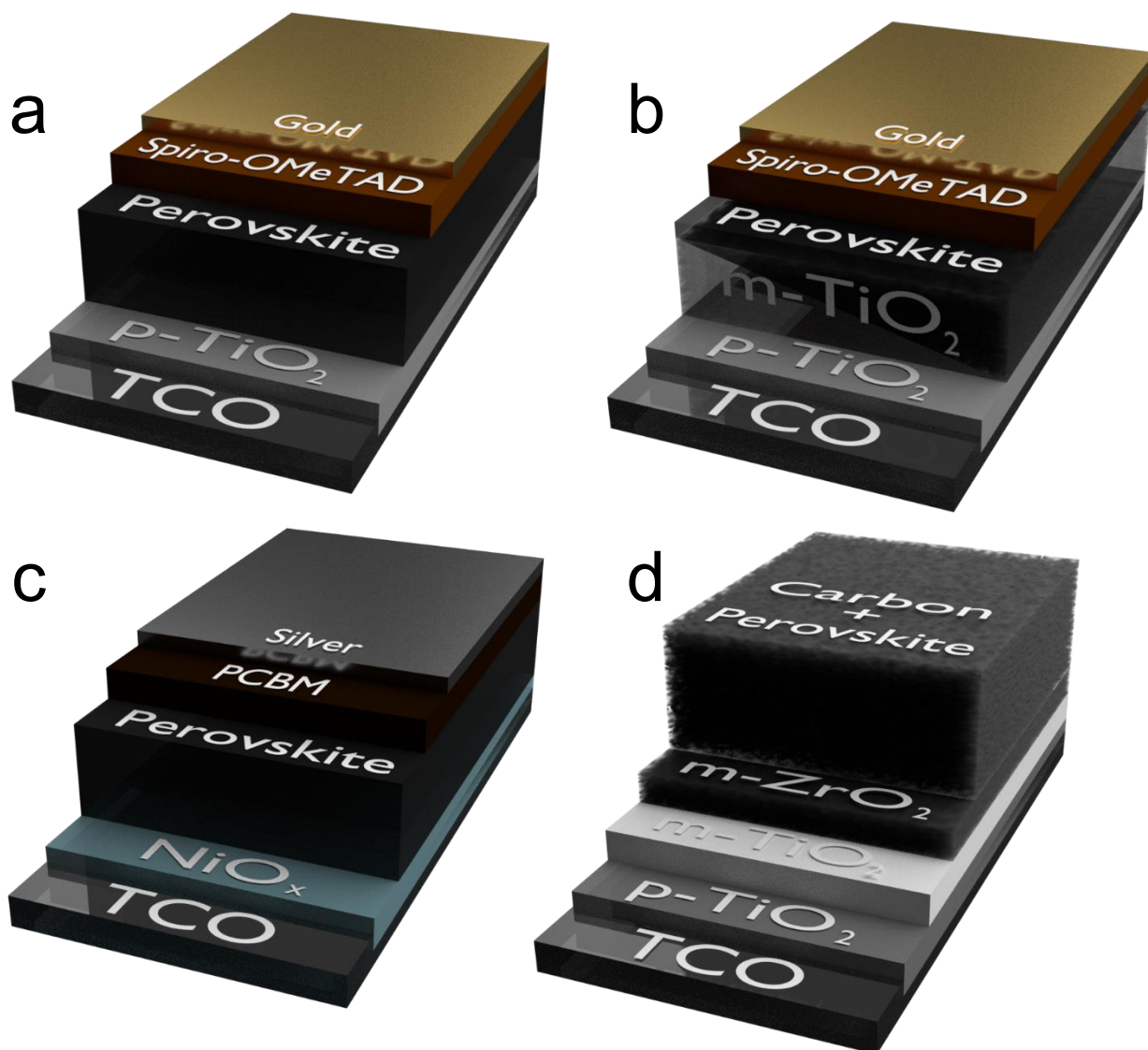
Figure 2.4.2.4. Diagrammatic representation of examples of the four main cell architectures: a) planar, b) mesoporous, c) inverted and (d) carbon (layers not to scale)

2.4.3. Constructing the cell

The chosen architecture determines the method of cell construction. As perovskite solar cells were a development of DSSC, they also share many of the same fabrication methods.[52] One major advantage of PSC compared to many other photovoltaic technologies is the use of solution based processing, enabling facile deposition and opportunity for scale-up.[177,178] Regardless of cell architecture, the initial layer on top of the transparent conducting oxide is usually deposited by spin-coating.[179–181] However spin-coating has some significant issues for the development of PSCs; most notably that it is not a scalable technology. Furthermore the importance of the perovskite morphology for efficient charge transfer cannot be understated, therefore it

is necessary that the material onto which the perovskite is to be deposited is suitable.[182] Spray pyrolysis is another popular choice for the deposition of the primary layer, another continuation of the DSSC manufacturing methods.[52] Spray pyrolysis requires high annealing temperatures, which not only increases energy payback time, but prolonged exposure to high temperature can reduce the conductivity of the TCO.[99,100] Atomic Layer Deposition (ALD) allows for precise thickness control and pinhole free transport materials, which reduces the possibility of short-circuiting the cell and increases shunt resistance.[183] Although it can produce PSC with a high efficiency, its use is currently limited to inorganic transport layers.[184,185] Two lower temperature methods for the deposition of the first blocking layer are electrodeposition and chemical bath deposition (CBD); the latter can be used for both planar and scaffold layers.[131] The electrodeposition of TiO_2 can produce an ETM that provides full coverage of the substrate, which as it prevents pinholes and therefore alternate paths for charge transfer increases the shunt resistance within the cell.[186] Similar results are observed with the chemical bath deposition of titania.[187] Although electrodeposition and chemical bath deposition are more suited to scale-up than the previously discussed methods, printing all the layers would allow for roll-to-roll production of PSC, dramatically increasing the output. PSC made using printing tend to be of the carbon cell architecture (Figure 2.4.2.4.d), as all the non-perovskite layers can be printed before the deposition of the absorber layer.[172,176] A study by Zhang *et al.* compared PSC made using printed TiO_2 layers to those prepared by spin-coating and CBD.[188] They found that layers deposited by screen-printing were rougher, with larger pinholes than their counterparts and that those deposited by CBD provided the best morphology for perovskite deposition.

The initial layer is the substrate for perovskite deposition. An imperfect layer will affect perovskite growth, morphology and in turn cell performance.[182] Perovskite morphology is still most affected by its own deposition method, hence there has been a large amount of research dedicated to perfecting this step.[189–192] The main perovskite deposition methods are illustrated in Figure 2.4.3.1, grouping methods into four main categories: solution based; vapour based; one-step and two-step.
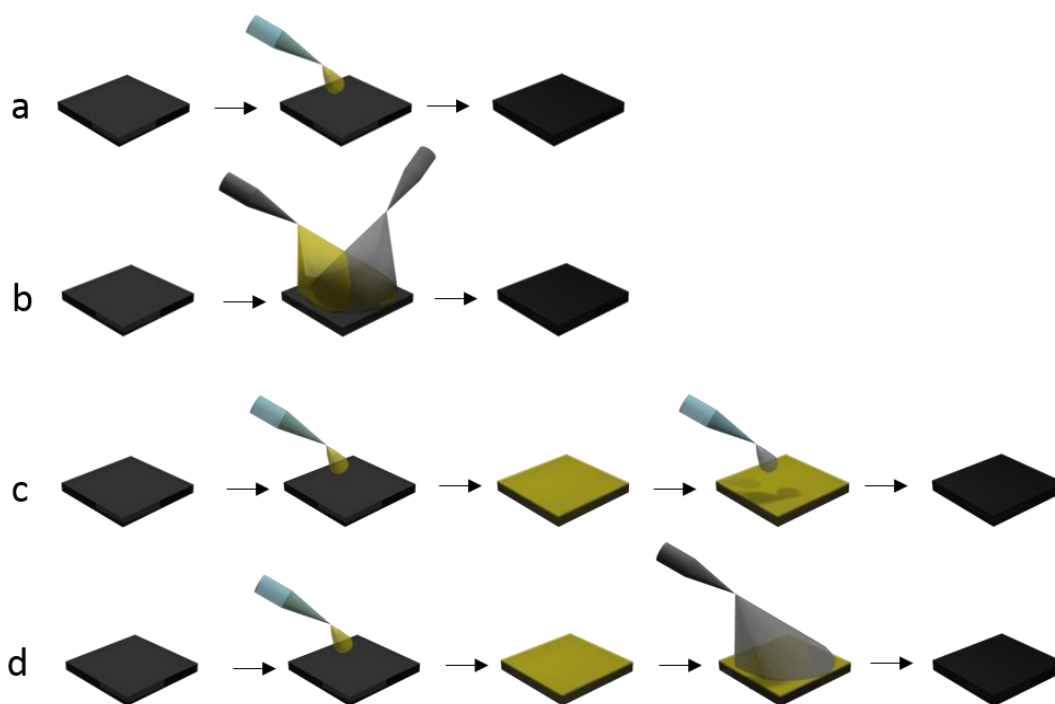
Figure 2.4.3.1. *Illustration of perovskite deposition methods: a) single-step spin coating; b) dual source vapour deposition; c) two-step spin-coating, and d) two-step vapour assisted deposition*

One-step solution based spin-coating is probably the most widely used of these methods, largely due to its facile nature and the ubiquity of spin coaters. An early development of one-step deposition was the use of an antisolvent during the spin-coating process in order to improve the morphology and reduce the annealing time.[193] The deposition of an antisolvent rapidly induces crystallisation of the perovskite, resulting in uniform films with reduced numbers of pinholes, and therefore enhanced performance, as this improves the interfaces between layers allowing for more efficient charge transfer.[194] An absence of pinholes also prevents short-circuiting in the cell. Common antisolvents include toluene,[195] chlorobenzene,[196] hexane[197] and ethyl acetate[198] – all of which have a similar effect on the perovskite crystallisation, the biggest result of this is an improved fill factor as the interfaces between layers are improved.[199] Mixed antisolvent systems have also been tested.[200] It was determined that with one mixed anti solvent, ethyl acetate and *n*-hexane, a combination of the dense crystallite formation caused by the former and the control of annealing rate caused by the latter lead to a marked improvement in cell performance.[201] For 2D perovskites the deposition is altered slightly; the perovskite solution is often deposited onto a heated substrate in a process known as hot-casting, which ensures the correct alignment of the 2D sheets.[104]

Two-step deposition, in which a PbI$_2$ film is deposited before being exposed to the organic cation in solution, either by dipping, spin-coating or spraying, was developed as another processing option to improve morphology and cell efficiency.[177,202,203] Two-step synthesis allows for a greater control of crystal growth, and by altering variables such as substrate temperature,[204] solvent additives,[150] and solution concentration[205] the density and uniformity of the perovskite crystals can be improved, resulting in increased efficiencies. Two-step deposition has also benefited the fabrication of FAPI cells – by including a small amount of methylammonium iodide in the FAI solution the photo-active α phase of FAPI can be stabilised at lower temperatures.[206] Interestingly, FAPI can be made indirectly through a two-step process by depositing MAPI then dipping in FAI (and *vice versa*), with uniform exchange showing that the cations in the perovskite are also mobile.[98] Mixed-cation films created by two-step deposition are rarer, possibly due to the differing crystallisation kinetics of the different cations during a long dipping step.[81] In the two-step method any excess solvent left in the lead iodide can be removed with a further antisolvent step.[207]

As previously mentioned, spin-coating is not suitable for mass production of PSC, so several other methods of perovskite production have been tested. The first of these involves the complete vapour deposition of the perovskite layer, using sources of both the inorganic and organic components – removing the edge effects associated with spin-coating and produces very flat perovskite films producing improved interfacial contacts.[178]

Electrodeposition has been identified as another scalable technique for the fabrication of perovskite solar cells.[208] Although it reduces the required temperature and the associated energy costs, it does involve the necessity of another step, as the lead precursor is most commonly deposited as PbO.[209] The conversion of PbO to PbI$_2$ requires the use of HI, increasing the environmental risk involved with the processing. Kosta *et al.* developed a method using I$_2$ in an ionic liquid for the direct electrodeposition of PbI$_2$ and prepared PSC with 9 % efficiency, competitive with those produced via PbO.[210,211]

Printing is the ideal deposition method for large-scale manufacture and eventually commercialisation of PSC. A key feature of this is the reduced Pb waste involved in production.[212] Usefully, these methods are more appropriate for all cell architectures,

which means the choices of contact materials and absorber material can be optimised to maximise efficiency.[213] Slot-die coating is one of the most common printing methods for PSC, in which the perovskite is stored in a reservoir above two blocks that control the flow of the solution.[214] The dynamics of perovskite crystallisation are greatly changed by printing the precursor solution, although the parameters may sound similar, *e.g.* coating speed and solution viscosity/concentration.[215] Uniform removal of the solvent is critical for good morphology when the perovskite is printed over a large area, otherwise the absorber layer retains many large pinholes; this can be aided by gas-quenching or substrate heating.[216,217] As with the previously discussed spin-coating methods, printing can also be done in either a one-step or two-step fashion, the efficiency records for both being around 15 % - near to commercially viable performance.[216,218] Household inkjet printers have also been modified for use in the fabrication of PSC, but with lower efficiencies than the slot-die equivalents at 12%.[219] Even with multiple printing passes, large pinholes are still endemic with PSC made using this procedure – a vacuum-drying step is required to improve the morphology, boosting the efficiency to over 17 %.[220,221]

The carbon cell architecture mentioned in the previous section is heavily reliant on printing, indeed it is one of its main features/advantages.[174] The absorber layer in these cases is drop-casted into the printed carbon electrode and allowed to infiltrate.[222] Where in spin-coating a large proportion of the solution is wasted (by being spun off the substrate in the machine), for drop-casting into the carbon the amount required is greatly reduced, typically less than 2 μL is needed, as opposed to 100 μL.[176] Fully printable carbon based solar cells are often hole-conductor free and the porous carbon acts as the electrode, removing the requirement of any more materials or processing steps.[175,223] A transport material on top of the absorber layer reduces the scalability, as it interrupts the printing process for a spin-coating step.[224]

As the standard architecture tends to use small molecule organic HTM for high efficiencies, it limits the possibilities for deposition, mainly to spin-coating.[225] With the inverted architecture the top contact can be inorganic which although also usually deposited by spin-coating, can be deposited by ALD to enhance HTM quality.[226] Removing pinholes and imperfections from this layer can enhance the stability of the PSC by reducing the number of sites where unwanted molecules (such as water) can diffuse into the cell.[227]

This leads us to the deposition of the final essential layer for the PSC, the contact layer that completes the circuit. With carbon based cells the already printed porous carbon is used as the external contact, however further carbon layers can also be printed on top of the perovskite or transport material after synthesis.[95,175] For the other cell architectures contact deposition is highly reliant on energy intensive thermal evaporation of one or multiple metals.[52,125,165,228–230]

2.4.4. Problems and Challenges with Perovskite Solar Cells

As of yet only the advantages and improvements of PSC have been discussed. Unfortunately before large scale production there are a few fundamental problems that need to be solved. Firstly, and perhaps most importantly, is the stability of the absorber layer. To be competitive with silicon they need to maintain 80 % of their efficiency over 20 years, and at the time of writing stability has been shown over one year by measuring the efficiency at regular intervals (that being said, the technology is not yet 20 years old).[109]

The first problem encountered when measuring a perovskite solar cell is a phenomenon known as hysteresis, in which the forward and reverse scans do not completely overlap (illustrated in Figure 2.4.4.1).
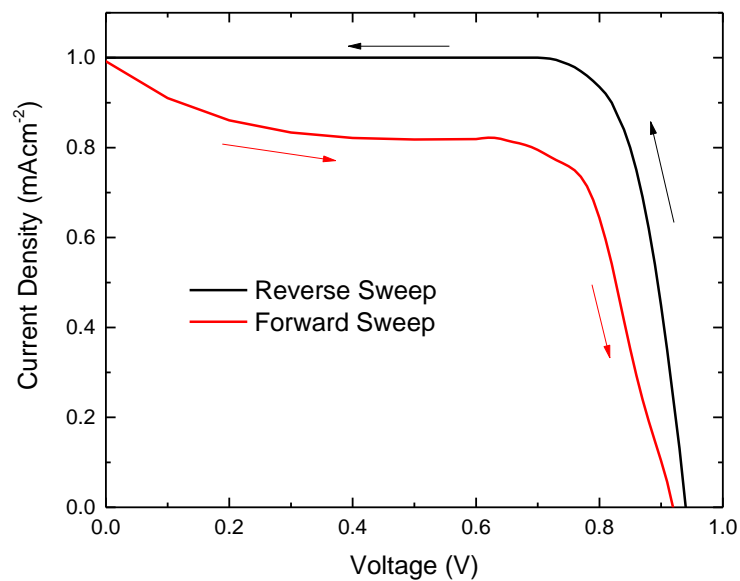
Figure 2.4.4.1. *A JV curve showing hysteresis in PSC*

If hysteresis is present in the solar cell, it does not present a true efficiency, which needs to be taken using a stabilised efficiency measurement. The ratio between the two curves has been quantified as the hysteresis index (HI) – although its efficacy has been questioned due to it being based on a transient measurement (the JV sweep), which will be less reliable than steady state measurements:[231]

$$HI = \frac{J_R\left(\frac{V_{OC}}{2}\right) - J_F\left(\frac{V_{OC}}{2}\right)}{J_R\left(\frac{V_{OC}}{2}\right)} \qquad (2.2)$$

where J_R ($V_{OC}/2$) is the photocurrent at the voltage value in the reverse scan which is half that of V_{OC}, and J_F ($V_{OC}/2$) is that of the forward scan. The lower the value, the less hysteresis in the cell. Experimentally, hysteresis is affected by variables such as the scan rate and pre-treatment time/voltage.[232,233] Although the cause of hysteresis is yet to be definitively proven, many different theories have been proposed, focussing on properties of the absorber layer itself such as ferroelectric behaviour,[234] or trap states that hold and release charge on the timescale of the experiment.[235] The most widely accepted theory is that hysteresis is caused by ion migration in the perovskite lattice.[236–239] Either illumination or the applied voltage can cause the diffusion of iodide ions resulting in a changed electric field within the cell, altering the JV behaviour on the return sweep.[240] Low-temperature Transient Photovoltage measurements have shown that recombination at the interface of the perovskite with TiO_2 is a major cause of hysteresis, a process that can be affected by ion diffusion.[241] Changing the illumination intensity or applied voltage affects the bias present on the perovskite solar cell, which will affect the band bending (Section 3.3).

Several different experimental approaches have been trialled to suppress hysteresis. Several reports have shown that changing contact layers, or using a completely different cell architecture can lead to reduced hysteresis.[242] Hysteresis is most prominent in planar cells based on TiO_2 and Spiro-OMeTAD; addition of a mesoporous TiO_2 layer, replacement of the TiO_2 for SnO_2 or using inverted/carbon cells regardless of which contact layer is used has been shown to reduce or eliminate hysteresis.[165,185,193,223,243] It has however recently been shown that *all* cells exhibit hysteresis, and changing the architecture simply shifts the temperatures and scan rates at which hysteresis is visible; again this observation has been linked to iodide diffusion

and also how the double layer at the interfaces changes what is measured, as injection or recombination are modified if ion distribution changes.[244,245]

Another option is to alter the perovskite itself. Mixed component systems seem to universally possess a lower hysteresis than systems with no mixing, be it mixing in the A, B or X site.[59,246–249] A computational study by Ghosh *et al.* into the effects of cation mixing showed that the inclusion of small molar percentages of Rb into FAPI distorted the perovskite lattice to the extent that it was in effect 'locked', hindering ionic movement.[102] This is not limited to smaller cations, the addition of larger cations such as guanidinium also suppresses hysteresis.[250] Further evidence for the advantageous consequences of distorting the perovskite structure come from the use of cations that cause 2D/3D hybrid structures; in these the buffer layers of organic cation block the long range ion diffusion, and these cells also exhibit negligible hysteresis.[104,106,109] Another stability advantage is that formation of mixed-component perovskites can be energetically favourable, making their deposition easier.[251]

Unfortunately ion diffusion is not the only cause of long-term instability. Water, oxygen, excessive heat, and UV light are also detrimental to the perovskite, problems which are essential to solve for the outdoor installation of PSC.[252,253] The proposed scheme for the degradation pathway of MAPI is shown below.[254]

$$CH_3NH_3PbI_3 \text{ (s)} \underset{}{\overset{H_2O}{\rightleftharpoons}} CH_3NH_3I \text{ (aq)} + PbI_2 \text{ (s)} \qquad (2.3a)$$

$$CH_3NH_3I \text{ (aq)} \rightleftharpoons CH_3NH_2 \text{ (aq)} + HI \text{ (aq)} \qquad (2.3b)$$

$$4HI \text{ (aq)} + O_2 \text{ (g)} \rightleftharpoons 2I_2 \text{ (s)} + 2H_2O \text{ (l)} \qquad (2.3c)$$

$$2HI \text{ (aq)} \underset{}{\overset{hv}{\rightleftharpoons}} H_2 \text{ (g)} + I_2 \text{ (s)} \qquad (2.3d)$$
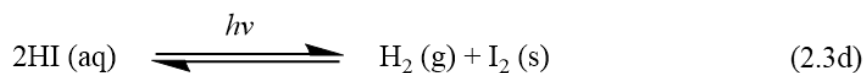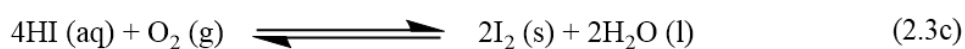
The instability of MAPI to water is due to the disruption of the hydrogen bonding network and the hygroscopic nature of the methylammonium cation.[177] Thus most PSC fabrication takes place in a glove box of controlled humidity (and oxygen content), as degradation has been observed to occur at humidities of over 55%.[59,255] Efforts to improve the stability of PSC have focussed on preventing the ingress of the water and O_2, for example by adding a protective layer on top. Perovskite protection can either take the form of a layer on top of the perovskite, or encapsulation of the entire device.

An interfacial layer of Al_2O_3 was shown to decrease the degradation of PSC over an extended period by forming a physical barrier to water penetration into the perovskite.[254,256] Replacing Spiro-OMeTAD with inorganic transport layers has a similar beneficial effect.[183,255,257] Encapsulating PSC involves the use of epoxy resin to coat the cell, providing a significant physical barrier. This is what enabled early PSC (*circa* 2013) to maintain their efficiency over large periods of time (500 hours).[177,258] A study of various encapsulation methods showed that although degradation by water and oxygen was prevented, prolonged exposure to light and heat still caused an eventual decline in performance.[259] Degradation can be exacerbated by the formation of metal halides upon corrosion of the cathode material, an unavoidable consequence of halide diffusion.[260]

The alteration of the chemical structure by using mixed-cation or mixed-anion systems also improves moisture stability.[59,246] This is particularly true for cells based on FAPI; the increased size of the A-site cation causes an expanded perovskite lattice which allows for more rapid degradation.[251,261] The aforementioned "locking" of the perovskite by smaller cations can therefore improve long-term stability.[99,100,102] 2D/3D hybrid perovskites are among the most stable over extended application, as the 2D layers consist of hydrophobic elements such as the aromatic group of PEA, or a long alkyl chain as in n-Bu or 5-AVA which prevent the ingress of water.[106,262–264] Porous carbon electrodes are strongly hydrophobic and can provide an additional organic block to water – in fact carbon architecture cells have been used in water splitting applications.[265] The current most-stable cell uses a combination of a porous carbon electrode and a 2D/3D perovskite to enable it to maintain a large percentage of its efficiency over a year.[109]

PSC require annealing at elevated temperatures in order to remove the solvent and promote crystallisation of the material.[266] This is important as more crystalline films with fewer pinholes have been shown to possess improved stability, as with time pinholes provide areas for defects to grow or water to access the material.[182,199,267] However under operation at elevated temperatures this can effect phase transitions; the tetragonal to cubic transition happens at around 52 °C.[268,269] The effect of heating to temperatures of up to 70 °C has been shown to be in most part reversible on cooling, suggesting that the change in performance is as a result of the phase transition.[270] Above these temperatures degradation is apportioned to the degradation of Spiro-

OMeTAD, and in extreme cases, sublimation of the organic amine.[271,272] The solution to the thermal stability of PSC lies mainly within the perovskite layer itself; FAPI based perovskites are more-stable, either on their own or in mixed-cation PSC, due to the higher phase transition temperatures of the material.[71,96,99]

Where the HTM is partly to blame for thermal instability, the mesoporous TiO_2 ETM is implicit in the light-based instability of PSC.[47] TiO_2 is itself a semiconductor with a wide bandgap of 3.2 eV, which corresponds to UV wavelengths. As a result, under sunlight electrons can be photoexcited in TiO_2, which results in the desorption of O_2 from titania and consequently changes at the TiO_2 – perovskite interface.[273] Light is also required for the splitting of HI (Equation 2.3d), resulting in further structural breakdown of the absorber layer.[253] In the presence of oxygen in the cell, O_2^- is formed by the UV light, which leads to rapid degradation of the perovskite – this can be suppressed by using a more efficient ETM.[274,275] Whilst using a UV filter and removing the mesoporous layers are possibilities, these come with a sacrifice in efficiency.[273] Using SnO_2 is another option, as it has a wider band gap and is thus more suitable for stable cells yet it still produces highly efficient cells.[185,226,276]

The current record stability for a PSC based on the efficiency measured at regular intervals is over a year.[109] The cell manages this by using a variety of methods. Perhaps the most significant development it implements is the use of a 2D/3D hybrid perovskite structure, which protects the perovskite from unwanted ion and water diffusion.[104] The porous carbon electrode is also a huge advancement for the stability of perovskites, which appears to improve the stability with respect to all possible degradation pathways whilst still producing competitive efficiencies; further enhanced by the removal of the requirement for an HTM such as Spiro-OMeTAD.[223,277] As the carbon cell and 2D/3D technology are further researched it is likely that the efficiency and stability of the most stable cells will increase.

2.4.5. Impedance Spectroscopy of Perovskite Solar Cells

Ion movement in cells exhibiting hysteretic behaviour has been predicted and observed computationally and experimentally respectively, both techniques giving similar activation energies for this process.[278–281] Activation energies for ion migration in PSC

are discussed in Chapter 7 and 8. The experimental method used in this thesis is Electrochemical Impedance Spectroscopy (EIS, introduced in more detail section 3.4). Using EIS the response of the cell to a modulated voltage can be probed, and the result fitted using an equivalent circuit consisting of resistances and capacitances. However different researchers use different equivalent circuit models (see Chapter 3 and Figure 2.4.5.1), and although it has been determined that mathematically there is little to no difference between various different models, the implications of different arrangements of the circuit elements can be significant.[282] Different equivalent circuits can be related to different physical phenomena in PSCs. *Author's note: For the purposes of the results sections of this report, each semicircle will be treated independently, and no equivalent circuit will be used. Derivation of an equivalent circuit requires complex mathematical modelling, complicated by the uncertain nature of the processes happening within the PSC during measurement. As the main features of interest are the low-frequency and mid-frequency semicircles (demonstrated in Figure 2.4.5.2), this will make the fitting easier, and treat them as physically distinct features.*
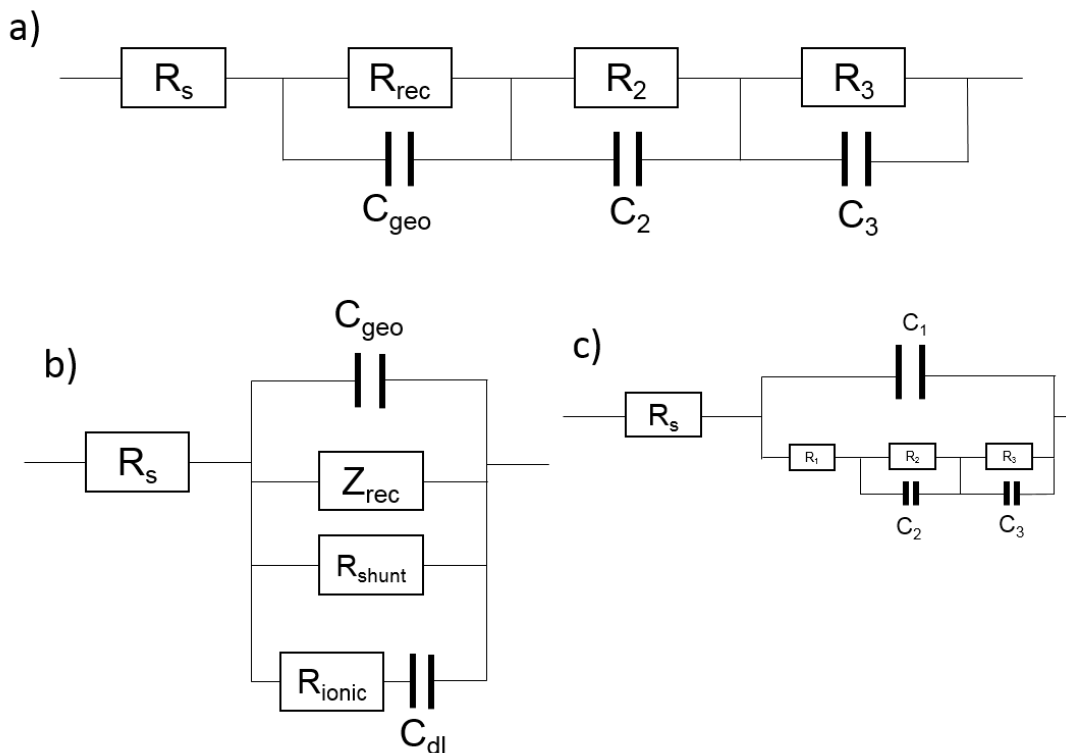
Figure 2.4.5.1. *Example equivalent circuit models for PSC from the literature, where R_s is the series resistance, R_{rec} and Z_{rec} are the recombination resistance and impedance respectively, C_{geo} is geometric capacitance, C_{dl} is double layer capacitance. All numbered elements are undefined. Circuits are taken from a) Ref 240, b) Ref 241 and c) Ref 242*

Impedance spectra are typically displayed on the complex plane, also called a Nyquist plot (discussed in more detail in chapter 3.4), an example of which is shown below in Figure 2.4.5.2.
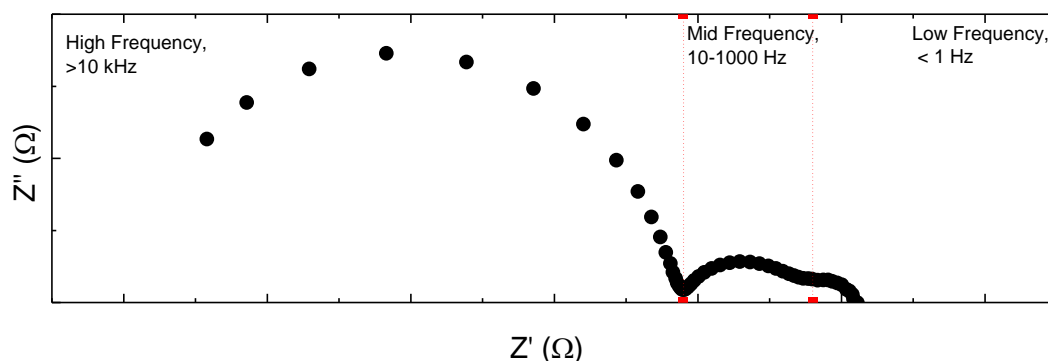
Figure 2.4.5.2. *An example Nyquist plot of a Perovskite Solar Cells, with frequency regions marked*

Each semicircle in the Nyquist plot represents a different process – a semicircle usually is caused by a resistor and capacitor in parallel. For perovskite solar cells it is generally accepted that after the series resistance (which is usually close to the value of the TCO resistance) the first semicircle relates to the recombination resistance (or injection resistance) and geometric capacitance.[283–286] The differences occur after this, as either two or three further semicircles are observed in the Nyquist plot, depending on the cell.[282] Contact layers have a significant impact on the EIS response, as they determine charge transfer kinetics, recombination and resistances at the interfaces, which will in turn affect the behaviour of the bulk perovskite.[287] An increase in the recombination resistance (R1) is seen as beneficial for solar cell performance as it means carrier lifetime is longer, improving the chances for charge collection.

The lower frequency behaviour has been attributed to various effects such as a change in recombination resistance due to the instability of the perovskite, or with charge accumulation at the interfaces.[285,288] Charge accumulation leads to extremely high capacitance values, and this has sometimes been referred to as a "giant dielectric" effect that causes the low frequency response in perovskite solar cells.[289] However the number of carriers required for charge accumulation to result in such large capacitances is far larger than known carrier densities in perovskites would allow.[245] The feature has since been identified to be caused by slow ionic motion in the perovskite causing time-dependent changes to the resistance.[245,290] The ionic motion theory has been corroborated by data showing that the characteristic time constant of

this circuit element is temperature dependent, and shows an activation energy similar to that for iodide diffusion calculated from other methods.[278–281,284] The exact interaction that causes the changes in impedance displayed by the mid-frequency and low-frequency semi-circles is not yet known, however there are many possibilities (Figure 2.4.5.3).[291]
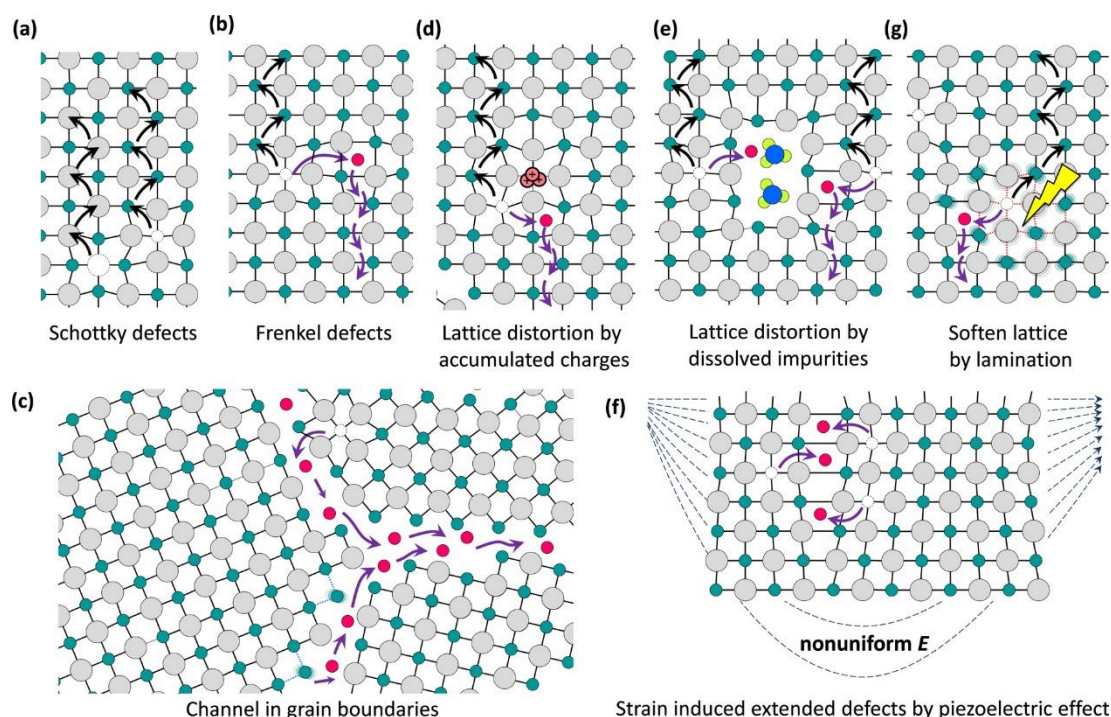
Figure 2.4.5.3. *Illustration of the ion migration pathways enabled by (a) Schottky defects, (b) Frenkel defects, (c) open space and wrong bonds at grain boundaries, (d–f) lattice distortions due to accumulated charges (d), dissolved impurities (e), and nonuniform strain caused by piezoelectric effect (f), and (g) Soften lattice caused by the light illumination induced bond weakening -* Reprinted with permission from Y. Yuan and J. Huang, Acc. Chem. Res., 2016, 49, 286–293 Copyright (2016) American Chemical Society

The diffusion of methylammonium ions was also considered, however the activation energy calculated through computational measurements is higher (0.84 eV) than the experimentally observed values (the activation energy for lead diffusion was also calculated to be 2.31 eV).[53] The same study looked at the diffusion coefficients of both MA^+ and I^-, calculating 10^{-16} cm^2s^{-1} and 10^{-12} cm^2s^{-1} respectively. The difference in magnitude suggests that methylammonium diffusion within the perovskite is negligible and that the overwhelming contribution to ion motion will be iodide diffusion.

Recently a semicircle below the *x*-axis (real) has also been observed, either as a loop between the high-frequency and mid-frequency semicircles or at very low frequencies.[285,286,292–294] Whilst theoretically anything below the *x*-axis (real) relates to

an induction process (*i.e.* the current is *greater* than the voltage at these frequencies), the physical explanation of the phenomenon in perovskite solar cells is not certain. Like the other lower frequency semicircles it has been attributed to a giant dielectric effect.[288,289] However the independence of the low frequency response to light intensity suggests that the process is not due to electrons and holes – and that this negative feature is also likely to be a result of slow ionic movement within the perovskite.[245,286]

Although several reports agree that ionic movement is the cause of the low-frequency semi-circles, the appearance of the Nyquist plots can be quite different from cell-to-cell, depending on efficiency or architecture (both variables which are out of the scope of this work). Therefore the specifics of the impedance response that is seen during the measurements undertaken as part of this research are discussed in more detail in section 7.4, along with how this may relate to ion diffusion within the perovskite lattice.

2.4.6. Environmental Aspects of Perovskite Solar Cells

The instability of perovskites is not only a performance issue, it is one of environmental safety. The primary problem is lead. Lead is a well-known toxic element, and before any widespread installation of PSC technology the stigma attached to using a product including lead needs to be addressed.

Life-Cycle Assessments (LCAs) are a useful method to assess the sustainability of PSC and identify the most problematic steps or components. Many LCAs have been carried out on PSC; all agree that the environmental risk of using lead is low, and that the thermal evaporation of the metal contact (particularly gold) is the most detrimental part due to its energy intensity.[295–299] Particular care also needs to be paid to the HTM and mesoporous layer, as they increase energy payback time. The efficiency and stability would therefore need to be much greater to justify their use.[297,298] These results would suggest that carbon based solar cells would perform well in an LCA, and it has been calculated that their overall environmental impact is lower than other cell architectures – yet energy consumption from the manufacturing process is still the largest negative factor.[300]

As discussed in the previous section, the degradation of perovskite solar cells results in the formation of the metal-iodide salt. Sn-based perovskites have been touted as potentially more environmentally friendly perovskites, however they are less stable and the degradation product (SnI_2) was found to be more damaging *in vivo* than PbI_2.[301] As Sn-based perovskites are much less efficient than their lead analogues, research has instead focussed on intercepting the Pb degradation products. Before the cell degrades and releases Pb it can be recycled – and the PbI_2 can either be safely disposed of or reused.[302,303] The resulting cells after several recycling cycles maintained an average efficiency of 13%, the same as that of the fresh devices; importantly this also means the expensive TCO can be re-used.[304] Moreover it has been demonstrated that PSC can be recycled following exposure to heat and moisture, which is useful for the application of cell recycling to commercial PSC.[305]

Keeping the PbI_2 layer whole is of special importance for two reasons. Firstly as it reduces the need for toxic solvents like DMF or DMSO, as the organic cation can be deposited from less toxic solvents like isopropanol.[177] Secondly it has been estimated that through traditional spin-coating methods that 90 % of the solution is wasted, meaning that a vast amount of Pb-containing organic solvent must be disposed of.[306] A potential solvent to reduce the environmental cost is acetonitrile. Noel *et al.* discovered that by bubbling methylamine gas through acetonitrile that the perovskite precursor became soluble, and the resulting films could be easily annealed by vacuum without the requirement for heat, and could be applied to more scalable manufacturing methods such as inkjet printing.[307] Again the problem is overcome with the use of a porous carbon electrode, as the required amount of solution is $1/50^{th}$ that of traditional spin-coating.[176]

2.4.7. Upscaling and Commercial prospects

The environmental impact and risk of Perovskite Solar Cells is an important barrier to their commercialisation as it affects the manufacturing cost, and in turn market cost and energy payback time. One of the major attractions of PSC technology is that the energy payback time is shorter than for already established technologies.[298] The reduction is facilitated by high efficiencies and low materials/processing costs (however the low stability is still a major barrier).[124,297]

Although the field of perovskite photovoltaics is still in its infancy, some steps towards upscaling have already been taken. The first stages involved increasing the size of the cell, as most research cells have an active area of less than 1 cm^2. The efficiency drops as size increases, for example from 13.3% at 0.0625 cm^2, to 10.1% at 10 cm^2 and 4.3% at 100 cm^2.[308] The reduction in performance is partly due to the difficulties in controlling the absorber layer morphology, but also with problems due to the carrier diffusion length; as distance between contacts increases, the probability of recombination increases.[309] Advances in the printing of perovskites (and again, with carbon cell technology) are likely to decrease the loss with the expansion of active area.

Given the easily tunable band gap demonstrated by PSC, building integrated photovoltaic devices have always been a commercial possibility.[310] Despite this the majority of PSC designed for building-integrated applications have been semi-transparent MAPI cells.[227,311] As may be expected the performance of these is tied to the transparency of the absorber layer.[312] Efficiencies of 4 % are still obtainable with layers of high transparency (47 % transmission corresponding to a layer thickness of 65 nm), suggesting that PSC could be viable for use as photovoltaic windows.[313] However as of yet no large scale tests of semi-transparent PSC have been undertaken.

Another use of semi-transparent perovskite absorber layers is for tandem cells, an attractive prospect as the manufacturing and industry for other PV technology (such as silicon) is already well established.[314] Tandem cells use two absorber layers in order to boost the cell efficiency past the limit of one absorber on its own. Thus the band gaps of the top and bottom layer must be carefully chosen, and to go with Silicon's 1.1 eV bandgap, the optimum top layer was calculated to possess a gap of 1.7 eV.[315] With the tunability of perovskite bandgaps they are a perfect candidate for multijunction cells. When used in a tandem cell with a silicon solar cell of 23 % efficiency, a CsFAPIBr perovskite can push the efficiency to 23.9 %.[316]

To improve the opportunity for commercialisation, the efficiency, stability and variety of PSC need to be improved. Further understanding of the internal electronic and ionic processes that happen within the perovskite is also required to better understand stability. In this thesis both avenues will be explored.

2.5. References

1   W. Smith, *Nature*, 1873, **7**, 303.

2   D. M. Chapin, C. S. Fuller and G. L. Pearson, *J. Appl. Phys.*, 1954, **25**, 676–677.

3   M. K. T. Matsui, H. Sai, T. Suezaki, M. Matsumoto, K. Saito, I. Yoshida, in *28th European Photovoltaic Solar Energy Conference and Exhibition*, 2013, pp. 2213–2217.

4   F. I. for S. E. S. I. with support of P. AG, *Photovoltaics Report*, 2018.

5   M. Z. Pakhuruddin, Y. Yusof, K. Ibrahim and a. Abdul Aziz, *Optik (Stuttg).*, 2013, **124**, 5397–5400.

6   T. Jana, S. Mukhopadhyay and S. Ray, *Sol. Energy Mater. Sol. Cells*, 2002, **71**, 197–211.

7   D. Zielke, D. Sylla, T. Neubert, R. Brendel and J. Schmidt, *IEEE J. Photovoltaics*, 2013, **3**, 656–661.

8   J. Zhao, A. Wang, M. A. Green and F. Ferrazza, *Appl. Phys. Lett.*, 1998, **73**, 1991–1993.

9   D. D. Smith, P. Cousins, S. Westerberg, R. D. Jesus-Tabajonda, G. Aniero and Y. C. Shen, *IEEE J. Photovoltaics*, 2014, 4, 1465–1469.

10   A. Descoeudres, C. Allebé, N. Badel, L. Barraud, Jonathan Champliaud, F. Debrot, A. Faes, A. Lachowicz, J. Levrat, S. Nicolay, L. Sansonnens, M. Despeisse and C. Ballif, *Energy Procedia*, 2015, **77**, 508–514.

11   A. Richter, M. Hermle and S. W. Glunz, *IEEE J. Photovoltaics*, 2013, 3, 1184–1191.

12   D. A. Jenny and R. H. Bube, *Phys. Rev.*, 1954, **96**, 1190–1191.

13   J. Britt and C. Ferekides, *Appl. Phys. Lett.*, 1993, **62**, 2851–2852.

14   M. A. Green, Y. Hishikawa, W. Warta, E. D. Dunlop, D. H. Levi, J. Hohl-Ebinger and A. W. H. Ho-Baillie, *Prog. Photovoltaics Res. Appl.*, 2017, **25**, 668–676.

15   B. M. Kayes, H. Nie, R. Twist, S. G. Spruytte, F. Reinhardt, I. C. Kizilyalli and G. S. Higashi, *2011 37th IEEE Photovolt. Spec. Conf.*, 2011, 4–8.

16   R. Venkatasubramanian, B. C. O'Quinn, J. S. Hills, P. R. Sharps, M. L. Timmons, J. A. Hutchby, H. Field, R. Ahrenkiel and B. Keyes, *Conf. Rec. Twenty Fifth IEEE Photovolt. Spec. Conf. - 1996*, 1996, 31–36.

17   D. A. Jenny, J. J. Loferski and P. Rappaport, *Phys. Rev.*, 1956, **101**, 1208–1209.

18   H. Hahn, G. Frank, W. Klingler, A.-D. Meyer and G. Störger, *Zeitschrift für Anorg. und Allg. Chemie*, 1953, **271**, 153–170.

19   T. Tinoco, C. Rincón, M. Quintero and G. S. Pérez, *Phys. status solidi*, 1991, **124**, 427–434.

20   D. E. Carlson and C. R. Wronski, *Appl. Phys. Lett.*, 1976, **28**, 671–673.

21   D. E. Carlson, *IEEE Trans. Electron Devices*, 1977, 24, 449–453.

22   B. Shin, O. Gunawan, Y. Zhu, N. A. Bojarczuk, S. J. Chey and S. Guha, *Prog. Photovoltaics Res. Appl.*, 2013, **21**, 72–76.

23   W. Wang, M. T. Winkler, O. Gunawan, T. Gokmen, T. K. Todorov, Y. Zhu and D. B. Mitzi, *Adv. Energy Mater.*, 2014, **4**, n/a-n/a.

24   Z. Guan, W. Luo and Z. Zou, *CrystEngComm*, 2014, **16**, 2929–2936.

25   K. Zhang and H. Guo, *J. Mater. Sci. Mater. Electron.*, , DOI:10.1007/s10854-017-7629-4.

26   T. K. Todorov, O. Gunawan, T. Gokmen and D. B. Mitzi, *Prog. Photovoltaics Res. Appl.*, 2013, **21**, 82–87.

27   H. Hoppe and N. S. Sariciftci, *J. Mater. Res.*, 2004, **19**, 1924–1945.

28   Y.-J. Cheng, S.-H. Yang and C.-S. Hsu, *Chem. Rev.*, 2009, **109**, 5868–5923.

29   F. Hakim and M. K. Alam, *2017 Int. Conf. Electr. Comput. Commun. Eng.*, 2017, 170–174.

30   Z. He, B. Xiao, F. Liu, H. Wu, Y. Yang, S. Xiao, C. Wang, T. P. Russell and Y. Cao, *Nat Phot.*, 2015, **9**, 174–179.

31   S.-H. Liao, H.-J. Jhuo, Y.-S. Cheng and S.-A. Chen, *Adv. Mater.*, 2013, **25**, 4766–4771.

32   X. Liu, H.-Q. Wang, Y. Li, Z. Gui, S. Ming, K. Usman, W. Zhang and J. Fang, *Adv. Sci.*, 2017, **4**, 1700053-n/a.

33   T. Ameri, P. Khoram, J. Min and C. J. Brabec, *Adv. Mater.*, 2013, **25**, 4245–4266.

34   L. Meng, Y. Zhang, X. Wan, C. Li, X. Zhang, Y. Wang, X. Ke, Z. Xiao, L. Ding, R. Xia, H.-L. Yip, Y. Cao and Y. Chen, *Science (80-.).*, 2018, **361**, 1094 LP – 1098.

35   W. Shockley and H. J. Queisser, *J. Appl. Phys.*, 1961, **32**, 510–519.

36   K. W. J. Barnham and G. Duggan, *J. Appl. Phys.*, 1990, **67**, 3490–3493.

37   P. V Kamat, *J. Phys. Chem. C*, 2008, **112**, 18737–18753.

38   A. J. Nozik, *Phys. E Low-dimensional Syst. Nanostructures*, 2002, **14**, 115–120.

39   R. J. Ellingson, M. C. Beard, J. C. Johnson, P. Yu, O. I. Micic, A. J. Nozik, A. Shabaev and A. L. Efros, *Nano Lett.*, 2005, **5**, 865–871.

40   P. Guyot-Sionnest, *J. Phys. Chem. Lett.*, 2012, **3**, 1169–1175.

41   M. Liu, O. Voznyy, R. Sabatini, F. P. Garcia de Arquer, R. Munir, A. H. Balawi, X. Lan, F. Fan, G. Walters, A. R. Kirmani, S. Hoogland, F. Laquai, A. Amassian and E. H. Sargent, *Nat Mater*, 2017, **16**, 258–263.

42   S. Pradhan, A. Stavrinadis, S. Gupta and G. Konstantatos, *ACS Appl. Mater.*

Interfaces, 2017, **9**, 27390–27395.

43   H. TRIBUTSCH and M. CALVIN, *Photochem. Photobiol.*, 1971, **14**, 95–112.

44   H. TRIBUTSCH, *Photochem. Photobiol.*, 1972, **16**, 261–269.

45   B. O'Regan and M. Gratzel, *Nature*, 1991, **353**, 737–740.

46   S. G. Hashmi, M. Ozkan, J. Halme, S. M. Zakeeruddin, J. Paltakari, M. Gratzel and P. D. Lund, *Energy Environ. Sci.*, 2016, **9**, 2453–2462.

47   M. Grätzel, *J. Photochem. Photobiol. C Photochem. Rev.*, 2003, **4**, 145–153.

48   W. M. Campbell, K. W. Jolley, P. Wagner, K. Wagner, P. J. Walsh, K. C. Gordon, L. Schmidt-Mende, M. K. Nazeeruddin, Q. Wang, M. Grätzel and D. L. Officer, *J. Phys. Chem. C*, 2007, **111**, 11760–11762.

49   H. Wang, B. Bao, X. Hu and J.-K. Fang, *Electrochim. Acta*, , DOI:http://dx.doi.org/10.1016/j.electacta.2017.08.089.

50   S. Mathew, A. Yella, P. Gao, R. Humphry-Baker, C. F. E., N. Ashari-Astani, I. Tavernelli, U. Rothlisberger, N. Khaja and M. Grätzel, *Nat Chem*, 2014, **6**, 242–247.

51   Y. Cao, Y. Saygili, A. Ummadisingu, J. Teuscher, J. Luo, N. Pellet, F. Giordano, S. M. Zakeeruddin, J.-E. Moser, M. Freitag, A. Hagfeldt and M. Grätzel, 2017, **8**, 15390.

52   A. Kojima, K. Teshima, Y. Shirai and T. Miyasaka, *J. Am. Chem. Soc.*, 2009, **131**, 6050–6051.

53   C. Eames, J. M. Frost, P. R. F. Barnes, B. C. O'Regan, A. Walsh and M. S. Islam, *Nat. Commun.*, 2015, **6**, 7497.

54   G. Kieslich, S. Sun and A. K. Cheetham, *Chem. Sci.*, 2014, **5**, 4712–4715.

55   V. M. Goldschmidt, *Naturwissenschaften*, 1926, **14**, 477–485.

56   W. Travis, E. N. K. Glover, H. Bronstein, D. O. Scanlon and R. Palgrave, *Chem. Sci.*, 2016, **7**, 4548–4556.

57   H.-S. Kim, C.-R. Lee, J.-H. Im, K.-B. Lee, T. Moehl, A. Marchioro, S.-J. Moon, R. Humphry-Baker, J.-H. Yum, J. E. Moser, M. Grätzel and N.-G. Park, *Sci. Rep.*, 2012, **2**, 591.

58   N. Ahn, D.-Y. Son, I.-H. Jang, S. M. Kang, M. Choi and N.-G. Park, *J. Am. Chem. Soc.*, 2015, **137**, 8696–8699.

59   J. H. Noh, S. H. Im, J. H. Heo, T. N. Mandal and S. Il Seok, *Nano Lett.*, 2013, **13**, 1764–1769.

60   M. L. Davies, M. Carnie, P. J. Holliman, A. Connell, P. Douglas, T. Watson, C. Charbonneau, J. Troughton and D. Worsley, *Mater. Res. Innov.*, 2014, **18**, 482–485.

61   A. Sadhanala, S. Ahmad, B. Zhao, N. Giesbrecht, P. Pearce, F. Deschler, R. L. Z. Hoye, K. C. Goedel, T. Bein, P. Docampo, S. E. Dutton, M. De Volder and R. H. Friend, *Nano Lett.*, 2015, **15**, 6095–6101.

62   N. K. Noel, B. Wenger, S. N. Habisreutinger, J. B. Patel, T. Crothers, Z. Wang, R. J. Nicholas, M. B. Johnston, L. M. Herz and H. J. Snaith, *ACS Energy Lett.*, , DOI:10.1021/acsenergylett.8b00509.

63   E. L. Unger, A. R. Bowring, C. J. Tassone, V. Pool, A. Gold-Parker, R. Cheacharoen, K. H. Stone, E. T. Hoke, M. F. Toney and M. D. McGehee, *Chem. Mater.*, 2014, **26**, 7158–7165.

64   K. T. Butler, J. M. Frost and A. Walsh, *Mater. Horiz.*, 2015, **2**, 228–231.

65   S. Colella, E. Mosconi, P. Fedeli, A. Listorti, F. Orlandi, P. Ferro, T. Besagni, A. Rizzo, G. Calestani, G. Gigli, F. De Angelis, R. Mosca and F. Gazza, *Chem. Mater.*, 2013, **25**, 4613.

66   G. R. Berdiyorov, F. El-Mellouhi, M. E. Madjet, F. H. Alharbi, F. M. Peeters and S. Kais, *Sol. Energy Mater. Sol. Cells*, 2015, 1–9.

67   N. K. Kumawat, A. Dey, A. Kumar, S. P. Gopinathan, K. L. Narasimhan and D. Kabra, *ACS Appl. Mater. Interfaces*, 2015, **7**, 13119–13124.

68   Q. Tai, P. You, H. Sang, Z. Liu, C. Hu, H. L. W. Chan and F. Yan, *Nat. Commun.*, 2016, **7**, 11105.

69   S. Nagane, U. Bansode, O. Game, S. Chhatre and S. Ogale, *Chem. Commun.*, 2014, **50**, 9741–9744.

70   C. H. Hendon, R. X. Yang, L. a. Burton and A. Walsh, *J. Mater. Chem. A*, 2015, **3**, 9067–9070.

71   G. E. Eperon, S. D. Stranks, C. Menelaou, M. B. Johnston, L. M. Herz and H. J. Snaith, *Energy Environ. Sci.*, 2014, **7**, 982.

72   Y. Takahashi, H. Hasegawa, Y. Takahashi and T. Inabe, *J. Solid State Chem.*, 2013, **205**, 39–43.

73   S. Gupta, T. Bendikov, G. Hodes and D. Cahen, *ACS Energy Lett.*, 2016, acsenergylett.6b00402.

74   R. X. Yang, K. T. Butler and A. Walsh, *J. Phys. Chem. Lett.*, 2015, **6**, 5009–5014.

75   S. S. Mali, C. S. Shim and C. K. Hong, *NPG Asia Mater.*, 2015, **7**, e208.

76   N. De Marco, H. Zhou, Q. Chen, P. Sun, Z. Liu, L. Meng, E.-P. Yao, Y. Liu, A. Schiffer and Y. Yang, *Nano Lett.*, , DOI:10.1021/acs.nanolett.5b04060.

77   A. H. Slavney, T. Hu, A. M. Lindenberg and H. I. Karunadasa, *J. Am. Chem. Soc.*

78   A. Halder, R. Chulliyil, A. S. Subbiah, T. Khan, S. Chattoraj, A. Chowdhury, S. K. Sarkar, R. Chulliyul, A. S. Subbiah, T. Khan, S. Chattoraj, A. Chowdhury and S. K. Sarkar, *J. Phys. Chem. Lett.*, 2015, **6**, 150817172749006.

79   A. F. Akbulatov, L. A. Frolova, D. A. Anokhin, K. L. Gerasimov, N. N. Dremova and P. Troshin, *J. Mater. Chem. A*, 2016, **4**, 18378–18382.

80   M. Chen, M.-G. Ju, A. D. Carl, Y. Zong, R. L. Grimm, J. Gu, X. C. Zeng, Y. Zhou and N. P. Padture, *Joule*, 2018, **2**, 558–570.

81   S. R. Pering, W. Deng, J. R. Troughton, P. S. Kubiak, D. Ghosh, R. G. Niemann, F. Brivio, F. E. Jeffrey, A. B. Walker, M. S. Islam, T. M. Watson, P. R. Raithby, A. L. Johnson, S. E. Lewis and P. J. Cameron, *J. Mater. Chem. A*, 2017, **5**, 20658–20665.

82   O. J. Weber, K. L. Marshall, L. M. Dyson and M. T. Weller, *Acta Crystallogr. B. Struct. Sci. Cryst. Eng. Mater.*, 2015, **71**, 668–78.

83   C. C. Stoumpos, D. H. Cao, D. J. Clark, J. Young, J. M. Rondinelli, J. I. Jang, J. T. Hupp and M. G. Kanatzidis, *Chem. Mater.*, 2016, **28**, 2852–2867.

84   Y. Yang, J. Song, Y. L. Zhao, L. Zhu, X. Q. Gu, Y. Q. Gu, M. Che and Y. H. Qiang, *J. Alloys Compd.*, 2016, **684**, 84–90.

85   M. Zhang, J. S. Yun, Q. Ma, J. Zheng, C. F. J. Lau, X. Deng, J. Kim, D. Kim, J. Seidel, M. A. Green, S. Huang and A. W. Y. Ho-Baillie, *ACS Energy Lett.*, 2017, **2**, 438–444.

86   G. Kieslich, S. Sun and T. Cheetham, *Chem. Sci.*, 2014, **5**, 4712–4715.

87   M. R. Filip and F. Giustino, *J. Phys. Chem. C*, 2015, **120**, acs.jpcc.5b11845.

88   Y.-K. Jung, J.-H. Lee, A. Walsh and A. Soon, *Chem. Mater.*, 2017, **29**, 3181–3188.

89   M. T. Weller, O. J. Weber, J. M. Frost and A. Walsh, *J. Phys. Chem. Lett.*, 2015, **6**, 3209–3212.

90   S. Lv, S. Pang, Y. Zhou, N. P. Padture, H. Hu, L. Wang, X. Zhou, H. Zhu, L. Zhang, C. Huang and G. Cui, *Phys. Chem. Chem. Phys.*, 2014, **16**, 19206.

91   G. E. Eperon, G. M. Paterno, R. J. Sutton, A. Zampetti, A. A. Haghighirad, F. Cacialli, H. J. Snaith, G. M. Paterno', R. J. Sutton, A. Zampetti, A. A. Haghighirad, F. Cacialli and H. J. Snaith, *J. Mater. Chem. A*, 2015, **3**, 19688–19695.

92   G. Giorgi, J. Fujisawa, H. Segawa and K. Yamashita, *J. Phys. Chem. C*, 2015, **119**, 4694–4701.

93   K. Wu, G. Liang, Q. Shang, Y. Ren, D. Kong and T. Lian, *J. Am. Chem. Soc.*

94   K. Y. Tsui, N. Onishi and R. F. Berger, *J. Phys. Chem. C*, 2016, acs.jpcc.6b09277.

95   Z. Liu, B. Sun, X. Liu, J. Han, H. Ye, T. Shi, Z. Tang and G. Liao, *Nano-Micro Lett.*, 2018, **10**, 34.

96   O. J. Weber, B. Charles and M. T. Weller, *J. Mater. Chem. A*, 2016, **4**, 15375–15382.

97   J. Liu, Y. Shirai, X. Yang, Y. Yue, W. Chen, Y. Wu, A. Islam and L. Han, *Adv. Mater.*, 2015, **27**, 4918–4923.

98   G. E. Eperon, C. E. Beck and H. J. Snaith, *Mater. Horizons*, , DOI:10.1039/C5MH00170F.

99   M. Saliba, T. Matsui, J.-Y. Seo, K. Domanski, J.-P. Correa-Baena, N. Mohammad K., S. M. Zakeeruddin, W. Tress, A. Abate, A. Hagfeldt and M.

Grätzel, *Energy Environ. Sci.*, 2016, **9**, 1989.

100 M. Saliba, M. Saliba, T. Matsui, K. Domanski, J.-Y. Seo and A. Ummadisingu, *Science (80-.).*, 2016, **354**, 206–209.

101 W.-L. Yan, G.-H. Lu and F. Liu, *J. Phys. Chem. C*, 2016, acs.jpcc.6b06242.

102 D. Ghosh, P. Walsh Atkins, M. S. Islam, A. B. Walker and C. Eames, *ACS Energy Lett.*, 2017, **2**, 2424–2429.

103 D. H. Cao, C. C. Stoumpos, O. K. Farha, J. T. Hupp and M. G. Kanatzidis, *J. Am. Chem. Soc.*

104 H. Tsai, W. Nie, J.-C. Blancon, C. C. Stoumpos, R. Asadpour, B. Harutyunyan, A. J. Neukirch, R. Verduzco, J. J. Crochet, S. Tretiak, L. Pedesseau, J. Even, M. A. Alam, G. Gupta, J. Lou, P. M. Ajayan, M. J. Bedzyk, M. G. Kanatzidis and A. D. Mohite, *Nature*, , DOI:10.1038/nature18306.

105 I. C. Smith, E. T. Hoke, D. Solis-Ibarra, M. D. McGehee and H. I. Karunadasa, *Angew. Chemie Int. Ed.*, 2014, **53**, 11232–11235.

106 X. Zhang, G. Wu, W. Fu, M. Qin, W. Yang, J. Yan, Z. Zhang, X. Lu and H. Chen, *Adv. Energy Mater.*, 1702498-n/a.

107 L. N. Quan, M. Yuan, R. Comin, O. Voznyy, E. M. Beauregard, S. Hoogland, A. Buin, A. R. Kirmani, K. Zhao, A. Amassian, D. H. Kim and E. H. Sargent, *J. Am. Chem. Soc.*

108 K. T. Cho, G. Grancini, Y. Lee, E. Oveisi, J. Ryu, O. Almora, M. Tschumi, P. Schouwink, G. Seo, sung heo, J. Park, J. Jang, S. Paek, G. Garcia-Belmonte and M. K. Nazeeruddin, *Energy Environ. Sci.*, , DOI:10.1039/C7EE03513F.

109 G. Grancini, C. Roldán-Carmona, I. Zimmermann, E. Mosconi, X. Lee, D. Martineau, S. Narbey, F. Oswald, F. De Angelis, M. Graetzel and M. K. Nazeeruddin, 2017, **8**, 15684.

110 M. Chunqing, S. Dong, N. Tsz-Wai, L. Ming-Fai and L. Chun-Sing, *Adv. Mater.*, 2018, **0**, 1800710.

111 M. Ozaki, Y. Katsuki, J. Liu, T. Handa, R. Nishikubo, S. Yakumaru, Y. Hashikawa, Y. Murata, T. Saito, Y. Shimakawa, Y. Kanemitsu, A. Saeki and A. Wakamiya, *ACS Omega*, 2017, **2**, 7016–7021.

112 F. Hao, C. C. Stoumpos, D. H. Cao, R. P. H. Chang and M. G. Kanatzidis, *Nat. Photonics*, 2014, **8**, 489–494.

113 W. Liao, D. Zhao, Y. Yu, C. R. Grice, C. Wang, A. J. Cimaroli, P. Schulz, W. Meng, K. Zhu, R.-G. Xiong and Y. Yan, *Adv. Mater.*, 2016, **28**, 9333–9340.

114 N. K. Noel, S. D. Stranks, A. Abate, C. Wehrenfennig, S. Guarnera, A.-A. Haghighirad, A. Sadhanala, G. E. Eperon, S. K. Pathak, M. B. Johnston, A. Petrozza, L. M. Herz and H. J. Snaith, *Energy Environ. Sci.*, 2014, **7**, 3061–3068.

115 Y. Li, W. Sun, W. Yan, S. Ye, H. Rao, H. Peng, Z. Zhao, Z. Bian, Z. Liu, H. Zhou and C. Huang, *Adv. Energy Mater.*, 2016, 1601353.

116   R. Hoye, R. E. Brandt, A. Osherov, V. Stevanovic, S. D. Stranks, M. W. B. Wilson, H. Kim, A. J. Akey, R. C. Kurchin, J. R. Poindexter, E. N. Wang, M. G. Bawendi, V. Bulovic and T. Buonassisi, *Chem. - A Eur. J.*, 2015, n/a-n/a.

117   J.-C. Hebig, I. Kühn, J. Flohre and T. Kirchartz, *ACS Energy Lett.*, 2016, **1**, 309–314.

118   B.-W. Park, B. Philippe, X. Zhang, H. Rensmo, G. Boschloo and E. M. J. Johansson, *Adv. Mater.*, 2015, **9**, n/a-n/a.

119   G. Volonakis, M. R. Filip, A. A. Haghighirad, N. Sakai, B. Wenger, H. J. Snaith and F. Giustino, *J. Phys. Chem. Lett.*, 2016, **7**, 1254–1259.

120   M. R. Filip, S. Hillman, A.-A. Haghighirad, H. J. Snaith and F. Giustino, *J. Phys. Chem. Lett.*, 2016, **7**, 2579–2585.

121   C. Wu, Q. Zhang, Y. Liu, W. Luo, X. Guo, Z. Huang, H. Ting, W. Sun, X. Zhong, S. Wei, S. Wang, Z. Chen and L. Xiao, *Adv. Sci.*, 1700759-n/a.

122   C. Zheng and O. Rubel, *J. Phys. Chem. Lett.*, 2018, **9**, 874–880.

123   M. Becker, T. Kluner and M. Wark, *Dalt. Trans.*, 2017, **46**, 3500–3509.

124   A. Kojima, K. Teshima, Y. Shirai and T. Miyasaka, *J. Am. Chem. Soc.*, 2009, **131**, 6050–1.

125   J. M. Ball, M. M. Lee, A. Hey and H. J. Snaith, *Energy Environ. Sci.*, 2013, **6**, 1739–1743.

126   M. a. Green, A. Ho-Baillie and H. J. Snaith, *Nat. Photonics*, 2014, **8**, 506–514.

127   P. Schulz, E. Edri, S. Kirmayer, G. Hodes, D. Cahen and A. Kahn, *Energy Environ. Sci.*, 2014, **7**, 1377–1381.

128   P. Docampo, J. M. Ball, M. Darwich, G. E. Eperon and H. J. Snaith, *Nat. Commun.*, 2013, **4**, 2761.

129   D. Liu and T. L. Kelly, *Nat. Photonics*, 2013, **8**, 133–138.

130   J. P. Correa Baena, L. Steier, W. Tress, M. Saliba, S. Neutzner, T. Matsui, F. Giordano, T. J. Jacobsson, A. R. Srimath Kandada, S. M. Zakeeruddin, A. Petrozza, A. Abate, M. K. Nazeeruddin, M. Gratzel and A. Hagfeldt, *Energy Environ. Sci.*, 2015, **8**, 2928–2934.

131   M. H. Kumar, N. Yantara, S. Dharani, M. Graetzel, S. Mhaisalkar, P. P. Boix and N. Mathews, *Chem. Commun.*, 2013, **49**, 11089–11091.

132   M. Abulikemu, J. Barbé, A. El Labban, J. Eid and S. Del Gobbo, *Thin Solid Films*, 2017, **636**, 512–518.

133   J. Barbé, M. L. Tietze, M. Neophytou, B. Murali, E. Alarousu, A. El Labban, M. Abulikemu, W. Yue, O. F. Mohammed, I. McCulloch, A. Amassian and S. Del Gobbo, *ACS Appl. Mater. Interfaces*, 2017, **9**, 11828–11836.

134   W. Zhang, J. Xiong, L. Jiang, J. Wang, T. Mei, X. Wang, H. Gu, W. A. Daoud and J. Li, *ACS Appl. Mater. Interfaces*, 2017, **9**, 38467–38476.

135   Y. H. Lee, J. Luo, M.-K. Son, P. Gao, K. T. Cho, J. Seo, S. M. Zakeeruddin, M.

Grätzel and M. K. Nazeeruddin, *Adv. Mater.*, 2016, **28**, 3966–3972.

136 J. Peng, Y. Wu, W. Ye, D. A. Jacobs, H. Shen, X. Fu, Y. Wan, T. Duong, N. Wu, C. Barugkin, H. T. Nguyen, D. Zhong, J. Li, T. Lu, Y. Liu, M. N. Lockrey, K. J. Weber, K. R. Catchpole and T. P. White, *Energy Environ. Sci.*, 2017, **10**, 1792–1800.

137 M. J. Carnie, C. Charbonneau, M. L. Davies, J. Troughton, T. M. Watson, K. Wojciechowski, H. Snaith and D. A. Worsley, *Chem. Commun.*, 2013, **49**, 7893–7895.

138 U. Bach, D. Lupo, P. Comte, J. E. Moser, F. Weissörtel, J. Salbeck, H. Spreitzer and M. Grätzel, *Nature*, 1998, **395**, 583–585.

139 A. Abate, D. R. Staff, D. J. Hollman, H. J. Snaith and A. B. Walker, *Phys. Chem. Chem. Phys.*, 2014, **16**, 1132–8.

140 J. Burschka, A. Dualeh, F. Kessler, E. Baranoff, N.-L. Cevey-Ha, C. Yi, M. K. Nazeeruddin and M. Grätzel, *J. Am. Chem. Soc.*, 2011, **133**, 18042–18045.

141 Q. Wang, C. Bi and J. Huang, *Nano Energy*, 2015, **15**, 275–280.

142 H. Bi and Y. Zhang, *Mater. Lett.*, 2015, **161**, 767–769.

143 E. Edri, S. Kirmayer, D. Cahen and G. Hodes, *J. Phys. Chem. Lett.*, 2013, **4**, 897–902.

144 K. T. and Y. Suzuki, *Jpn. J. Appl. Phys.*, 2017, **56**, 08MC04.

145 J. A. Christians, R. C. M. Fung and P. V Kamat, *J. Am. Chem. Soc.*, 2014, **136**, 758–764.

146 W.-D. Hu, C. Dall'Agnesel, X.-F. Wang, G. Chen, M.-Z. Li, J.-X. Song, Y.-J. Wei and T. Miyasaka, *J. Photochem. Photobiol. A Chem.*, 2018, **357**, 36–40.

147 S. H. Im, J.-H. Heo, H. J. Han, D. Kim and T. Ahn, *Energy Environ. Sci.*, 2015, **8**, 1602–1608.

148 C. Müller, T. Glaser, M. Plogmeyer, M. Sendner, S. Döring, A. A. Bakulin, C. Brzuska, R. Scheer, M. S. Pshenichnikov, W. Kowalsky, A. Pucci and R. Lovrincic, *Chem. Mater.*, 2015, acs.chemmater.5b03883.

149 D.-X. Yuan, A. Gorka, M.-F. Xu, Z.-K. Wang and L.-S. Liao, *Phys. Chem. Chem. Phys.*, 2015, **17**, 19745–19750.

150 C.-G. Wu, C.-H. Chiang, Z.-L. Tseng, N. Mohammad K., A. Hagfeldt and M. Grätzel, *Energy Environ. Sci.*

151 J. Cui, F. Meng, H. Zhang, K. Cao, H. Yuan, Y. Cheng, F. Huang and M. Wang, *ACS Appl. Mater. Interfaces*, 2014, **6**, 22862–22870.

152 A. Garcia, G. C. Welch, E. L. Ratcliff, D. S. Ginley, G. C. Bazan and D. C. Olson, *Adv. Mater.*, 2012, **24**, 5368–5373.

153 G. Kakavelakis, I. Paradisanos, B. Paci, A. Generosi, M. Papachatzakis, T. Maksudov, L. Najafi, A. E. Del Rio Castillo, G. Kioseoglou, E. Stratakis, F. Bonaccorso and E. Kymakis, *Adv. Energy Mater.*, 1702287-n/a.

154 L. Hu, J. Peng, W. Wang, Z. Xia, J. Yuan, J. Lu, X. Huang, W. Ma, H. Song, W. Chen, Y.-B. Cheng and J. Tang, *ACS Photonics*, 2014, **1**, 547–553.

155 S. Yoon and D.-W. Kang, *Ceram. Int.*, , DOI:https://doi.org/10.1016/j.ceramint.2018.02.147.

156 G. Niu, S. Wang, J. Li, W. Li and L. Wang, *J. Mater. Chem. A*, , DOI:10.1039/C8TA00161H.

157 J. Zheng, L. Hu, J. S. Yun, M. Zhang, C. F. J. Lau, J. Bing, X. Deng, Q. Ma, Y. Cho, W. Fu, C. Chen, M. A. Green, S. Huang and A. W. Y. Ho-Baillie, *ACS Appl. Energy Mater.*, 2018, **1**, 561–570.

158 Z. Hu, D. Chen, P. Yang, L. Yang, L. Qin, Y. Huang and X. Zhao, *Appl. Surf. Sci.*, 2018, **441**, 258–264.

159 J. H. Kim, P.-W. Liang, S. T. Williams, N. Cho, C.-C. Chueh, M. S. Glaz, D. S. Ginger and A. K.-Y. Jen, *Adv. Mater.*, 2015, **27**, 695–701.

160 W. Chen, Y. Zhou, G. Chen, Y. Wu, B. Tu, F.-Z. Liu, L. Huang, A. M. C. Ng, A. B. Djurišić and Z. He, *Adv. Energy Mater.*, 2019, **0**, 1803872.

161 P. Qin, S. Tanaka, S. Ito, N. Tetreault, K. Manabe, H. Nishino, M. K. Nazeeruddin and M. Grätzel, *Nat. Commun.*, 2014, **5**, 3834.

162 S. Ye, W. Sun, Y. Li, W. Yan, H. Peng, Z. Bian, Z. Liu and C. Huang, *Nano Lett.*, 2015, **15**, 3723–3728.

163 J.-Y. Jeng, Y.-F. Chiang, M.-H. Lee, S.-R. Peng, T.-F. Guo, P. Chen and T.-C. Wen, *Adv. Mater.*, 2013, **25**, 3727–3732.

164 C. Tian, E. Castro, T. Wang, G. Betancourt-Solis, G. Rodriguez and L. Echegoyen, *ACS Appl. Mater. Interfaces*, 2016, **8**, 31426–31432.

165 J. H. Heo, H. J. Han, D. Kim, T. K. Ahn and S. H. Im, *Energy Environ. Sci.*, 2015, **8**, 1602–1608.

166 C.-H. Chiang, Z.-L. Tseng and C.-G. Wu, *J. Mater. Chem. A*, 2014, **2**, 15897–15903.

167 C. Tian, E. Castro, G. Betancourt-Solis, Z. Nan, O. Fernandez-Delgado, S. Jankuru and L. Echegoyen, *New J. Chem.*, 2018, **42**, 2896–2902.

168 K. A. Bush, C. D. Bailie, Y. Chen, A. R. Bowring, W. Wang, W. Ma, T. Leijtens, F. Moghadam and M. D. McGehee, *Adv. Mater.*, 2016, **28**, 3937–3943.

169 Z. Zhu, Y. Bai, X. Liu, C.-C. Chueh, S. Yang and A. K.-Y. Jen, *Adv. Mater.*, 2016, **28**, 6478–6484.

170 R. Fang, S. Wu, W. Chen, Z. Liu, S. Zhang, R. Chen, Y. Yue, L. Deng, Y.-B. Cheng, L. Han and W. Chen, *ACS Nano*, , DOI:10.1021/acsnano.7b07754.

171 K. O. Brinkmann, J. Zhao, N. Pourdavoud, T. Becker, T. Hu, S. Olthof, K. Meerholz, L. Hoffmann, T. Gahlmann, R. Heiderhoff, M. F. Oszajca, N. A. Luechinger, D. Rogalla, Y. Chen, B. Cheng and T. Riedl, *Nat. Commun.*, 2017, **8**, 13938.

172 A. Mei, X. Li, L. Liu, Z. Ku, T. Liu, Y. Rong, M. Xu, M. Hu, J. Chen, Y. Yang, M. Grätzel and H. Han, *Sci.* , 2014, **345**, 295–298.

173 Z. Liu, B. Sun, T. Shi, Z. Tang and G. Liao, *J. Mater. Chem. A*, 2016, **4**, 10700–10709.

174 Z. Ku, Y. Rong, M. Xu, T. Liu and H. Han, *Sci. Rep.*, 2013, **3**, 3132.

175 G. Liao, Z. Liu, B. Sun, X. Liu, J. Han, H. Ye, Y. Tu, C. Chen, T. Shi and Z. Tang, *J. Mater. Chem. A*, , DOI:10.1039/C8TA00526E.

176 S. Liu, W. Huang, P. Liao, N. Pootrakulchote, H. Li, J. Lu, J. Li, F. Huang, X. Shai, X. Zhao, Y. Shen, Y.-B. Cheng and M. Wang, *J. Mater. Chem. A*, 2017, **5**, 22952–22958.

177 J. Burschka, N. Pellet, S.-J. Moon, R. Humphry-Baker, P. Gao, M. K. Nazeeruddin and M. Grätzel, *Nature*, 2013, **499**, 316–9.

178 M. Liu, M. B. Johnston and H. J. Snaith, *Nature*, 2013, **501**, 395–8.

179 J. M. Ball, M. M. Lee, A. Hey and H. J. Snaith, *Energy Environ. Sci.*, 2013, **6**, 1739.

180 W.-Y. Chen, L.-L. Deng, S.-M. Dai, X. Wang, C.-B. Tian, X.-X. Zhan, S.-Y. Xie, R.-B. Huang and L. Zheng, *J. Mater. Chem. A*.

181 K. Sun, P. Li, Y. Xia, J. Chang and J. Ouyang, *ACS Appl. Mater. Interfaces*.

182 G. E. Eperon, V. M. Burlakov, P. Docampo, A. Goriely and H. J. Snaith, *Adv. Funct. Mater.*, 2014, **24**, 151–157.

183 S. Seo, I. J. Park, M. Kim, S. Lee, C. Bae, H. S. Jung, N.-G. Park, J. Y. Kim and H. Shin, *Nanoscale*, 2016, **8**, 11403–11412.

184 X. Dong, H. Hu, B. Lin, J. Ding and N. Yuan, *Chem. Commun.*, 2014, **50**, 14405–14408.

185 E. H. Anaraki, A. Kermanpur, L. Steier, K. Domanski, T. Matsui, W. Tress, M. Saliba, A. Abate, M. Gratzel, A. Hagfeldt and J.-P. Correa-Baena, *Energy Environ. Sci.*, 2016, **9**, 3128–3134.

186 S. Tzu-Sen, H. Tsung-Yu and W. Tzu-Chien, *Sol. RRL*, 2018, **2**, 1700120.

187 W. Shufang, C. Chi, J. Jingpeng, W. Jinming and P. Tianyou, *Sol. RRL*, 2017, **2**, 1700164.

188 C. Zhang, Y. Luo, X. Chen, W. Ou-Yang, Y. Chen, Z. Sun and S. Huang, *Appl. Surf. Sci.*, 2016, **388**, 82–88.

189 H.-S. Ko, J.-W. Lee and N.-G. Park, *J. Mater. Chem. A*, 2015, **3**, 8808–15.

190 S. Ito, S. Tanaka and H. Nishino, *Chem. Lett.*, 2015, **44**, 849–851.

191 J. Huang, K. Jiang, X. Cui, Q. Zhang, M. Gao, M. Su, L. Yang and Y. Song, *Sci. Rep.*, 2015, **5**, 15889.

192 P. Fan, D. Gu, G. Liang, J. Chen, J. Luo, Y. Xie, Z. Zheng and D. Zhang, *J. Mater. Sci. Mater. Electron.*, 2015, 1–7.

193 N. J. Jeon, J. H. Noh, Y. C. Kim, W. S. Yang, S. Ryu and S. Il Seok, *Nat. Mater.*, 2014, **13**, 897–903.

194 M. Xiao, F. Huang, W. Huang, Y. Dkhissi, Y. Zhu, J. Etheridge, A. Gray-Weale, U. Bach, Y.-B. Cheng and L. Spiccia, *Angew. Chemie Int. Ed.*, 2014, **53**, 9898–9903.

195 B.-E. Cohen, S. Aharon, A. Dymshits and L. Etgar, *J. Phys. Chem. C*, 2016, **120**, 142–147.

196 B. Xia, Z. Wu, H. Dong, J. Xi, W. Wu, T. Lei, K. Xi, F. Yuan, B. Jiao, L. Xiao, Q. Gong and X. Hou, *J. Mater. Chem. A*, 2016, **4**, 6295–6303.

197 N. Lin, J. Qiao, H. Dong, F. Ma and L. Wang, *J. Mater. Chem. A*, 2015, **3**, 22839–22845.

198 M. Yin, F. Xie, H. Chen, X. Yang, F. Ye, E. Bi, Y. Wu, M. Cai and L. Han, *J. Mater. Chem. A*, 2016, **4**, 8548–8553.

199 J. Chen, J. Ren, Z. Li, H. Wang and Y. Hao, *Org. Electron.*, 2018, **56**, 59–67.

200 Y. Wang, J. Wu, P. Zhang, D. Liu, T. Zhang, L. Ji, X. Gu, Z. David Chen and S. Li, *Nano Energy*, 2017, **39**, 616–625.

201 Y. Yu, S. Yang, L. Lei, Q. Cao, J. Shao, S. Zhang and Y. Liu, *ACS Appl. Mater. Interfaces*, 2017, **9**, 3667–3676.

202 S. Ito, S. Tanaka and H. Nishino, *J. Phys. Chem. Lett.*, 2015, **6**, 881–886.

203 H. Zhou, Q. Chen and Y. Yang, *MRS Bull.*, 2015, **40**, 667–673.

204 H.-S. Ko, J.-W. Lee and N.-G. Park, *J. Mater. Chem. A*.

205 J.-H. Im, I.-H. Jang, N. Pellet, M. Grätzel and N.-G. Park, *Nat. Nanotechnol.*, 2014, **9**, 927–932.

206 A. Binek, F. C. Hanusch, P. Docampo and T. Bein, *J. Phys. Chem. Lett.*, 2015, **6**, 150316103833007.

207 W. Li, J. Fan, J. Li, G. Niu, Y. Mai and L. Wang, *ACS Appl. Mater. Interfaces*, 2016, **8**, 30107–30115.

208 H. Chen, Z. Wei, X. Zheng and S. Yang, *Nano Energy*, 2015, **15**, 216–226.

209 U. A. Charles, M. A. Ibrahim and M. A. M. Teridi, *J. Power Sources*, 2018, 378, 717–731.

210 I. Kosta, H. Grande and R. Tena-Zaera, *Electrochim. Acta*, 2017, **246**, 1193–1199.

211 X.-P. Cui, K.-J. Jiang, J.-H. Huang, X.-Q. Zhou, M.-J. Su, S.-G. Li, Q.-Q. Zhang, L.-M. Yang and Y.-L. Song, *Chem. Commun.*, 2015, **51**, 1457–1460.

212 S.-G. Li, K.-J. Jiang, M.-J. Su, X.-P. Cui, J.-H. Huang, Q.-Q. Zhang, X.-Q. Zhou, L.-M. Yang and Y.-L. Song, *J. Mater. Chem. A*, 2015, **3**, 9092–9097.

213 J. Yen-Sook, H. Kyeongil, H. Youn-Jung, K. Jueng-Eun, V. Doojin and K. Dong-Yu, *Adv. Opt. Mater.*, 2018, **0**, 1701182.

214   V. Doojin, H. Kyeongil, F. Andrew, J. Yen-Sook, C. Noel, K. Dong-Yu, W. G. J. and W. S. E., *Adv. Energy Mater.*, 2014, **5**, 1401539.

215   K. Hwang, Y. S. Jung, Y. J. Heo, F. H. Scholes, S. E. Watkins, J. Subbiah, D. J. Jones, D. Y. Kim and D. Vak, *Adv. Mater.*, 2015, **27**, 1241–1247.

216   Q. Hu, L. Zhao, J. Wu, K. Gao, D. Luo, Y. Jiang, Z. Zhang, C. Zhu, E. Schaible, A. Hexemer, C. Wang, Y. Liu, W. Zhang, M. Grätzel, F. Liu, T. P. Russell, R. Zhu and Q. Gong, *Nat. Commun.*, 2017, **8**, 15688.

217   Y.-J. Heo, J.-E. Kim, H. Weerasinghe, D. Angmo, T. Qin, K. Sears, K. Hwang, Y.-S. Jung, J. Subbiah, D. J. Jones, M. Gao, D.-Y. Kim and D. Vak, *Nano Energy*, 2017, **41**, 443–451.

218   T. Qin, W. Huang, J.-E. Kim, D. Vak, C. Forsyth, C. R. McNeill and Y.-B. Cheng, *Nano Energy*, 2017, **31**, 210–217.

219   W. Zhanhua, C. Haining, Y. Keyou and Y. Shihe, *Angew. Chemie*, 2014, **126**, 13455–13459.

220   F. Mathies, T. Abzieher, A. Hochstuhl, K. Glaser, A. Colsmann, U. W. Paetzold, G. Hernandez-Sosa, U. Lemmer and A. Quintilla, *J. Mater. Chem. A*, 2016, **4**, 19207–19213.

221   L. Chao, L. Pengwei, G. Hao, Z. Yiqiang, L. Fengyu, S. Yanlin, S. Guosheng, M. Nripan and X. Guichuan, *Sol. RRL*, 2018, **2**, 1700217.

222   L. Liu, A. Mei, T. Liu, P. Jiang, Y. Sheng, L. Zhang and H. Han, *J. Am. Chem. Soc.*, 2015, **137**, 1790–1793.

223   M. Xiangyue, Z. Junshuai, H. Jie, T. Xia, C. S. Hang, S. S. Kong and Y. Shihe, *Adv. Mater.*, 2018, **0**, 1706975.

224   F. Zhang, X. Yang, M. Cheng, J. Li, weihan wang, H. Wang and L. Sun, *J. Mater. Chem. A*, , DOI:10.1039/C5TA07507F.

225   P. Vivo, K. J. Salunke and A. Priimagi, *Mater.* , 2017, 10.

226   L. Hoffmann, K. O. Brinkmann, J. Malerczyk, D. Rogalla, T. Becker, D. Theirich, I. Shutsko, P. Görrn and T. Riedl, *ACS Appl. Mater. Interfaces*, 2018, **10**, 6006–6013.

227   C.-Y. Chang, K.-T. Lee, W.-K. Huang, H.-Y. Siao and Y.-C. Chang, *Chem. Mater.*, 2015, **27**, 5122–5130.

228   Y. M. Yang, Q. Chen, Y.-T. Hsieh, T.-B. Song, N. De Marco, H. Zhou and Y. Yang, *ACS Nano*.

229   W.-C. Lai, K.-W. Lin, Y.-T. Wang, T.-Y. Chiang, P. Chen and T.-F. Guo, *Adv. Mater.*, 2016, n/a-n/a.

230   W.-C. Lai, K.-W. Lin, T.-F. Guo, P. Chen and Y.-Y. Liao, *Appl. Phys. Lett.*, 2018, **112**, 71103.

231   S. N. Habisreutinger, N. K. Noel, and H. J. Snaith, ACS Energy Lett., 2018, 3, 2472–2476.

232   H. J. Snaith, A. Abate, J. M. Ball, G. E. Eperon, T. Leijtens, N. K. Noel, S. D.

Stranks, J. T.-W. Wang, K. Wojciechowski and W. Zhang, *J. Phys. Chem. Lett.*, 2014, **5**, 1511–1515.

233 W. Tress, N. Marinova, T. Moehl, S. M. Zakeeruddin, M. K. Nazeeruddin and M. Grätzel, *Energy Environ. Sci.*, 2015, **8**, 995–1004.

234 J. M. Frost, K. T. Butler, F. Brivio, C. H. Hendon, M. Van Schilfgaarde and A. Walsh, *Nano Lett.*, 2014, **14**, 2584–2590.

235 Z. Xiao, Y. Yuan, Y. Shao, Q. Wang, Q. Dong, C. Bi, P. Sharma, A. Gruverman and J. Huang, *Nat. Mater.*, 2014, **14**, 193–198.

236 M. De Bastiani, G. Dell'Erba, M. Gandini, V. D'Innocenzo, S. Neutzner, A. R. S. Kandada, G. Grancini, M. Binda, M. Prato, J. M. Ball, M. Caironi and A. Petrozza, *Adv. Energy Mater.*, 2015, n/a-n/a.

237 T. Zhang, H. Chen, Y. Bai, S. Xiao, L. Zhu, C. Hu, Q. Xue and S. Yang, *Nano Energy*.

238 G. Richardson, S. O'Kane, R. G. Niemann, T. A. Peltola, J. M. Foster, P. J. Cameron and A. Walker, *Energy Environ. Sci.*, 2016, **9**, 1476–1485.

239 K. Miyano, M. Yanagida, N. Tripathi and Y. Shirai, *J. Phys. Chem. Lett.*, 2016, 2240–2245.

240 S. Meloni, T. Moehl, W. Tress, M. Franckevičius, M. Saliba, Y. H. Lee, P. Gao, M. K. Nazeeruddin, S. M. Zakeeruddin, U. Rothlisberger and M. Graetzel, *Nat. Commun.*, 2016, **7**, 10334.

241 A. Pockett and M. J. Carnie, *ACS Energy Lett.*, 2017, **2**, 1683–1689.

242 W. Chen, Y. Wu, Y. Yue, J. Liu, W. Zhang, X. Yang, H. Chen, E. Bi, I. Ashraful, M. Grätzel and L. Han, *Science (80-.).*, , DOI:10.1126/science.aad1015.

243 J.-Y. Jeng, K.-C. Chen, T.-Y. Chiang, P.-Y. Lin, T.-D. Tsai, Y.-C. Chang, T.-F. Guo, P. Chen, T.-C. Wen and Y.-J. Hsu, *Adv. Mater.*, 2014, **26**, 4107–4113.

244 N. E. Courtier, J. M. Cave, J. M. Foster, A. B. Walker and G. Richardson, *Energy Environ. Sci.*, 2019, **12**, 396–409.

245 D. A. Jacobs, H. Shen, F. Pfeffer, J. Peng, T. P. White, F. J. Beck and K. R. Catchpole, *J. Appl. Phys.*, 2018, **124**, 225702.

246 A. D. Jodlowski, C. Roldán-Carmona, G. Grancini, M. Salado, M. Ralaiarisoa, S. Ahmad, N. Koch, L. Camacho, G. de Miguel and M. K. Nazeeruddin, *Nat. Energy*, 2017, **2**, 972–979.

247 R. G. Niemann, L. Gouda, J. Hu, S. Tirosh, R. Gottesman, P. J. Cameron and A. Zaban, *J. Mater. Chem. A*, 2016, **4**, 17819–17827.

248 W. Rehman, R. L. Milot, G. E. Eperon, C. Wehrenfennig, J. L. Boland, H. J. Snaith, M. B. Johnston and L. M. Herz, *Adv. Mater.*, 2015, n/a-n/a.

249 W. Liao, D. Zhao, Y. Yu, N. Shrestha, K. Ghimire, C. R. Grice, C. Wang, Y. Xiao, A. Cimaroli, R. J. Ellingson, N. Podraza, K. Zhu, R.-G. Xiong and Y. Yan, *J. Am. Chem. Soc.*, 2016, jacs.6b08337.

250   N. De Marco, H. Zhou, Q. Chen, P. Sun, Z. Liu, L. Meng, E.-P. Yao, Y. Liu, A. Schiffer and Y. Yang, *Nano Lett.*, 2016, **16**, 1009–1016.

251   C. Yi, J. Luo, S. Meloni, A. Boziki, N. Ashari-Astani, C. Gratzel, S. M. Zakeeruddin, U. Rothlisberger and M. Gratzel, *Energy Environ. Sci.*, 2016, **9**, 656–662.

252   G. Niu, X. Guo and L. Wang, *J. Mater. Chem. A*, 2015, **3**, 8970–8980.

253   B. Salhi, Y. S. Wudil, M. K. Hossain, A. Al-Ahmed and F. A. Al-Sulaiman, *Renew. Sustain. Energy Rev.*, 2018, **90**, 210–222.

254   G. Niu, W. Li, F. Meng, L. Wang, H. Dong and Y. Qiu, *J. Mater. Chem. A*, 2014, **2**, 705.

255   S. Zhaoning, A. Antonio, W. S. C., L. G. K., P. A. B., S. Ullrich, G. Michael and H. M. J., *Adv. Energy Mater.*, 2016, **6**, 1600846.

256   X. Dong, X. Fang, M. Lv, B. Lin, S. Zhang, J. Ding and N. Yuan, *J. Mater. Chem. A*, 2015, **3**, 5360–5367.

257   J. Liu, Y. Wu, C. Qin, X. Yang, T. Yasuda, A. Islam, K. Zhang, W. Peng, W. Chen and L. Han, *Energy Environ. Sci.*, 2014, **7**, 2963–2967.

258   T. Leijtens, G. E. Eperon, S. Pathak, A. Abate, M. M. Lee and H. J. Snaith, *Nat. Commun.*, 2013, **4**, 2885.

259   Y. Han, S. Meyer, Y. Dkhissi, K. Weber, J. M. Pringle, U. Bach, L. Spiccia and Y.-B. Cheng, *J. Mater. Chem. A*, 2015, **3**, 8139–8147.

260   K. Domanski, J.-P. Correa-Baena, N. Mine, M. K. Nazeeruddin, A. Abate, M. Saliba, W. Tress, A. Hagfeldt and M. Grätzel, *ACS Nano*, 2016, acsnano.6b02613.

261   M. T. Weller, O. J. Weber, J. M. Frost and A. Walsh, *J. Phys. Chem Lett.*, 2015, **6**, 3209–3212.

262   T. M. Koh, B. Febriansyah and N. Mathews, *Chem*, 2017, **2**, 326–327.

263   Y. Sheng, A. Mei, S. Liu, M. Duan, P. Jiang, C. Tian, Y. Xiong, Y. Rong, H. Han and Y. Hu, *J. Mater. Chem. A*, 2018, **6**, 2360–2364.

264   Z. Haiying, L. Guozhen, Z. Liangzheng, Y. Jiajiu, Z. Xuhui, A. Ahmed, H. Tasawar, P. Xu and D. Songyuan, *Adv. Energy Mater.*, 2018, **0**, 1800051.

265   J. Duan, T. Hu, Y. Zhao, B. He and Q. Tang, *Angew. Chem. Int. Ed. Engl.*, , DOI:https://doi.org/10.1002/anie.201801837.

266   D. Amalie, T. Nicolas, M. Thomas, G. Peng, N. M. Khaja and G. Michael, *Adv. Funct. Mater.*, 2014, **24**, 3250–3258.

267   J. Troughton, K. Hooper and T. M. Watson, *Nano Energy*, 2017, **39**, 60–68.

268   M. T. Weller, O. J. Weber, P. F. Henry, A. M. Di Pumpo and T. C. Hansen, *Chem. Commun.*, 2015, **51**, 4180–4183.

269   A. Poglitsch and D. Weber, *J. Chem. Phys.*, 1987, **87**, 6373–6378.

270   A. Dualeh, P. Gao, S. Il Seok and M. K. Nazeeruddin, .

271   C. D. Bailie, E. L. Unger, S. M. Zakeeruddin, M. Grätzel and M. D. McGehee, *Phys. Chem. Chem. Phys.*, 2014, **16**, 4864.

272   A. Dualeh, P. Gao, S. Il Seok, M. K. Nazeeruddin and M. Gratzel, *Chem. Mater.*, 2014, **26**, 4675–4678.

273   T. Leijtens, G. E. Eperon, S. Pathak, A. Abate, M. M. Lee and H. J. Snaith, *Nat. Commun.*, 2013, **4**, 2885.

274   G. Abdelmageed, L. Jewell, K. Hellier, L. Seymour, B. Luo, F. Bridges, J. Z. Zhang and S. Carter, *Appl. Phys. Lett.*, 2016, **109**, 233905.

275   D. Bryant, N. Aristidou, S. Pont, I. Sanchez-Molina, T. Chotchunangatchaval, S. Wheeler, J. R. Durrant and S. A. Haque, *Energy Environ. Sci.*, 2016, **9**, 1655–1660.

276   O. Mounkachi, E. Salmani, M. Lakhal, H. Ez-Zahraouy, M. Hamedoun, M. Benaissa, A. Kara, A. Ennaoui and A. Benyoussef, *Sol. Energy Mater. Sol. Cells*, 2016, **148**, 34–38.

277   S. G. Hashmi, A. Tiihonen, D. Martineau, M. Ozkan, P. Vivo, K. Kaunisto, V. Ulla, S. M. Zakeeruddin and M. Gratzel, *J. Mater. Chem. A*, 2017, **5**, 4797–4802.

278   J. M. Azpiroz, E. Mosconi, J. Bisquert and F. De Angelis, *Energy Environ. Sci.*, 2015, **8**, 2118–2127.

279   O. Almora, I. Zarazua, E. Mas-Marza, I. Mora-Sero, J. Bisquert and G. Garcia-Belmonte, *J. Phys. Chem. Lett.*, 2015, **6**, 1645–1652.

280   A. Senocrate, I. Moudrakovski, G. Y. Kim, T.-Y. Yang, G. Gregori, M. Grätzel and J. Maier, *Angew. Chemie Int. Ed.*, 2017, **56**, 7755–7759.

281   J. Haruyama, K. Sodeyama, L. Han and Y. Tateyama, *J. Am. Chem. Soc.*, 2015, **137**, 10048–10051.

282   A. Todinova, L. Contreras-Bernal, M. Salado, S. Ahmad, N. Morillo, J. Idígoras and J. J. A. Anta, *ChemElectroChem*, 2017, **4**, 2891–2901.

283   A. Dualeh, T. Moehl, N. Tétreault, J. Teuscher, P. Gao, M. K. Nazeeruddin and M. Grätzel, *ACS Nano*, 2014, **8**, 362–373.

284   A. Pockett, G. E. Eperon, N. Sakai, H. J. Snaith, L. M. Peter and P. J. Cameron, *Phys. Chem. Chem. Phys.*, 2017, **19**, 5959–5970.

285   A. Guerrero, G. Garcia-Belmonte, I. Mora-Sero, J. Bisquert, Y. S. Kang, T. J. Jacobsson, J. P. Correa-Baena and A. Hagfeldt, *J. Phys. Chem. C*, 2016, **120**, 8023–8032.

286   F. Ebadi, N. Taghavinia, R. Mohammadpour, A. Hagfeldt and W. Tress, *Nat. Commun.*, 2019, **10**, 1574.

287   E. J. Juarez-Perez, M. Wußler, F. Fabregat-Santiago, K. Lakus-Wollny, E. Mankel, T. Mayer, W. Jaegermann and I. Mora-Sero, *J. Phys. Chem. Lett.*, 2014, **5**, 680–685.

288   E. J. Juarez-Perez, R. S. Sanchez, L. Badia, G. Garcia-Belmonte, Y. S. Kang, I.

Mora-Sero and J. Bisquert, *J. Phys. Chem. Lett.*, 2014, **5**, 2390–2394.

289   I. Zarazua, J. Bisquert and G. Garcia-Belmonte, *J. Phys. Chem. Lett.*, 2016, **7**, 525–528.

290   C. Juan-Pablo, A. Miguel, L. Gabriel, T. Wolfgang, D. Konrad, S. Michael, M. Taisuke, J. T. Jesper, C. M. E., A. Antonio, G. Michael, M. Hernán and H. Anders, *Adv. Mater.*, 2016, **28**, 5031–5037.

291   Y. Yuan and J. Huang, *Acc. Chem. Res.*, 2016, **49**, 286–293.

292   F. Fabregat-Santiago, M. Kulbak, A. Zohar, M. Valles-Pelarda, G. Hodes, D. Cahen and I. Mora-Sero, *ACS Energy Lett.*, , DOI:10.1021/acsenergylett.7b00542.

293   A. Kovalenko, J. Pospisil, O. Zmeskal, J. Krajcovic and M. Weiter, *Phys. status solidi – Rapid Res. Lett.*, 2017, **11**, 1600418-n/a.

294   E. Ghahremanirad, A. Bou, S. Olyaee and J. Bisquert, *J. Phys. Chem. Lett.*, 2017, **8**, 1402–1406.

295   J. Gong, S. Darling and F. You, *Energy Environ. Sci.*, 2015, **8**, 1953–1968.

296   J. Zhang, X. Gao, Y. Deng, B. Li and C. Yuan, *ChemSusChem*, 2015, n/a-n/a.

297   J.-A. Alberola-Borràs, R. Vidal, E. J. Juárez-Pérez, E. Mas-Marzá, A. Guerrero and I. Mora-Seró, *Sol. Energy Mater. Sol. Cells*, 2018, **179**, 169–177.

298   I. Celik, Z. Song, A. J. Cimaroli, Y. Yan, M. J. Heben and D. Apul, *Sol. Energy Mater. Sol. Cells*.

299   J. Zhang, X. Gao, Y. Deng, Y. Zha and C. Yuan, *Sol. Energy Mater. Sol. Cells*, 2017, **166**, 9–17.

300   J.-A. Alberola-Borràs, J. A. Baker, F. De Rossi, R. Vidal, D. Beynon, K. E. A. Hooper, T. M. Watson and I. Mora-Seró, *iScience*, 2018, **9**, 542–551.

301   A. Babayigit, D. Duy Thanh, A. Ethirajan, J. Manca, M. Muller, H.-G. Boyen and B. Conings, *Sci. Rep.*, 2016, **6**, 18721.

302   J. M. Kadro, N. Pellet, F. Giordano, A. Ulianov, O. Muntener, J. Maier, M. Gratzel and A. Hagfeldt, *Energy Environ. Sci.*, 2016, **9**, 3172–3179.

303   J. Xu, Z. Hu, L. Huang, X. Huang, X. Jia, J. Zhang, J. Zhang and Y. Zhu, *Prog. Photovoltaics Res. Appl.*, 2017, **25**, 1022–1033.

304   A. Binek, M. L. Petrus, N. Huber, H. Bristow, Y. Hu, T. Bein and P. Docampo, *ACS Appl. Mater. Interfaces*.

305   A. K. Jena, Y. Numata, M. Ikegami and T. Miyasaka, *J. Mater. Chem. A*, 2018, **6**, 2219–2230.

306   N. Espinosa, L. Serrano-Luj??n, A. Urbina and F. C. Krebs, *Sol. Energy Mater. Sol. Cells*, 2015, **137**, 303–310.

307   N. K. Noel, S. N. Habisreutinger, B. Wenger, M. T. Klug, M. T. Horantner, M. B. Johnston, R. J. Nicholas, D. T. Moore and H. J. Snaith, *Energy Environ. Sci.*, 2017, **10**, 145–152.

308   S. Razza, F. Di Giacomo, F. Matteocci, L. Cinà, A. L. Palma, S. Casaluci, P. Cameron, A. D'Epifanio, S. Licoccia, A. Reale, T. M. Brown and A. Di Carlo, *J. Power Sources*, 2015, **277**, 286–291.

309   D. Lee, Y.-S. Jung, Y.-J. Heo, S. Lee, K. Hwang, Y.-J. Jeon, J.-E. Kim, J. Park, G. Y. Jung and D.-Y. Kim, *ACS Appl. Mater. Interfaces*, , DOI:10.1021/acsami.8b02549.

310   Q. Xue, R. Xia, C. J. Brabec and H.-L. Yip, *Energy Environ. Sci.*, , DOI:10.1039/C8EE00154E.

311   G. Yunlong, S. Kazutaka, S. Wataru and N. Eiichi, *Adv. Energy Mater.*, 2016, **6**, 1502317.

312   G. E. Eperon, V. M. Burlakov, A. Goriely and H. J. Snaith, *ACS Nano*, 2014, **8**, 591–598.

313   S. Bag and M. F. Durstock, *Nano Energy*, 2016, **30**, 542–548.

314   H. J. Snaith, *Nat. Mater.*, 2018, **17**, 372–376.

315   C. T. J., E. K. A. and S. W. J., *Prog. Photovoltaics Res. Appl.*, 2002, **10**, 195–203.

316   M. Jaysankar, M. Filipic, B. Zielinski, R. Schmager, W. Song, W. Qiu, U. W. Paetzold, T. Aernouts, M. Debucquoy, R. Gehlhaar and J. Poortmans, *Energy Environ. Sci.*, , DOI:10.1039/C8EE00237A.

3: Theory

3.1. The sun

The illumination required for solar energy generation can come from any source, with the most sustainable and powerful of these being the sun, an extensive source of radiation that delivers a large amount of potential power to the surface of the Earth. The sun can be modelled as a black body radiation source, i.e. it emits radiation based on its temperature. The spectrum generated by our sun (at 6500 K) is given by the black line in Figure 3.1.1. Absorption of photons by molecules in the atmosphere contributes to a reduction in the amount of solar radiation which reaches the Earth's surface. The severity of this loss is determined by the angle of the Earth's surface to the incident radiation. At a greater zenith angle the light has a longer path to travel before it reaches the surface of the Earth, and is therefore absorbed more by molecules such as O_3 and H_2O in the atmosphere. In practical terms, this means a solar farm on the equator would receive a greater irradiance than one in the tropics, or in the Arctic/Antarctic. To standardise solar cell measurements a zenith angle of 48 ° is used, and the resulting irradiance spectrum is classed as the Air Mass (AM) 1.5G spectrum (in blue on Figure 3.1.1).
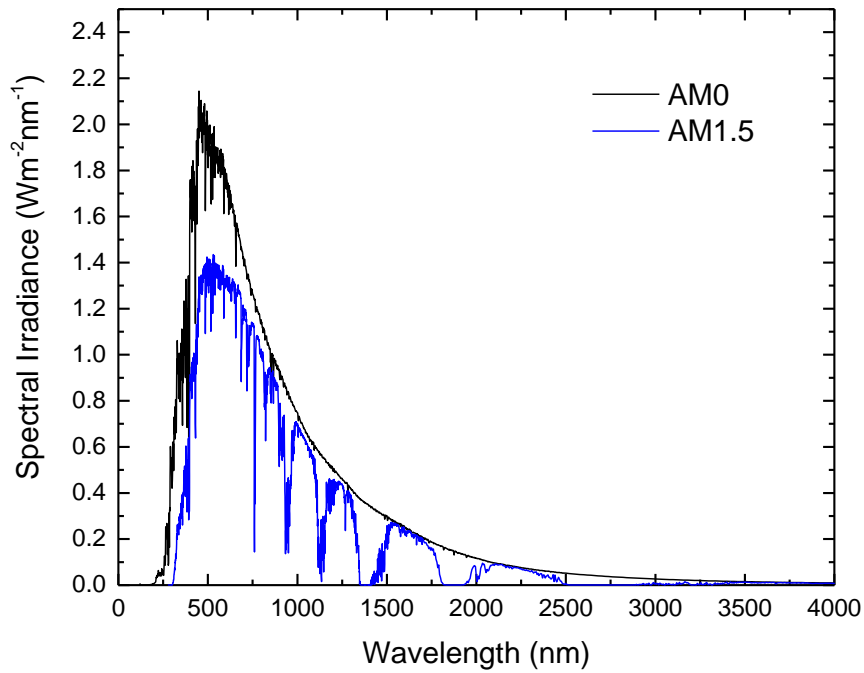
Figure 3.1.1. *Spectral Irradiance at the surface of the Sun (AM0, black), and using the standard solar angle of 48 ° at the surface of the earth (AM1.5, blue).*

Other uncontrollable meteorological and seasonal factors must be considered when positioning photovoltaic modules, such as cloud cover which would affect irradiance, and therefore the power output of the solar cell. Furthermore, greenhouse gas emissions will serve to increase the Air Mass by polluting the sky with more light absorbing molecules. Despite these barriers it is estimated that the amount of incident power is enough that if 1 % of the Earth's surface was covered in 10 % efficient solar cells, it would more than satisfy global energy demands.[1]

3.2. Semiconductors

When Molecular Orbital (MO) theory is applied over vast systems the resulting orbitals merge into 'bands'; the energetic positions of which determine whether the material is an insulator, a conductor (metal), or a semiconductor (Figure 3.2.1.). The bonding/filled orbitals become the *valence* band, and the antibonding/unfilled orbitals average out to the *conduction* band.
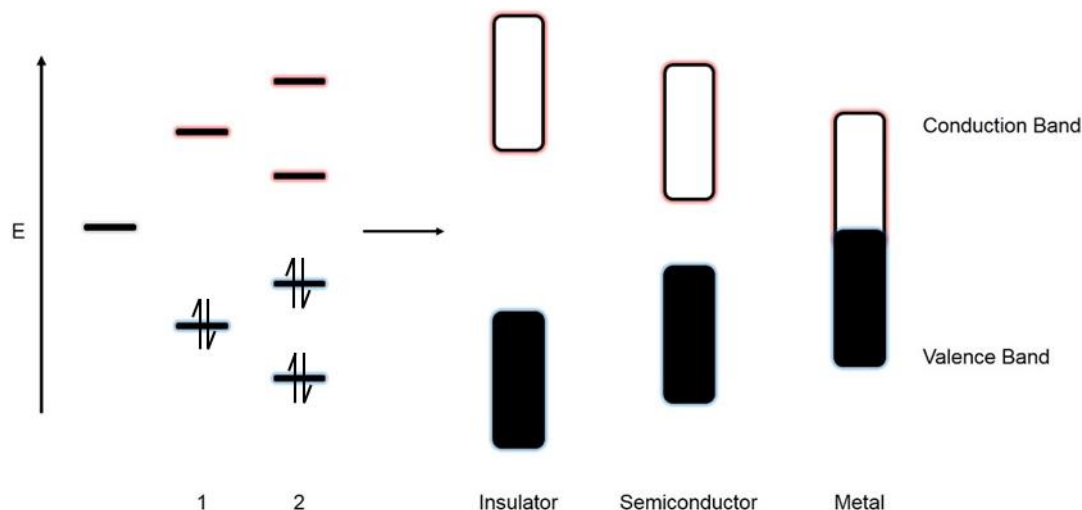
Figure 3.2.1. *Expansion of MO theory to explain the origin of Insulators, Semiconductors, and Metals*

If the energy gap, or band gap, is such that it requires extremely high energy to promote electrons to the conduction band then the material is an insulator. In a metal the bands overlap, allowing full conduction throughout the material. Semiconductors have a band gap that enables the population of the conduction band by doping, thermal excitation, or in the case of solar cells, photoexcitation of electrons. For solar cell absorber materials, the band gap is usually within the near IR to visible light region – which exists between 380-900 nm, or 1.3 – 3.3 eV. Promotion of an electron to the conduction band leaves a vacancy, or hole, in the valence band and conduction requires the movement of both electrons and holes (charge carriers) throughout the crystal lattice. Band gaps can be either direct or indirect, depending on the overlap of the conduction and valence band energy minima. A direct transition is one in which the ground state for the valence band is directly above that of the conduction band, *i.e.* upon excitation the electron enters the ground electronic state immediately. In an indirect band gap semiconductor this is not the case, and vibrations in the crystal lattice (or electron scattering in highly doped materials) are required for the excitation.

The occupation of energy levels by electrons in a semiconductor is determined by the Fermi-Dirac distribution $f(E)$ (Equation 3.1):

$$f(E) = \frac{1}{e^{\left(E-E_F/k_BT\right)} + 1} \tag{3.1}$$

where E is the energy, E_F the Fermi Level, k_B Boltzmann's constant and T temperature (in Kelvin). The Fermi level is the energy that an electron has a 50 % chance of occupying at equilibrium. However it is a theoretical level with no actual occupation. An intrinsic semiconductor is one in which E_F is halfway between the top of the valence band and the bottom of the conduction band. Figure 3.1.2 shows the effect of doping semiconductor materials on the position of the Fermi level within the band gap.
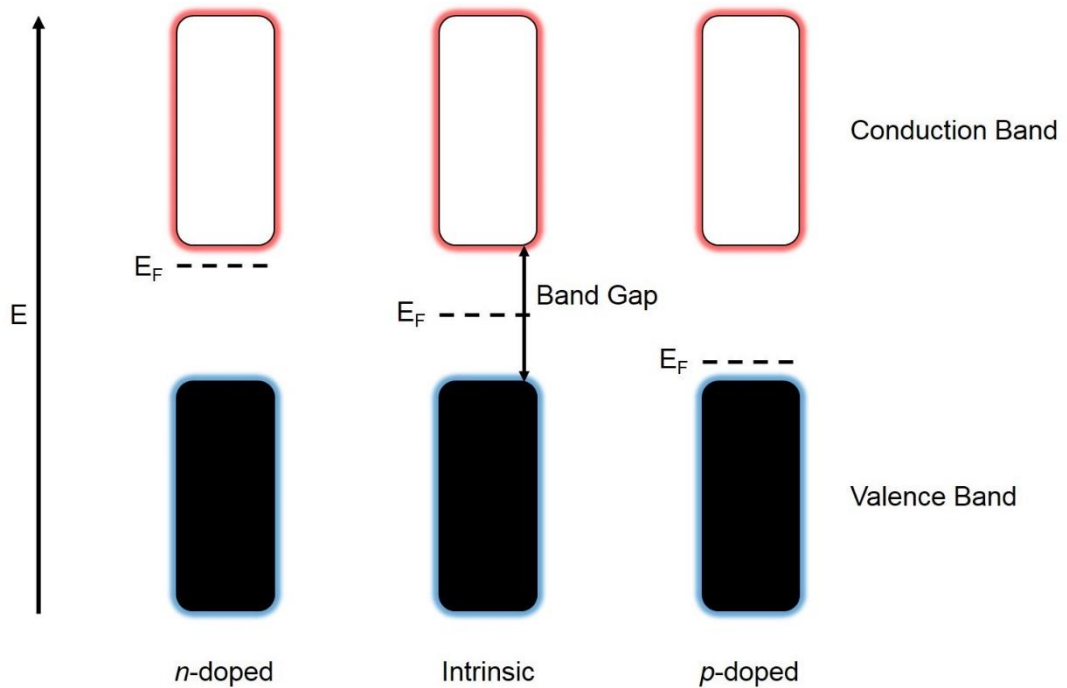
Figure 3.2.2. The effect of doping on the Fermi level of a semiconductor material

Dopants are either electron donors or acceptors that change the balance of charge carriers in the material. An *n*-type material is one that has been doped with electron donors, making electrons the majority carrier; in *p*-type materials holes are the majority carrier. The extent of doping in a semiconductor material can affect the lifetime of the charge carriers, *i.e.,* how long it takes for electrons and holes to recombine. The lifetime is directly related to the excess concentration of minority carriers (Δn).

$$\tau = \frac{\Delta n}{R} \qquad\qquad (3.2)$$

where τ is the carrier lifetime and R is recombination rate. Recombination can occur by three different pathways, each of which are illustrated in Figure 3.2.3. Radiative recombination involves the relaxation of an electron from the conduction to the valence band with the emission of a photon with equal energy to the band gap energy. The second method, Auger recombination, involves the transfer of energy from one electron to a second before relaxation; this second electron is promoted further up the energy levels in the conduction band before thermal relaxation back to the ground state. Auger recombination is common in highly doped materials, as doping increases the probability that an electron will be in the proximity of another for energy transfer. For Shockley-Read-Hall recombination, a defect state lying in the band gap is involved. It is a two-stage recombination, first the electron relaxes to the defect state before it relaxes again to the valence band, eliminating a hole.[2] Defect states are common at interfaces and grain boundaries, so this recombination method is important in polycrystalline materials (such as perovskites).
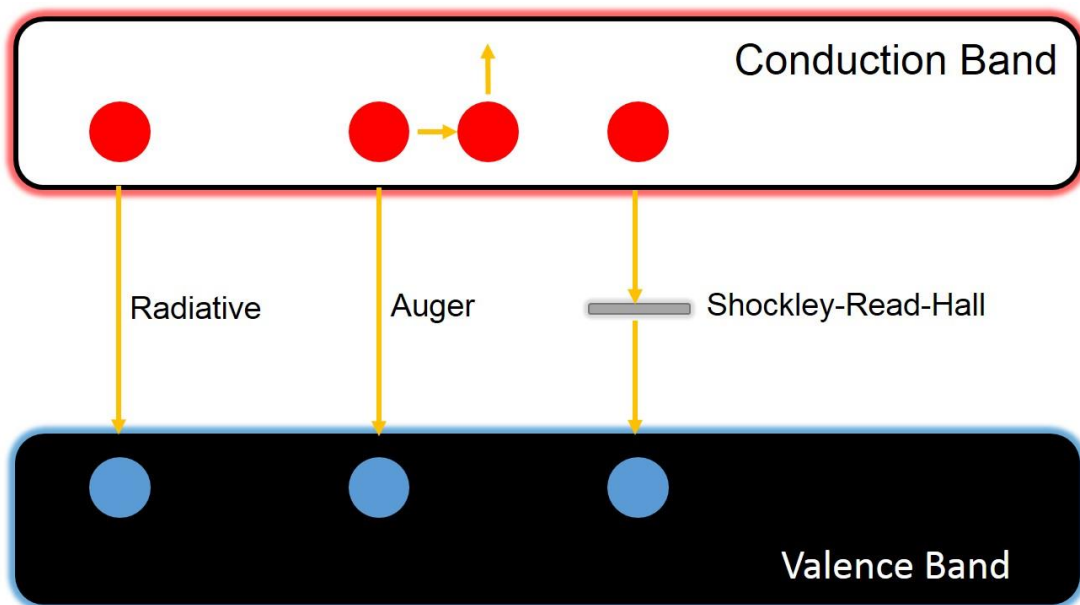
Figure 3.2.3. The different recombination mechanisms for electrons (red) and holes (blue)

The lifetime of minority carriers is defined as the length of time for the minority carrier concentration to reach $1/e$ its original concentration, and can be calculated using equation 3.3.

$$\frac{1}{\tau_{total}} = \frac{1}{\tau_r} + \frac{1}{\tau_{Aug}} + \frac{1}{\tau_{SRH}} \qquad (3.3)$$

where τ_r, τ_{Aug} and τ_{SRH} are the lifetimes with respect to radiative, Auger and Shockley-Read-Hall recombination respectively.

Electrons and holes are free to move in three dimensions throughout the crystal lattice. If an *n*-type and *p*-type material are combined, the movement of charge carriers is altered. When two phases come into contact, the Fermi levels must equilibrate. This requires band bending at the interface, between the *p* and *n*-type materials (Figure 3.2.4). As the two materials will have different concentrations of charge carriers, the majority carrier in each case will diffuse down the newly formed concentration gradient (charge carrier movement is illustrated in Figure 3.2.4).
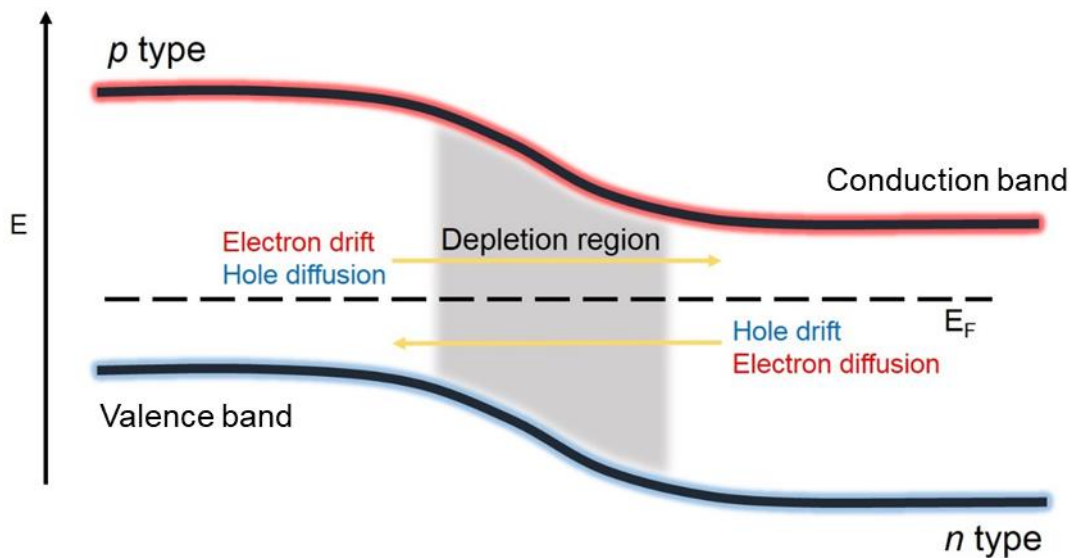
Figure 3.2.4. Charge Carrier movement in a p-n junction

Diffusion leaves exposed ion cores at the interface, creating an electric field. Any charge carriers present are rapidly swept away from the area, hence its name as the depletion region. Electrons and holes can also move against the field, this drift would result in for example movement of an electron from the *p*-type side to the *n*-type side. The depletion region is the optimum place for charge carrier generation, as the electric field means that the carriers are separated instantaneously, reducing the chances of recombination. The probability of charge carrier separation decreases with distance from the depletion region, as there is no field to separate them. Hence, for the design of solar cells, the *p-n* junction is often manufactured to be near the entry point for light,

as this maximises the probability for charge carrier generation in the depletion region.[3] A perovskite solar cell is modelled slightly differently, as a *p-i-n* junction in which the perovskite absorber is an intrinsic semiconductor between the *p*-type and *n*-type materials. The model remains largely the same, only the electric field is over a wider region. The depletion region is assumed to be the entire thickness of the perovskite absorber layer.

The electric field present at the depletion region can be changed by placing the *p-n* junction under forward or reverse bias, most commonly by applying a voltage. Placing the *p-n* junction under forward bias reduces the strength of the electric field, increasing the probability of charge carrier diffusion and collection in the external circuit. The opposite is true when under reverse bias.

If current in the *p-n* junction is only flowing in one direction, it can be modelled as a diode; a device that allows conduction in only one direction. The Ideal Diode Law (Equation 3.4) relates the applied bias (*V*) to the current (*I*) in the dark:

$$I = I_0 \left(e^{\frac{qV}{kT}} - 1 \right) \tag{3.4}$$

where I_0 is the dark saturation current, q the charge of an electron (1.602×10^{-19} C), V the applied voltage, k is Boltzmann's constant (1.38×10-23 m^2 kgs^{-2} K^{-1}) and T is temperature. The dark saturation current is a constant related to the recombination. The value of I_0 is higher if there are a large number of defects in the material, so the quality of material is important for current generation. For non-ideal systems an ideality factor typically between 1 and 2 is added to the equation, as n.

$$I = I_0 \left(e^{\frac{qV}{nkT}} - 1 \right) \tag{3.5}$$

Modelling of the current in the dark is important when calculating the photovoltaic parameters of a solar cell.

3.3. Photovoltaics

Illumination of the *p-n* junction (with radiation of energy greater than the band gap) generates carrier pairs throughout the whole junction. Separation of the electrons and holes at the depletion region causes a change in the density of the carriers from the equilibrium position where the Fermi levels on the *n* and *p*-type side were equal. As a result, the Fermi levels are split, leading to the formation of quasi Fermi levels for both electrons (E_{Fn}) and holes (E_{Fp}), shown in Figure 3.3.1. Using quasi Fermi levels is enabled as the relaxation to the ground state in either the conduction or valence band is much quicker than recombination with another carrier.[4] This process is the photovoltaic effect; under open-circuit conditions (*i.e.,* the carriers are prevented from leaving the *p-n* junction) there is the build-up of a potential difference between the Fermi levels of the *p* and *n*-type material. This is the *open-circuit voltage* (V_{OC}).
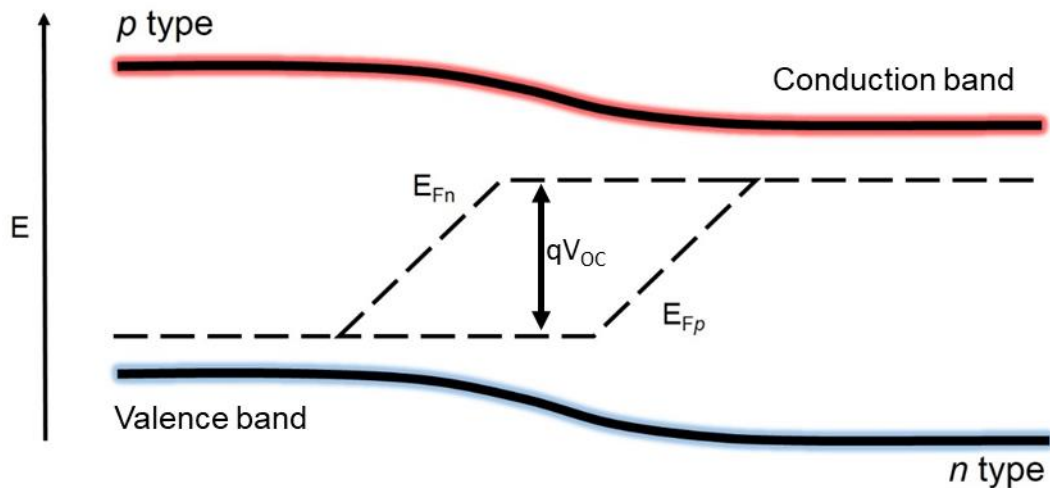
Figure 3.3.1. *The effect of illumination on the p-n junction and the formation of Quasi-Fermi Levels*

To model the V_{OC} it is necessary to look at the other extreme, where there is zero resistance to carrier movement. These are short-circuit conditions. Light-generated current is reliant on the quantum efficiency (EQE) of a material; the ratio of the charge carriers generated to the incident power on the solar cell *at one wavelength*. To get the short-circuit current (I_{SC}) the EQE of the photovoltaic material must be integrated over the entire wavelength range of the solar spectrum, shown in equation 3.6.

$$I_{SC} = q \int \Phi(E) EQE\,(E) dE \qquad (3.6)$$

J_{SC}, the short-circuit current density, is used because in solar cells the illumination is applied over a defined area. The photon flux density, $\Phi(E)$, for light of energy E and the *EQE(E)* is the corresponding External Quantum Efficiency value for this wavelength.

Open-circuit voltage can be defined as the point where the net current is zero. The net current is acquired by subtracting equation 3.5 from equation 3.6 at each applied potential, resulting in an IV curve – when corrected for the active area current becomes current density (J), resulting in the more commonly used JV curve. Rearranging for voltage when net current is zero results in equation 3.7 for the open-circuit voltage.

$$V_{OC} = \frac{nkT}{q}\ln\left(\frac{J_L}{J_0} + 1\right) \qquad (3.7)$$

The JV curve is the primary experiment for analysis of solar cell performance, and is effectively the illuminated cyclic voltammetry of the solar cell. An example is shown in Figure 3.3.2.
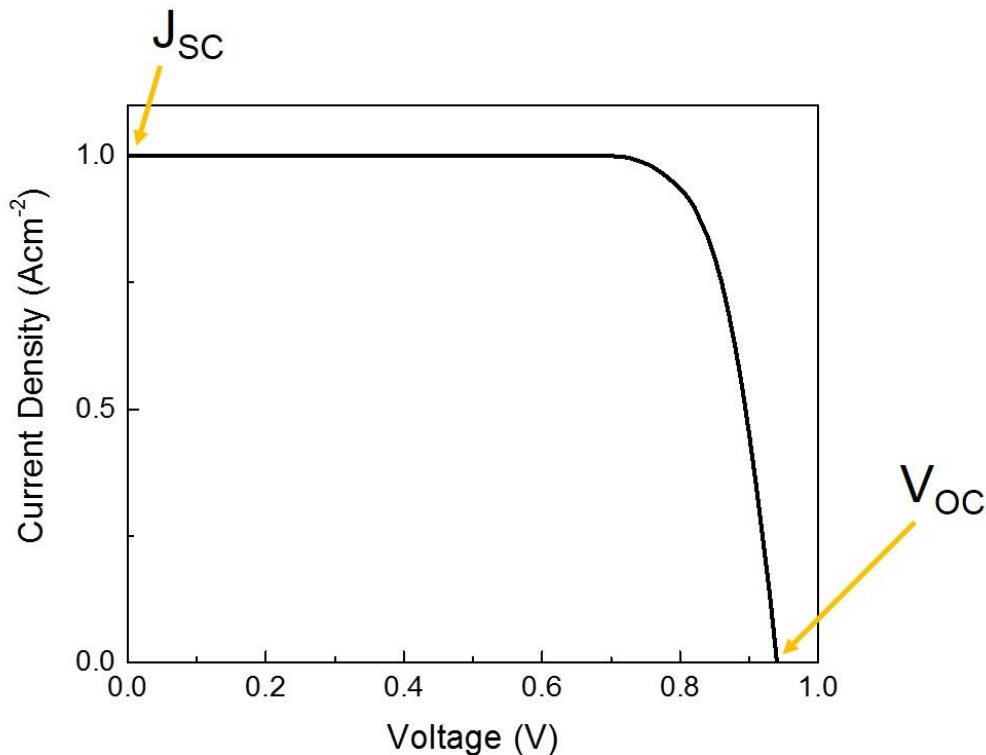
Figure 3.3.2. *An example JV curve with V_{OC} and J_{SC} highlighted*

The JV curve, however, does not provide all the photovoltaic parameters. The ultimate goal in photovoltaics is to generate as much power relative to the incident power from

the sun, or to be as efficient as possible. The power density generated by the solar cell can be calculated by J × V, and the resulting graph can be overlaid onto the JV curve (Figure 3.3.3).
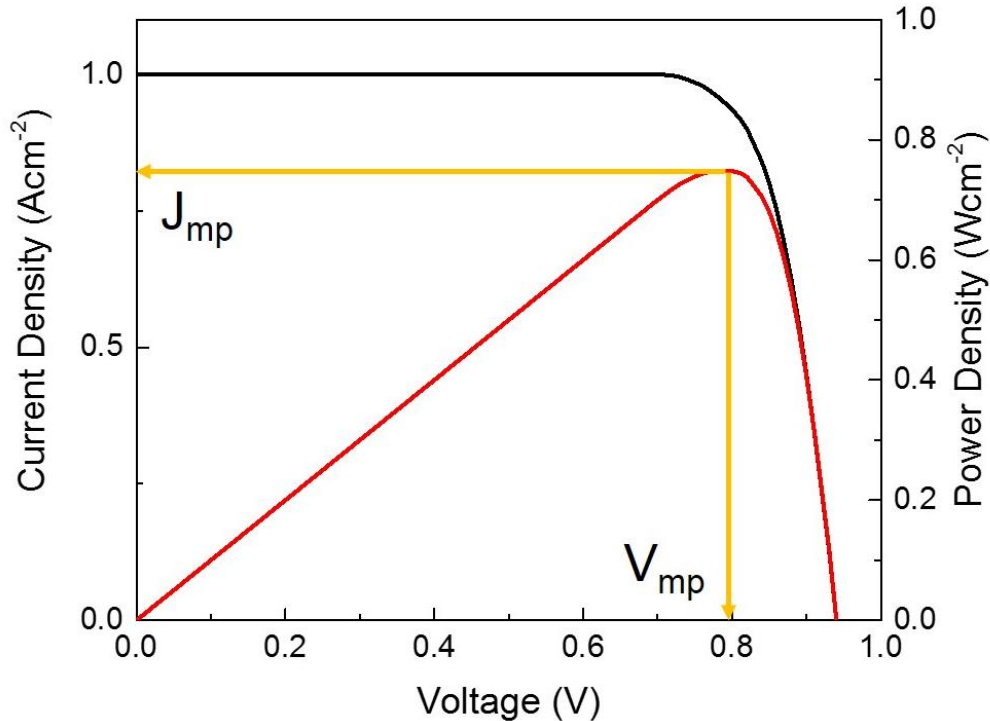
Figure 3.3.3. An example JV curve with the power density overlaid

The voltage and current density at the maximum power point (V_{mp} and J_{mp}) is used for the calculation of the Fill Factor, *FF*, by equation 3.8:

$$FF = \frac{V_{mp}J_{mp}}{V_{oc}J_{sc}} \tag{3.8}$$

The Fill Factor is often referred to as a measure of squareness of the curve, and a value as close to 1 (or 100%) as possible is desirable. Deviations from the ideal JV square, where there are no power losses until the cell reaches open-circuit voltage, are caused by two characteristic resistances, the series resistance and the shunt resistance. Series resistance is an unavoidable consequence of putting the solar cell as part of an external circuit. Contacts made to the solar cell add resistance to electron flow – in the JV curve this has a greater effect on V_{mp}. Shunt resistance is the resistance to alternate current routes, and therefore this needs to be maximised to boost cell performance, and reduce the effect on J_{mp}. The effect of parasitic resistances is visualised in Figure 3.3.4.
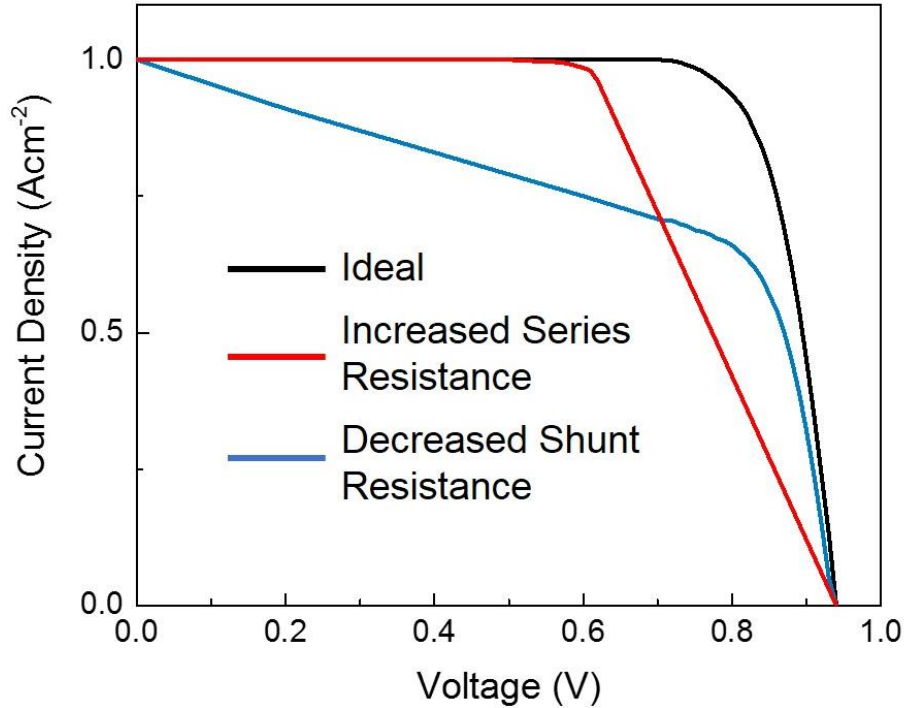
Figure 3.3.4. *The effect of parasitic losses on the JV curve*

Although the V_{OC} and J_{SC} are not affected by these losses, they do contribute negatively to the overall efficiency of the solar cell. The Fill Factor is included into the efficiency calculation to account for these:

$$\eta = \frac{V_{OC}J_{SC}FF}{P_{in}} \qquad (3.9)$$

where η is the efficiency, and P_{in} is the incident power density onto the cell during the measurement. Under standard measuring conditions P_{in} is at 1 sun, or 1 kWm^{-2}.

The theoretical efficiency of a solar cell is largely dependent on the band gap of the material being used. Shockley and Queisser analysed the relationship between band gap and the efficiency limit based on the black body radiation of the Sun.[5] For high band gap materials, the main efficiency losses are caused by an inability to absorb photons from a large proportion of the solar spectrum. For lower band gap materials, a lot of energy is wasted from the relaxation of electrons to the band edge following the absorption of photons with an energy larger than that of the band gap. Another factor that limits the efficiency of a solar cell is radiative recombination, which reduces the theoretical V_{OC} maximum to less than that of the band gap. Taking all these considerations into account, the optimal band gap for a solar cell is 1.34 eV, which

would result in a maximum theoretical efficiency of 33 %.[6] The causes of the efficiency limit are illustrated in Figure 3.3.5b.
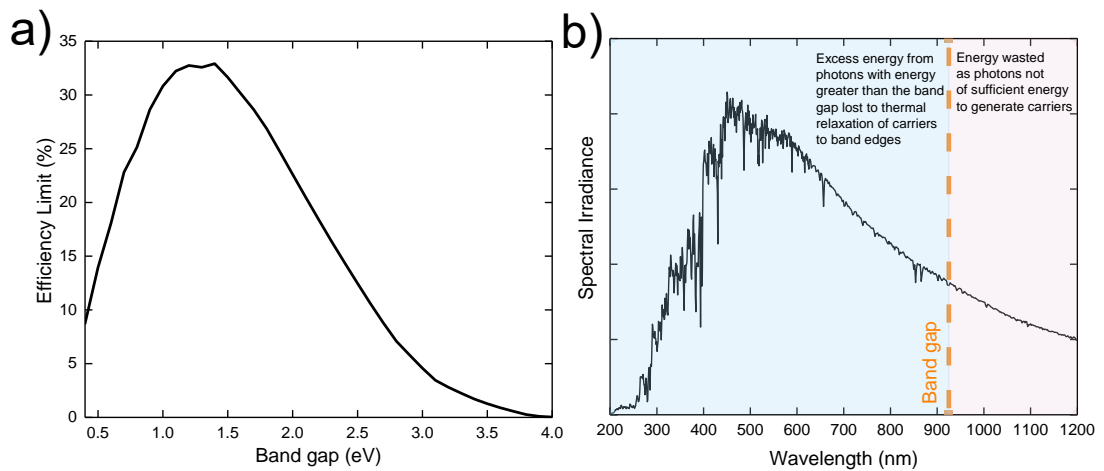
Figure 3.3.5. *a) the thermodynamic efficiency limit of solar cells as a function of band gap, data taken from reference 6 and b) an illustration of the major losses overlaid onto the solar spectrum*

The efficiency limit is based on there being only one *p-n* junction in the solar cell; it can be 'beaten' by adding another complementary *p-n* junction. Solar cells with more than one absorber layer are called multi-junction solar cells, the most common being tandem cells that have two absorber materials. Using similar methods to Shockley and Queisser, with the inclusion of radiation being trapped in the tandem structure, De Vos calculated the best possible combinations for various types of multijunction solar cell. Whereas for a single *p-n* junction the optimum band gap is 1.3 eV, for two junctions band gaps of 1.9 eV and 1.0 eV are most complementary with a theoretical efficiency of 42 %.[7] As the number of junctions increases, the complementary band gaps also change, allowing for a broader absorption of the solar spectrum and therefore a greater efficiency overall. Efficiency can also be increased by concentrating light onto the solar cell, *e.g.,* with mirrors. In the most extreme case, the maximum efficiency for an infinite junction solar cell (in standard sunlight) is over 60 %.[7,8]

3.4. AC Circuit theory and Electrochemical Impedance Spectroscopy

Creating a JV curve is a Direct Current (DC) method that requires a large sweep in the voltage, typically of over 1 V and at a single scan rate at a time. Alternating Current (AC) measurements, most commonly Electrochemical Impedance Spectroscopy (EIS) are a good way of elucidating further information about the solar cell from the time and frequency domain.

AC measurements involve the application of a sinusoidal voltage, typically with a 10 mV amplitude around an applied DC bias. From the JV curves there is very little current change with voltage around the short-circuit current. Therefore the most interesting place to measure is at the open-circuit voltage, where the greatest change in current response will occur as the voltage is modulated, as shown in Figure 3.4.1. It is also vital that the current response is linear to the applied voltage.
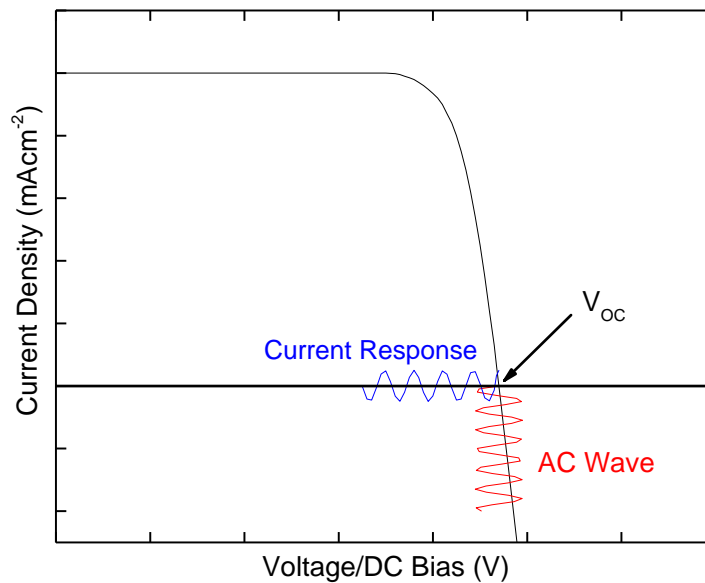
Figure 3.4.1. A graphical representation of the effect of DC bias on EIS response

As the sinusoidal voltage is applied (over a large range of frequencies, hence spectroscopy) the amplitude and phase shift of the current response is measured (Figure 3.4.2).
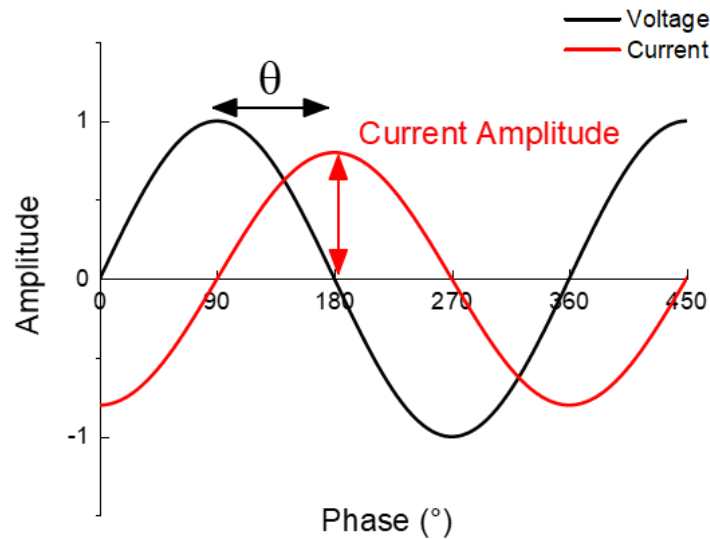
Figure 3.4.2. An example response of current to an applied sinusoidal voltage wave

The resistance of a DC system is calculated via Ohm's law, $V = IR$. For an AC system, where the Voltage and Current change with time, a transfer function is required to relate the input to the output. The input is the sinusoidal voltage:

$$V_t = V_0 cos(\omega t) \tag{3.10}$$

where V_0 is the voltage amplitude, ω is the angular frequency (2πf with respect to a frequency f), and t is time.

The output response is the current:

$$I_t = I_0 cos(\omega t - \varphi) \tag{3.11}$$

where I_0 is the current amplitude, and φ is the phase shift.

By extension of Ohm's law, the AC form is shown below:

$$Z = \frac{V_0 cos(\omega t)}{I_0 cos(\omega t + \varphi)} \tag{3.12}$$

The EIS response of the solar cell (and any other electrochemical system) is often modelled using a series of resistors and capacitors (Section 3.4.4). The impedance of a resistor and a capacitor is derived from Equation 3.12. For a resistor, there is no phase shift, so the *cos(ωt)* terms in the above equation cancel:

$$Z_R = \frac{V_0}{I_0} \tag{3.13}$$

A capacitor does cause a phase shift in the output response, so the impedance of a capacitor is complicated. The equation is solved by converting the sine and cosine functions into complex exponentials, by way of Euler's formula.

$$e^{jx} = \cos(x) + j\sin(x) \qquad (3.14)$$

This means that the input voltage can be described as (only one exponential term is required for analysis, as the second is symmetrical, *i.e.* the $e^{-j\omega t}$ is removed):

$$V_0\cos(\omega t) = Ve^{j\omega t} \qquad (3.15)$$

The derivation proceeds as follows, from the equation for the charge of a capacitor:

$$Q_t = CV_t \qquad (3.16)$$

$$\int I(t)dt = CV(t) \qquad (3.17)$$

$$I(t) = C\frac{dV(t)}{dt} \qquad (3.18)$$

$$V_{(t)} = Ve^{j\omega t} \qquad (3.19)$$

$$\frac{dV}{dt} = j\omega Ve^{j\omega t} \qquad (3.20)$$

$$Z_C = \frac{V_c(t)}{I_c(t)} = \frac{Ve^{j\omega t}}{Cj\omega Ve^{j\omega t}} \qquad (3.21)$$

This then can be simplified to equation 3.22.

$$Z_C = \frac{1}{j\omega C} \qquad (3.22)$$

Overall, this means that the impedance of any pure resistors in the cell are constant throughout the measurement, whereas the response of the capacitor varies with frequency.

The equivalent circuit (Figure 3.4.3) is a model that shows the electrical system as a series of simple circuit elements, either arranged in parallel or series, depending on the path of the current. If current must flow through each element they are displayed in series, if the current has a choice (in EIS this is dependent on frequency), then the circuit elements are in parallel.
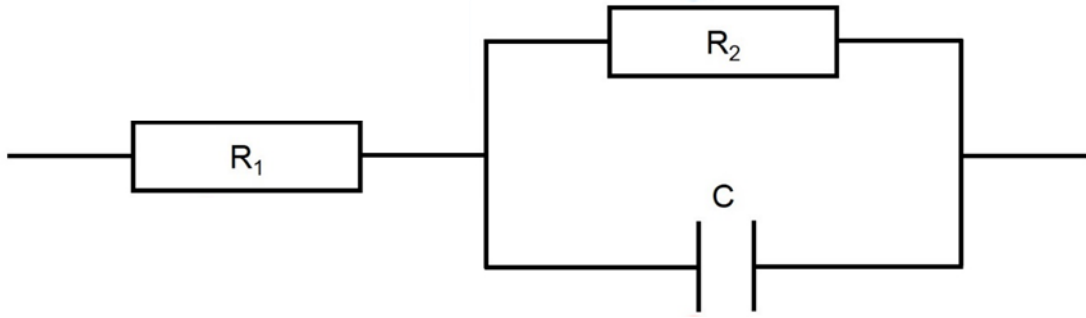
Figure 3.4.3. An equivalent circuit model for an R(RC) circuit

The current will always follow the path of least resistance. As in Equation 3.22, the impedance of a capacitor is inversely proportional to the frequency. At high frequencies this means that the impedance of the capacitor is very low. Hence at the highest frequencies the phase is 0 ° as the series resistance R1 dominates the response. As the frequency of the applied voltage decreases, the impedance of the capacitor increases; the phase angle increases to 90 ° when the impedance of the capacitance is dominant. At low frequencies the impedance of the capacitor becomes so great that the current response is dominated by the two resistances, so the phase shift returns to 0 ° at a point on the *x* axis equal to $R_1 + R_2$. R_1 is present in all electrical systems; it is the series resistance of contacts and interfaces in the circuit.

The change in phase shift is displayed graphically in Figure 3.4.4, the result of an impedance measurement on the equivalent circuit shown in Figure 3.4.3.
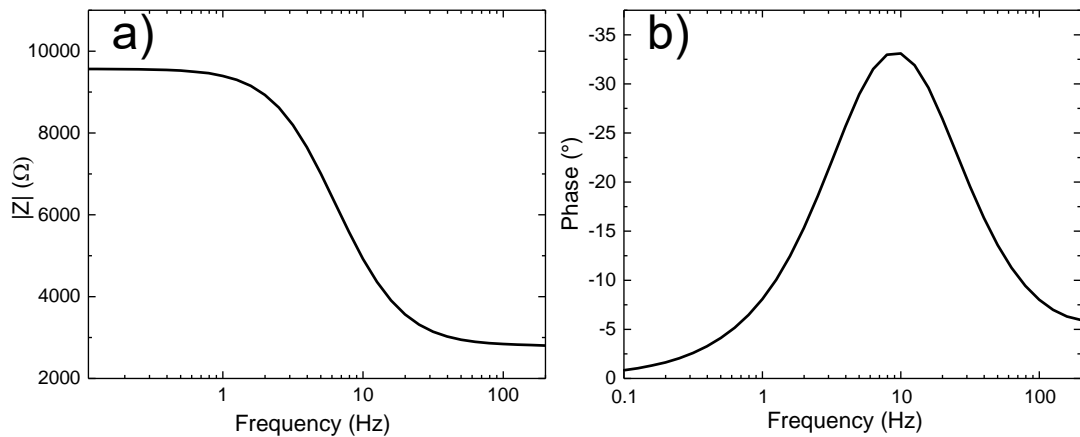
Figure 3.4.4. Example Bode plots: (a) |Z| and (b) Phase angle against Frequency

These two plots are called *Bode* plots, and show simple graphs of either the phase or the magnitude of impedance against frequency. The phase shift caused by a resistive element is 0 °, and of a pure capacitor is 90 °.

A plot of the absolute value of impedance (|Z|) against frequency will start at a value of the series resistance with the highest measured frequency, then a smooth line towards $Z_{R1} + Z_{R2}$. |Z| is the absolute magnitude of the total impedance. The total impedance can be treated as the sum of individual impedances in the circuit. This requires the addition of the impedances of the individual components. Summing the impedance values is different depending on whether the elements are in series (Equation 3.23) or in parallel (3.24).

$$Z_{total} = Z_1 + Z_2 \qquad (3.23)$$

$$\frac{1}{Z_{total}} = \frac{1}{Z_1} + \frac{1}{Z_2} \qquad (3.24)$$

Another way of visualising impedance data is to plot the data on a complex plot. Using Euler's equation (3.14), the input signal and output signals are converted as follows:

$$V_0 cos(\omega t) = V_0 e^{j\omega t} \qquad (3.15)$$

$$I_0 cos(\omega t + \varphi) = I_0 e^{j\omega t} e^{-j\varphi} \qquad (3.25)$$

From this the impedance becomes:

$$Z = \frac{V_0 e^{j\omega t}}{I_0 e^{j\omega t} e^{-j\varphi}} = \frac{V_0}{I_0} e^{j\varphi} \qquad (3.26)$$

as:

$$|Z| = \frac{V_0}{I_0} \qquad (3.27)$$

then:

$$Z = |Z| e^{j\varphi} \qquad (3.28)$$

Therefore in a Nyquist plot (complex plane plot, Figure 3.4.5), each point at each frequency represents the absolute value of the impedance along the *x*-axis, elevated into the imaginary plane (on the *y*-axis) by a phase shift, shown in blue on Figure 3.4.5. If there were no capacitive elements in the circuit, the response would be frequency invariant and give a single point on the *x*-axis. The shift in phase angle caused by a capacitance brings the data into the complex plane, and in the case of the equivalent circuit introduced in Figure 3.4.2, a semicircle is formed with the second *x*-axis intercept at a value of $R_1 + R_2$.
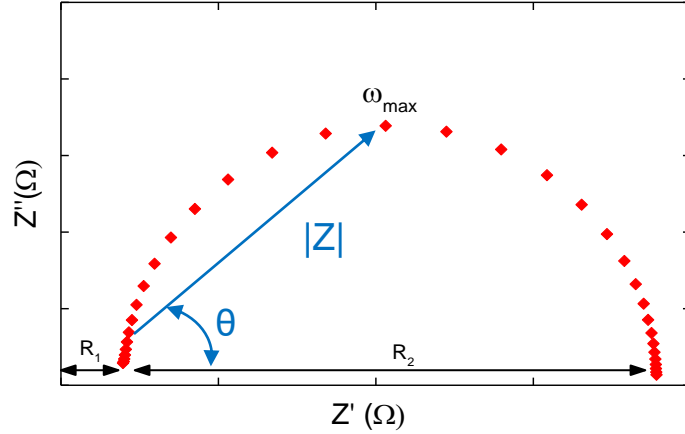
Figure 3.4.5. An example Nyquist plot for a simple circuit with one time constant

From the value of ω_{max} taken at the top of the semicircle, the time constant τ can be calculated by its inverse. Using R_2 (the diameter of the semicircle), the capacitance can then be calculated (Equation 3.29).

$$\tau = \frac{1}{\omega_{max}} = R_2 C \tag{3.29}$$

The time constant is characteristic for a specific process, and can help to analyse the system, *e.g.* a process with a fast time constant ($\leq \mu s$) is likely to be electronic, and a slow time constant (s) could be due to ionic diffusion in a material. Depending on the process, the time constant can change with different voltages, light intensities or temperatures – indeed which one of these variables that affects the process can help to determine its identity. In solar cells, measuring the impedance under different controlled conditions can lead to the determination of detailed material properties such as ideality factor, or activation energies for ion diffusion (see section 2.4.4. and Chapters 7 & 8) as voltage changes ion distribution, which affects the current. Calculation of the activation energy for a process uses the time constant, τ, in the place of k in the Arrhenius equation:

$$k = Ae^{\frac{-E_A}{RT}} \tag{3.30}$$

where k is the rate constant, A the pre-exponential factor, E_A the activation energy and R the gas constant. Taking the natural logarithm of each side results in Equation 3.31.

$$ln\ k = \ln A - \frac{E_A}{RT} \tag{3.31}$$

Hence a plot of $\ln(k)$, or $\ln(\tau)$ in the case of EIS, against $1/T$ will allow the calculation of the activation energy from the gradient.

3.5. Powder/thin film X-ray diffraction

In this report thin-film X-ray diffraction is used to identify the structure of the perovskite materials, and to analyse differences in the structure upon the inclusion of additives. The X-ray diffractogram shows a series of reflections based on the crystal planes in the material. Crystal planes are made up of lattice points, which are the smallest repeating unit within the crystal structure. The angle of allowed observed 'refractions' is determined by Bragg's law, demonstrated graphically below.
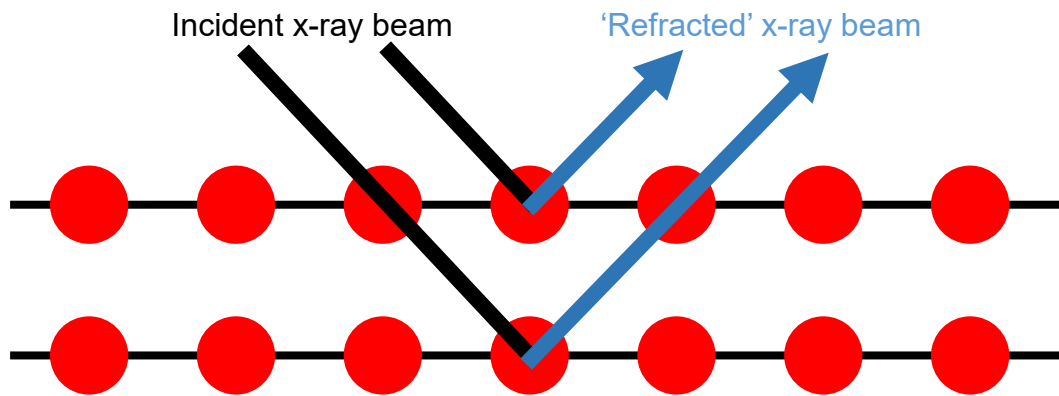
Figure 3.5.1. *Reflections in X-ray diffractometry*

Both X-rays in the above figure have the same wavelength and incident angle. This allows the path difference between the two to be calculated.
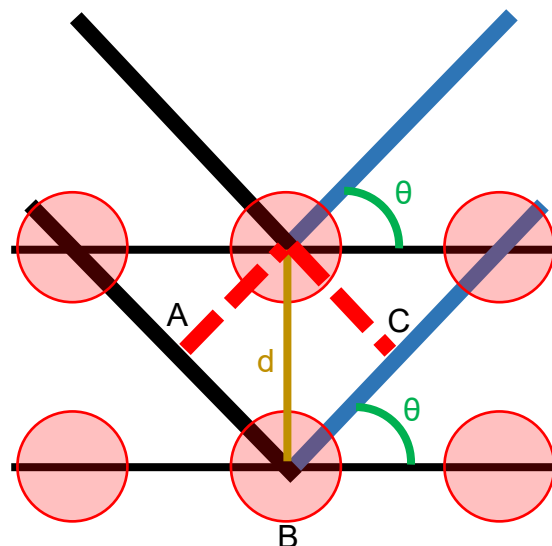
Figure 3.5.2. *Graphical representation for demonstrating Bragg's law*

From this:

$$AB + BC = n\lambda \tag{3.32}$$

$$\sin(\theta) = \frac{AB}{d} \tag{3.33}$$

$$AB = BC = d\sin(\theta) \tag{3.34}$$

$$2d\sin(\theta) = n\lambda \tag{3.35}$$

For a particular angle to be observed, the n value must be an integer, to allow for constructive interference of the resulting x-rays. Bragg's law means that the d-spacing can be related to the peak in the diffractogram. The d-spacing is also linked to the lattice parameters by the following equation (if all angles in the lattice are 90 °):

$$\frac{1}{d^2} = \frac{h^2}{a^2} + \frac{k^2}{b^2} + \frac{l^2}{c^2} \tag{3.36}$$

Where h, k, and l are the corresponding numbers for the crystal plane's Miller index, and a, b, and c are the lattice parameters – in this case for an orthogonal system. As a result, if the lattice is distorted to smaller sizes, a, b and c will change whilst h, k and l remain constant. This affects the d-spacing, and the resulting peak for the same hkl values is shifted to larger angles.

3.6. References

1   L. M. Peter, *Philos. Trans. R. Soc. London A Math. Phys. Eng. Sci.*, 2011, **369**, 1840–1856.

2   W. Shockley and W. T. Read, *Phys. Rev.*, 1952, **87**, 835–842.

3   S. Xiao and S. Xu, *Crit. Rev. Solid State Mater. Sci.*, 2014, **39**, 277–317.

4   J. Nelson, *The Physics of Solar Cells*, Imperial College Press, 2003.

5   W. Shockley and H. J. Queisser, *J. Appl. Phys.*, 1961, **32**, 510–519.

6   S. Rühle, *Sol. Energy*, 2016, **130**, 139–147.

7   A. De Vos, *J. Phys. D. Appl. Phys.*, 1980, **13**, 839.

8   J. E. Parrott, *J. Phys. D. Appl. Phys.*, 1979, **12**, 441–450.

4: Common Experimental Methods

4.1: Introduction

In this section common synthetic and analytical methods will be outlined. These are general procedures, and are used throughout the thesis unless otherwise specified in the relevant chapter.

4.2: Common Synthesis Methods

4.2.1. Glass preparation:

Either Fluorine doped Tin Oxide glass (FTO) (Solaronix, unless otherwise specified) with a sheet resistance of 15 Ω/square or microscope glass (VWR) was used. For film measurements, the glass was used as purchased. Glass was cut to 25 mm × 25 mm pieces. For Solar Cell fabrication a 5 mm strip was etched from the middle of the glass using 2 M HCl (Sigma) and Zn powder (Sigma) before the cleaning step.

Glass was cleaned in an ultrasonic bath at a temperature of 80 °C using the following solvents: 2 % Hellmanex in MilliQ water, water, acetone, isopropanol and ethanol. Following the final step the glass was dried using N_2 gas and placed in a UV/Ozone cleaner for 20 minutes.

4.2.2. Perovskite preparation and deposition:

Perovskite precursors and film/cell fabrication methods are specific to each chapter.

4.3: Common Analysis Methods

4.3.1. Crystallography:

Single Crystal X-ray diffraction was performed on an Agilent Technologies EOS S2 Supernova, using a Cu X-ray source. A Bruker AXS D8 advance powder x-ray diffractometer with a Cu Kα source and Ge monochromator was used for Powder/Thin film X-ray diffraction. Measurements were taken from 2θ values of 5 ° to 80 °.

4.3.2. Spectroscopic methods:

Thin film optical Transmission and Reflectance measurements were performed on a PerkinElmer Lambda 750S UV/Vis spectrometer, from 1000 nm to 250 nm. Absorption was calculated as incident light – (transmission + reflectance).

4.3.3. Atomic Force Microscopy

AFM images were taken on a Nanosurf easyscan 2 FlexAFM system in dynamic mode using a force of 20 nN. A ContAl0F Tip was used for measurements.

4.3.4. Current density-voltage curves

Current density-voltage curves were measured using a 2400 series Sourcemeter (Keithley Instruments), under simulated AM1.5 sunlight at 100 mW cm^{-2} irradiance generated using a class AAA solar simulator (TS-Space Systems) at room temperature in air. The intensity was calibrated using a certified silicon reference cell (Fraunhofer). The active area of the pixels was 0.0625 cm^2, measured using a mask of the same area. Voltage scans were taken from 1.1 V (preconditioning time 5s) to 0 V at 100 mVs^{-1}.

4.3.5. Electrochemical Impedance Spectroscopy:

EIS measurements were taken on a Solartron Modulab, measurements were taken under 73 mW cm^{-2} illumination at open circuit between 1MHz and 5mHz with a 10 mV perturbation. A 560 nm blue LED was used as the illumination source. The temperature of the cell was controlled by a Peltier element.

5: Azetidinium as a New Cation for Perovskite Solar Cells

5.1) Introduction

Since their invention in 2009, the chemical composition of the perovskite (ABX_3) absorber has remained largely unchanged, the most commonly used ions are still methylammonium (A), lead (B), and iodine (X_3).[1] This is perhaps due to the lack of suitable ion combinations that can produce a compound with a suitable 'tolerance factor' – a parameter based on the size of the ions that suggests whether a 3D perovskite is made.[2,3] Anion-mixing has proved easier in this regard; band-gap engineering is possible with the inclusion of small amounts of bromine or chlorine in the perovskite, allowing for a range of coloured perovskites to be produced, with enhanced photovoltaic properties and stability. [4–6]

The most popular alternative cation for methylammonium is formamidinium. Formamidinium Lead Iodide has a band gap of 1.38 eV, which is closer to the ideal value for maximum solar cell efficiency, however it is much less stable and requires higher processing temperatures.[7,8]. Caesium has also been used, although $CsPbI_3$ has a wider band gap of 1.73 eV and is unlikely to challenge the others in terms of efficiency.[9] Hybrid systems can enhance the performance of the perovskite; by mixing both the organic cation and the halide anion in a $Cs_5(MA_{0.17}FA_{0.83})_{95}Pb(I_{0.83}Br_{0.17})_3$ perovskite, PSC of over 22 % efficiency is achievable.[10] Mixing the cations has also been shown to improve the stability of the solar cell.[11] In order to further improve the efficiency and stability, different cations need to be researched, so that a wide range can be used in mixed cation materials. Other cations that have been used either on their own or as an additive in perovskites for photovoltaic applications include guanidinium,[12] rubidium,[13] hydrazinium,[14] potassium,[15] and ammonium.[16]

Computational studies can narrow down the pool of potential cations by sorting for tolerance factor.[2,17,18] One computationally suggested cation is azetidinium, a secondary amine with an ionic radius of 250 pm. It is smaller than formamidinium (253 pm) so it could be predicted to form a 3D perovskite – although it was suggested that the azetidinium cation would not be stable at the temperatures used in material

synthesis.[17] In this chapter the azetidinium cation is presented as a potential alternative for perovskite solar cells, both on its own and in mixed-cation solar cells.

5.2) Specific Experimental

5.2.1. Azetidinium iodide preparation

5 ml of Azetidine (Alfa Aesar) at 0 °C had 55 mL hydroiodic acid (Sigma) added to it under argon atmosphere, and the solution was stirred for one hour. The solution was then left on a rotary evaporator until dry, leaving a bright orange solid. This was washed with diethyl ether to remove the iodine, and recrystallized in isopropanol, leaving white needle-like crystals. The identity of azetidinium iodide (AzI) was confirmed by ^{1}H NMR (Figure S1): (300 MHz, D_2O, δ): 2.46 (quin, $J = 8.29$ Hz, 2 H) δ 4.04 (t, $J = 8.5$ Hz, 4 H)

5.2.2. Dipole Calculations

The calculated dipoles have been obtained using the NWChem code.[19] The initial input obtained by geometrical intuition has been optimized. To express the wavefunction the cc-pVTZ basis set provided within the package was used and the exchange correlation functional, B3LYP, was used. The obtained values are in good agreement with other reports in literature. [20,21]

5.2.3. Crystal formation

0.1 mmol PbI_2 and AzI were dissolved in 1 mL *N,N*-dimethylformamide, and single crystals were grown by the solvent evaporation method.

5.2.4. Film deposition

For optical and structural measurements the perovskite films were deposited on to microscope glass following a method by Zheng *et al.*[22] Glass was cleaned as per the method outlined in Section 4.2. 100 µL of a 1 M solution of PbI_2 (Sigma-Aldrich, 99%) in *N,N*-dimethylformamide is spin-coated at 2000 rpm for 60 seconds, followed immediately by 100 µL of isopropanol spun at the same rate. The resulting PbI_2 film was dried at 60 °C for 30 minutes. Solutions containing varying molar ratios of azetidinium iodide to methylammonium iodide (Greatcell Solar, purity not stated by manufacturer) were prepared in isopropanol, with a concentration of 20 mgml^{-1}. 100

µL of these solutions were pipetted onto the PbI_2 films, and spun for 60 seconds at 2000 rpm. The perovskite films were annealed at 100 °C for 20 minutes.

5.2.5. Solar cell fabrication

Pre-etched FTO glass (Kintek) was cleaned in 2% Hellmanex solution in water, followed by deionised water, acetone and isopropanol. A compact TiO_2 layer was deposited by spray pyrolysis. A hand held atomiser was used to spray a solution of 10 vol% solution of titanium isopropoxide (bisacetylacetonate) (Sigma-Aldrich, 75 wt% in isopropanol) in isopropanol onto the substrates, which were kept at 550 °C for the procedure, and sintered for 30 minutes at the same temperature. A mesoporous layer consisting of a 2:7 mixture of 30NRD TiO_2 paste (Dyesol) in ethanol was spun onto the compact layer with a further 30 minute sintering step at 550 °C. After cooling, a 0.1 M solution of Li-TFSI (Sigma) solution was spin-coated at 3000 rpm for 10 seconds and the substrates were then re-sintered at 550 °C for 30 minutes.

Perovskite deposition was performed in a nitrogen filled glove box. A two-step dip-coating method was used to fabricate the solar cells. 1M PbI_2 in DMF was kept at 70 °C for spin-coating. 100 µL of lead iodide solution was spin-coated at 6500 rpm for 30s, then dried at 100 °C for 30 minutes. A 5 minute dipping step in the MAI or mixed MAI/AzI in IPA solution (10 mgml^{-1}, AzI fractions in mol% with respect to MAI). The films were annealed at 100 °C for 1 hour.

The hole transport layer solution consisted of 85 mgml^{-1} Spiro-OMeTAD (Ossila) in chlorobenzene, with additives of: 30 µLml^{-1} t-butyl pyridine (Sigma), 20 µLml^{-1} of 520 mgmL^{-1} Li-TFSI in acetonitrile and 30 µgmL^{-1} FK209-TFSI solution. This was spin-coated onto the perovskite at 4000 rpm for 30 seconds.

To establish the contacts, 2 mm of perovskite was removed from the centre of the substrate. 100 nm of gold (Kurt J Lesker) was deposited by thermal evaporation.

5.2.6. SCXRD, PXRD

Crystal X-ray diffraction was performed on an Agilent Technologies EOS S2 Supernova, using a Cu X-ray source.

A Bruker AXS D8 advance powder x-ray diffractometer with a Cu Kα source and Ge

monochromator was used for Powder X-ray diffraction. Measurements were taken from 2θ values of 5 ° to 80 °.

5.2.7. Raman spectroscopy

Raman measurements were performed with a Renishaw Reflex microRaman spectrometer equipped with solid state lasers emitting at 514 and 785 nm with a resolution of < 2 cm^{-1}. The laser beam was focused with a x50 magnification lens, giving a laser spot size of about 1 µm in diameter. Rayleigh scattering was rejected with a 110 cm^{-1} cutoff dielectric edge filter. The AzI sample was measured with a 514 nm laser and the orange AzPI with the 785 nm laser in order to avoid resonant effects in the sample. All measurements were performed in air and with different laser powers to ensure that the laser probe did not induce damage or changes in the sample

5.2.8. Electrochemical measurements

An Autolab potentiostat/galvanostat was used for solution-based electrochemistry, using an Ag/AgCl reference electrode and a platinum counter electrode. 0.1 mol azetidinium iodide in isopropanol was used as the electrolyte.

5.2.9. J-V curves

J-V curves were measured using a Keithley 2601A potentiostat, under 1 Sun intensity and at AM 1.5. The cell was swept at 100 mVs^{-1} from 1.1 V to -0.1 V and back to 1.1 V. The 8 pixels with a 0.1 cm^2 active area (obtained using a mask) were measured independently. A Newport Oriel 91150-KG5 reference cell with a KG5 filter was used for instrument calibration. EQE measurements were taken in 10 nm steps from 380-850 nm.

5.2.10. Scanning Electron Microscopy

SEM images were taken on a JEOL SEM 6480LV, at an acceleration voltage of 10kV.

5.3) Azetidinium lead iodide

Two organic cations are most commonly used for perovskite solar cells, these are methylammonium and formamidinium, which have ionic radii of 217 pm and 253 pm respectively. Based on computational calculations of perovskite tolerance factors, the azetidinium cation has been identified as a potential candidate for perovskite solar cells with a tolerance factor of 0.98 (or 1.03 when considering the interactions of the lead and iodide ions).[2,18] The azetidinium cation is compared to methylammonium and formamidinium in Table 5.3.1.

Table 5.3.1: Comparison of Az^+ to MA^+ and FA^+, including ionic size, tolerance factor, perovskite structure at RT, dipole moment and chemical structure. Dipole moments were calculated for this study.

Cation	Methylammonium	Formamidinium	Azetidinium
Effective radius[34]	217	253	250
Tolerance Factor[27]	0.912	0.987	0.980
RT Structure	tetragonal	hexagonal	unresolved
Dipole moment (DFT calc.)	2.176 D	0.605 D	2.519 D
Chemical Structure	$H_3C{-}\overset{+}{N}H_3$	$H_2\overset{+}{N}{=}\!\!\diagdown\!\!{NH_2}$	azetidinium ring structure

Azetidinium has an ionic radius of 250 pm, however is chemically quite different to methylammonium and formamidinium, so could potentially have very different properties.

To properly determine the structure of azetidinium lead iodide, single crystal X-ray diffraction must be performed. Unfortunately, due to the large difference in atomic/molecular mass for the inorganic and organic ions, an accurate picture of the positions of all atoms in the structure could not be determined, further complicated by the motion of the organic molecule and a large amount of twinning in the crystals. However the data produced from the single crystals may still be useful, especially if it

can be corroborated with other experiment, although the positions of the cations could not be categorically solved.

The observed structure of the lead iodide octahedra (Figure 5.3.1.) obtained shows a very interesting result, that this structure is neither a 3-dimensional perovskite (as predicted by tolerance factor calculations), nor is it a true 2-dimensional perovskite, in which there are layers of lead iodide sheets separated by the organic cation. It appears to be a hybrid, 2.5-dimensional structure consisting at its core of groups of 3 face-sharing Pb-I octahedra, which in turn are corner-sharing with other groups of octahedra. Unlike 2-D perovskites, the continuous Pb-I backbone could still promote effective charge transfer.
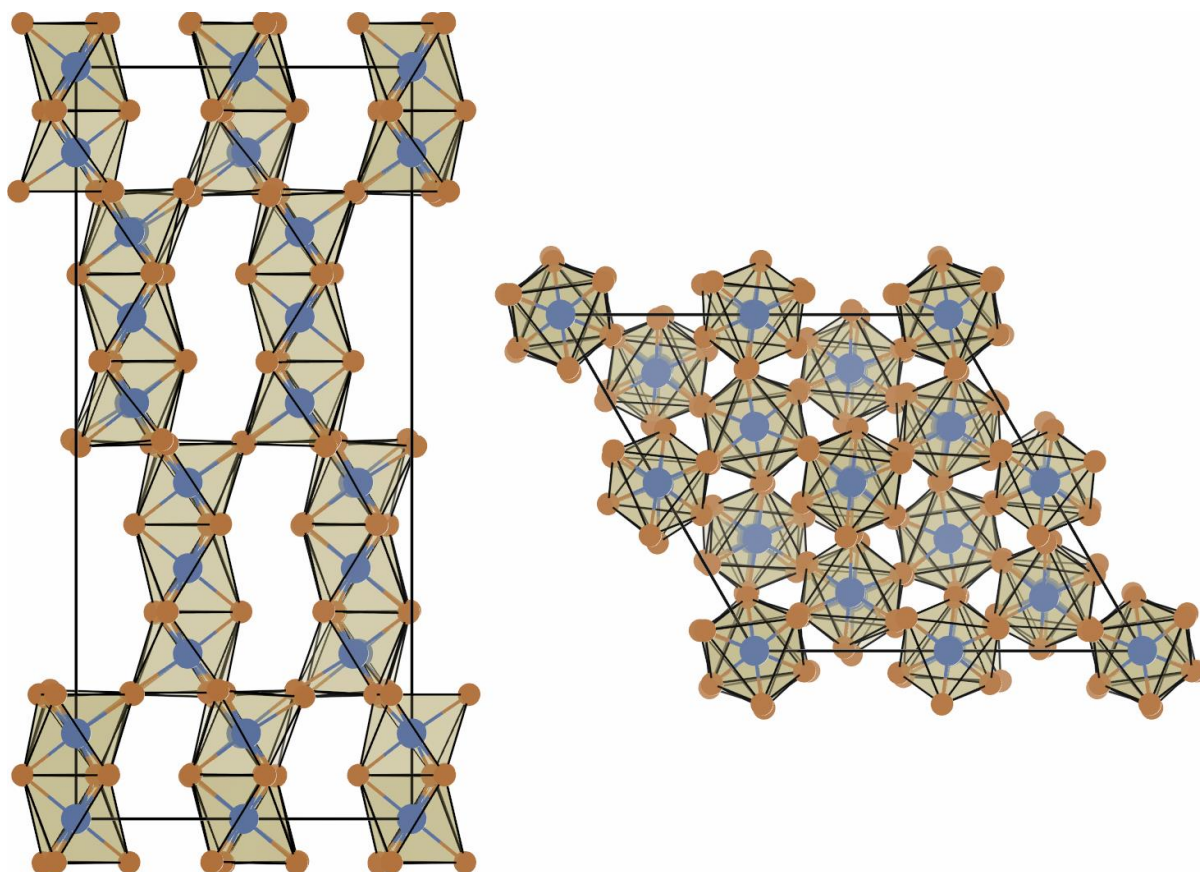
Figure 5.3.1. *Image of the Pb-I skeleton determined by Single Crystal X-ray Diffraction, (left) side-on and (right) top-down images*

To calculate possible positions for the azetidinium cations, caesium was chosen as a substitute ion for Density Functional Theory (DFT) calculations, to suggest cation positions that would preserve the derived lead iodide structure (Fig. 5.3.2.a). The azetidinium ion is however not spherical – it is a near planar molecule, and inclusion of this cation breaks all symmetry of the crystal. Azetidinium could exist in the

structure in various orientations, either perpendicular to the z-axis, or in the plane of the ZX or ZY (in this case assumed to be degenerate). Both simulations are shown alongside the caesium case in Figure 5.3.2 b and c. The size of the crystallographic unit is 576 atoms, which is very large to predict a structure, so approximation and lower accuracy were needed to perform complete calculations. The most stable structure predicted by these calculations is that of Fig. 5.3.2.b, in which the alignment of the azetidinium cations is perpendicular to the z-axis.
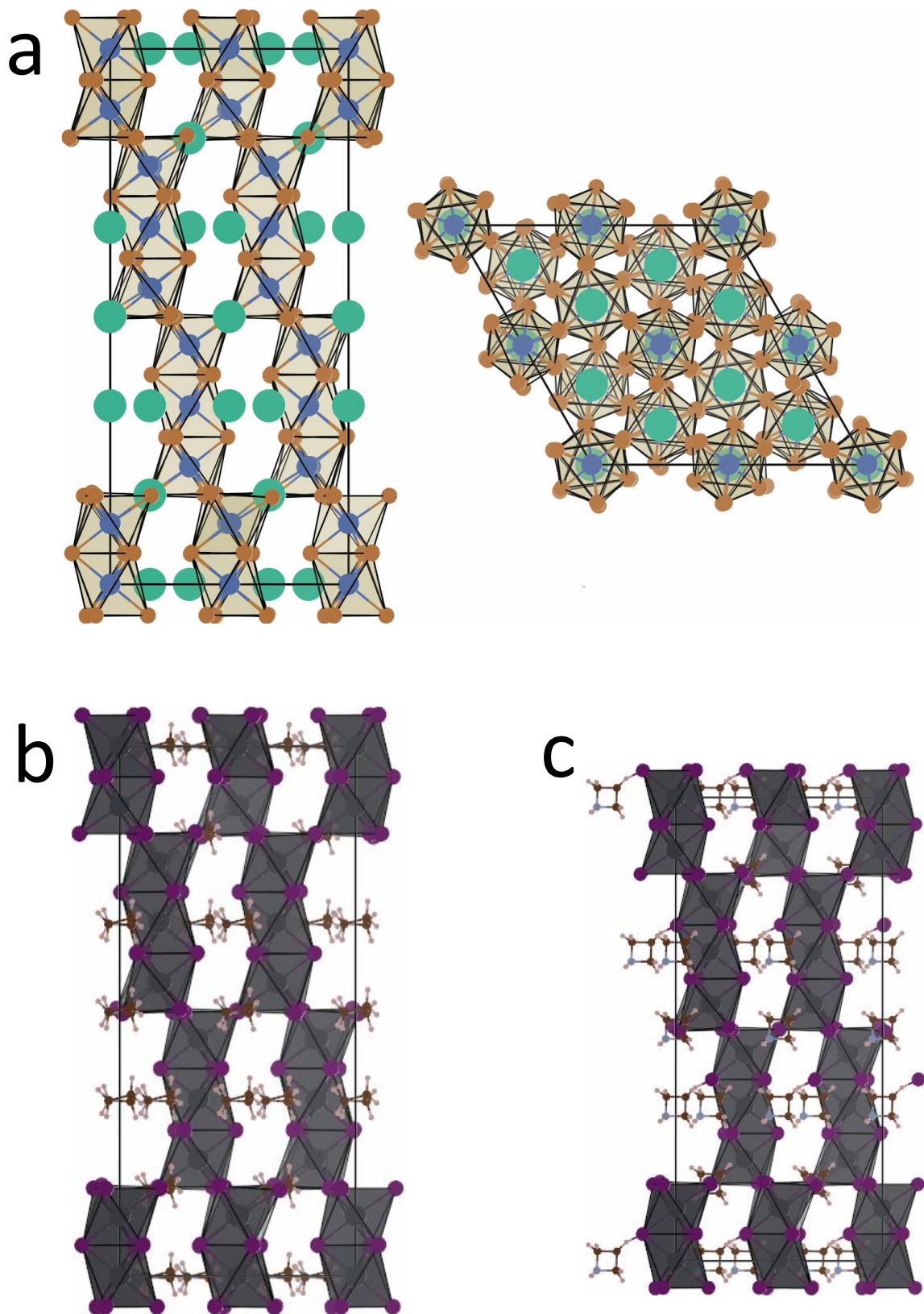
Figure 5.3.2. *Filling the blanks of the AzPI structure: (a) Simulation using caesium as a substitute for azetidinium; (b) AzPI structure with the azetidinium ions perpendicular to the z-axis, and (c) azetidinium ions in the ZX or ZY planes (assumed degenerate for this simulation)*

The structure shown in Figure 5.3.2.b was used to simulate a PXRD pattern, to compare with the experimental PXRD, displayed in Figure 5.3.3. The two show very similar peaks – there are no low-angle peaks (less than 10 °), which would be indicative of a more traditional 2D perovskite. This is a very rough approximation of the AzPI structure, as the single crystal XRD could not be completely fitted. However there appears to be agreement with the PXRD pattern and the computational/single crystal results, which means that AzPI could be a previously unseen perovskite structure. A later study obtained a more complete dataset, with similar groups of 3 Pb-I octahedra but a slightly different overall structure.[30]
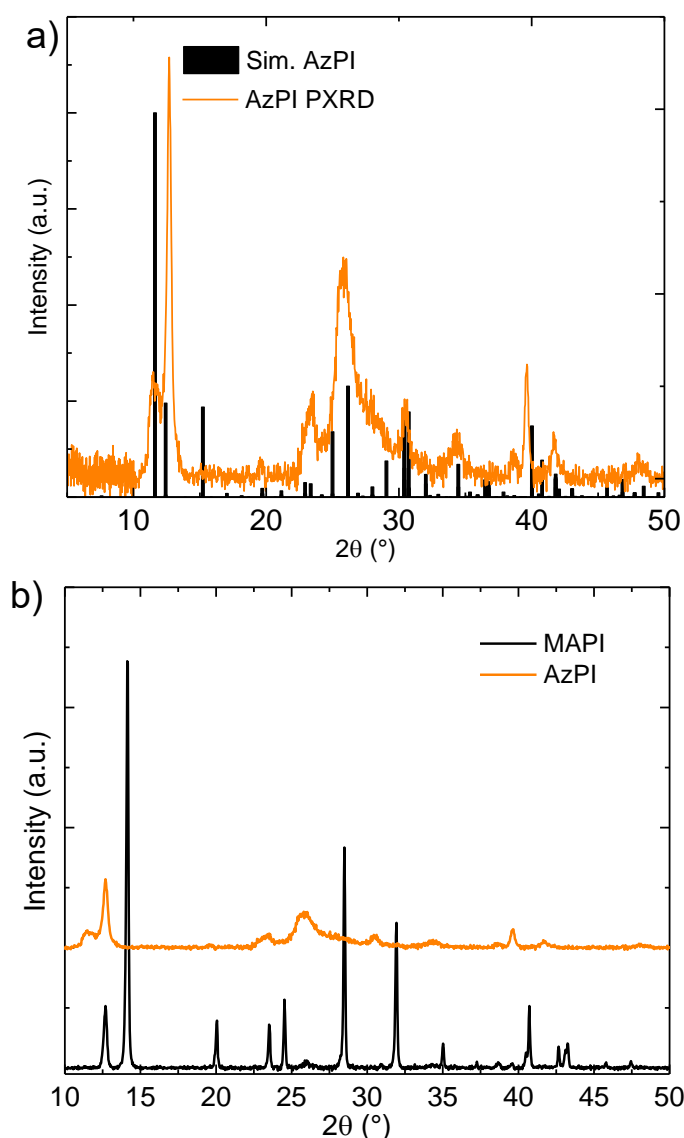
Figure 5.3.3. a) A comparison of the obtained Thin Film XRD of AzPI and the pattern generated by the proposed crystal structure and b) Thin-Film X-ray diffractogram for AzPI and MAPI

A comparison of the X-ray diffraction analysis of AzPI to MAPI in Fig. 5.3.3b shows that AzPI has an altogether more amorphous structure than that of MAPI, as is evident by the reduced peak intensity (and broadening) of the AzPI diffraction pattern in Figure 5.3.7. Aside from the lead iodide peak at 12 °, other major peaks in the AzPI structure are predicted from analysing the unit cell to be: (2,0,-1) at 11.5 °, (4,0,4) at 24.9 ° and the (4,0,-5) at 26.2 °. There is a reduction in the number of peaks visible in the pattern, also suggesting a less crystalline structure. The cause of the differences is likely to be chemical differences between methylammonium and azetidinium, a reduction in the bonding strength with azetidinium that breaks down the 3-dimensional structure.

Azetidinium lead iodide (AzPI) films are a bright, glassy orange film, shown below (Figure 5.3.4). The colour suggests that it will not be at the optimum band gap for peak solar cell performance, however if it does exhibit a photoresponse and generate any power it could be used as a colourful alternative or be used in patterned solar cells.

Figure 5.3.4. An Azetidinium Lead Iodide (AzPI) film

SEM analysis of the film in Figure 5.3.5a shows that the film consists of a large number of densely packed small crystals, around 100 nm in size. It is encouraging that there are very few pinholes in the film and it appears to have a very low surface roughness, which was determined by Atomic Force Microscopy to be around 100 nm (Fig. 5.3.5b) – this should enable a better contact between the perovskite film and other contact layers to ensure efficient charge transport. A high surface coverage will improve the shunt resistance of the solar cell, as pinholes in the material allow for unwanted recombination pathways.
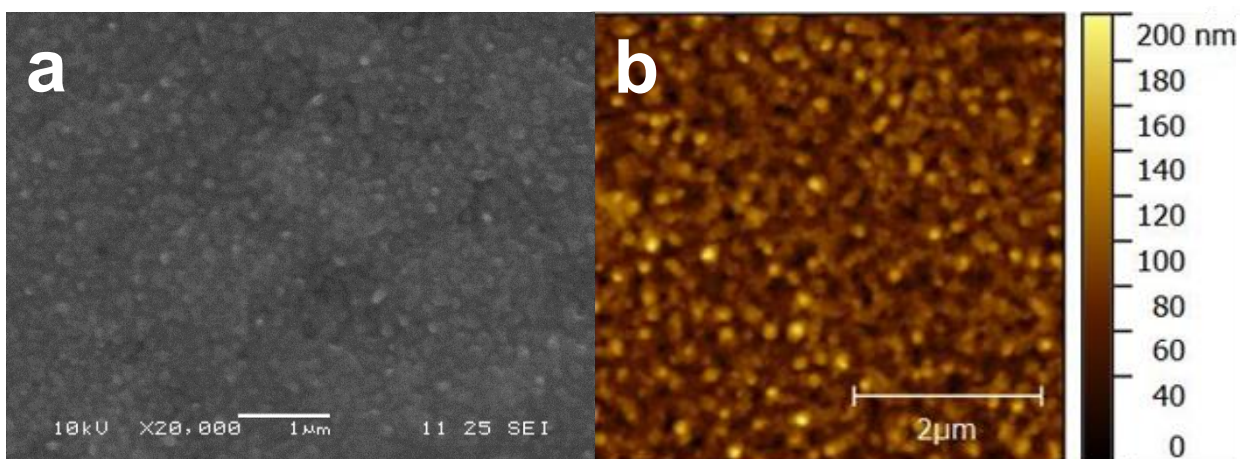
Figure 5.3.5. Imaging analysis of an AzPI film, (a) SEM, and (b) AFM

Before proceeding further it was necessary to determine if AzPI was photoactive. A simple electrochemical cell was set up with an AzPI film in a three-electrode setup with a platinum counter electrode and Ag/AgCl reference electrode, using IPA with AzI as the electrolyte. CV scans were made in the absence and presence of a pulsed light stimulus, the results of which are shown in Figure 5.3.6 below.
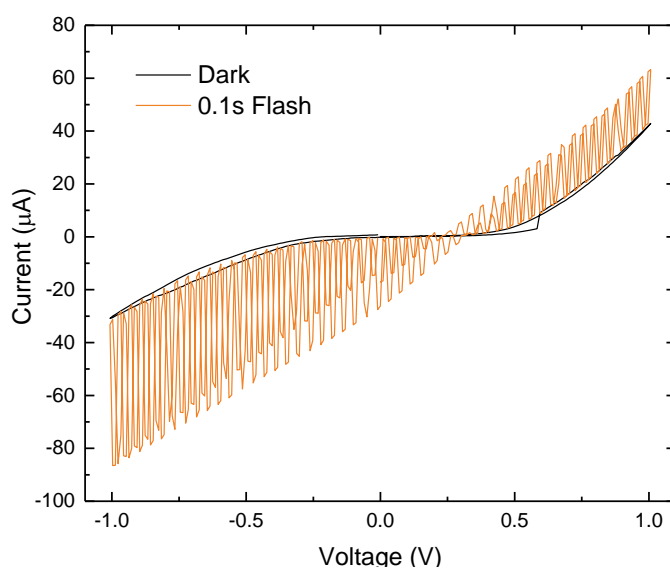
Figure 5.3.6. Photoresponse measurement of azetidinium lead iodide

There is a clear photocurrent generated during the light flash, up to over 80 μA in the reverse sweep. As a response is seen at both positive and negative potentials it is likely that AzPI is ambipolar, as indeed are most hybrid organic-inorganic perovskites.[23]

As expected for an orange film compared to the black MAPI film there is less absorbance over the visible region (Figure 5.3.7). The optical band gap of AzPI taken

from this graph is 2.15 eV, compared to 1.5 eV for MAPI – which is similar to literature values.[24] Mixed organic cation solar cells have been shown to have improved solar cell parameters, and inclusion of a cation that produces a larger band gap material on its own often leads to an increase in the open-circuit voltage of a MAPI cell in the new material.[12,25] The improved absorbance in the UV region may make AzPI an attractive material for multijunction solar cells.
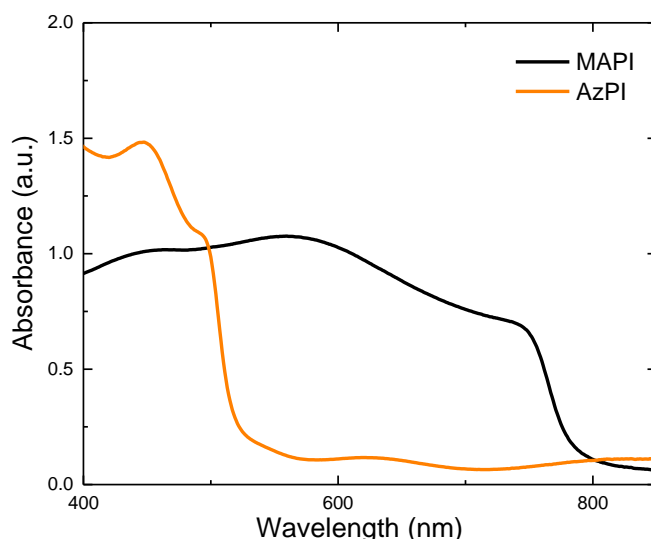
Figure 5.3.7. *UV/Vis spectroscopy of azetidinium lead iodide, with methylammonium lead iodide in comparison*

Raman spectroscopy was used to evaluate the bonding of the azetidinium cation to the $[PbI_3]_n$ cage in AzPI, and therefore hopefully elucidate the structural role of Az^+. AzPI was compared to AzI and Az^+ in Figure 5.3.8 (A full listing of measured modes is in Table 5.3.2).[27] A red-shift was observed in almost all AzPI modes compared to those taken from AzI. The magnitude of this shift is caused partly by chemical Stark shift, and it also depends on the interaction between the Az^+ cation and the $[PbI_3]_n$ cage, which is increased due to the spatial constraint on the system relative to the individual components. In most cases the magnitude of this shift is between 5 to 10 cm^{-1}. Stronger shifts can be seen for the ring deformation (v_3) and the NH$_2$ wagging (v_{13}) modes. Firstly, the v_3 mode shows a red-shift of 15 cm^{-1} for the AzPI structure, potentially caused by steric hindrance of the cation inside the inorganic cage. The largest shift of 61 cm^{-1} is for the v_{13} NH$_2$ wagging mode. The decrease in frequency suggests a weakening of the N-H bond strength in Az^+. Aside from the increased interaction with the inorganic components caused by the higher dipole moment (Table 5.3.1) and favourable out-of-ring position of hydrogen atoms for bonding with the inorganic

scaffold, Az$^+$ also possesses fewer internal degrees of freedom due to the ring shape that will block some molecular movement. This could force AzPI into a lower-dimensional (not 3D) structure. The generally stronger shifting of modes associated to the 2C-position and the ambivalent behaviour of 1C-positioned modes suggests that the Az$^+$ could have a bridging function in the orange phase.
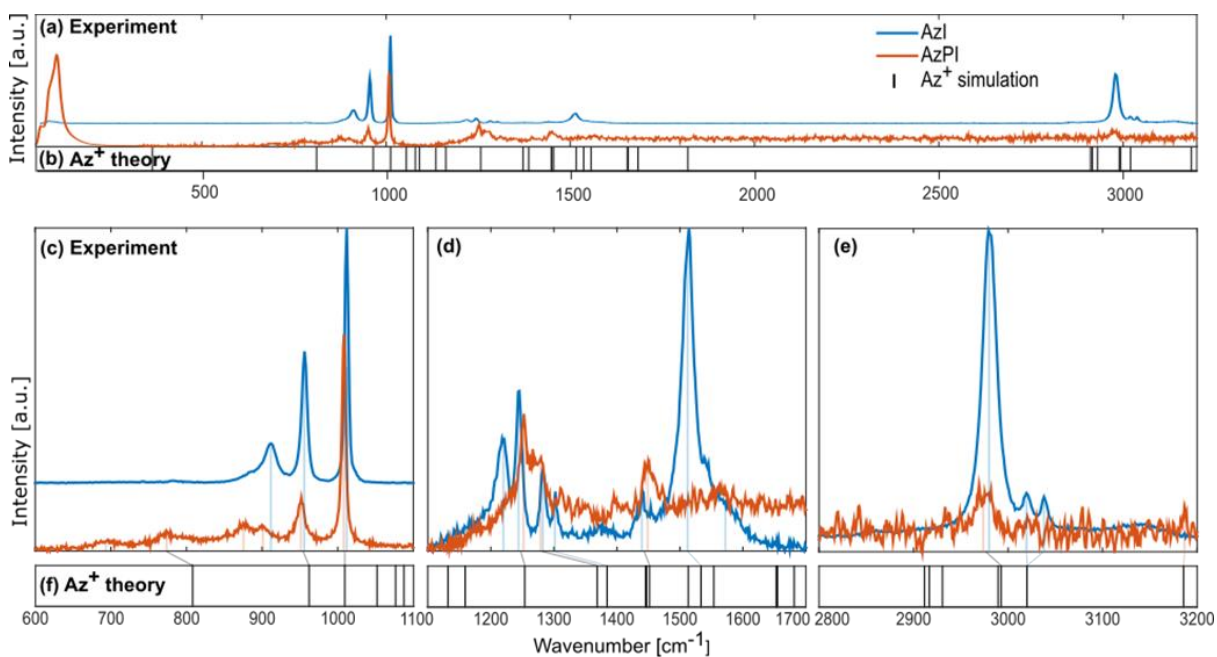
Figure 5.3.8. *(a-b) Full spectra of AzI and AzPI including comparison to Az$^+$ modes (c-e) zoomed region with shifts of assigned peaks against Az$^+$*

Table 5.3.2. *Comparison of all measured Raman modes of AzPbI₃, AzI and Az with provisional peak assignment*

Az$^+$ (DFT)	AzI	rel. shift	AzPI		Assignment
361				ν_1	Ring pucker
			693	ν_2	N-H bend (in plane)
808	785	↓ 15	770	ν_3	Ring deform
	883	↓ 8	875	ν_4	2-CH$_2$ twist
	911	↓ 12	899	ν_5	2-CH$_2$ rock
961	956	↓ 5	951	ν_6	1-CH$_2$ rock
1009	1012	↓ 4	1008	ν_7	2-CH$_2$ rock
	1217			ν_8	1-CH$_2$ wag
1254	1245	↑ 7	1252	ν_9	1-CH$_2$ twist
1313	1283	↓ 6	1277	ν_{10}	2-CH$_2$ twist
1385	1302			ν_{11}	1-CH$_2$ twist
1452	1455			ν_{12}	1-CH$_2$ wag
1534	1511	↓ 61	1450	ν_{13}	NH$_2$ wag
1655	1582			ν_{14}	2-CH$_2$ scissor
2982	2980	↓ 8	2972	ν_{15}	1-C-H stretch
3020	3019			ν_{16}	2-C-H-stretch

Reduced dimensionality perovskites are known to be more stable to ambient conditions than 3D perovskites.[31-33] As was discovered through attempts to synthesise the perovskite, azetidinium iodide was not soluble in DMF and sparingly soluble in other traditional solvents for perovskite fabrication. The insolubility of the AzI precursor suggested that AzPI film's resistance to water exposure may be higher than other perovskites. Figure 5.3.9 shows the process of dipping both a MAPI and AzPI film into water. On the surface it appears that the film remains orange throughout the

process. MAPI however changes colour with immediate contact to water as the methylammonium dissolves. The black to yellow colour change renders the film, and therefore any solar cell exposed to water useless. If left for long enough the PbI_2 film breaks off into solution. In contrast the AzPI film remains bright orange
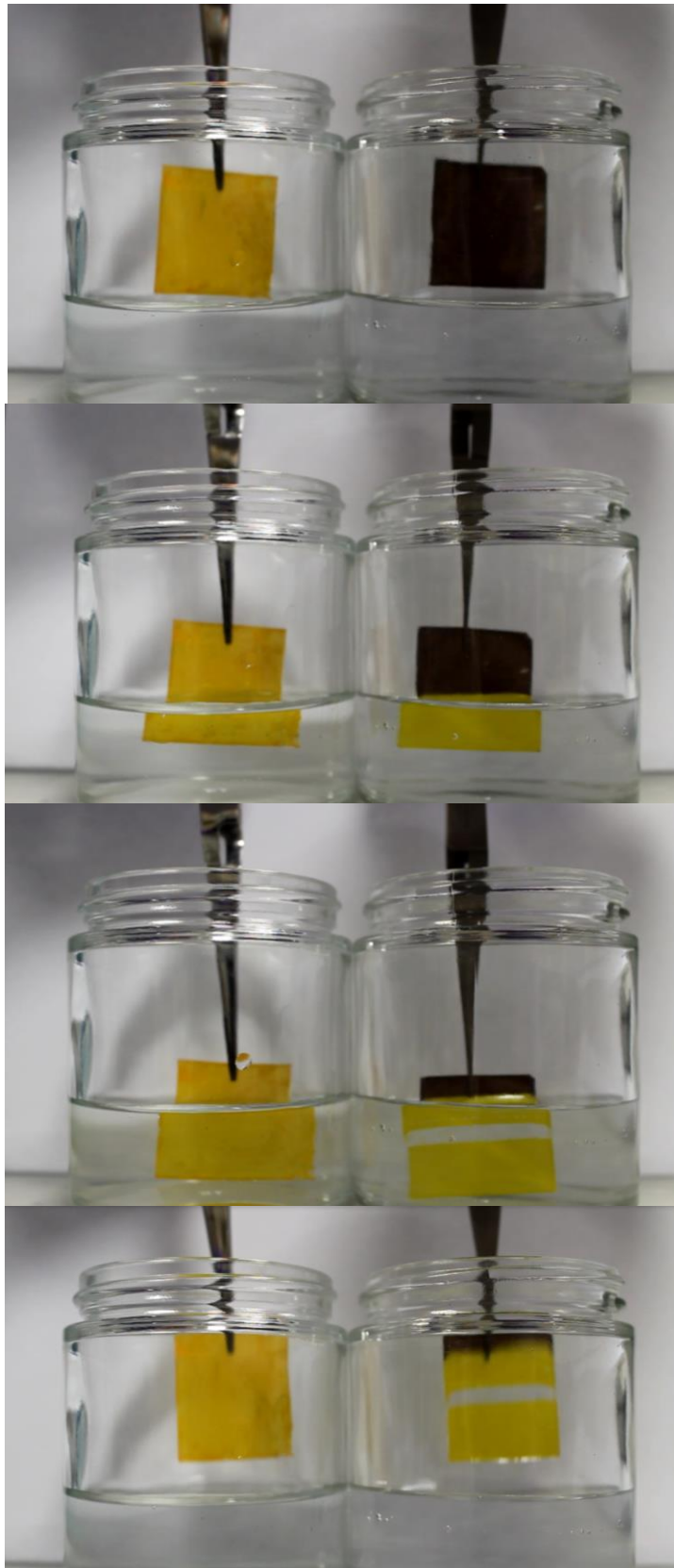
Figure 5.3.9. *Water stability test of AzPI (left) with a MAPI film (right) for comparison*

XRD data obtained (in Figure 5.3.10) from the dipped AzPI film shows that despite being submerged in a large amount of water there are still some identifiable peaks in the diffractogram. The primary AzPI peaks at 11.5 °, 24.9 ° and 26.2 ° are still present after submersion in water. There is also no increase in the PbI_2 peak intensity at 12 ° for AzPI, however for MAPI there is a sevenfold increase in the size of the PbI_2 peak. Along with the almost complete loss of the cubic perovskite peak at 14 °, this suggests decomposition of the MAPI film. AzPI is clearly more resistant to water (and therefore ambient humidity) than MAPI, but not completely water stable over longer times.
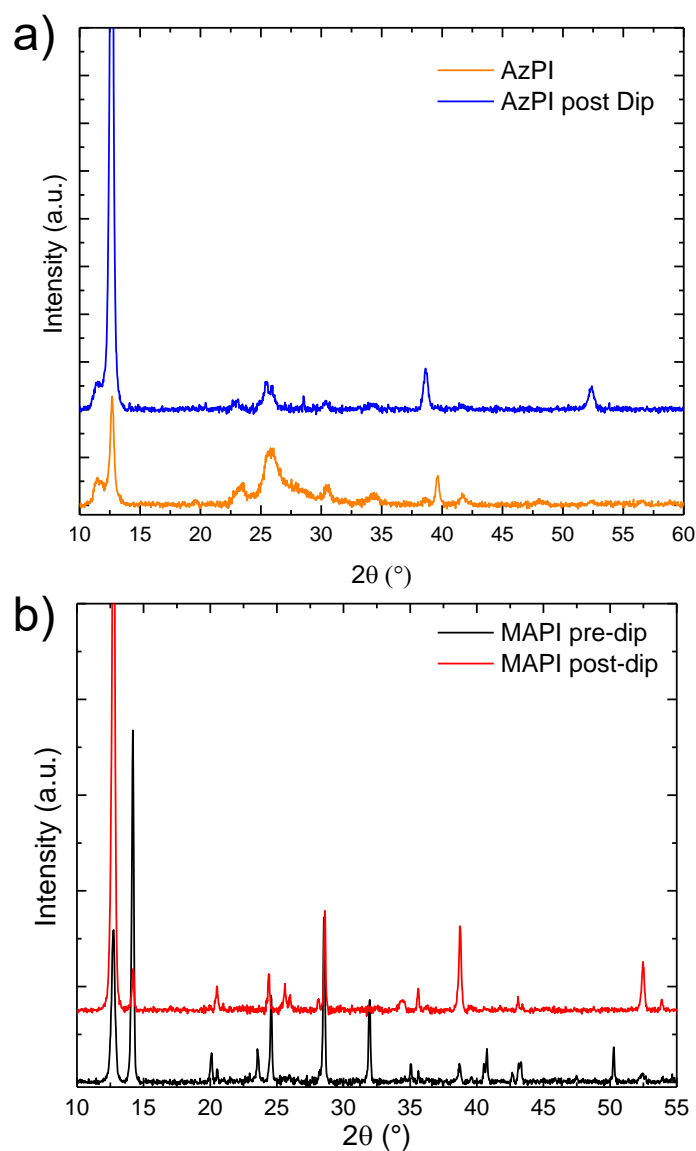
Figure 5.3.10. X-ray diffractogram of (a) AzPI, pre (orange) and post (blue) submersion in water and (b) MAPI pre-dip (black) and post-dip (red)

Having analysed the inherent properties of AzPI, it was then used as an absorber layer in a mesoporous solar cell, the results of which are shown in Figure 5.3.11. An efficiency of just over 1 % is recorded, which means that a successful photovoltaic device has been fabricated. The efficiency is lower than for 3D perovskites such as MAPI and FAPI, but it is a good start, and as it has a wider band gap the efficiency would be expected to be lower.
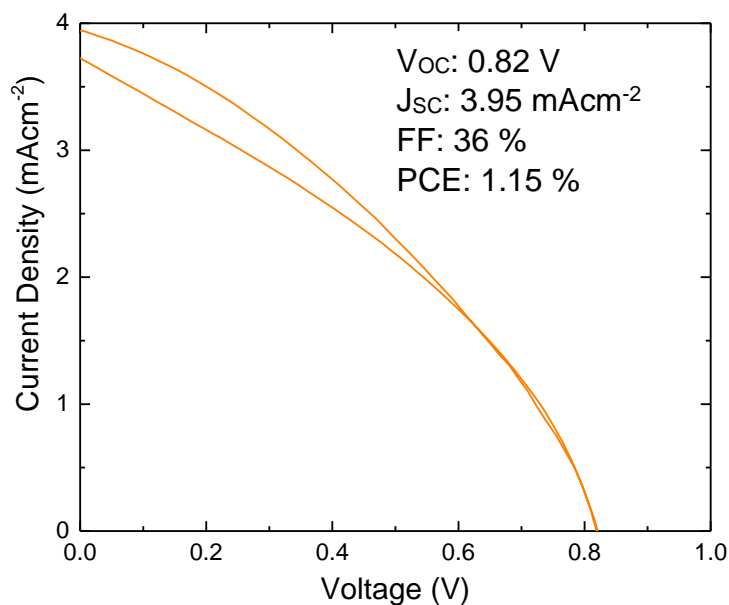
Figure 5.3.11. JV curve for an azetidinium lead iodide solar cell, with inset cell parameters

The origin of reduced performance compared to MAPI can be largely explained by the significant band gap of AzPI. This is demonstrated further in the External Quantum Efficiency (EQE), shown in Fig. 5.3.12 below. The onset of absorption is around 600 nm, similar to the results found via UV/Vis spectroscopy. With a peak in EQE of 33 % this means that a large proportion of energy of absorbed light is lost, perhaps due to high levels of recombination in the disordered structure. Although it contributes to a reduced efficiency, it could make AzPI an attractive material for use in tandem or multijunction cells.
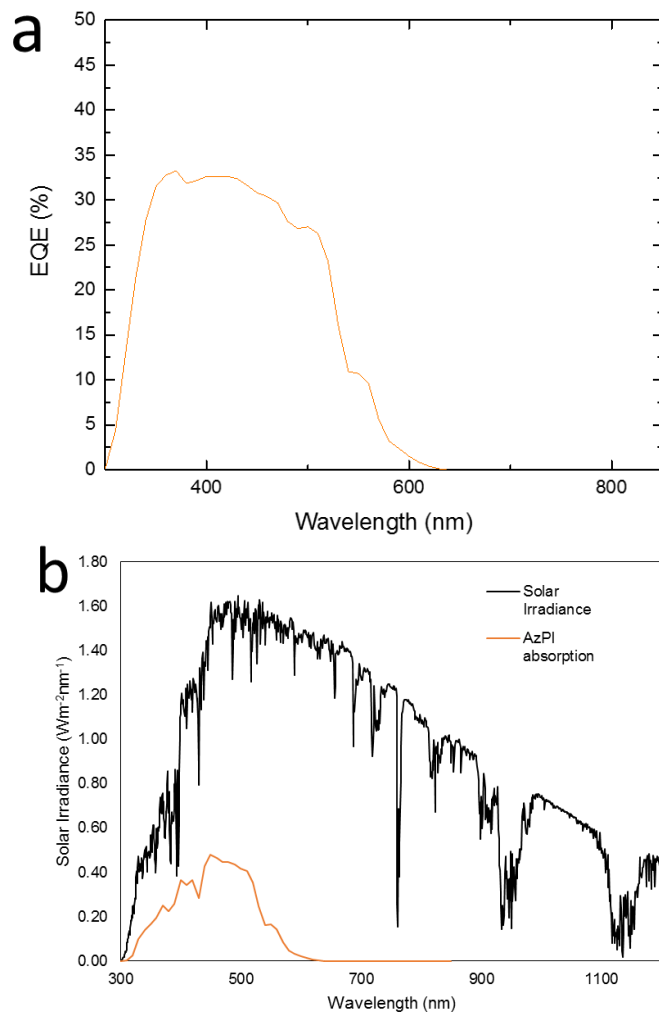
Figure 5.3.12. *(a) External Quantum Efficiency measurement for an Azetidinium Lead Iodide solar cell; (b) EQE relative to solar irradiance*

Methylammonium lead iodide has been reported to be able to undergo cation exchange with formamidinium, by adding a methylammonium or formamidinium iodide solution to either a FAPI or MAPI perovskite.[28] To see if this was the case for azetidinium and methylammonium, four films of AzPI were produced, which then had varying degrees of cation exchange performed on them: spin-coating MAI, subsequent spin-coating with AzI and then a second MAI spin-coating step (Fig. 5.3.13.a). Once methylammonium iodide has been spin-coated on to an AzPI film, there is a strong change of colour to a dark brown (with a hint of orange) – but not the pure black of MAPI, suggesting that not all the azetidinium cations have been removed. With the next AzI wash the film turns to an orange-brown, and the final MAI wash forms a lighter brown film. Thin film X-ray diffraction measurements were taken to attempt to

identify what is happening between depositions. The results of this are shown below in Figure 5.3.13b and c.
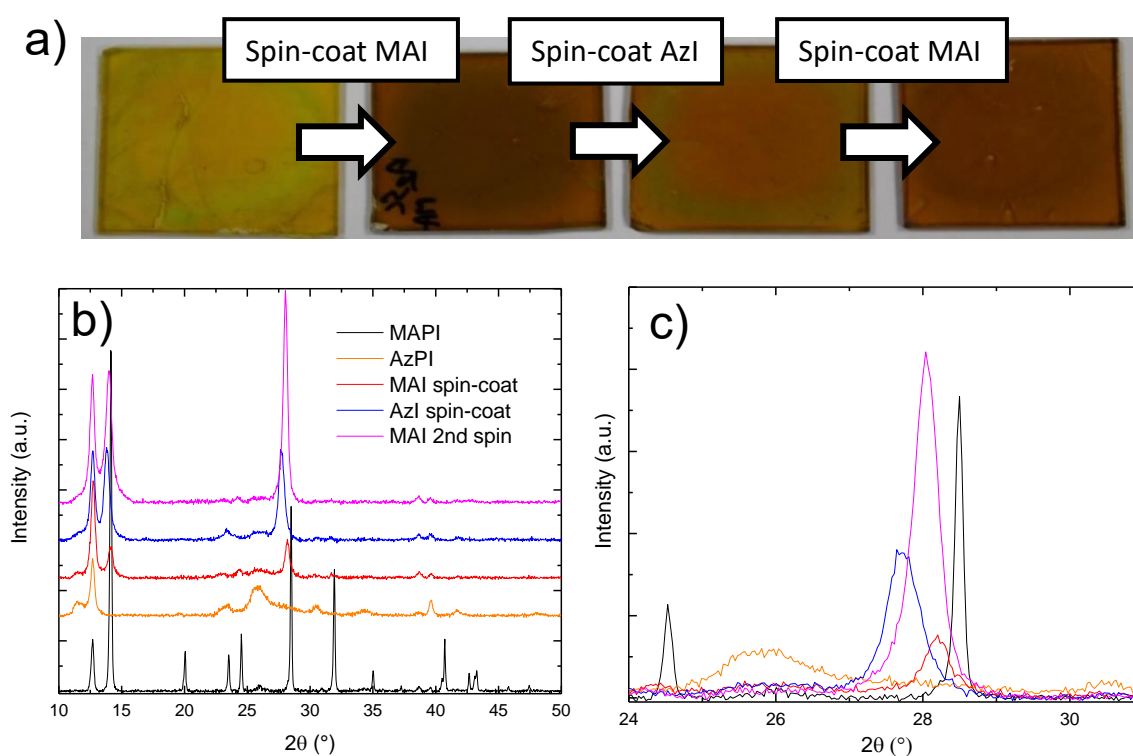
Figure 5.3.13. *An investigation of the exchange of methylammonium and azetidinium cations in the AzPI perovskite: a) photograph of four separate films, and the schematic of the process that has produced each one (starting from AzPI on the left); b) thin film X-ray diffractogram of the films, with c) zoomed in image of one portion of the diffractogram showing the switching of the (2,2,0) peak – both diffractograms have a MAPI comparison*

One of the first visible trends is the increase in intensity of the PbI_2 peak with increasing number of washes. Increasing impurity could be an undesirable side-effect of the spin-coating method, as the cations are somewhat soluble in isopropanol and may be removed during the process. After one methylammonium iodide spin, the AzPI peak at 26.2 ° all but disappears, and is replaced by a characteristic MAPI peak at 28 °, albeit much less intense than in a pure MAPI film. It is also shifted to slightly lower angles than in the pure MAPI peak. The larger radius of the azetidinium cation will increase the unit cell parameters and hence lower the 2θ value at which the diffraction occurs. Another interpretation could be a significant shift to higher angles of the AzPI peak, as it is not clear whether the whole crystal structure has changed, if there is a hybrid structure formed, or if there is phase segregation. The appearance of the cubic perovskite peak at 14.6 ° would suggest the first of these. Interestingly, when azetidinium iodide is then spin-coated onto the film, this peak becomes higher in

intensity (as is also the case for the second MAI spin). Aside from a shift to lower 2θ values of the MAPI peaks at 14.6 ° and 28 °, there is also the reappearance of AzPI peaks at 24 ° and 26 °, which subsequently disappear when the film is washed with MAI solution. The compatibility of these two cations to form a co-film (as shown by the absence of peak splitting in the above XRD measurements) using separate steps is encouraging for the possibility of depositing both at the same time.

5.4) Azetidinium/methylammonium mixed cation perovskites

Methylammonium has previously been used in combination with a large number of different A-site additives – these reports have shown that varying the cationic composition can improve solar cell performance.[12,25,29] As some compatibility between the two cations has been identified, the next step was to attempt to co-deposit azetidinium with methylammonium to see if it was feasible, and whether the inclusion of azetidine would improve the performance of a MAPI cell. To do this, solutions of increasing mol% azetidinium iodide (with respect to methylammonium iodide) were made to use as part of a two-step perovskite synthesis. The two-step method has been used as the required amounts of azetidinium iodide for one-step deposition are not soluble in the solvents used, DMF or DMSO. A photograph showing the difference in appearance of the resulting films is shown in Figure 5.4.1.

Figure 5.4.1. Photograph of films produced from solutions of varying azetidinium iodide mole percentage, from left to right **how they will be referenced from this point on is shown in bold**: *(top row)* **MAPI** *(A0, 0 mol% AzI), 1 mol% AzI* (**A1**)*, 2 mol % AzI* (**A2**)*, 5 mol% AzI* (**A5**)*; (bottom row) 10 mol% AzI* (**A10**)*, 25 mol% AzI* (**A25**) *and* **AzPI** *(A100, 100 mol% AzI)*

There is little effect on the visual appearance of the films at very low concentrations of azetidinium iodide – colour change starts to happen at 10 mol% AzI, from dark brown to a lighter brown at 25 mol%, before the orange colour of the AzPI film. The change in appearance is reflected in the UV/Vis spectroscopy (Figure 5.4.2). Interestingly the inclusion of azetidinium into the spin-coating solution with methylammonium does not appear to change the absorbance onset, which remains consistently around 800 nm. However for the film made using the 5 mol% solution, there is a reduction in absorbance between 750 – 600 nm. The reduction becomes more prominent throughout the rest of the samples, becoming shoulder-like in the 25 mol% sample, with an absorbance shoulder at 650 nm.
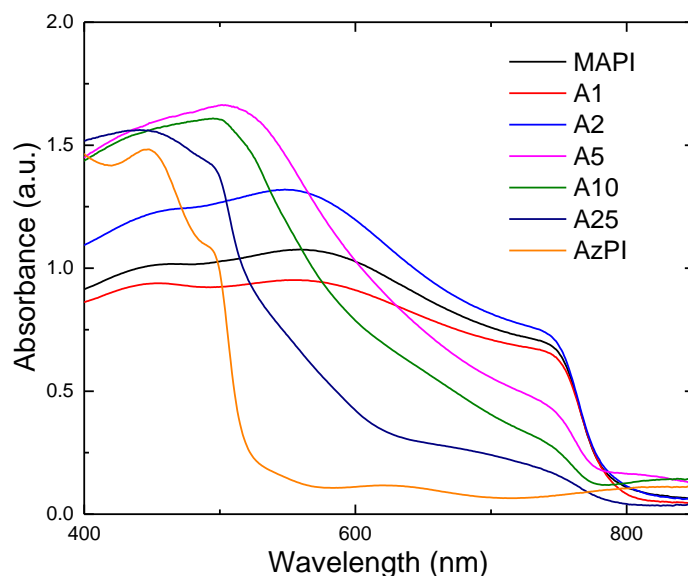
Figure 5.4.2. *UV/Vis spectroscopy of thin films of methylammonium/azetidinium mixed-cation perovskites*

Thin-film X-ray diffraction was performed on these films to examine whether the trend in structure, if there was one, matched that of the UV/Vis spectroscopy data. For samples with low proportions of azetidinium there is no drastic change in the diffractogram obtained, the absence of shoulders to any peaks suggests a continuous phase of $Az_xMA_{1-x}PbI_3$. The inclusion of the larger radius cation azetidinium also shifts the peaks slightly to lower 2θ values, as there is an increase in the size of the unit cell. This is shown in the inset image of Figure 5.4.3, which shows the change in reflection angle for the (2,2,0) peak at 28.5 °. For AzI ratios of 5-10 mol%, the broadened perovskite reflections indicate splitting into two domains. Peak splitting suggests phase separation into MAPI and AzPI regions, which could be the source of the trends in the UV/Vis spectra – the appearance of shoulders at higher AzI ratios rather than a larger shift in the band gap of a single-phase material. Upon further increasing the AzI proportion in the spin-coating solution to 25 mol%, the intensities of the 3D perovskite phase reflections decrease, while the $AzPbI_3$ reflections become more intense.
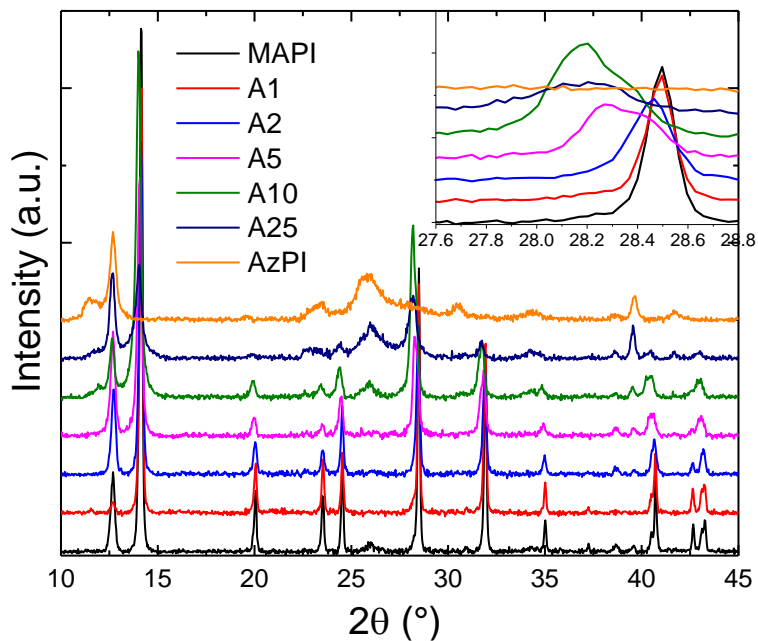
Figure 5.4.3. *XRD analysis of using azetidinium to alter the MAPI structure, with (inset) tracking the movement of the MAPI (2,2,0) peak at 28.5 °*

To make high efficiency solar cells a mesoporous TiO$_2$ layer was used, which meant the deposition method was changed to dip coating to ensure complete penetration of the mesoporous layer – a picture of the cells is shown in Figure 5.4.4.
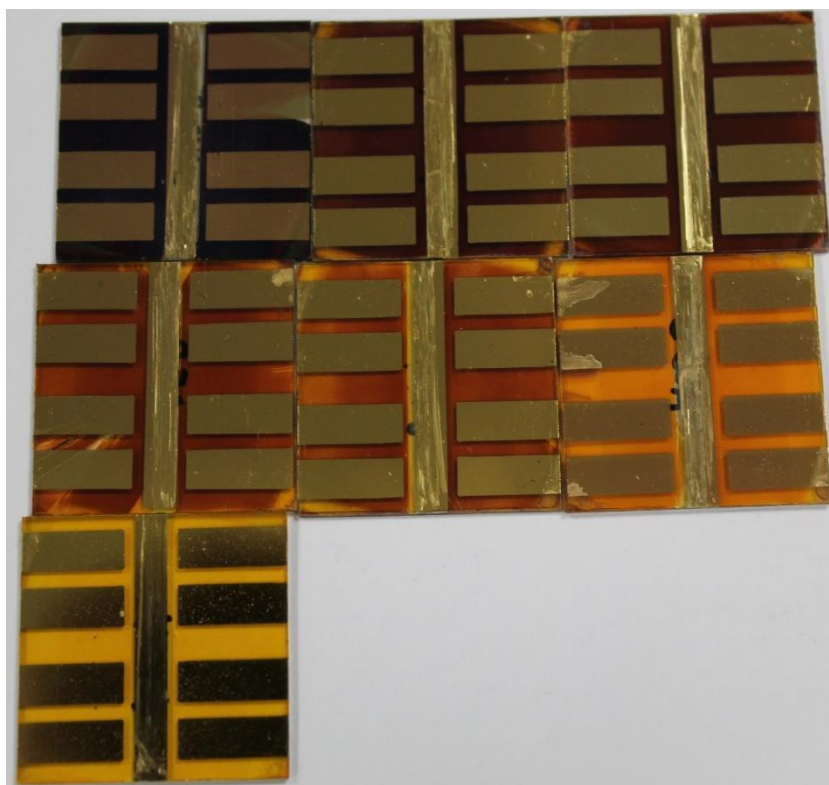
Figure 5.4.4. *Photograph of AzMAPI mixed-cation solar cells*

Figure 5.4.5 contains box plots for all the cell parameters. From these graphs there are two distinct regions, from 5 mol% azetidinium and greater, then MAPI, A1 and A2. The sharp drop in performance (most evident in Figures 5.4.5b and d) for cells containing greater than 5 mol% AzI in the dipping solution correlates with data from UV/Vis spectroscopy and X-ray diffractometry. Phase separation would disturb the continuous perovskite phase and inhibit charge transfer through the lattice, resulting in a greatly reduced current output (Fig.5.4.5b), whilst keeping a relatively high voltage due to the band gaps of the materials involved. There is a reduction in the average V_{OC} and J_{SC} upon the addition of any amount of azetidine, however the large drop in J_{SC} at higher percentages is what contributes to the reduction of efficiency.

It is therefore interesting that despite the J_{SC} and V_{OC} being reduced, the overall efficiency of the solar cells increases slightly with the incorporation of 1 or 2 mol% AzI into the dipping solution. This is likely due to the increase in Fill Factor. Further refinement of band-gap alignment and perovskite layer thickness could improve the efficiency of these AzMAPI cells even more.
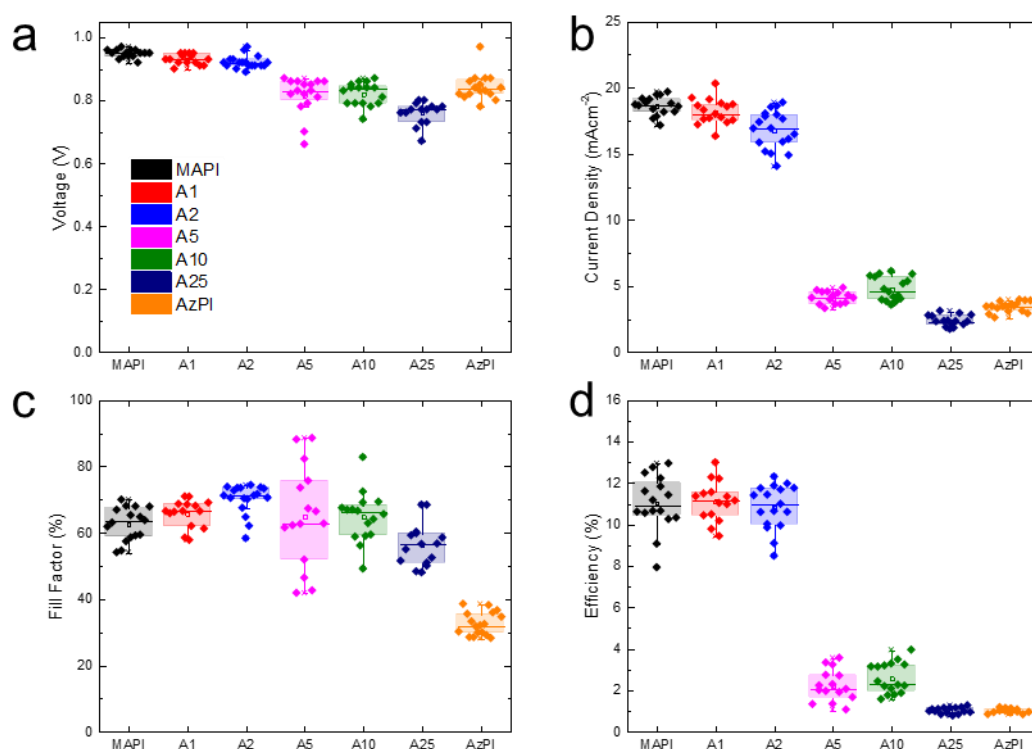
Figure 5.4.5. *Box plots for the solar cell parameters for the reverse sweep (V_{OC} - J_{SC}) of MAPI, AzPI and AzMAPI cells of varying Az concentration: (a) Open-circuit voltage; (b) Short-circuit current density; (c) Fill Factor and (d) Efficiency*

EQE measurements on the best pixels for the above provides further evidence for the phase separation observations, and are shown in Figure 5.4.6. Between MAPI, A1 and A2 there is little difference, the apparent improved EQE of the A1 sample is likely due to cell-to-cell variations. At AzI concentrations of 5 mol% or greater, two distinct regions in the spectrum are visible. There is also a massive drop in the overall EQE of these cells – around half that of the higher efficiency MAPI, A1 and A2 cells. This is significant considering that there was not a vast colour change from 2 to 5 mol% AzI, again suggesting that phase separation is occurring at proportions of Az^+ of greater than 2 mol%.
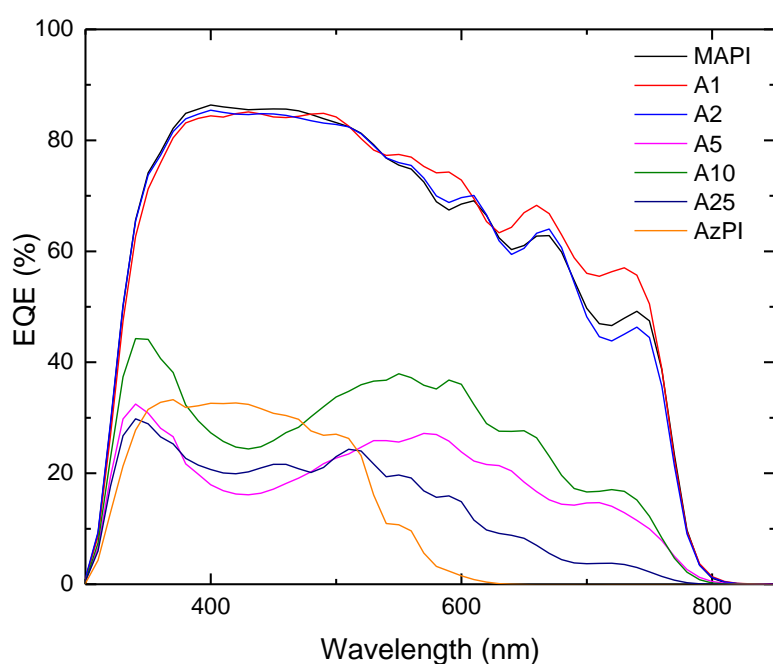
Figure 5.4.6. EQE measurements for the best pixels of MAPI, AzPI and AzMAPI cells

The highest efficiency pixel produced was in the A1 set (1 mol% AzI in the dipping solution). Remarkably, this cell was 13.00 % in the reverse sweep (from open-circuit to short-circuit), and 12.98 % in the forward sweep (from short-circuit to open-circuit). A complete lack of hysteresis is visible in the JV curve of the pixel, compared with the best performing MAPI pixel and AzPI pixel in Fig. 5.4.7.

128
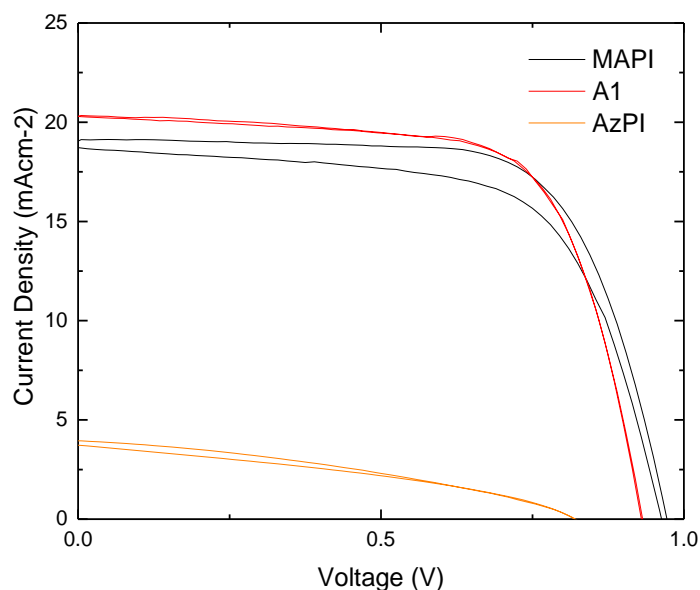
Figure 5.4.7. J-V curves for the best performing MAPI, A1 and AzPI pixels

Table 5.4.1 Photovoltaic parameters for MAPI and 1 mol% Azetidinium solar cells (average over 15 pixels)

	V_{OC} (mV)	J_{SC} (mAcm^{-2})	FF (%)	Champion Cell (%)	Efficiency (%)
MAPI	948 ± 13	18.6 ± 0.70	62 ± 5.1	12.9	11.0 ± 1.35
$Az_{0.01}MA_{0.99}PI$	925 ± 16	18.1 ± 0.95	65 ± 4.0	13.0	11.1 ± 0.95

Suppression of hysteresis is a very attractive property, as this means that the efficiency obtained is more reliable – and there was an overall reduction of hysteresis in all measurements on the addition of small concentrations of azetidinium to the perovskite. A possible explanation of hysteresis suppression is that azetidinium, acts as a block to ion diffusion, a process that has been linked to hysteresis.[70] This could also prevent the diffusion of I$^-$ out of the structure, improving long-term stability of the cell.

Lastly, stabilised power output measurements were performed on the best pixels, and Fig. 5.4.8 shows the results of the pixels being held at the maximum power point over 2.5 minutes. For the A1 sample the stabilised efficiency was 12.85 %, extremely close to the value calculated from the JV curve. The pixel with 2 mol% AzI, despite having a lower overall efficiency showed a slightly enhanced stability on the timescale of the experiment – suggesting that further experiment into concentrations of azetidinium cations in the perovskite between 0 and 2 mol% could produce a cell with a higher efficiency and greater stability.
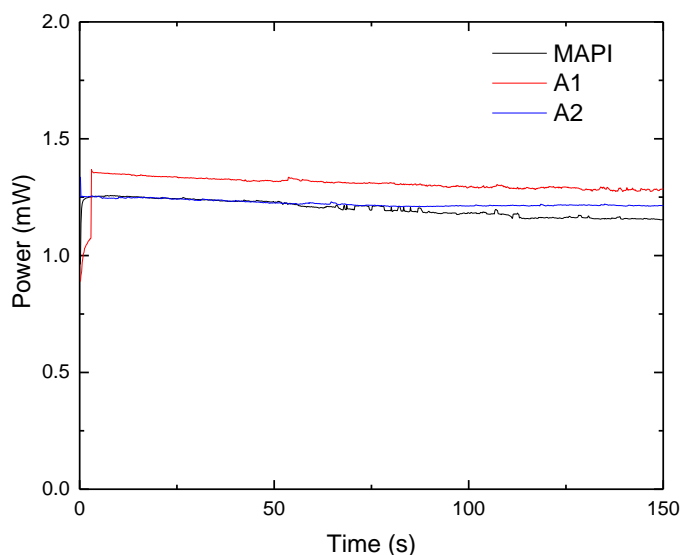
Figure 5.4.8. *Stabilised power output measurements for the best performing pixels, held at V_{mp} (Voltage at max power) – determined by the JV curves.*

With regards to the long-term stability of Azetidinium Lead Iodide, the AzPI cell was re-measured after being left in ambient conditions for over two years. A random pixel was chosen to be measured, and a comparison of that to the champion pixel from the initial measurements is shown in Figure 5.4.9.
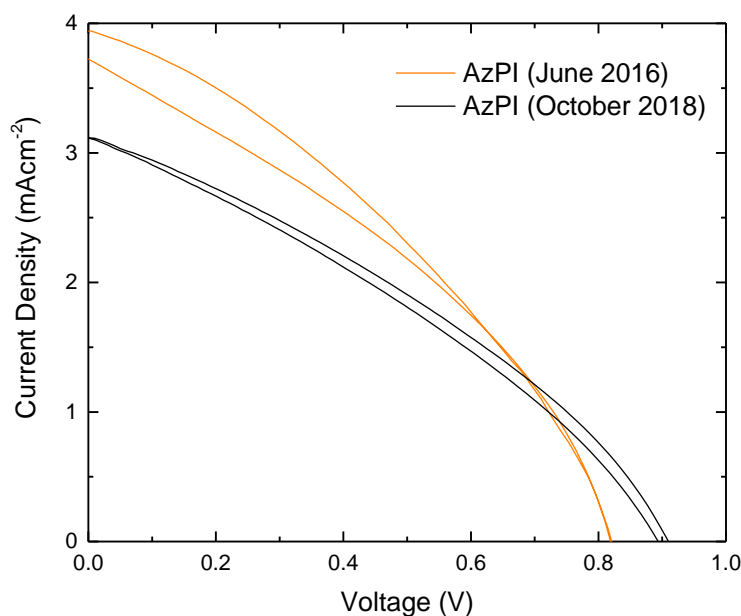
Figure 5.4.9. *JV curves for AzPI cells measured after 2 years stored in ambient conditions*

The pixel measured in October 2018 recorded an efficiency of 0.96 %, which means it has remained relatively unchanged. Unfortunately it is not a true measurement of the stability, as this requires regular measurement of the cell to test if activity also causes

130

a decay in performance. However this is still an impressive result and would be interesting for further testing.

5.6) Conclusions

In this chapter the azetidinium cation has been introduced as a new option for the A-site in perovskite solar cells. Films of AzPI were produced to determine their suitability for photovoltaic purposes. The bright orange films exhibited a photocurrent at both positive and negative voltages, suggesting that like other perovskites used for solar cells, it is ambipolar. AzPI has a wide band gap of 2.15 eV, opening the potential for its use in multi-junction devices. The crystal structure of the material was suggested to be neither 2D nor 3D, although it was impossible to determine an exact picture. Tolerance factor calculations therefore cannot predict the whole picture, as tolerance factor calculations suggest that azetidinium lead iodide is within the range for a 3D perovskite to form. Chemical differences of the cations, such as the dipole or N-H acidity should also be considered.

This chapter includes the first reported example of a 2.5-dimensional perovskite solar cell, which had an efficiency of 1.15 %. Its absorption in the UV, and low overall absorption could make it an attractive material for use in tandem solar cells, as it would not prevent too much light from reaching the bottom cell (typically silicon). AzPI also maintained a similar efficiency after two and a half years stored in ambient conditions.

Mixed-cation perovskites were synthesised to attempt to increase the efficiency and stability of MAPI cells, in a similar vein to experiments conducted using formamidinium or caesium. Phase separation appears to affect the perovskite at concentrations of over 5 mol% azetidine in the dipping solution, evident in UV/Vis measurements as shoulders in the spectrum, XRD as peak broadening and splitting, and in the EQE measurements as a splitting of the absorption regions. Phase separation inhibits the charge transfer, and results in poorly performing solar cells. Low percentages of azetidinium (≤ 2 mol%) appear to form a single-phase AzMAPI perovskite that improves the efficiency of the cell, with a champion device fabricated reaching 13.00 %, that had negligible hysteresis and high stability. This was theorised to be a result of the large Az^+ cations blocking ion movement.

5.7) References

1   A. Kojima, K. Teshima, Y. Shirai and T. Miyasaka, *J. Am. Chem. Soc.*, 2009, **131**, 6050–6051.

2   G. Kieslich, S. Sun and T. Cheetham, *Chem. Sci.*, 2014, **5**, 4712–4715.

3   H. Tsai, W. Nie, J.-C. Blancon, C. C. Stoumpos, R. Asadpour, B. Harutyunyan, A. J. Neukirch, R. Verduzco, J. J. Crochet, S. Tretiak, L. Pedesseau, J. Even, M. A. Alam, G. Gupta, J. Lou, P. M. Ajayan, M. J. Bedzyk, M. G. Kanatzidis and A. D. Mohite, *Nature*, 2016.

4   J. H. Noh, S. H. Im, J. H. Heo, T. N. Mandal and S. Il Seok, *Nano Lett.*, 2013, **13**, 1764–1769.

5   D. Cui, Z. Yang, D. Yang, X. Ren, Y. Liu, Q. Wei, H. Fan, J. Zeng and S. (Frank) Liu, *J. Phys. Chem. C*, 2015, acs.jpcc.5b09393.

6   M. Wei, Y.-H. Chung, Y. Xiao and Z. Chen, *Org. Electron.*, 2015, **26**, 260–264.

7   J.-W. Lee, D.-J. Seol, A.-N. Cho and N.-G. Park, *Adv. Mater.*, 2014, **6**, 1–8.

8   S. Lv, S. Pang, Y. Zhou, N. P. Padture, H. Hu, L. Wang, X. Zhou, H. Zhu, L. Zhang, C. Huang and G. Cui, *Phys. Chem. Chem. Phys.*, 2014, **16**, 19206.

9   G. E. Eperon, G. M. Paterno, R. J. Sutton, A. Zampetti, A. A. Haghighirad, F. Cacialli, H. J. Snaith, G. M. Paterno', R. J. Sutton, A. Zampetti, A. A. Haghighirad, F. Cacialli and H. J. Snaith, *J. Mater. Chem. A*, 2015, **3**, 19688–19695.

10   M. Saliba, T. Matsui, J.-Y. Seo, K. Domanski, J.-P. Correa-Baena, N. Mohammad K., S. M. Zakeeruddin, W. Tress, A. Abate, A. Hagfeldt and M. Grätzel, *Energy Environ. Sci.*, 2016.

11   J. Liu, Y. Shirai, X. Yang, Y. Yue, W. Chen, Y. Wu, A. Islam and L. Han, *Adv. Mater.*, 2015.

12   N. De Marco, H. Zhou, Q. Chen, P. Sun, Z. Liu, L. Meng, E.-P. Yao, Y. Liu, A. Schiffer and Y. Yang, *Nano Lett.*, 2016.

13   M. Zhang, J. S. Yun, Q. Ma, J. Zheng, C. F. J. Lau, X. Deng, J. Kim, D. Kim,

J. Seidel, M. A. Green, S. Huang and A. W. Y. Ho-Baillie, *ACS Energy Lett.*, 2017, **2**, 438–444.

14   A. F. Akbulatov, L. A. Frolova, D. A. Anokhin, K. L. Gerasimov, N. N. Dremova and P. Troshin, *J. Mater. Chem. A*, 2016.

15   J. K. Nam, S. U. Chai, W. Cha, Y. J. Choi, W. Kim, M. S. Jung, J. Kwon, D. Kim and J. H. Park, *Nano Lett.*, 2017.

16   Y. Yang, J. Song, Y. L. Zhao, L. Zhu, X. Q. Gu, Y. Q. Gu, M. Che and Y. H. Qiang, *J. Alloys Compd.*, 2016, **684**, 84–90.

17   G. Kieslich, S. Sun and T. Cheetham, *Chem. Sci.*, 2015, **6**, 3430–3433.

18   W. Travis, E. N. K. Glover, H. Bronstein, D. O. Scanlon and R. Palgrave, *Chem. Sci.*, 2016.

19   M. Valiev, E. J. Bylaska, N. Govind, K. Kowalski, T. P. Straatsma, H. J. J. Van Dam, D. Wang, J. Nieplocha, E. Apra, T. L. Windus and W. A. de Jong, *Comput. Phys. Commun.*, 2010, **181**, 1477–1489.

20   J. M. Frost, K. T. Butler, F. Brivio, C. H. Hendon, M. Van Schilfgaarde and A. Walsh, *Nano Lett.*, 2014, **14**, 2584–2590.

21   F. Zheng, H. Takenaka, F. Wang, N. Z. Koocher and A. M. Rappe, *J. Phys. Chem. Lett.*, 2015, **6**, 31–37.

22   H. Zheng, W. Wang, S. Yang, Y. Liu and J. Sun, *RSC Adv.*, 2016, **6**, 1611–1617.

23   J. M. Ball, M. M. Lee, A. Hey and H. J. Snaith, *Energy Environ. Sci.*, 2013, **6**, 1739–1743.

24   H.-S. Kim, C.-R. Lee, J.-H. Im, K.-B. Lee, T. Moehl, A. Marchioro, S.-J. Moon, R. Humphry-Baker, J.-H. Yum, J. E. Moser, M. Grätzel and N.-G. Park, *Sci. Rep.*, 2012, **2**, 591.

25   C. Yi, J. Luo, S. Meloni, A. Boziki, N. Ashari-Astani, C. Grätzel, S. M. Zakeeruddin, U. Rothlisberger and M. Grätzel, *Energy Environ. Sci.*, 2015.

26   S. Pang, H. Hu, J. Zhang, S. Lv, Y. Yu, F. Wei, T. Qin, H. Xu, Z. Liu and G. Cui, *Chem. Mater.*, 2014, **26**, 1485–1491.

27   R. Dutler, A. Rauk and R. A. Shaw, *J. Phys. Chem.*, 1990, **94**, 118–124.

28   G. E. Eperon, C. E. Beck and H. J. Snaith, *Mater. Horiz.*, 2016, **3**, 63–71.

29   N. J. Jeon, J. H. Noh, W. S. Yang, Y. C. Kim, S. Ryu, J. Seo and S. Il Seok, *Nature*, 2015, **517**, 476–480.

30   R. Panetta, G. Righini, M. Colapietro, L. Barba, D. Tedeschi, A. Polimeni, A. Ciccioli and A. Latini, *J. Mater. Chem. A*, 2018, **6**, 10135–10148.

31   C. C. Stoumpos, D. H. Cao, D. J. Clark, J. Young, J. M. Rondinelli, J. I. Jang, J. T. Hupp and M. G. Kanatzidis, *Chem. Mater.*, 2016, **28**, 2852–2867.

32   M. Chunqing, S. Dong, N. Tsz-Wai, L. Ming-Fai and L. Chun-Sing, *Adv. Mater.*, 2018, **0**, 1800710.

33   C. Ma, C. Leng, Y. Ji, X. Wei, K. Sun, L. Tang, J. Yang, W. Luo, C. Li, Y. Deng, shuanglong feng, J. Shen, S. Lu, C. Du and H. Shi, *Nanoscale*, 2016.

34   G. Richardson, S. O'Kane, R. G. Niemann, T. A. Peltola, J. M. Foster, P. J. Cameron, A. Walker, S. E. J. O'Kane, R. G. Niemann, T. A. Peltola, J. M. Foster, P. J. Cameron and A. B.Walker, *Energy Environ. Sci.*, 2016, **9**, 1476–1485.

6: Standard and Inverted PSC

6.1) Introduction

In the previous chapter the cation Azetidinium was included in the perovskite precursor solution, which at very low percentages served to improve overall cell performance and reduce hysteresis. This is not an uncommon result, as the vast majority of cationic additives improve the performance of the base perovskite.[1–4]

To determine any common effects that are the cause of improved performance with these additives, more specifically with respect to iodide diffusion, a standard cell needs to be used. The activation energy for iodide diffusion can be measured by impedance, which is a measurement that can last several hours.[5] Thus the cell used must have a stable V_{OC} over this timescale, to ensure that observations are not due to any degradation that may occur. Furthermore the studies that have been previously conducted on mixed-cation perovskites do not often share identical cell architectures. As cell architecture is known to affect the degree of hysteresis (which has been linked to ion diffusion), it is important that in this study one architecture is used.[6–9]

The standard planar and mesoporous architectures are the most common used for PSC, which allow for the highest recorded efficiencies with simple deposition methods.[10,11] However the long-term stability of standard architecture compared to the inverted structure (in which the HTM is deposited first) is poor.[8,12–14] The inverted structure can, however, not reach the same efficiencies as the planar/mesoporous.

In this chapter planar TiO_2 based PSC will be briefly compared to inverted NiO_x PSC. Their performance and stability at open-circuit will be assessed to determine their suitability for an EIS based study into mixed-cation perovskites. Other factors such as the cost of fabrication will also be taken into account.

6.2) Specific experimental

6.2.1. Standard architecture cell preparation

The TiO$_2$ precursor solution was formed by diluting 4.9 mL of Titanium diisopropoxide(bisacetylacetonate) (Sigma, 75 wt% in IPA) to 50 mL using ethanol. This solution was sprayed onto the substrates at 500 °C using a hand-held atomiser. The films were annealed for 15 minutes at 500 °C. After cooling the films were UV/O$_3$ cleaned before perovskite deposition.

Methylammonium iodide (Greatcell Solar, purity not stated by manufacturer), lead iodide and lead chloride (Sigma, both 99 %) were dissolved in DMF in a 4:1:1 ratio at 60 °C. 100 µL of this solution was deposited by spin-coating at 3000 rpm for 30s. 500 µL of toluene was used as the antisolvent. Perovskite films were annealed at 100 °C for 30 minutes.

Spiro-OMeTAD was used as the hole transport material. The HTM solution consisted of 96 mgmL^{-1} Spiro-OMeTAD in chlorobenzene (99.8 %, Sigma), with 30 µL Li-TFSI in acetonitrile (170 mgmL^{-1}) and 10 µL *t*-butyl pyridine (99.8 %, Sigma). 100 µL of this solution was deposited by spin-coating at 3000 rpm for 45s. The cells were left overnight in air for the Spiro-OMeTAD layer to oxidise.

A 60 nm gold (Advent) layer was deposited by thermal evaporation.

6.2.2. Inverted architecture cell preparation

For these cells the HTM is deposited first. The HTM solution contained 50 mgmL^{-1} Nickel(II) acetate hexahydrate (Sigma, 99.998 %) in 2-methoxy ethanol (Sigma, 99.8 %). 12 µL ethanolamine (Sigma, 98 %) was added to this solution, and it was filtered before use. Films were deposited at 3000 rpm for 30 seconds and annealed at 500 °C for 30 minutes.

A 1.25:1.25 M solution of MAI and PbI$_2$ was dissolved in a 4:1 mixture of DMF and DMSO at 50 °C – also filtered before use. Perovskite films were formed by spin-coating at 4000 rpm for 30 seconds. Ethyl acetate (Sigma, 99.8 %) was used as the

antisolvent, deposited 6 seconds into the spin-coating process. Films were left to anneal at 100 °C for 15 minutes.

After cooling, a solution of 20 mgmL^{-1} PC$_{71}$BM (Ossila, 95 %) in chlorobenzene was filtered, and deposited onto the perovskite films for 30 seconds at 3000 rpm. A final spin-coating step used a solution of 0.5 mgmL^{-1} bathocuproine (Sigma, 96 %) in ethanol, deposited at 6000 rpm for 30 seconds.

A 60 nm silver (Alfa Aesar) contact was deposited by thermal evaporation.

6.2.3. Extended V$_{OC}$ measurement

Open-circuit measurements were taken over 7 hours on a Solartron Modulab using a 560 nm blue LED as the illumination source. These experiments were performed at room temperature.

6.2.4. Cost analysis

The cost incurred upon making each architecture of cell was analysed by using stock prices for chemicals. This was then used to work out the price of each solution (including solvents) based on how much by mass (or volume) is required for one substrate. For the metal contact, cost was calculated by the required amount of the metal divided by a typical number of substrates coated during one evaporation (8).

6.3) Comparing cells

The first assessment of both architectures is simply based on the solar cell parameters as obtained from J-V analysis. The findings are displayed in Figure 6.3.1 and Table 6.3.1 below. In this work the success rate has been defined to be the percentage of cells in the batch that have an efficiency of greater than 1%.
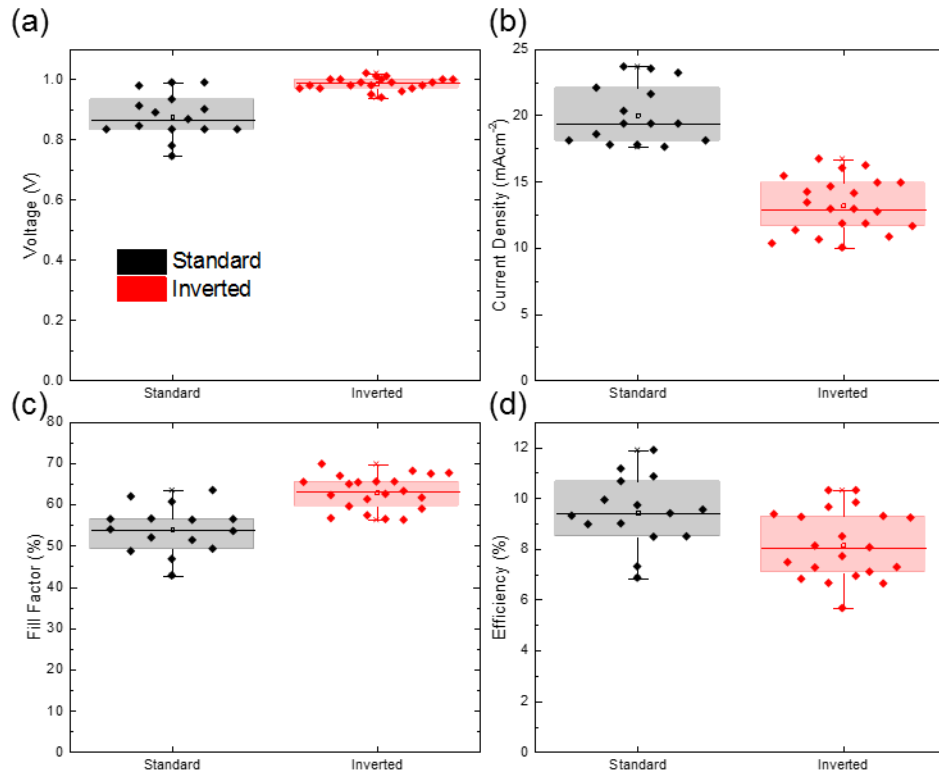
Figure 6.3.1. *Solar Cell Parameters for the standard and inverted cell architectures (a) Open-circuit voltage, (b) Short-circuit current density, (c) Fill Factor and (d) Efficiency*

Table 6.3.1. Solar Cell Parameters for the standard and inverted cell architectures (N=24)

Architecture	Success rate (%)	V_{OC} (V)	J_{SC} (mAcm^{-2})	FF (%)	η (%)
Standard	62.5	0.88 (±0.07)	20.02 (±2.15)	53.95 (±5.55)	9.43 (±1.33)
Inverted	87.5	0.98 (±0.02)	13.19 (±2.02)	62.95 (±4.10)	8.15 (±1.33)

There are some clear differences in the results obtained from the two cell architectures. Although the efficiency of the standard cells is better than that of the inverted cells, largely due to a significantly improved J_{SC}, this does not mean they are a better choice

for further experiments. It is apparent that the V_{OC} for the inverted cells is higher and more consistent than that of the standard cells.

Another useful benefit of the inverted cells is that the success rate of these is 25 % higher than those of the standard cells. This means that in this case 15/24 standard cells worked, whereas 21/24 of the inverted did. Factoring this difference in would greatly reduce the average efficiency of the standard cells.

A further indictment on the performance of the standard cells is that the data obtained from the J-V curve is only taken from the reverse sweep. The J-V curves (showing both forward and reverse sweep) for the best performing pixels in each set (Figure 6.3.2) show a marked reduction in the hysteresis for the inverted NiO_x based cells. The V_{OC} of the standard cells drops by over 0.2 V from the reverse sweep (V_{OC} to J_{SC}) to the forward sweep (*vice versa*), with a similar reduction in the Fill Factor. Hysteresis introduces a large amount of uncertainty into the actual efficiency of the cell. On the reverse sweep the displayed curve has an efficiency of 11.9 %, whereas it is only 7.3 % on the forward sweep. Although there is some hysteresis in the inverted cell, the difference in efficiencies between each sweep is only 0.5 %, compared to 4.6 % in the standard cells.
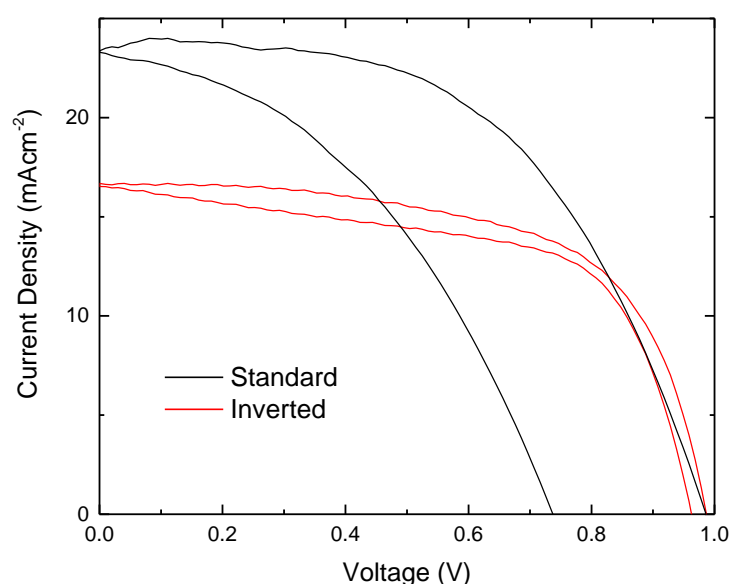

Figure 6.3.2. JV curves from the best performing pixel in each set

A low degree of hysteresis is also advantageous for the proposed impedance experiments as hysteresis has been linked to iodide diffusion throughout the lattice.[7] A large degree of hysteresis suggests that the cell (particularly the V_{OC} in this instance)

is more affected by the voltage sweep, which may have negative implications for AC based measurements – as ideally the cell should exhibit a linear response when subjected to a sinusoidal perturbation.

The last experiment undertaken on these cells was a basic measure of their stability. A random cell from each was left at open-circuit to analyse the time taken for the voltage to stabilise and how long it was stable thereafter. The results are shown in Figure 6.3.3.
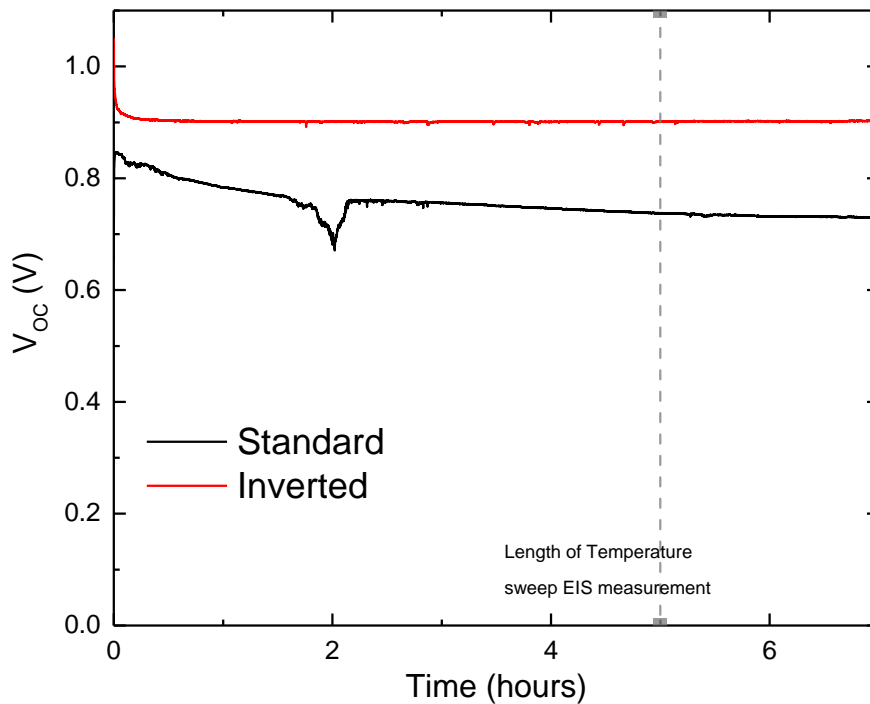
Figure 6.3.3. *7 hour V_{OC} measurement for each cell taken at room temperature, pressure and humidity*

The clearest observation from the extended measurement is that the V_{OC} stability of the inverted cell seems to be better than that of the standard architecture cell in this case. The inverted cell reached a stable voltage within 10 minutes and maintained over 0.9 V with no degradation over 7 hours. It took that long for the TiO_2 based standard cell to obtain a stable voltage, it had been degrading slowly until that point. It is not certain what is causing the anomaly in the TiO_2 result at 2 hours.

There is a mark on the above graph showing the potential length of time taken for temperature-dependent impedance. Over this timescale the NiO_x is definitely a better choice, as it requires much less stabilisation time before making the measurement than the TiO_2 cells – based on these results it would take around 60 hours to perform the same test. In that amount of time the cell would likely have degraded. Another benefit of the inverted cells is the higher stabilised voltage.

6.4) Other factors

There are several further advantages to using the inverted cell architecture. One of these is the ease of fabrication. Using spin-coating for all the steps removes the human element from synthesis, as spray pyrolysis can result in large variations in blocking layer quality from person-to-person. Also without the need to allow the Spiro-OMeTAD layer to oxidise overnight (unless more expensive additives were used), it means that NiO_x PSC can be made and measured within the same day. This prevents any degradation that may occur from prolonged exposure to the lab environment.

Another important factor to consider is the cost of manufacture. Although this project is not focussing on commercialisation and therefore does not have to consider profit margins, it is still useful to cut costs on the small scale. Table 6.4.1. breaks down the cost of making each cell (excluding FTO glass). The overwhelming source of the saving in the inverted cells is the ability to use silver as the metal contact as opposed to gold. A saving of around 95 % is achieved in this switch. Although PCBM (NiO_x blocking layer 2) may be more expensive per gram than Spiro-OMeTAD (planar blocking layer 2), the concentration in solution is lower so that the overall cost of this layer is also reduced.

When all the layers are considered the total price of the TiO_2 based cell is £4.04. A cell made in the inverted architecture is almost a third of the cost to produce, at £1.57. Assuming a batch size of 8 the price difference becomes even more attractive, especially when the prices are combined with the success rate of each architecture. The standard architecture cells are over 2.5 × more expensive to make and much less likely to work.

Table 6.4.1. *A comparison of the costs involved of producing the planar and inverted PSC (solvent included). All prices come from Sigma Aldrich, except MAI (GreatCell Solar), PCBM (NiO Blocking Layer 2, Ossila) and Gold/Silver (Alfa Aesar)*

Component	Cost per 1 substrate (£)	
	Planar	NiO_x Inverted
Blocking layer 1	0.19	0.32
Perovskite	0.10	0.10
Blocking layer 2	1.88	1.02
Layer 3	0	0.03
Metal deposition	1.87	0.10
Total per substrate	**4.04**	**1.57**
Total per 8 cell batch (Assuming 1mL of each solvent made (not incl. Titania))	**40.40**	**15.83**

6.5) Conclusions

Two different cell architectures have been compared in order to determine their suitability for a wide-scale project looking at cation mixing and iodide diffusion barriers. The first was the standard planar architecture, using TiO_2, Spiro-OMeTAD and Gold. The second cell architecture was the planar inverted, using NiO_x, PCBM and Silver.

This short comparison prioritised cell performance and stability. Although the standard cells had a greater average efficiency, the hysteresis in their measurements was significant and thus the result is not as reliable. The planar inverted cells showed a higher overall V_{OC} with less spread, which was also quicker to stabilise and more stable over the 10 hour measurement that was made. These are valuable traits for a study based on impedance, which requires the cell to spend long amounts of time at open-circuit. Also the reduced deviation in V_{OC} will allow for more accurate comparison between cells.

Less scientific factors were also considered, *i.e.* the ease and price of cell manufacture. The inverted cells were found to be much better value for money. Not only were the precursor materials cheaper, mainly thanks to the use of silver as the metal contact instead of gold, the cells could be made in a shorter amount of time. A further bonus was the fact that there was a greatly enhanced probability that the cell would be usable (*i.e.* have an efficiency > 1 %).

Based on these findings the inverted cell structure is used throughout the rest of this thesis.

6.6) References

1   N. De Marco, H. Zhou, Q. Chen, P. Sun, Z. Liu, L. Meng, E.-P. Yao, Y. Liu, A. Schiffer and Y. Yang, *Nano Lett.*, 2016, **16**, 1009–1016.

2   A. F. Akbulatov, L. A. Frolova, D. A. Anokhin, K. L. Gerasimov, N. N. Dremova and P. Troshin, *J. Mater. Chem. A*, 2016, **4**, 18378–18382.

3   R. G. Niemann, L. Gouda, J. Hu, S. Tirosh, R. Gottesman, P. J. Cameron and A. Zaban, *J. Mater. Chem. A*, 2016, **4**, 17819–17827.

4   C. Yi, J. Luo, S. Meloni, A. Boziki, N. Ashari-Astani, C. Gratzel, S. M. Zakeeruddin, U. Rothlisberger and M. Gratzel, *Energy Environ. Sci.*, 2016, **9**, 656–662.

5   A. Pockett, G. E. Eperon, N. Sakai, H. J. Snaith, L. M. Peter and P. J. Cameron, *Phys. Chem. Chem. Phys.*, 2017, **19**, 5959–5970.

6   D. Kubicki, D. Prochowicz, A. Hofstetter, M. Saski, P. Yadav, D. Bi, N. Pellet, J. Lewinski, S. M. Zakeeruddin, M. Grätzel and L. Emsley, *J. Am. Chem. Soc.*, 2018.

7   G. Richardson, S. O'Kane, R. G. Niemann, T. A. Peltola, J. M. Foster, P. J. Cameron, A. Walker, S. E. J. O'Kane, R. G. Niemann, T. A. Peltola, J. M. Foster, P. J. Cameron and A. B.Walker, *Energy Environ. Sci.*, 2016, **9**, 1476–1485.

8   J. H. Heo, H. J. Han, D. Kim, T. K. Ahn and S. H. Im, *Energy Environ. Sci.*, 2015, **8**, 1602–1608.

9   Y. Shao, Z. Xiao, C. Bi, Y. Yuan and J. Huang, *Nat. Commun.*, 2014, **5**, 5784.

10   M. M. Lee, J. Teuscher, T. Miyasaka, T. N. Murakami and H. J. Snaith, *Science*, 2012, **338**, 643–7.

11   M. Saliba, T. Matsui, J.-Y. Seo, K. Domanski, J.-P. Correa-Baena, N. Mohammad K., S. M. Zakeeruddin, W. Tress, A. Abate, A. Hagfeldt and M. Grätzel, *Energy Environ. Sci.*, 2016, **9**, 1989–1997.

12   G. Niu, X. Guo and L. Wang, *J. Mater. Chem. A*, 2015, **3**, 8970–8980.

13   K. A. Bush, C. D. Bailie, Y. Chen, A. R. Bowring, W. Wang, W. Ma, T. Leijtens, F. Moghadam and M. D. McGehee, *Adv. Mater.*, 2016, **28**, 3937–3943.

14   Z. Zhu, Y. Bai, X. Liu, C.-C. Chueh, S. Yang and A. K.-Y. Jen, *Adv. Mater.*, 2016, **28**, 6478–6484.

7: The Effect of Partial A-site Substitution on Ionic Diffusion in Perovskite Solar Cells

7.1) Introduction

The nature of the ABX_3 perovskite structure enables a large amount of variation in the components used. The current highest efficiency perovskite solar cells use a mixture of caesium, formamidinium (FA) and methylammonium (MA) 'A' site cations, with a binary halide system of iodide and bromide in the 'X' position.[1] Mixed cation/anion systems allow for the tuning of properties such as colour and band gap, as well as improving the stability of the perovskite.[2–4] Replacement of the Pb cation is less common, even though as a toxic metal its use is undesirable; Sn has been used to replace Pb both on its own and in mixed metal perovskite solar cells, although toxicity tests have shown tin-based perovskites to be more damaging *in vivo*.[5–7] Substitution of iodide anions for chloride or bromide anions enables a large range of colours to be formed, however in both cases the best performing cells only included low percentages of substitution.[2,8]

Mixing the organic cation can also lead to changes in the material properties.[9] Formamidinium lead iodide (FAPI) cells are less stable than the MA analogue and require higher temperatures to anneal.[10,11] Mixing FA with MA can overcome the need for higher annealing temperatures; the inclusion of bromide produces PSC with over 18 % efficiency.[12,13] Triple cation PSC are made by the addition of CsI to this perovskite mixture, this combination has the current highest recorded efficiencies of over 22 %.[1] Caesium can also be used as the A-site cation on its own, or in the aforementioned binary systems with FA or MA.[14,15] However there is a limit to the amount of Cs that can be incorporated into a perovskite, whereas with FA and MA there is no phase separation at any ratio of the two cations.[9,15] In order to broaden the possible combinations of cations to optimise efficiency and stability, other cations are required. Cations such as hydrazinium (HA), azetidinium (Az) and guanidinium (GA) have been identified by computational studies.[16] These studies have used the ionic radius of the cations to determine whether they are suitable, identifying whether they have an appropriate tolerance factor to form a 3D perovskite; this approach can be improved by adapting the model to include the effect the inorganic cage will have on

the organic cation.[17] Hydrazinium has a smaller ionic radius than methylammonium, and has been found to improve both the short-circuit current and stability of a binary MA:HA cell.[18] Azetidinium has an ionic radius that tolerance factor calculations would predict a 3D perovskite to be formed, but in the previous chapter it was found that experimentally this is not the case. When used in mixed-cation perovskites however it can serve to improve the fill factor. The largest of these cations, guanidinium, also improves cell performance and stability when used as an additive, in this case by increasing the open-circuit voltage.[19]

To further understand the effect of these additives on perovskite solar cells, and perhaps discover new criteria for suitable cations, we assessed eight different cationic additives of various sizes and dipole moments to use as additives in MAPI based perovskite cells.

7.2) Specific Experimental

7.2.1) Perovskite precursors

Reagents were purchased from the following major chemical manufacturers and used without further purification: PbI$_2$ (99 %) and *N*,*N*-Dimethylformamide (DMF) (99.8 %) were purchased from Sigma Aldrich and methyl ammonium iodide (MAI) was purchased from DyeSol/Greatcell (purity not stated by manufacturer). Dimethyl Sulfoxide (DMSO) was purchased from VWR. AzI was synthesised based on a previously reported procedure.[20] Ammonium Iodide (99.9 %) and Rubidium Iodide (99.9 %) were purchased from Sigma. Caesium Iodide (99.9%) was obtained from Alfa Aesar. Formamidinium Iodide, Guanidinium Iodide, Dimethylammonium Iodide and Acetamidinium Iodide were purchased from DyeSol/Greatcell (purity not stated by manufacturer).

7.2.2) Perovskite solutions

For methylammonium lead iodide (MAPI), a 1.25:1.25 mol solution was formed by dissolving 576 mg PbI$_2$ and 199 mg MAI in an 8:2 mixture of DMF:DMSO. For the substituted perovskite solutions, 5 mol% of the MAI was replaced by the appropriate additive. Cells were fabricated by the method introduced in section 6.2.2.
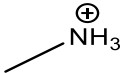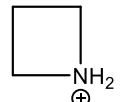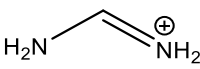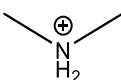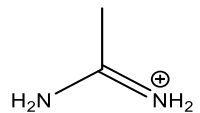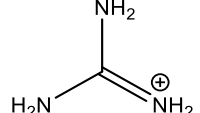
7.2.3) Computational methods (performed by Dibya Ghosh)

The perovskite structures and energies were calculated using density functional theory (DFT) methods (employing the *ab initio* code CP2K).[21] A 3×2×2 supercell (576 atoms) of the tetragonal unit cell was modelled. We employed the mixed Gaussian and plane-wave method, GGA of the PBEsol form, analytical dual-space pseudopotentials and Grimme-type dispersion corrections. Activation energies for diffusion processes were computed from the total energy difference between the diffusing species in their ground-state configuration and at the saddle point of the diffusion process. Ion transport mediated by ion vacancies was examined using nudged elastic band (NEB) and constrained energy minimisation methods.

7.3) Different size cations on thin film properties

The seven different cations chosen (and methylammonium) are shown in Table 7.3.1, with a focus on getting a wide range of different properties. As discussed above tolerance factor calculations are the most widely used way of identifying potential ions for the creation of perovskites, and are dependent on the ionic radius of the particular ion. For this reason the cations have been sorted by increasing size. Cations were also chosen to have varying chemical properties, such as whether they are primary or secondary amines, how many amine groups they have, and what the overall dipole of the molecule is.

Table 7.3.1. The cations used in this study, including assigned abbreviation, chemical structure, ionic radius and dipole moment

Cation	Abbreviation	Structure	Radius (pm) [17,22,23]	Dipole Moment (D)
Ammonium	Am	$NH_4^{\oplus}$	146	0
Rubidium	Rb	$Rb^{\oplus}$	152	0
Caesium	Cs	$Cs^{\oplus}$	167	0
Methylammonium	**MA**	$NH_3^{\oplus}$	**217**	**2.176**
Azetidinium	Az	$NH_2^{\oplus}$	250	2.519 [Chapter 5 and [20]]
Formamidinium	FA	H_2N—$NH_2^{\oplus}$	253	0.21 [24]
Dimethylammonium	DM	$N H_2^{\oplus}$	272	1.28 [25]
Acetamidinium	Ac	H_2N—$NH_2^{\oplus}$	277	1.20 [26]
Guanidinium	GA	H_2N—$NH_2^{\oplus}$, NH_2	278	0

Other than MA, the only other cation in the set capable of forming a 3D perovskite is FA – FA is also unique as no matter the FA:MA ratio a solid solution is formed.[9] Phase separation is, however, a problem with all the other cations in the set, therefore to maintain a 3-Dimensional perovskite structure a fixed amount of 5 mol% for each additive was used; a significant enough amount to hopefully solicit a change in the properties of the overall perovskite, yet not enough to change the 3D structure.

Figure 7.3.1. is a photograph of all the films, which shows no significant colour change, only a difference in the darkness/transparency of the film. Any cloudiness in the film is related to the timing of the antisolvent deposition.
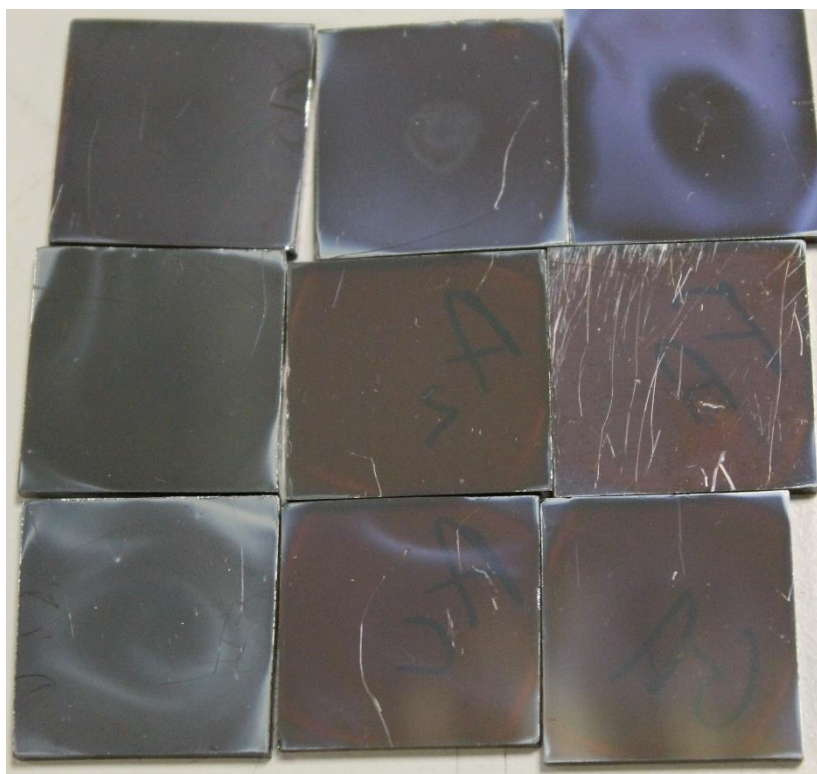

Figure 7.3.1. *A photograph of the perovskite films, from left to right (top row) 5 mol% Am, 5 mol% Rb, 5 mol% Cs (middle row) 100% MA, 5 mol% Az, 5 mol% FA, (bottom row) 5 mol% DM, 5 mol% Ac, 5 mol% GA*

The similarity between the samples is also evident in the UV/Vis spectra of each film (Figure 7.3.2). The two most transparent looking films, with 5 mol% DM and Ac show the lowest overall absorbance of all the films. All other films show an increase in the overall absorbance relative to MAPI, most notably for the Rb and Am samples. There is virtually no difference in the measured band gap, all are around 1.60 eV, with a statistically negligible difference of $\pm$ 0.05 eV. As band gap is related to the structure of the film, this suggests that the inclusion of 5 mol% of the additives does not induce major changes in the structure. In all the samples there is only one sharp absorption onset, implying that a single continuous-phase has been formed. If this were not the case, it would be likely that there would be a second absorption onset visible between 450 – 550 nm, the region in which the band gaps for either PbI_2 or a separate $APbI_3$ phase may be.[19,20,27]
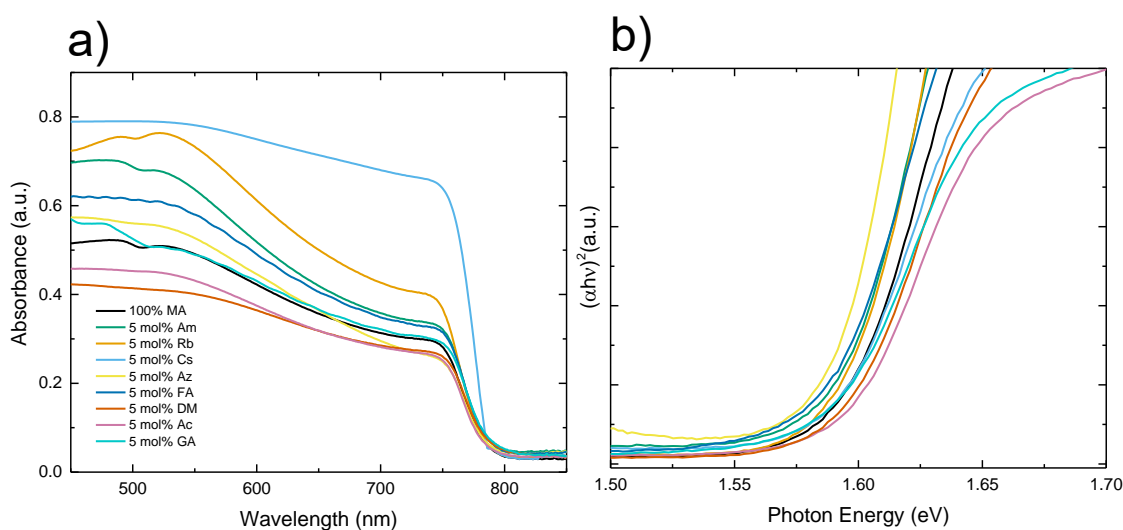
Figure 7.3.2. *UV/Vis spectroscopy of the eight mixed cation perovskite films: (a) absorbance plot and (b) Tauc plot*

The extent to which the perovskite structure is affected by the addition of these cations is visible in thin-film X-Ray Diffraction. Figure 7.3.3 shows the peak shift from the 100% MA standard normalised to FTO.
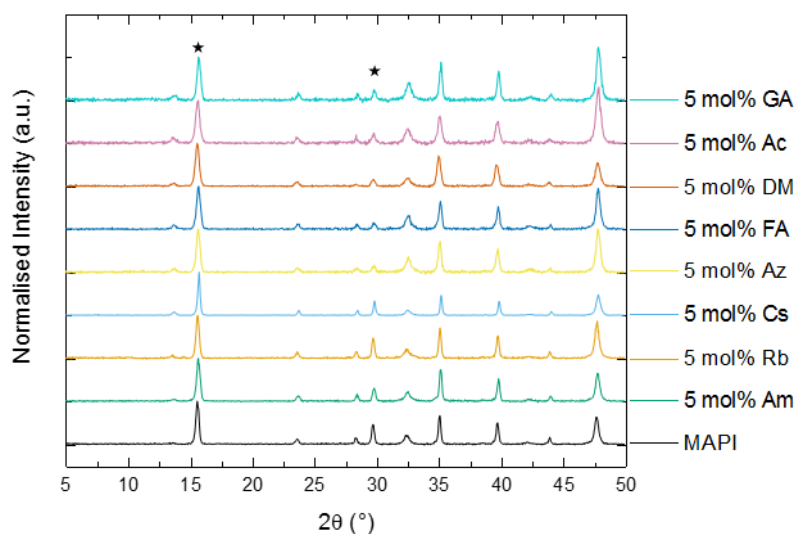
Figure 7.3.3. *Thin Film X-ray Diffractograms of the mixed-cation perovskites, with the (1,1,0) and (2,2,0) peaks starred*

Using a tolerance factor based approach it would be expected that the largest cation would give the largest shift in the main perovskite peaks (1,1,0 and 2,2,0), however this is not the case. It can be seen in Fig. 7.3.4.a, where the (2,2,0) peak shift is analysed with respect to ionic radius, that the largest shift comes from the 5 mol% Ac sample. Despite both Rb and Am being smaller than MA, the mixed-cation systems both show

shift to lower 2θ values. This suggests that even with the addition of smaller cations the unit cell is getting larger; which could be due to the 'locking effect' of Rb cations.[28]

As the Ac, Fa and Az samples are the most shifted, the next property to look at is dipole moment, as these cations are the ones in the set that possess dipoles. The relative shift with respect to dipole magnitude is shown in Figure 7.3.4b.
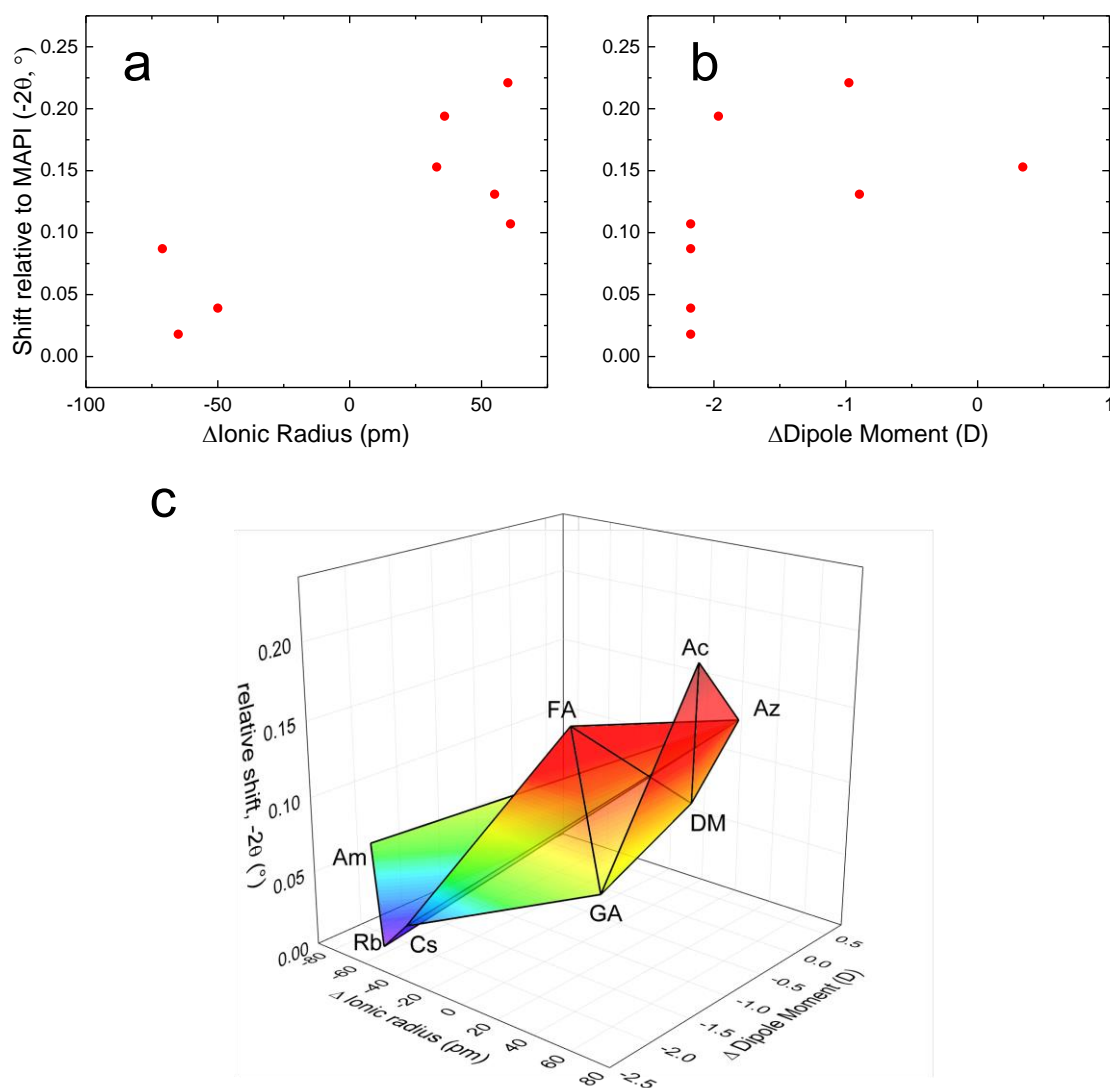
Figure 7.3.4. *Analysis of the (2,2,0) peak shifts compared to the difference relative to MA$^+$ in (a) ionic radius, (b) dipole moment and (c) a 3D plot against the effects of both Ionic Radius and Dipole Moment*

In both cases there is a general trend of a shift to lower 2θ values as either the ionic radius or dipole moment increases. For ionic radius, there is a much smaller change in the response with cationic additives that are smaller than methylammonium, whereas with larger cations there is a more significant shift. However the data for ionic radius is relatively random, and it doesn't appear to be the case that the largest cations result

156

in the largest shifts. For the dipole moment the trend is less clear. Azetidinium is the only cation that has a greater value of the dipole moment than methylammonium, but results in less of a shift than for example acetamidinium. Additives with no dipole moment appear to affect the lattice a lot less than those with a dipole moment.

A combination of the two parameters in a 3D plot (Figure 7.3.4c) shows that the largest shifts come from both a large ionic radius *and* a greater dipole moment. This could mean that there are several molecular properties that contribute to the way a dopant cation fits in the lattice and the extent of any effect it has. For example the fact that the Az^+ cation is a conformationally locked square and a secondary amine as opposed to a primary amine could also contribute to the compatibility of Az in the MAPI parent lattice.

The molecular volumes of each cation were calculated computationally, to further probe the effect of the size of the cation on its incorporation into the perovskite lattice. Molecular volume should be a more reliable indicator of size, as it considers the shape of the molecule – whereas using the ionic radius creates difficulties as the additives (with the exception of Rb and Cs) are not spherical. The calculated volumes are in table 7.3.2. Molecular volumes were then used to plot a similar graph to those for ionic radius and dipole moment (Figure 7.3.5.) There is a much clearer linear trend with increasing volume to increasing shift, showing that the larger cations are distorting the MAPI lattice to a greater extent.

Table 7.3.2. Computationally derived molecular volumes for the cations used in this study

Cation	Ionic Volume (Å^3)
Ammonium	33.02
Rubidium	10.17
Caesium	48.13
Methylammonium	53.45
Azetidinium	103.04
Formamidinium	62.29
Dimethylammonium	71.17
Acetamidinium	96.95
Guanidinium	72.90

***Figure* 7.3.5.** *Analysis of the peak shift of the (2,2,0) perovskite peak with the molecular volume difference of the cationic additives with respect to methylammonium*

If the cations are split into groups of those with similar chemistries, some interesting trends can be seen. In Figure 7.3.6. the 'secondary amine' set (MA → DM → Az) have been isolated in part *a*, and the 'primary amine' set (MA→FA→Ac→GA) in part *b*.
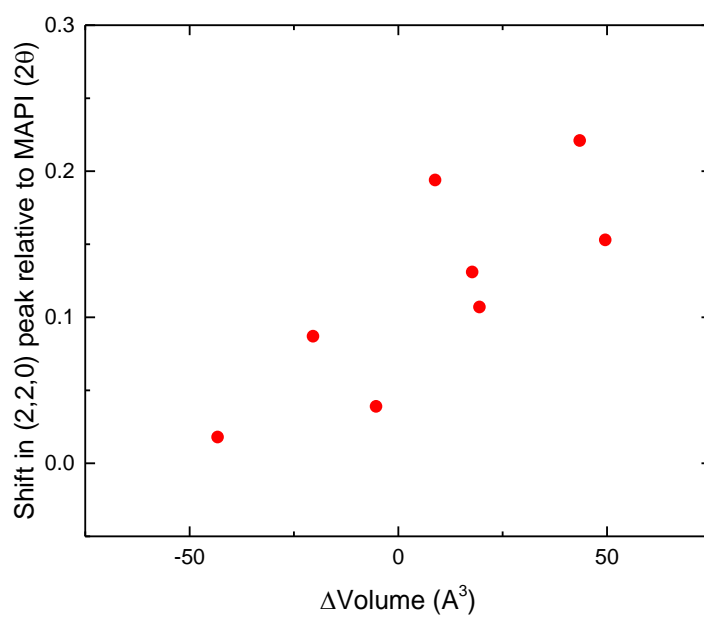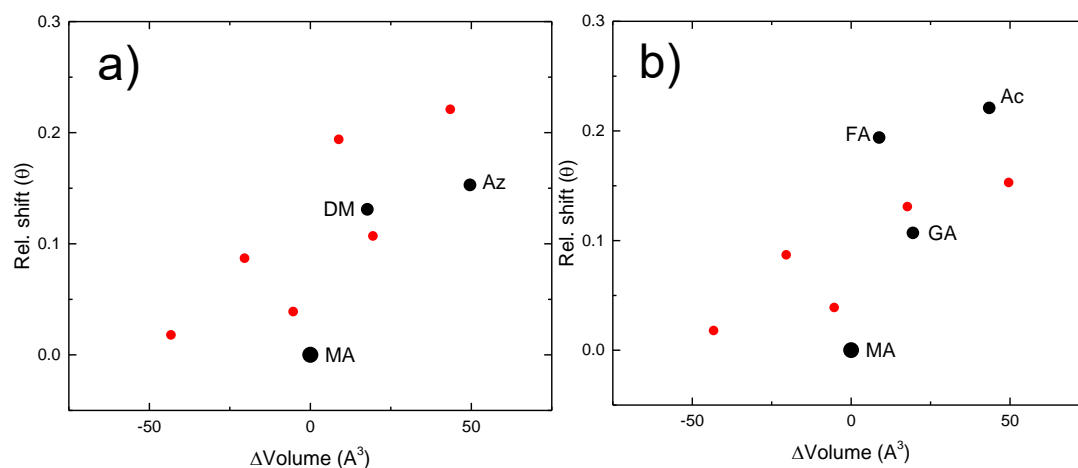

Figure 7.3.6. *Analysis of the peak shift of the (2,2,0) perovskite peak with the molecular volume difference of the cationic additives with respect to methylammonium: isolating the (a) secondary amine set and the (b) primary amine set*

The secondary amine set, as might be expected, shows a slight linear trend in the relative shift with the addition of the extra methyl groups. For the primary amine set the trend is not so simple. Upon the addition of another amine from MA→FA there is a large distortion of the MAPI lattice. Then with a third amine group, the GA sample shows less distortion relative to MAPI. Replacing one amine group with a methyl group (GA→Ac) results in one of the highest distortions, that is likely due to changes in dipole moment and the way the cation bonds into the lattice.

Computational methods were also used to visualise the cationic additives in the MAPI lattice, illustrated in Figure 7.3.7. Using GA as an example (as it had the largest ionic radius), it can be seen that the cation fits into the MAPI structure at 5 mol% with some, but not a large distortion. Solid state NMR has shown that guanidinium is able to infiltrate the MAPI lattice at proportions of up to 40 mol%, therefore it is to be expected that at 5 mol% it is incorporated – this was also confirmed by NMR studies performed in the group (paper not yet published).[29] It also shows that the frontier orbitals are unaffected by the inclusion of GA, which would mean that there should be little to no change in the band gap. These findings fit with the experimental UV/Vis data in Figure 7.3.2.
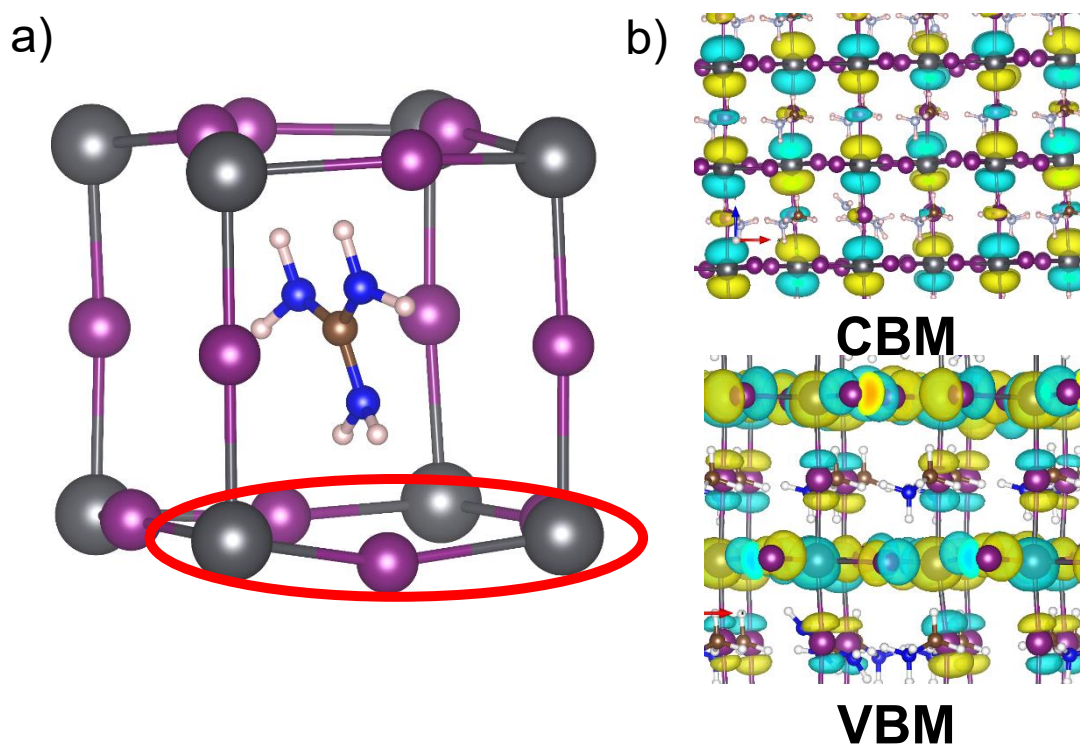
Figure 7.3.7. *The distortion of the crystal lattice by larger cations: (a) locally and (b) to the frontier bands*

Planar inverted PSC were made using these mixtures to investigate whether the structural effects had any bearing on solar cell performance, and to obtain further information on the behaviour of these mixed-cation systems. The results were taken from at least 15 devices for each cation. It should be noted that as 5 mol% is not necessarily the optimum percentage for each cationic additive in the system, the trend in efficiencies can only be superficially interpreted. The data for all the cells is shown in Figure 7.3.8 and Table 7.3.3.

Figure 7.3.8. *Box plots for V_{OC}, J_{SC}, Fill Factor and Efficiency for the cells with different cationic additives*
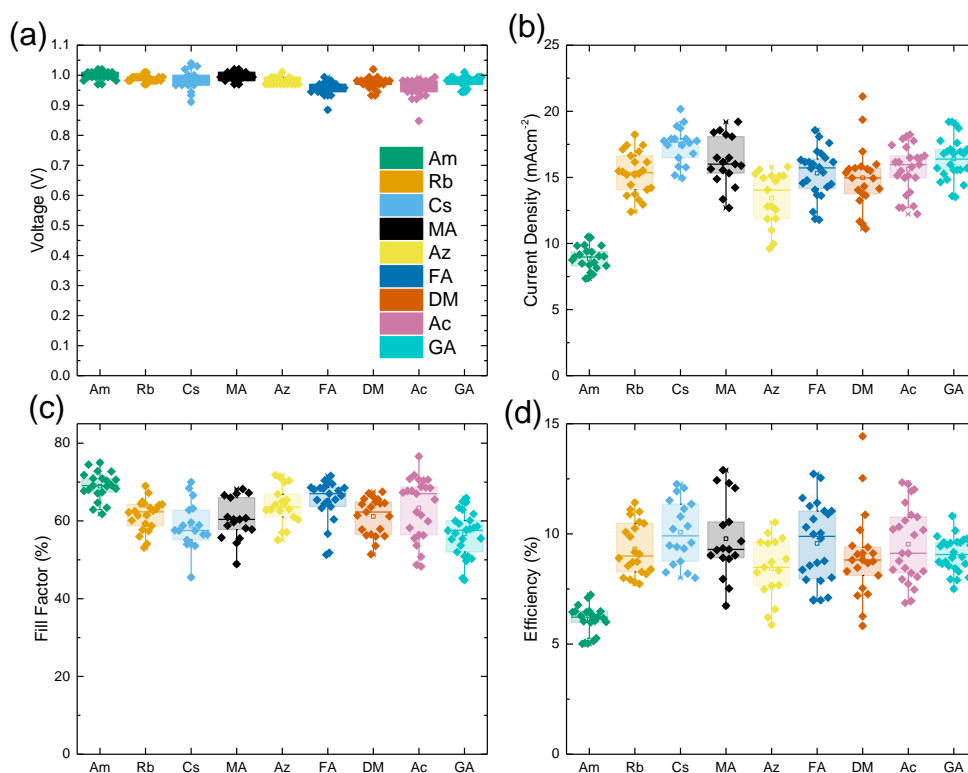
Table 7.3.3. Average Cell parameters for the cells with 5 mol% cationic additive (with standard deviation)

	V_{OC} (V)	J_{SC} (mAcm^{-2})	FF (%)	η (%)
Am	1.00 (±0.01)	8.9 (±0.9)	68.8 (±3.7)	6.1 (±0. 7)
Rb	0.99 (±0.01)	15.3 (±1.6)	61.4 (±4.0)	9.3 (±1.2)
Cs	0.98 (±0.03)	17.4 (±1.4)	58.7 (±5.7)	10.1 (±1.4)
MA	**1.00 (±0.01)**	**16.2 (±1.9)**	**60.4 (±5.3)**	**9.8 (±1.8)**
Az	0.98 (±0.01)	13.4 (±2.0)	64.0 (±4.9)	8.4 (±2.4)
FA	0.96 (±0.02)	15.3 (±1.8)	65.3 (±5.5)	9.6 (±1.8)
DM	0.97 (±0.02)	15.0 (±2.4)	61.2 (±4.8)	9.0 (±1.9)
Ac	0.96 (±0.03)	15.6 (±1.8)	63.3 (±7.9)	9.5 (±1.7)
GA	0.98 (±0.02)	16.4 (±1.6)	56.7 (±5.8)	9.0 (±0.8)

Whilst there is very little change in the average V_{OC} with each additive, the current density of each mixed-cation perovskite, with the exception of Cs, appears to be lower than that of the pure MA derivative. However this is counteracted by the most obvious change upon the addition of any additive, an increase in the fill factor. The result is very little average efficiency difference between the sets – except for the sample with ammonium, which is on average 3% lower than the other cationic additives.

Despite these differences, on the whole the cells exhibit very similar performance. Images of the mixed-cation films were taken on NiO_x coated FTO-glass to examine whether the differences can be explained by the crystallisation and/or coverage of the perovskite (Figure 7.3.9.)

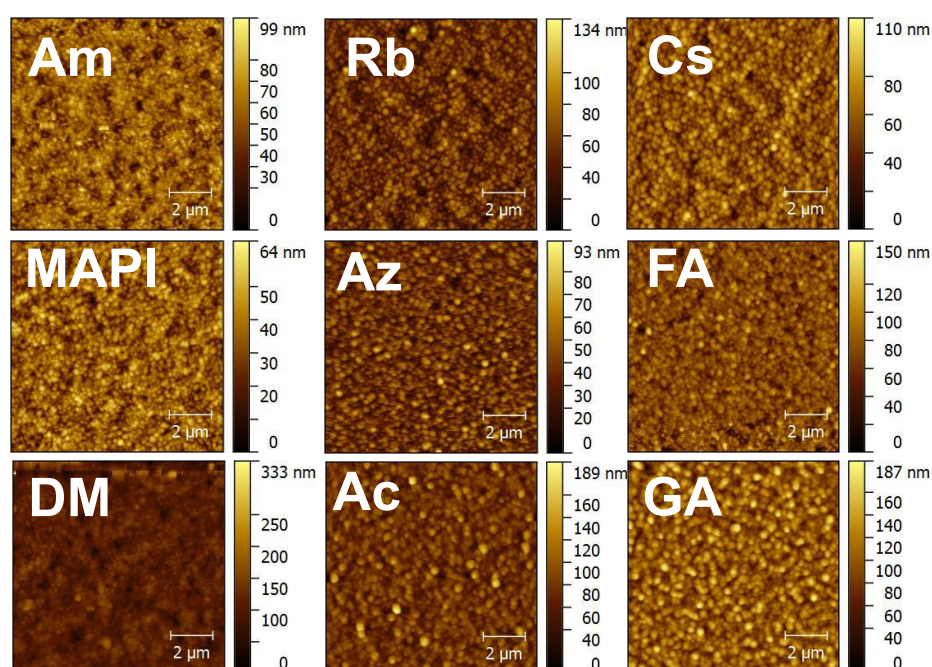*Figure 7.3.9. AFM Images for the perovskites with different cation additives*

There is little change in the overall crystalline size of the perovskites, as could be expected when using an antisolvent method for producing them. The antisolvent, in this case ethyl acetate, will cause the film to rapidly crystallise, and therefore the morphology is not affected by 5 mol% of the cationic additive.

7.4) The effect of lattice distortion on time/frequency dependent properties

Slow moving ions, more specifically iodide, have been observed to cause problems with the overall performance and stability of PSC.[30] The effect on recombination resistance of iodide diffusion has been observed using Electrochemical Impedance Spectroscopy (EIS), and temperature dependent measurements can be used to extract an activation energy for the low frequency process similar to computationally calculated values for iodide motion.[31] Previous EIS studies in this group have observed that there are three semi-circles in the Nyquist plot.[31,32] An example Nyquist plot with the expected frequency ranges for each semi-circle is shown below.
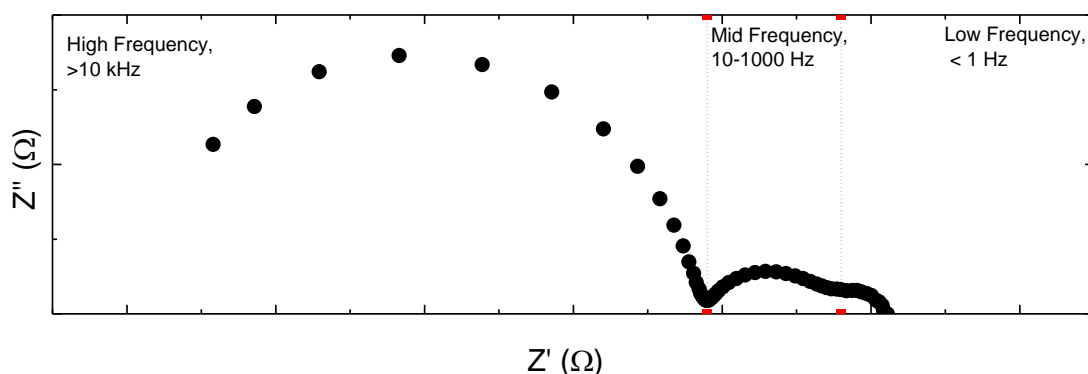

Figure 7.4.1. An example Nyquist plot of a Perovskite Solar Cells, with Frequency regions marked

Three distinct semi-circles would suggest that there are three separate processes in the solar cell, and as can be seen in Figure 7.4.1 each fits into its own frequency range. There are many ways to simulate a Nyquist plot with three semi-circles using an equivalent circuit, but as there is still a large amount of debate in the literature about the correct model no equivalent circuit will be used during this report, and each semicircle will be fitted individually.[31,33–37]

The high-frequency semi-circle, observed with an ω_{max} (the frequency value at the top of the semi-circle) of over 10 kHz is attributed to the recombination resistance, R_{recomb} and the geometric capacitance, C_{geo}. Values for these can vary depending on cell architecture as contact layers affect recombination in the cell.[34,38] The lower frequency semi-circles have been attributed to electronic processes such as a giant dielectric effect, however the carrier density in perovskites is too low to account for this – another explanation is that the recombination resistance changes over time as a result of slow ionic movement.[39,40] Using temperature dependent impedance measurements

and subsequently plotting the time constant, τ, of the process in an Arrhenius plot yields an activation energy of 0.3-0.5 eV – similar to computationally calculated values for iodide diffusion in the perovskite lattice.[31] The mid-frequency semi-circle, although occurring on timescales ten times faster than the low-frequency semi-circle, exhibits a near identical activation energy when its characteristic time constant is taken against temperature. It is however not yet certain what is the cause of this semicircle. For this chapter the effect of small levels of A-site substitution on the iodide diffusion in MAPI will be explored, by measuring the effect it has on R_{recomb} over a series of temperatures.

Computational studies performed by Dibya Ghosh as part of this study show that local distortions of the lattice can have a large effect on the path of iodide diffusion (Figure 7.4.2). Cation substitution was set at 25 mol% to aid calculation. As the largest cation, guanidinium, is introduced the distortion on the inorganic framework is such that the diffusion pathway becomes more difficult. This results in a larger activation energy for this process than in pure MAPI.
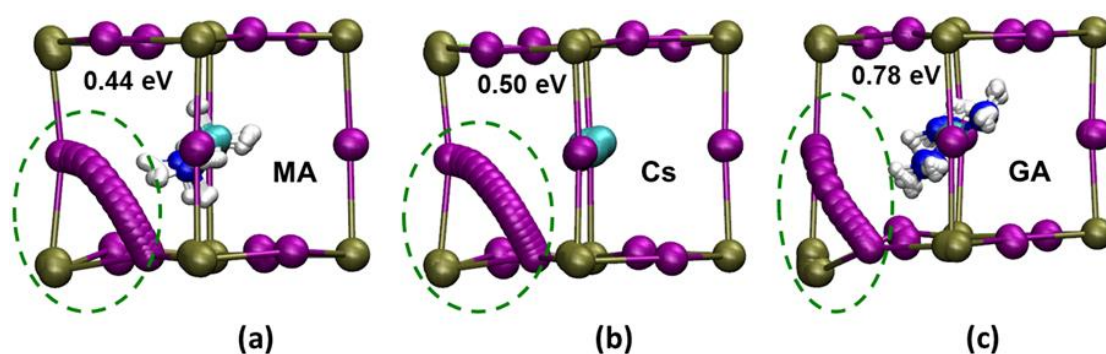

Fig. 7.4.2. *Ab initio simulations of the ion transport paths (using 18 intermediate images), the activation energies and the lattice ion displacements in (a) MAPI (b) $MA_{0.75}Cs_{0.25}PbI_3$ and (c) $MA_{0.75}GA_{0.25}PbI_3$. (Key: Pb, green; I, purple.) Local lattice relaxations near the diffusion path are highlighted by green circles, showing greater structural distortion in the GA-substituted material. Displacement values of the adjacent Pb ion in $MAPbI_3$, CsMAPI and GAMAPI are 0.2, 0.2 and 0.6Å respectively*

A further complication is that in tetragonal perovskites there are two different iodide sites, axial and equatorial (in relation to the inorganic octahedral framework). As a result there are further, possibly energetically different options for ion migration, illustrated below in Figure 7.4.3.
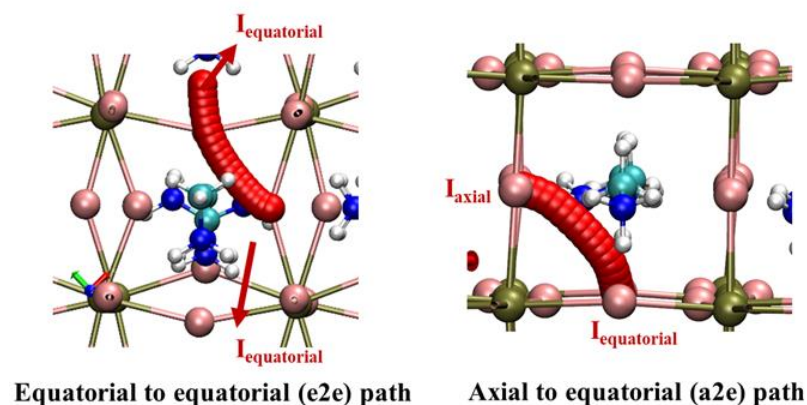
Equatorial to equatorial (e2e) path   **Axial to equatorial (a2e) path**

Fig. 7.4.3. The migration paths for iodide vacancies in tetragonal MAPI

It is possible that the mid-frequency semi-circle and low-frequency semi-circle could be caused by the two different diffusion pathways, e2e and a2e – as activation energies calculated from both have similar values (0.3-0.5 eV), or it could be there are two long range diffusion pathways, *e.g.* diffusion in the bulk and along grain boundaries (shown in Figure 3.4.5.2).[31,41] The aim of this chapter is to see whether the structural changes will affect the activation energy of (primarily, as it is better understood) the low frequency process, if the large bulky additives for example increase the barrier to iodide diffusion, and if so by how much.

10% efficient cells were chosen and (/or, in the case of the Am cells) 1 V open-circuit voltage, to ensure that any differences seen in the measurements were as a result of the cation additive, and not cell performance. Each cell was measured at seven temperatures between 45 °C and -12 °C to calculate the activation energy for the low frequency process observed in EIS.

Figure 7.4.4 shows the results for the control cell, both the Nyquist plots for each temperature, and the resulting Arrhenius plots obtained from the two lower frequency semicircles. For the MA sample, three processes are observed – the high frequency arc being R_{recomb} and C_{geo}. The lower frequency semicircles are the ones that have been linked to changes in the recombination resistance caused by iodide diffusion, with ω_{max} values in the 500-10 Hz range (with decreasing temperature) for the mid-frequency semicircle, and 50-0.5 Hz for the low-frequency feature. For MAPI, the values for the activation energy drawn from Arrhenius plots are 0.29 and 0.40 eV respectively – the latter being close to the value calculated from simulation. The error in the Arrhenius plot prepared using the low frequency time constant is larger than that for the mid-frequency element (Table 7.4.1). This is due to the temperature range where the low-

frequency feature is visible. It becomes much less visible (and therefore harder to fit) below 15 °C, hence there are fewer points in the Arrhenius plots for the lower frequency element.
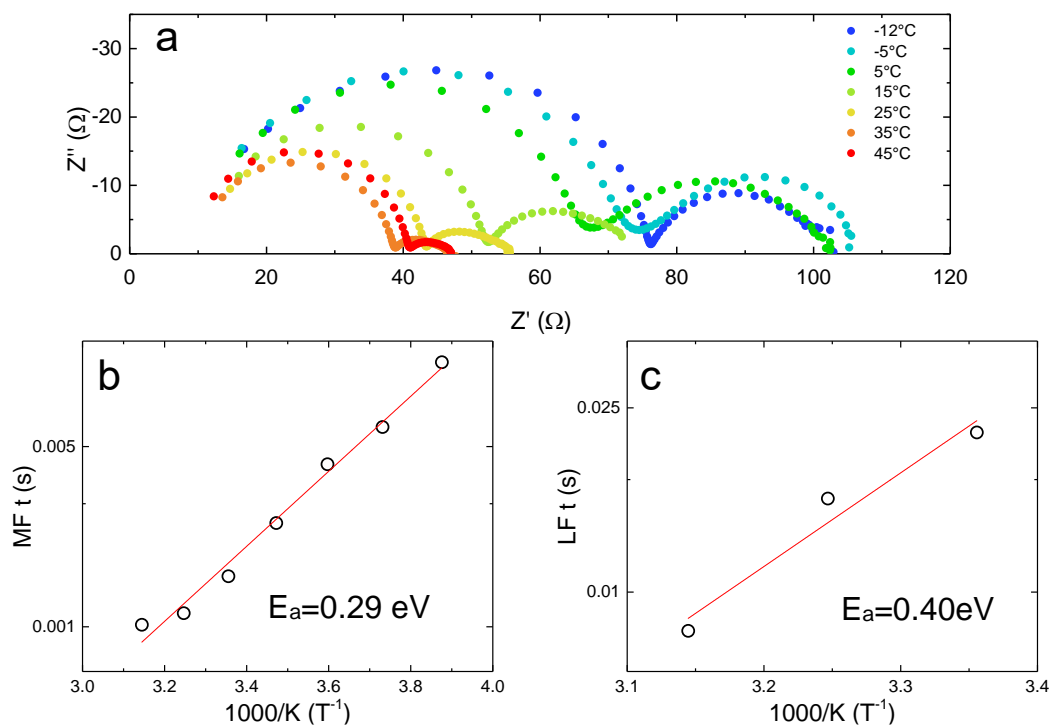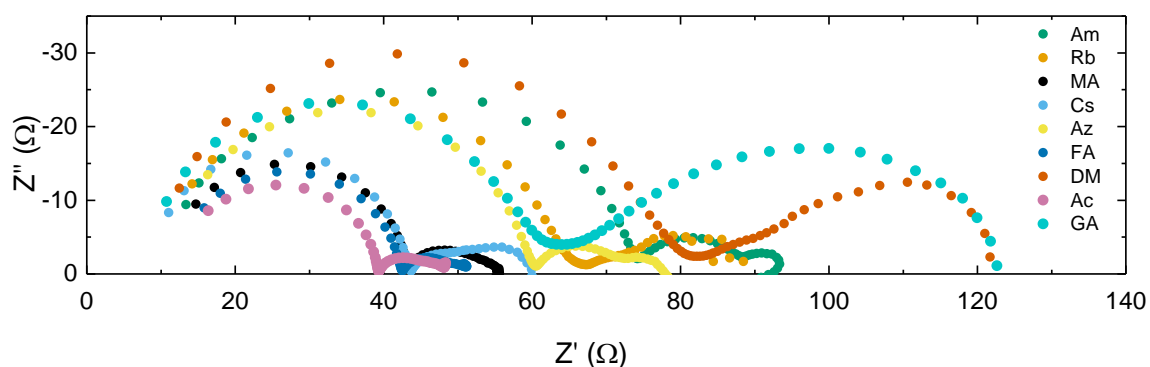

Figure 7.4.4. *Nyquist plots (a) and Arrhenius plots for the (b) low frequency feature and (c) mid frequency feature for the **MAPI** cell*

Table 7.4.1. Data extracted from the EIS experiments for each cation at 25 °C

Cation	R_{recomb} (High) (Ω)	C_{geo} (High) (nF)	τ (Mid) (s)	E_a (Mid) (eV)	τ (Low) (s)	E_a (Low) (eV)
Am	65.0	19.8	0.005	0.58 ($\pm$0.06)	0.76	0.53 ($\pm$0.08)
Rb	55.9	11.9	0.1	N/A	0.77	0.47 ($\pm$0.06)
Cs	35.4	15.6	0.028	0.51 ($\pm$0.05)	0.63	0.48 ($\pm$0.02)
MA	**36.9**	**13.0**	**0.00157**	**0.29 ($\pm$0.01)**	**0.02212**	**0.40 ($\pm$0.08)**
Az	49.4	10.3	0.005	0.29 ($\pm$0.01)	0.5	0.50 ($\pm$0.03)
FA	30.8	15.5	0.01	0.23 ($\pm$0.02)	0.22	0.54 ($\pm$0.10)
DM	66.0	12.5	0.2	1.16 ($\pm$0.17)	0.77	0.65 ($\pm$0.08)
Ac	27.3	16.1	0.008	0.31 ($\pm$0.03)	N/A	N/A
GA	51.3	13.5	0.03	0.38 ($\pm$0.01)	N/A	N/A

The vast majority of these cations have very little effect on the frequency dependent response of the solar cell – within the experimental differences it can be stated that R_{recomb} and C_{geo} do not change a significant amount with 5 mol% of most of the cationic additives at 25 °C. The shape of the Nyquist plots is also fairly consistent, one larger semicircle followed by two smaller circuit features. The results for all cells at 25 °C are displayed in Figure 7.4.5. Despite some minor differences which will be discussed later, the results for all nine are all similar.

Figure 7.4.5. Nyquist plots taken for all cells at 25 °C

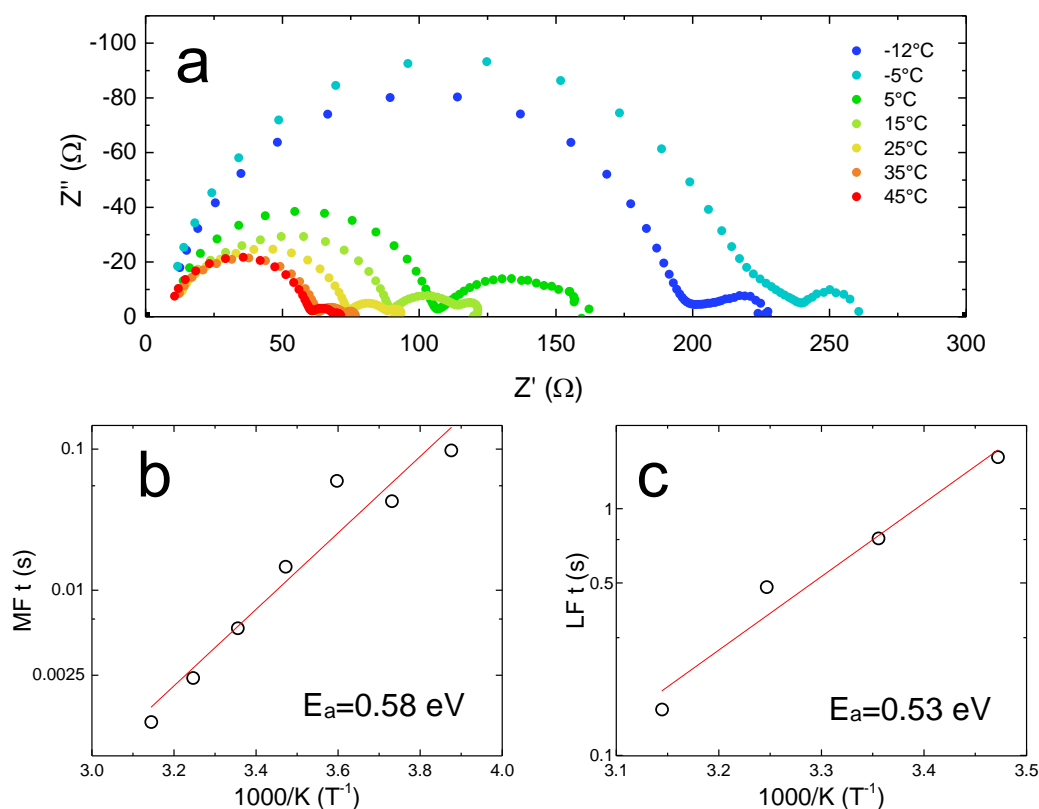Below in Figure 7.4.6 are the results for the cells with 5 mol% Am added.

Figure 7.4.6. *Nyquist plots (a) and Arrhenius plots for the (b) mid frequency feature and (c) low frequency feature for the **AmMAPI** cell*

From the JV data in table 7.3.3, the performance of the Am cells was on average 3% less than any of the others, although the voltage was still up around 1 V. The activation energies for the mid and low frequency semicircles is 0.58 and 0.53 eV respectively, which is relatively high, however as the efficiency of these cells is much lower it is difficult to draw any conclusions from the cells with ammonium as an additive. It is possible that ammonium is too small to fit in the lattice as an A-site cation and is instead leaving vacancies. It is however very difficult to prove either way.

Although the mid-frequency semicircle for Rb did not fit an Arrhenius plot, the low frequency semicircle showed an E_a value of 0.47 eV (Figure 7.4.7.).
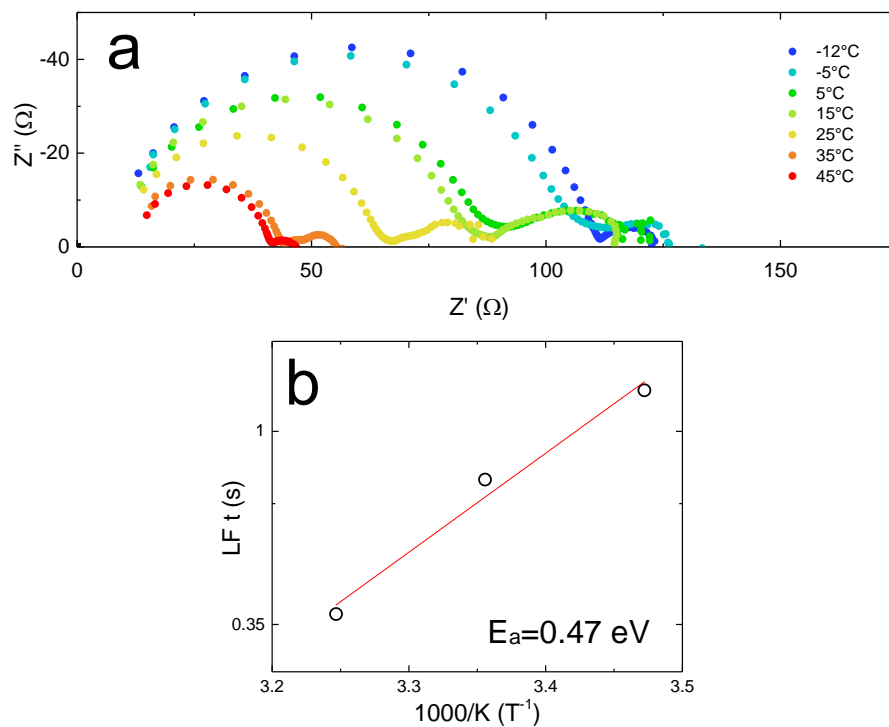
Figure 7.4.7. *Nyquist plots (a) and (b) Arrhenius plot for the low frequency circuit element for the* **RbMAPI** *cell*

The Cs sample (Figure 7.4.8.) is quite similar to Rb, with 3 semicircles clearly visible above 15 °C. The time constants and E_a values are also quite similar to Rb. This could be caused by the similar effect of the spherical cation on the perovskite lattice. It should also be noted that with more measurable points the error in the activation energy values has dropped dramatically.
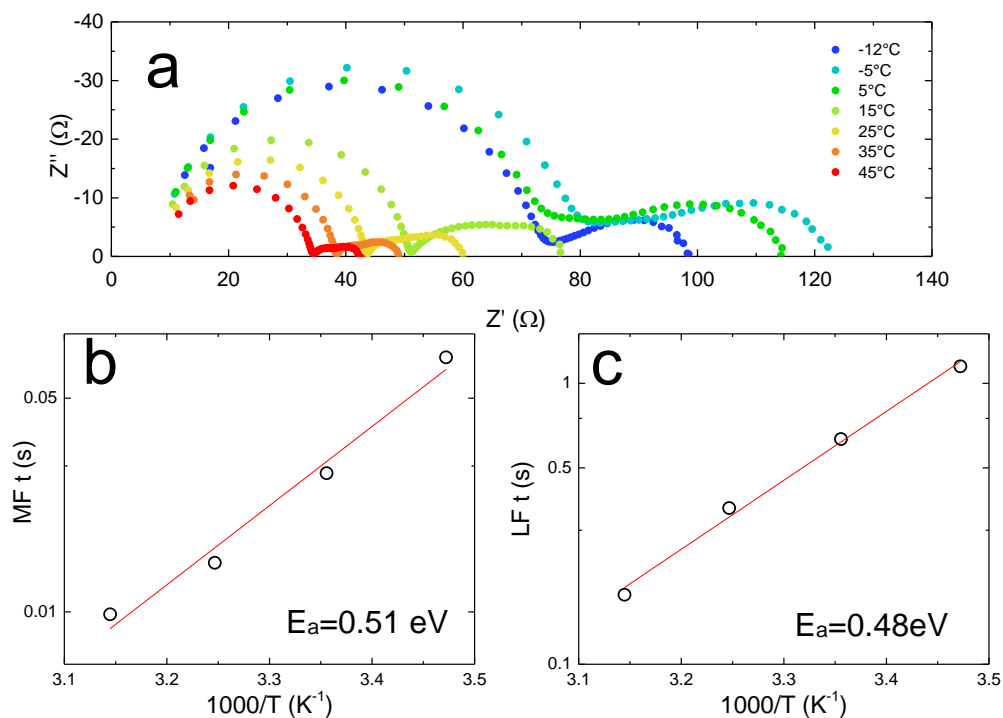
Figure 7.4.8. *Nyquist plots (a) and Arrhenius plots for the (b) mid frequency feature and (c) low frequency feature for the **CsMAPI** cell*

Azetidinium (Figure 7.4.9) and Formamidinium (Figure 7.4.10.), despite having slightly different shapes, show very similar activation energies and trends.

Figure 7.4.9. *Nyquist plots (a) and Arrhenius plots for the (b) mid frequency feature and (c) low frequency feature for the **AzMAPI** cell*

The Azetidinium cell provided much better resolution than that for FA – for FA the low frequency semicircle even at high temperatures was difficult to fit, and this makes

the data obtained less reliable. However the fit that is obtained follows the trend observed for other cations, (especially the mid-frequency circuit element). In the case of FA the activation energy is lowered for the mid frequency circuit element.
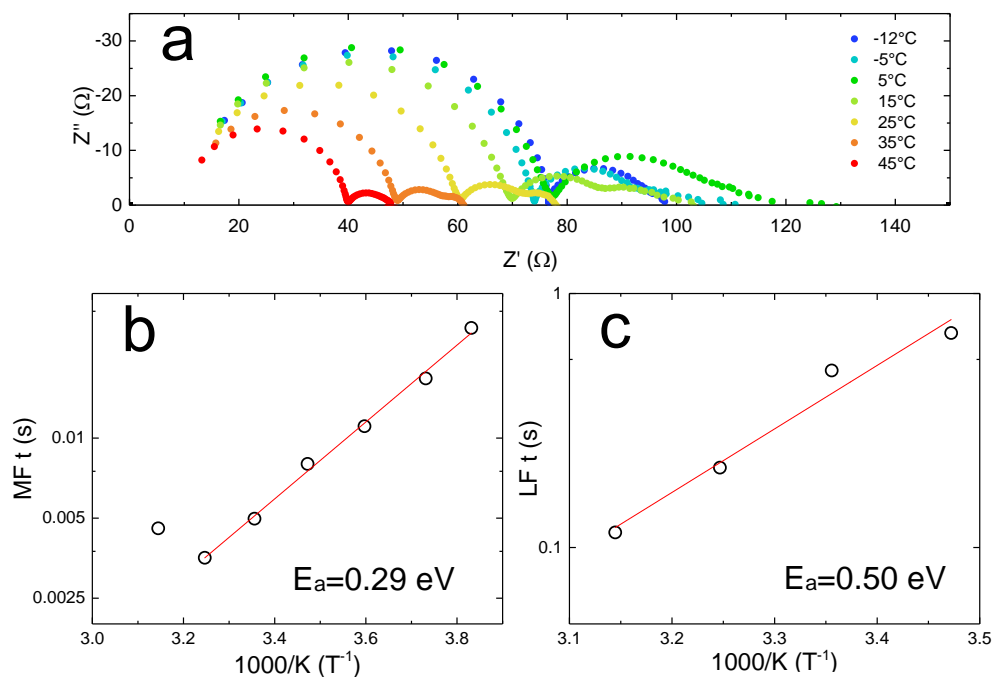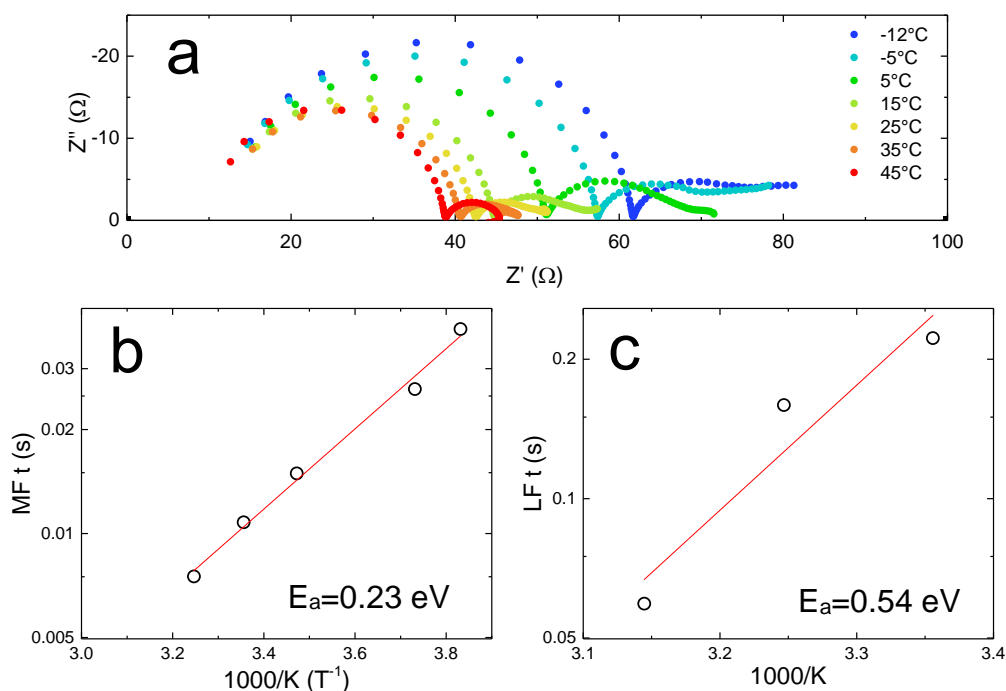

Figure 7.4.10. *Nyquist plots (a) and Arrhenius plots for the (b) mid frequency feature and (c) low frequency feature for the **FAMAPI** cell*

Another difference when formamidinium is added is the tendency for the Nyquist plot not to have reached the *x* axis by the end of the experiment (5 mHz), indicating that iodide diffusion at these temperatures is on a timescale not measurable by the experiment. The time constant for the low frequency process is therefore likely to be over a minute, making it difficult to measure using regular equipment (if ω_{max} was 5 mHz, the last frequency measured in these experiments, the time constant for that feature would be 3 minutes 20 seconds).

Moving through the set, as the cation gets larger, the impedance response starts to deviate more and more from that of the MAPI control. The result for DMMAPI is shown in Figure 7.4.11.
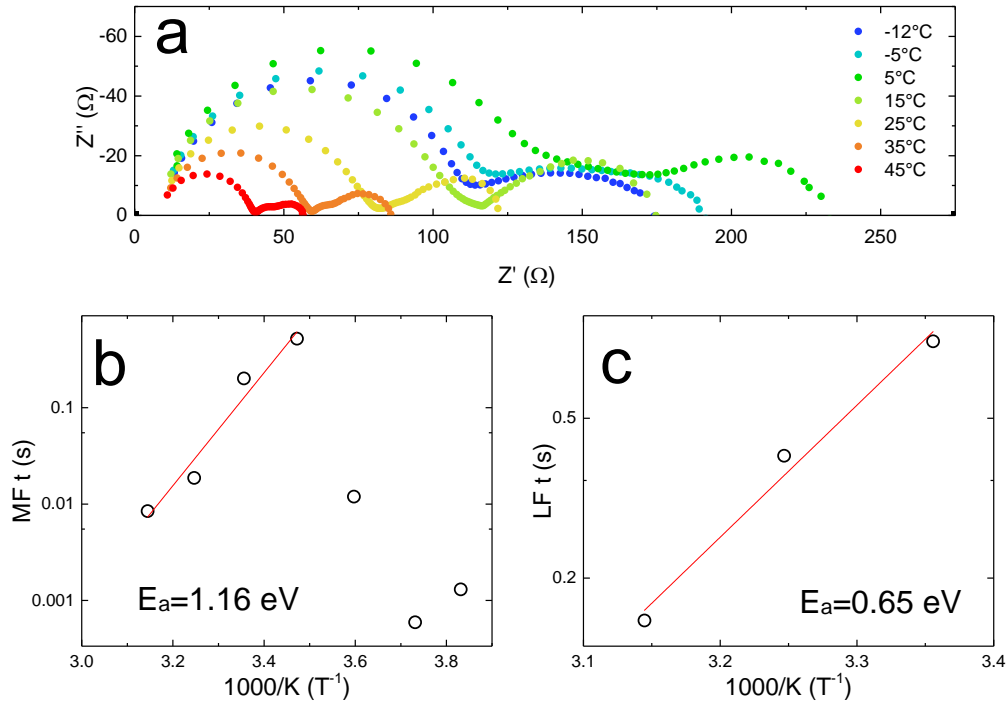
Figure 7.4.11. *Nyquist plots (a) and Arrhenius plots for the (b) mid frequency feature and (c) low frequency feature for the **DMMAPI** cell*

It is first interesting to note that with the Nyquist plots for DMMAPI, the low frequency element has a larger diameter than the high frequency element above 15 °C. It also has a higher activation energy, at 0.65 eV than the low frequency equivalent for MAPI, 0.40 eV without any additives. Although it is difficult to fit the data with only three points, the R^2 value is high enough that trends can be drawn from it. The Mid Frequency element also shows a much steeper trend with temperature until 5 °C – with an activation energy of 1.16 eV, although at lower temperatures the linear trend is lost. It is therefore not clear whether this is the same process as in the other cells, as with all the other perovskite compositions there has been a clear linear trend in the mid-frequency time constant with temperature.

To see if there was a trend with cation size, a plot of low frequency feature activation energy against cation additive size relative to MAPI is shown below, in Figure 7.4.12.
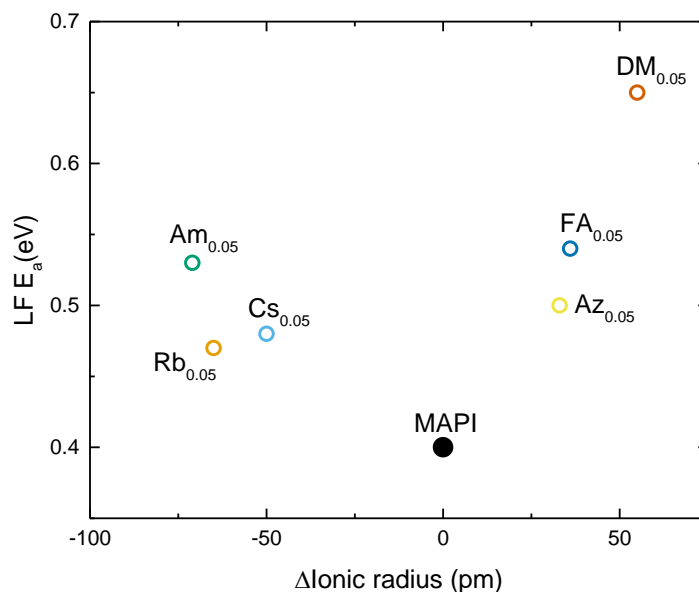
Figure 7.4.12. A plot of the activation energy for the low frequency feature against ionic radius (relative to methylammonium)

The resulting bowl shape, with the result from MAPI at the lowest apex, shows that not only with the introduction of any cation does the activation energy increase, it appears to be that there are larger increases with a greater size differential of the additive. This could be as a greater distortion is brought to the lattice the diffusion of iodide through it is made more difficult. Oxygen migration energy in solid oxide battery materials shows the same dependence on dopant size.[42]   A similar trend is observed in the low frequency time constants (Figure 7.4.13). It shows that the process is significantly slower in the mixed-cation systems.
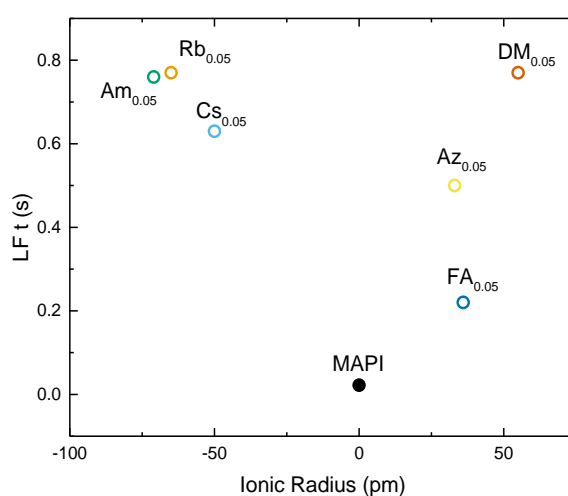

Figure 7.4.13. A plot of the time constant for the low frequency feature against ionic radius (relative to methylammonium, at 25 °C)

Upon further increase of cation size the impedance response changes dramatically.
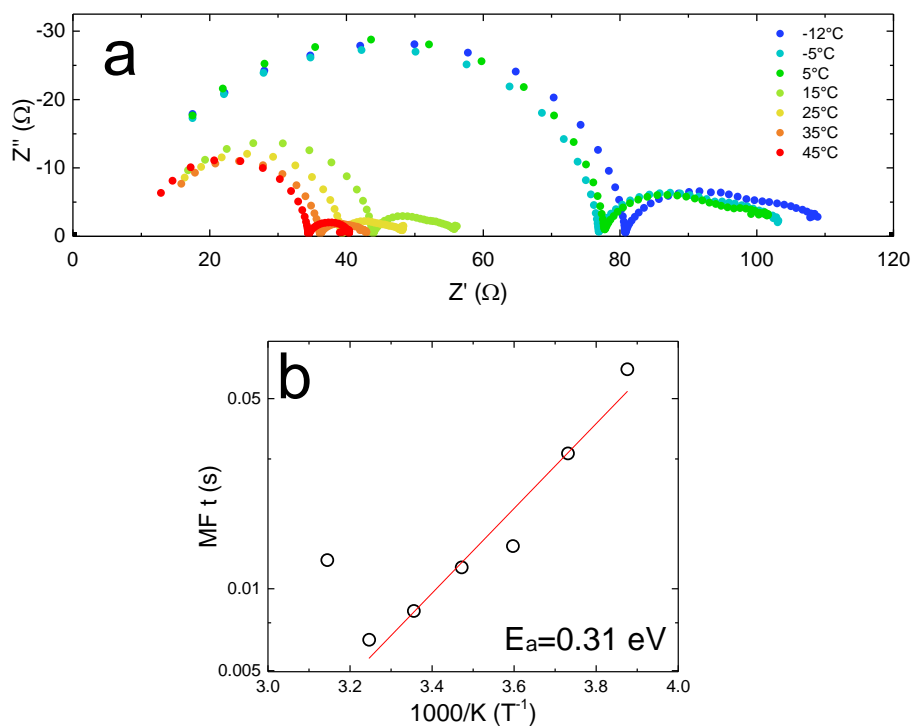
*Figure 7.4.14. Nyquist plots (a) and (b) Arrhenius plot for the mid frequency feature for the **AcMAPI** cell*

With AcMAPI the lowest frequency semi-circle is no longer resolvable. From Figure 7.4.13, it was shown that the time constant for the process causing the change in R_{recomb} at low frequency was getting significantly longer as cation size increased. With a further increase in size the time constant has become so large that the accompanying semi-circle is no longer visible on the timescale (and frequency range) of the experiment. The mid frequency semicircle shows good correlation with that of MAPI – so whichever process this is remains unaffected by the addition of Ac cations. The same is true of GAMAPI, as shown below in Figure 7.4.15.
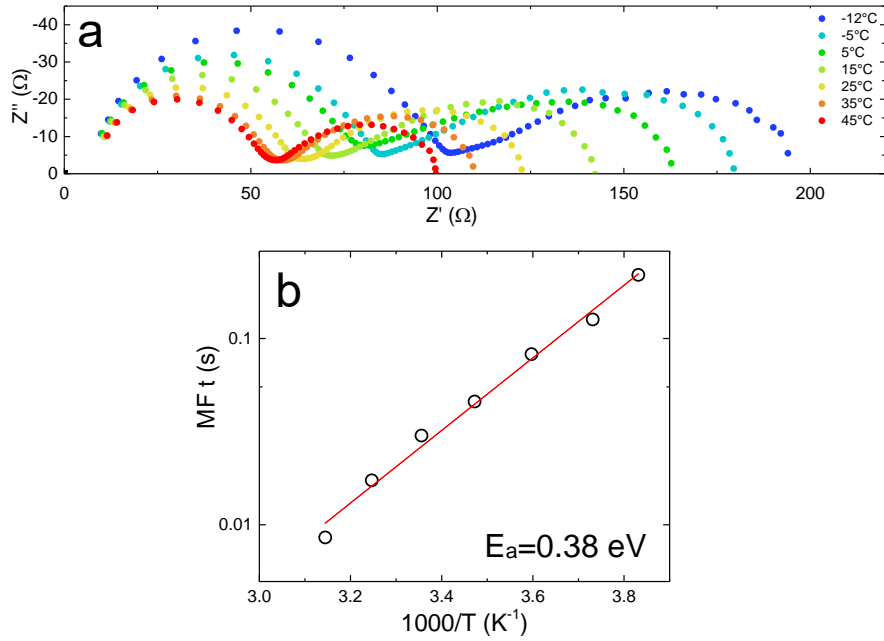
Figure 7.4.15. *Nyquist plots (a) and (b) Arrhenius plot for the mid frequency feature for the **GAMAPI** cell*

A plot of the imaginary component of the impedance and the frequency is shown below (Figure 7.4.16). To confirm that the lowest frequency element is being lost it is compared to two other perovskites that did show three obvious semicircles. The lower frequency peak in the GA plot is much closer to the mid-frequency peak of the others, suggesting that the process this refers to is the mid-frequency process and it is the low frequency iodide diffusion that is no longer observed.

Figure 7.4.16. Cole plots for the GAMAPI, AzMAPI and CsMAPI cells

The absence of iodide diffusion in GAMAPI perovskite powders has also been shown by muon spin relaxation spectroscopy (μSR, not yet published). This fits with the EIS spectra of GA, and suggests that the size of the Ac cation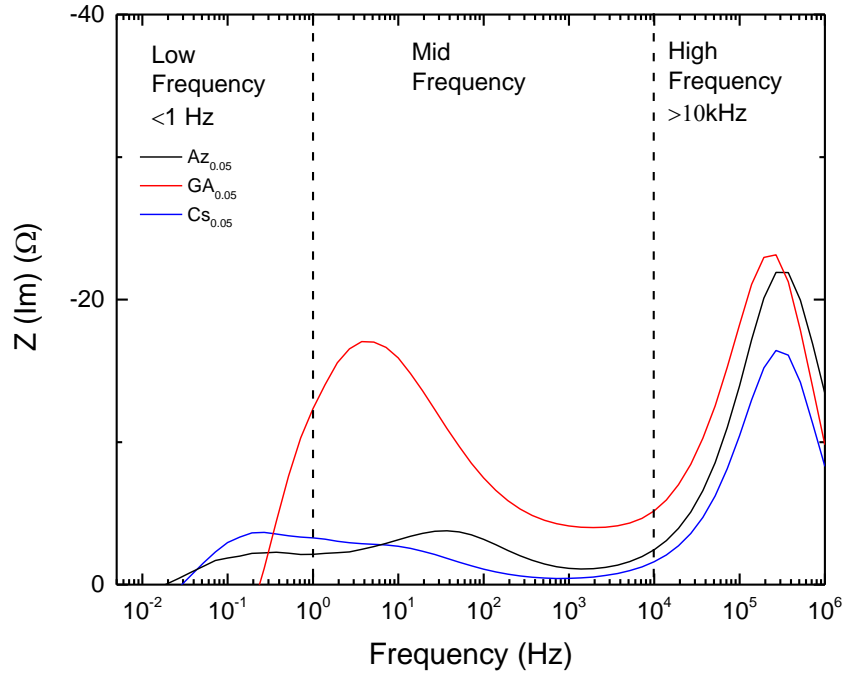 also prevents iodide diffusion. The mid-frequency semicircle in this case is much larger than for all the other cations, with similar time constants. The question remains as to what this mid-frequency semicircle relates to, as it often exhibits a good Arrhenius fit. It occurs at slightly faster speeds (shown by the lower time constants), so it could be that it is diffusion at the surface, facilitated by the HTM and ETM in the solar cell – this would not be picked up by μSR as that measured powders, not complete cells. A plot of the mid frequency activation energy with relative ionic radius shows a general downward trend, however it is much less regular than that of the low frequency element.
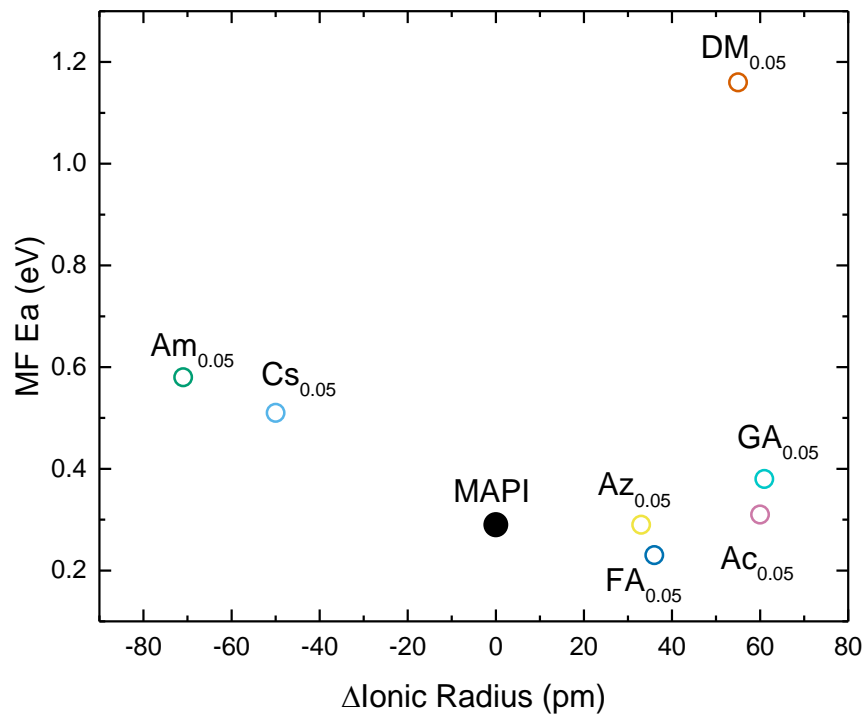
Figure 7.4.17. *A plot of the activation energy for the mid frequency feature against ionic radius (relative to methylammonium)*

7.5) Conclusions

In this chapter the effect of small amounts of A-site cation additives to the 3D MAPI lattice was investigated. The additives were found to have little to no-effect on band gap. There was some slight structural distortion with all the additives that was greater with a larger size/dipole moment of the cation. Molecular volumes for the additives were calculated, which gave a more accurate representation and fit of the trends seen. Cells made with the additives exhibited a lower current density than MAPI, attributed to the distortion of the structure inhibiting effective charge transfer. However the cells with 5 mol% of the additive also had a higher fill factor, which resulted in the efficiencies over the entire set being very similar. Atomic Force Microscopy images of the perovskite films showed very little difference in the overall crystallinity, surface coverage and roughness, likely to be caused using the antisolvent method in perovskite deposition.

These similarities allowed the internal processes to be properly examined by EIS, as any differences in the resulting spectra should be caused by the internal structure, rather than differences in efficiency, V_{OC}, or film crystallinity. On the whole the spectra looked very similar, with some notable trends. All the cells made with additives that had low frequency features showed a higher activation energy for iodide diffusion than that of MAPI, and the time constants were larger. The larger the deviation of the ionic radius from MA, the greater the increase in E_a/τ. For the largest two cations, Ac and GA, this deviation was so great that the low frequency iodide diffusion element was no longer visible on the timescale of the measurement by EIS. This means that even at low mol%, the distortion in the lattice caused by these cations is enough to change the iodide diffusion pathway to a less favourable direction. These results could explain why mixed-cation cells are consistently more stable, as one of the processes that has been shown to cause degradation in perovskite solar cells has been slowed.

7.6) References

1   M. Saliba, T. Matsui, J.-Y. Seo, K. Domanski, J.-P. Correa-Baena, N. Mohammad K., S. M. Zakeeruddin, W. Tress, A. Abate, A. Hagfeldt and M. Grätzel, *Energy Environ. Sci.*, 2016, **9**, 1989.

2   J. H. Noh, S. H. Im, J. H. Heo, T. N. Mandal and S. Il Seok, *Nano Lett.*, 2013, **13**, 1764–1769.

3   A. Walsh, *J. Phys. Chem. C*, 2015, **119**, 5755–5760.

4   C. Yi, J. Luo, S. Meloni, A. Boziki, N. Ashari-Astani, C. Grätzel, S. M. Zakeeruddin, U. Rothlisberger and M. Grätzel, *Energy Environ. Sci.*

5   F. Hao, C. C. Stoumpos, D. H. Cao, R. P. H. Chang and M. G. Kanatzidis, *Nat. Photonics*, 2014, **8**, 489–494.

6   A. Mancini, P. Quadrelli, C. Milanese, M. Patrini, G. Guizzetti and L. Malavasi, *Inorg. Chem.*, 2015, **54**, 8893–8895.

7   A. Babayigit, D. Duy Thanh, A. Ethirajan, J. Manca, M. Muller, H.-G. Boyen and B. Conings, *Sci. Rep.*, 2016, **6**, 18721.

8   M. M. Lee, J. Teuscher, T. Miyasaka, T. N. Murakami and H. J. Snaith, *Science*, 2012, **338**, 643–7.

9   O. J. Weber, B. Charles and M. T. Weller, *J. Mater. Chem. A*, 2016, **4**, 15375–15382.

10   J.-W. Lee, D.-J. Seol, A.-N. Cho and N.-G. Park, *Adv. Mater.*, 2014, **6**, 1–8.

11   S. Pang, H. Hu, J. Zhang, S. Lv, Y. Yu, F. Wei, T. Qin, H. Xu, Z. Liu and G. Cui, *Chem. Mater.*, 2014, **26**, 1485–1491.

12   J. Liu, Y. Shirai, X. Yang, Y. Yue, W. Chen, Y. Wu, A. Islam and L. Han, *Adv. Mater.*, 2015, **27**, 4918–4923.

13   J. P. C. Baena, L. Steier, W. Tress, M. Saliba, S. Neutzner, T. Matsui, F. Giordano, T. J. Jacobsson, A. R. S. Kandada, S. M. Zakeeruddin, A. Petrozza, A. Abate, M. K. Nazeeruddin, M. Grätzel, A. Hagfeldt, J. P. Correa Baena, L. Steier, W. Tress, M. Saliba, S. Neutzner, T. Matsui, F. Giordano, J. Jacobsson,

A. R. Srimath Kandada, S. M. Zakeeruddin, A. Petrozza, A. Abate, N. Mohammad K., M. Grätzel and A. Hagfeldt, *Energy Environ. Sci.*, 2015, **8**, 2928–2934.

14 G. E. Eperon, G. M. Paterno, R. J. Sutton, A. Zampetti, A. A. Haghighirad, F. Cacialli, H. J. Snaith, G. M. Paterno', R. J. Sutton, A. Zampetti, A. A. Haghighirad, F. Cacialli and H. J. Snaith, *J. Mater. Chem. A*, 2015, **3**, 19688–19695.

15 R. G. Niemann, L. Gouda, J. Hu, S. Tirosh, R. Gottesman, P. J. Cameron and A. Zaban, *J. Mater. Chem. A*, 2016, **4**, 17819–17827.

16 G. Kieslich, S. Sun and A. K. Cheetham, *Chem. Sci.*, 2014, **5**, 4712–4715.

17 W. Travis, E. N. K. Glover, H. Bronstein, D. O. Scanlon and R. Palgrave, *Chem. Sci.*, 2016, **7**, 4548–4556.

18 A. F. Akbulatov, L. A. Frolova, D. A. Anokhin, K. L. Gerasimov, N. N. Dremova and P. Troshin, *J. Mater. Chem. A*, 2016, **4**, 18378–18382.

19 N. De Marco, H. Zhou, Q. Chen, P. Sun, Z. Liu, L. Meng, E.-P. Yao, Y. Liu, A. Schiffer and Y. Yang, *Nano Lett.*, , DOI:10.1021/acs.nanolett.5b04060.

20 S. R. Pering, W. Deng, J. R. Troughton, P. S. Kubiak, D. Ghosh, R. G. Niemann, F. Brivio, F. E. Jeffrey, A. B. Walker, M. S. Islam, T. M. Watson, P. R. Raithby, A. L. Johnson, S. E. Lewis and P. J. Cameron, *J. Mater. Chem. A*, 2017, **5**, 20658–20665.

21 J. Hutter, M. Iannuzzi, F. Schiffmann and J. VandeVondele, *Wiley Interdiscip. Rev. Comput. Mol. Sci.*, 2014, **4**, 15–25.

22 G. Kieslich, S. Sun and T. Cheetham, *Chem. Sci.*, 2014, **5**, 4712–4715.

23 M. Becker, T. Kluner and M. Wark, *Dalt. Trans.*, 2017, **46**, 3500–3509.

24 G. E. Eperon, C. E. Beck and H. J. Snaith, *Mater. Horizons*, , DOI:10.1039/C5MH00170F.

25 M. Simenas, S. Balciunas, M. M[a with combining cedilla]czka, J. Banys and E. E. Tornau, *Phys. Chem. Chem. Phys.*, 2016, **18**, 18528–18535.

26 W.-J. Xu, K.-P. Xie, Z.-F. Xiao, W.-X. Zhang and X.-M. Chen, *Cryst. Growth*

Des., 2016, **16**, 7212–7217.

27   Y. Yang, J. Song, Y. L. Zhao, L. Zhu, X. Q. Gu, Y. Q. Gu, M. Che and Y. H. Qiang, *J. Alloys Compd.*, 2016, **684**, 84–90.

28   D. Ghosh, P. Walsh Atkins, M. S. Islam, A. B. Walker and C. Eames, *ACS Energy Lett.*, 2017, **2**, 2424–2429.

29   D. Kubicki, D. Prochowicz, A. Hofstetter, M. Saski, P. Yadav, D. Bi, N. Pellet, J. Lewinski, S. M. Zakeeruddin, M. Grätzel and L. Emsley, *J. Am. Chem. Soc.*, , DOI:10.1021/jacs.7b12860.

30   G. Richardson, S. O'Kane, R. G. Niemann, T. A. Peltola, J. M. Foster, P. J. Cameron and A. Walker, *Energy Environ. Sci.*, 2016, **9**, 1476–1485.

31   A. Pockett, G. E. Eperon, N. Sakai, H. J. Snaith, L. M. Peter and P. J. Cameron, *Phys. Chem. Chem. Phys.*, 2017, **19**, 5959–5970.

32   A. Pockett, G. E. Eperon, T. Peltola, H. J. Snaith, A. Walker, L. M. Peter and P. J. Cameron, *J. Phys. Chem. C*, 2015, **119**, 3456–3465.

33   A. Dualeh, T. Moehl, N. Tétreault, J. Teuscher, P. Gao, M. K. Nazeeruddin and M. Grätzel, *ACS Nano*, 2014, **8**, 362–373.

34   A. Todinova, L. Contreras-Bernal, M. Salado, S. Ahmad, N. Morillo, J. Idígoras and J. J. A. Anta, *ChemElectroChem*, 2017, **4**, 2891–2901.

35   A. Guerrero, G. Garcia-Belmonte, I. Mora-Sero, J. Bisquert, Y. S. Kang, T. J. Jacobsson, J. P. Correa-Baena and A. Hagfeldt, *J. Phys. Chem. C*, 2016, **120**, 8023–8032.

36   P. Wang, M. Ulfa and T. Pauporte, *J. Phys. Chem. C*, , DOI:10.1021/acs.jpcc.7b11010.

37   O. Almora, K. T. Cho, S. Aghazada, I. Zimmermann, G. J. Matt, C. J. Brabec, M. K. Nazeeruddin and G. Garcia-Belmonte, *Nano Energy*, 2018, **48**, 63–72.

38   E. J. Juarez-Perez, M. Wuβler, F. Fabregat-Santiago, K. Lakus-Wollny, E. Mankel, T. Mayer, W. Jaegermann and I. Mora-Sero, *J. Phys. Chem. Lett.*, 2014, **5**, 680–685.

39   D. A. Jacobs, H. Shen, F. Pfeffer, J. Peng, T. P. White, F. J. Beck and K. R.

Catchpole, *J. Appl. Phys.*, 2018, **124**, 225702.

40   F. Ebadi, N. Taghavinia, R. Mohammadpour, A. Hagfeldt and W. Tress, *Nat. Commun.*, 2019, **10**, 1574.

41   Y. Yuan and J. Huang, *Acc. Chem. Res.*, 2016, **49**, 286–293.

42   M. J. D. Rushton and A. Chroneos, *Sci. Rep.*, 2014, **4**, 6068.

8: From FAPI to $Cs_{0.05}(FA_{0.83}MA_{0.17}Pb(I_{0.83}Br_{0.17})_3)$: The Effect of Compositional Variation on the Impedance Response

8.1) Introduction

In the previous chapter (and other previous work) the mid-frequency and low-frequency semi-circles in the impedance spectrum have been shown to change their characteristic time constant with temperature, enabling for the calculation of activation energies for these processes of 0.4-0.6 eV – corresponding to that of iodide diffusion.[1,2] These studies were performed on MAPI (or MAPI with the inclusion of low amounts of A-site additives), and activation energy values agree with those calculated using other methods on hybrid organic inorganic halide perovskites.[3–8] Although the most well explored by EIS, MAPI is not the most efficient (or most stable) PSC. The current record for PSC uses $Cs_{0.05}(FA_{0.83}MA_{0.17}Pb(I_{0.83}Br_{0.17})_3)$.[9] The parent structure in this case is FAPI – which in its black phase is cubic, as opposed to tetragonal in MAPI.[10,11] A different structure leads to vastly different properties, for example in the band gap. In cubic FAPI the band gap is smaller, and closer to the ideal for solar cells.[12–14] The cubic structure of FAPI is however very unstable, and degrades readily to an inactive δ-phase.[15,16] Adding MA, Cs or Rb have been shown to prevent this degradation.[17–19]

Furthermore, a possible contribution to the greater long-term stability of mixed cation perovskites is the suppression of iodide diffusion.[19–21] This was observed in the previous chapter by the increase in activation energy for I^- diffusion upon the addition of 5 mol% of a wide range of cationic additives. Previous EIS studies on FAPI or the mixed component perovskites thereof have shown that much like in MAPI, the high frequency response does not change greatly with the addition of small cationic additives (Cs^+ and MA^+), and it is the lower frequency elements that are altered.[22,23] As of yet no temperature dependent measurements have been performed on these perovskites to attempt to extract activation energies (if there are any).

To examine the $Cs_{0.05}(FA_{0.83}MA_{0.17}Pb(I_{0.83}Br_{0.17})_3)$ perovskite, it will be broken down into each of its elements. In the triple-cation perovskite the substitution ratios of the additives are greater (17 mol% for MA^+ and Br^-, 5 mol% for Cs^+), so should have a much larger effect on the perovskite lattice (and therefore ion diffusion). Cation

mixing is compounded by the size differences; whereas Cs^+ is only 50 pm smaller than MA^+, it is 86 pm smaller than FA^+. In this chapter the role of each component will be investigated, with emphasis on their effect on ion diffusion, to suggest potential new perovskite compounds that may generate high efficiencies and stabilities.

8.2) Specific Experimental

8.2.1. Formamidinium perovskite synthesis

FAPI perovskites were made using a 1:1 molar ratio of formamidinium iodide (FAI, Greatcell Solar) and PbI_2 (Sigma, 99 %) in a solution using a solvent ratio of 4:1 DMF:DMSO. For the substituted perovskite in section 8.4, 5 mol% of the FAI was replaced by the appropriate additive, CsI (Alfa Aesar, 99.9 %), MAI, AcI and GAI (Greatcell Solar). Precursor solutions for the triple-cation perovskite were made using the proportions and methods reported by Saliba *et al.*[9]

All films were deposited at 5000 rpm for 30 seconds, with an ethyl acetate antisolvent being used 15 seconds into the spin-coating method. Films were annealed at 150 °C unless otherwise stated.

8.3) Formamidinium Lead Iodide: the scaffold

To accurately compare all the different compositions that can be used to make the triple-cation perovskite, Formamidinium Lead Iodide (FAPI) was investigated to provide a baseline.

In its photoactive phase, FAPI has a cubic perovskite structure. To reach the black α-phase an annealing temperature of 150 °C is required.[24] At lower temperatures FAPI forms an inactive, yellow hexagonal δ-phase.[11] Thin film XRD shown below in Figure 8.3.1. shows evidence of both α and δ-phases when a 1:1 $FAI:PbI_2$ solution is deposited and annealed at 150 °C.
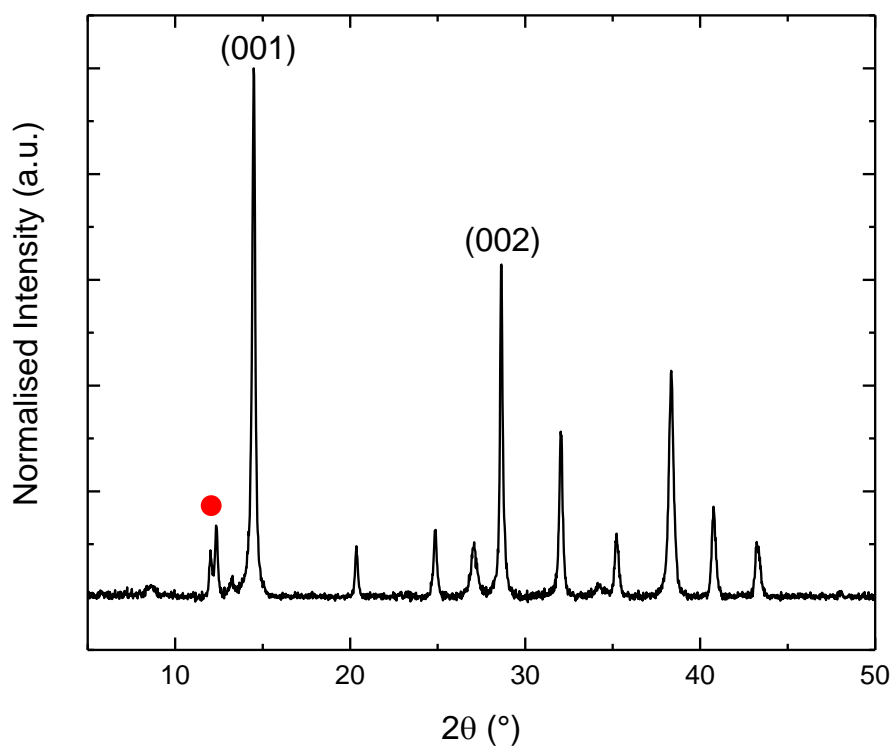

Figure 8.3.1. *Thin Film X-ray Diffractogram of Formamidinium Lead Iodide, with the (001) and (002) peaks labelled, and the δ-phase peak/PbI_2 peak marked with a red circle – the response was normalised to the FTO substrate*

The peak at 14.5 ° corresponds to the 001 plane of the cubic FAPI perovskite.[11] Although this is the dominant peak, there is a dual peak at 12-13 °, which is likely to be a combination of the δ-FAPI phase and PbI_2.[25] Despite peaks being present for multiple phases in the XRD, there was no obvious phase separation observed in the UV/Vis spectrum of FAPI (Figure 8.3.2).
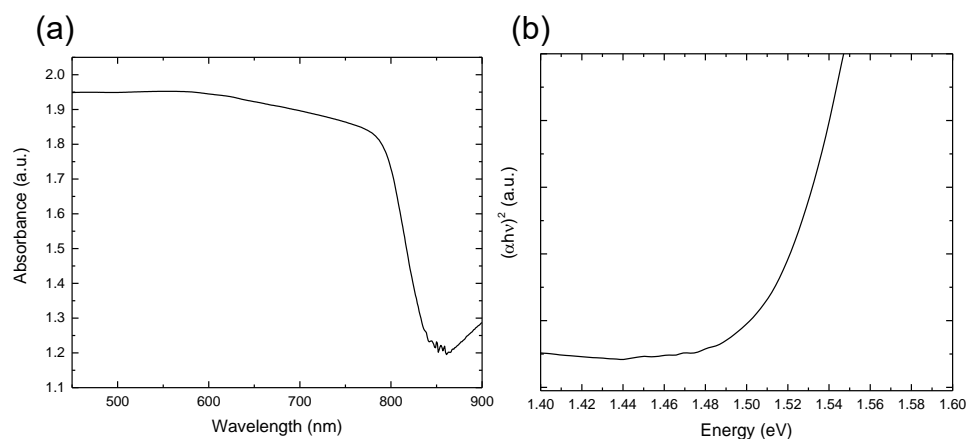
186

Figure 8.3.2. *a) UV/Vis spectroscopy of a FAPI film and b) Tauc transformation for band gap determination*

By using a Tauc plot, the band gap of FAPI was determined to be 1.50 eV – lower energy than MAPI from the previous chapters. A broader absorption range allows for greater absorption in the red wavelengths of the visible spectrum. It does however mean that the open-circuit voltage for any FAPI based cell is likely to be relatively low compared to that of MAPI, as V_{OC} is limited by the band gap.

The resulting pure FAPI cells, with all parameters displayed in Figure 8.3.2, do have a lower V_{OC}, with a narrow distribution of values for 20 cells of around 0.8 V. The average efficiency of this cell set is 7.9 % (±1.08), with champion efficiencies above 9 %. FAPI is not well studied on its own in the inverted NiO_x based structure, and record efficiencies are lower than in standard architecture cells (pure FAPI is around 15 %).[26] These efficiencies are also similar to the MAPI cells made in our lab, and therefore are a good base for starting the study.
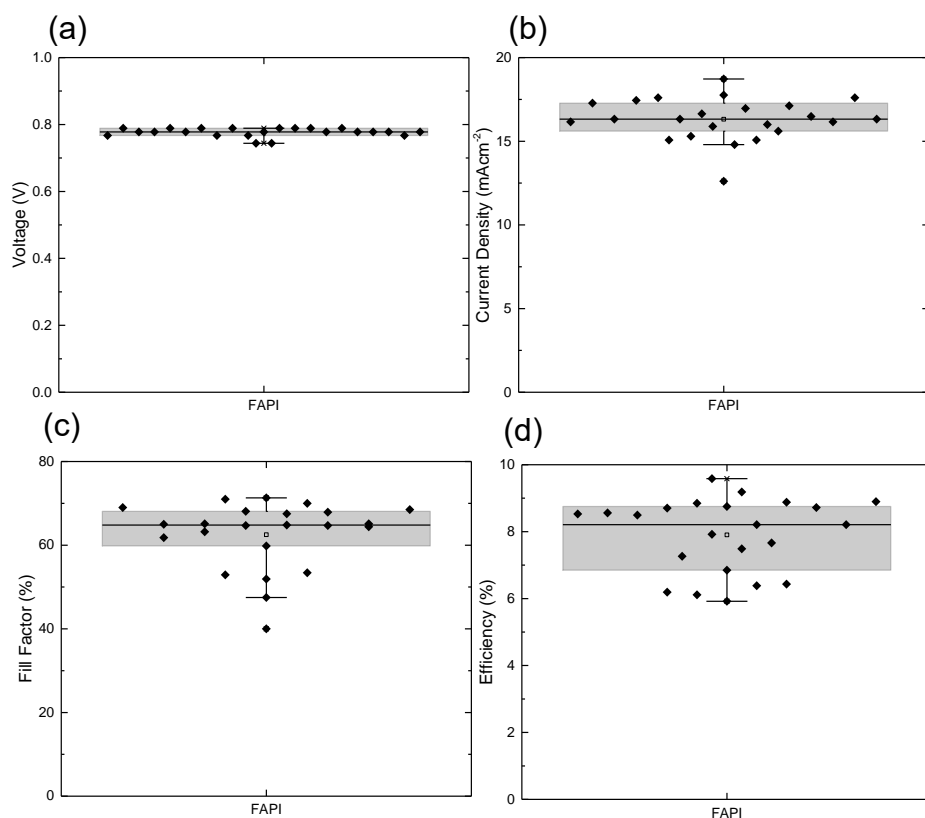
Figure 8.3.3. *Solar cell parameters for **FAPI**: a) Open-circuit voltage, b) short-circuit current density, c) Fill Factor and d) Efficiency*

Atomic Force Microscopy (AFM) was performed on thin films of FAPI to analyse the surface morphology. The image, shown in Figure 8.3.4, shows tightly packed small crystals, with few small pinholes. The film has similar morphology to those exhibited by the films in the last chapter, and this is also likely to be caused by the antisolvent deposition method.
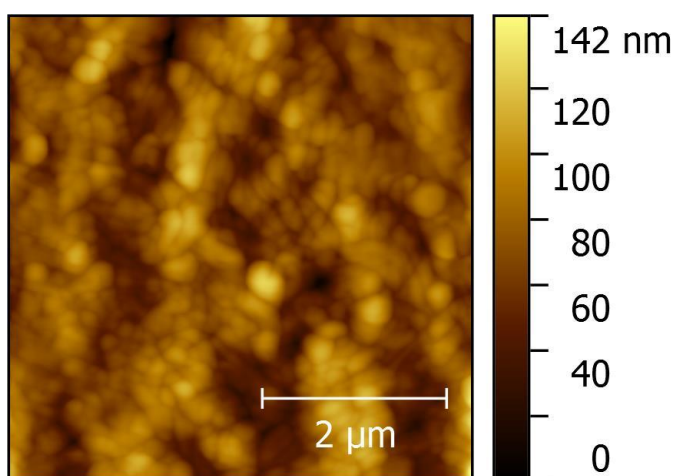

Figure 8.3.4. *AFM image of a FAPI thin film (taken over 5 μm in phase contrast mode)*

The EIS response of FAPI at V_{OC}, taken at 25 °C and 73 mWcm^{-2} illumination is shown below. The Nyquist plot (Figure 8.3.5a) looks remarkably similar to that of MAPI. There are two distinctly separate processes, and low values for the recombination resistance (37 Ω in MAPI, and 19 Ω in FAPI). Further similarities to MAPI shown by FAPI are a low series resistance ($\leq 10\ \Omega$), due to the use of the same sheet resistance FTO and same cell architecture, and a similar geometric capacitance, 14 nF in FAPI and 13 nF in MAPI – also likely due to the identical fabrication procedure. The Cole plot shown in Figure 8.3.4b shows that the high frequency and mid frequency elements occur at very similar frequencies to other measured cells, at between 10^5 and 10^6 Hz and 10-100 Hz respectively. This suggests that these processes are unaffected by the principal A-site cation.

There is however no low-frequency semi-circle in the EIS for FAPI. The similarities in fabrication of MAPI and FAPI would suggest that it is not related to the transport layers. Diffusion that may be happening at the grain boundaries instead of in the bulk of the perovskite can also be discounted as the cause of the low-frequency semicircle, because the AFM images for both MAPI and FAPI show very similar morphology. As discussed in the previous chapter, iodide diffusion in tetragonal perovskites can occur by two distinct pathways, axial-to-equatorial and equatorial-to-equatorial. FAPI is cubic, therefore all iodide sites within the lattice should be equivalent and there would be only one possible pathway for iodide diffusion. Although it is unclear if the merging of the two iodide diffusion pathways would result in a faster process (and be visible in the mid-frequency semi-circle still observed in FAPI impedance), or a slower one that has moved out of the range of the experiment.
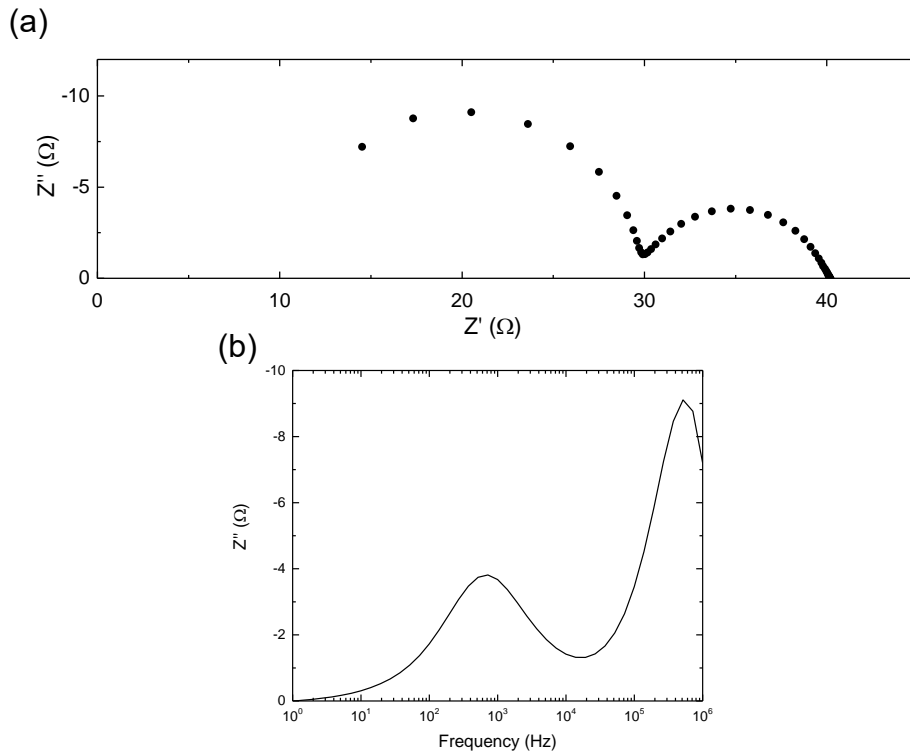
Figure 8.3.5. *Impedance analysis of FAPI at 25 °C: a) Nyquist plot and b) Cole plot*

Impedance measurements over a range of temperatures are shown in Figure 8.3.6. In the last chapter, the low frequency semicircle was most visible between 45 °C and 15 °C; the temperature range of these impedance measurements has therefore been adjusted to 7 points between these two temperatures. This step has been taken to improve the reliability of the activation energy calculations by ensuring that more data points will be observed.
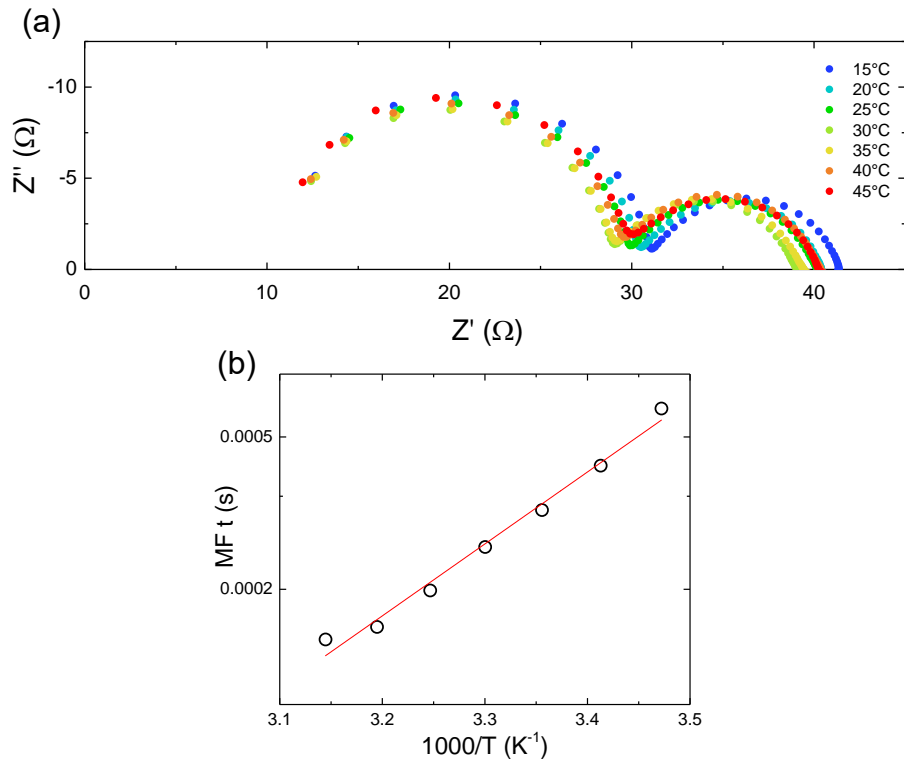
Figure 8.3.6. *The change in FAPI impedance with temperature: a) Nyquist plots, b) Arrhenius plot for the mid-frequency feature*

FAPI cells show a similar response to pure MAPI cells when subjected to measurements over a series of temperatures. As the temperature is lowered, the recombination resistance increases slightly and the ω_{max} values for the mid-frequency semi-circle decreases. When the resulting time constants are displayed in an Arrhenius plot it is evident that the mid-frequency feature is due to an activated process. The mid-frequency process has an activation energy of 0.37 eV. Again the E_a is almost identical to that found in MAPI, which suggests that it is the same process happening in both perovskites, strengthening the theory that it could be iodide diffusion at the grain boundaries and interfaces, which should be similar in both cells.

8.4) The case with FAPI: A-site additive effects

Before the triple-cation perovskites are explored, it is first necessary to determine what happens to FAPI as the lattice is changed by single additives. As FAPI is cubic, and formamidinium as a cation is larger than methylammonium cation substitution may have different consequences in FAPI. To do this four cations have been chosen for partial A-site substitution into FAPI. Caesium (Cs) and methylammonium (MA), two cations which are smaller than FA, and Acetamidinium (Ac) and Guanidinium (GA), both of which are bigger than FA. They were included at 5 mol%, and all films were annealed at 150 °C. Thin film XRD was taken of the films to analyse any difference from the original FAPI structure (Figure 8.4.1).
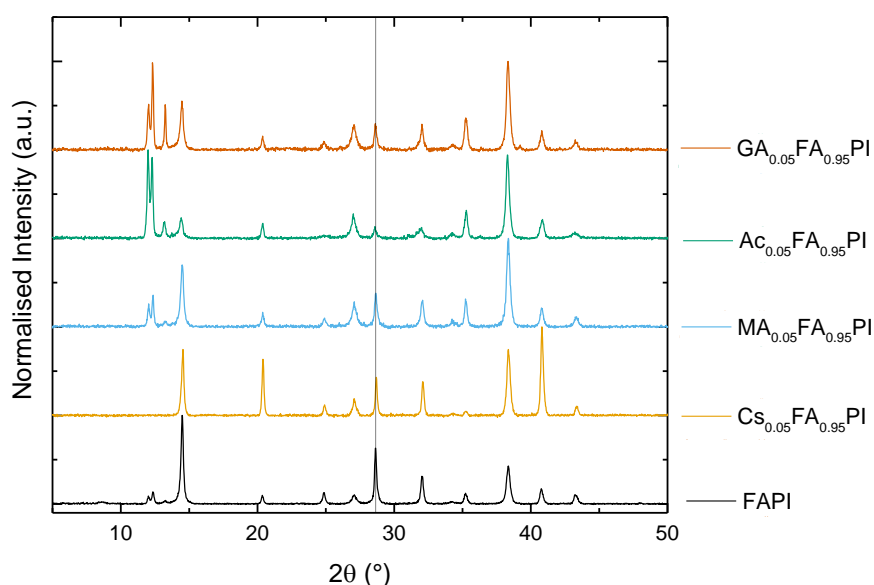

Figure 8.4.1. Thin Film XRD analysis of FAPI with the inclusion of the cationic additives, with line representing the (002) peak in FAPI

With 5 mol% Cs the δ-phase and PbI_2 peaks are completely removed. However this is not the case for any of the other cation substitutions. Based on these measurements there seems to be a high degree of phase impurity, due to the presence of characteristic δ-FAPI and PbI_2 peaks in the 12-13 ° region. The major FAPI 001 (at around 14 °) and 002 (at around 28 °) peaks are still visible. There are very small shifts in the peaks for the mixed-cation perovskites. As may be expected for Cs the peak is shifted to larger angles suggesting a reduction in lattice size, and *vice versa* for Ac and GA. For $MA_{0.05}FA_{0.95}PI$ there is no significant shift in the peak at all.

Based on the results from the solar cells in Figure 8.4.2, it would appear that any shifts or phase impurities do not cause a dramatic change in PSC efficiency, despite significant changes in V_{OC} and J_{SC}.
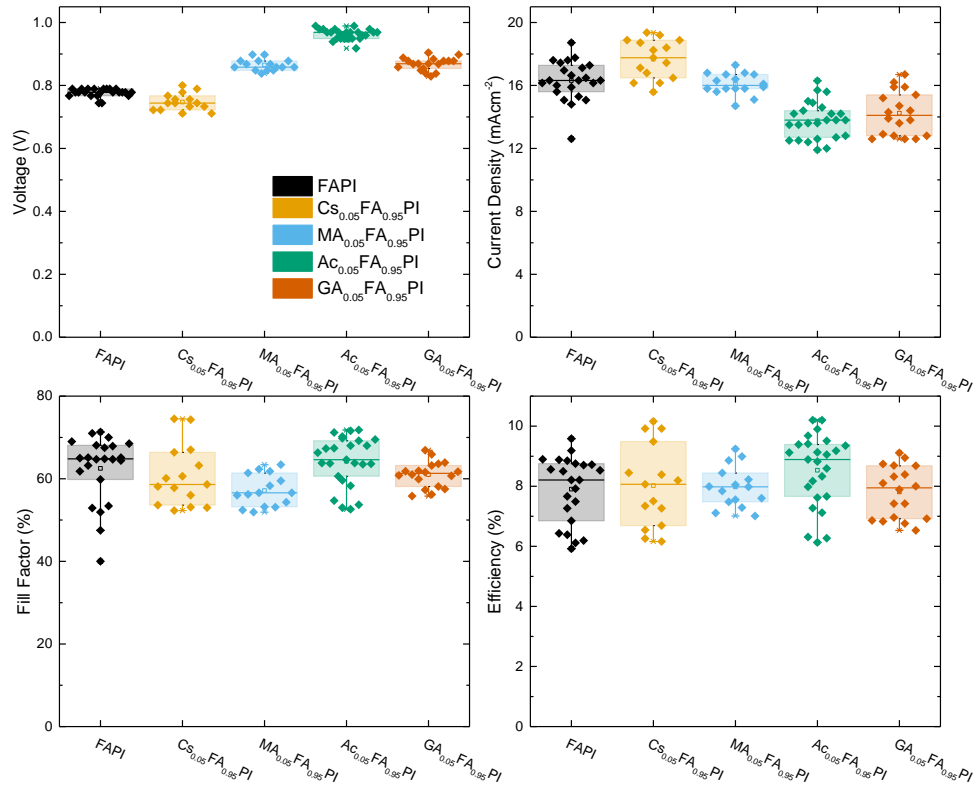

Figure 8.4.2. *Solar cell parameters a) Open-circuit voltage, b) short-circuit current density, c) Fill Factor and d) Efficiency*

As for MAPI, the introduction of larger cations (in this case Ac and GA) reduced the current density but improved the voltage, whereas Cs increased J_{SC} at the expense of some V_{OC}.

The aim of this sub-section was to briefly analyse the impedance of dual-cation perovskites with the cubic FAPI parent structure, in order to understand the behaviour that may occur in the triple-cation perovskite, $Cs_{0.05}(FA_{0.83}MA_{0.17}Pb(I_{0.83}Br_{0.17})_3)$. At 25 °C (Figure 8.4.3) it is evident that in each case at least two RC processes are visible in each mixed-cation perovskite, as there was with FAPI. There is a slight shift in the ω_{max} values for the mid-frequency semi-circle at 25 °C, but all are within a 100-1000 Hz range. It is difficult to draw conclusions from these values at one measurement as there may be small differences in the experiment – this is why the trends over the temperature range will be used.
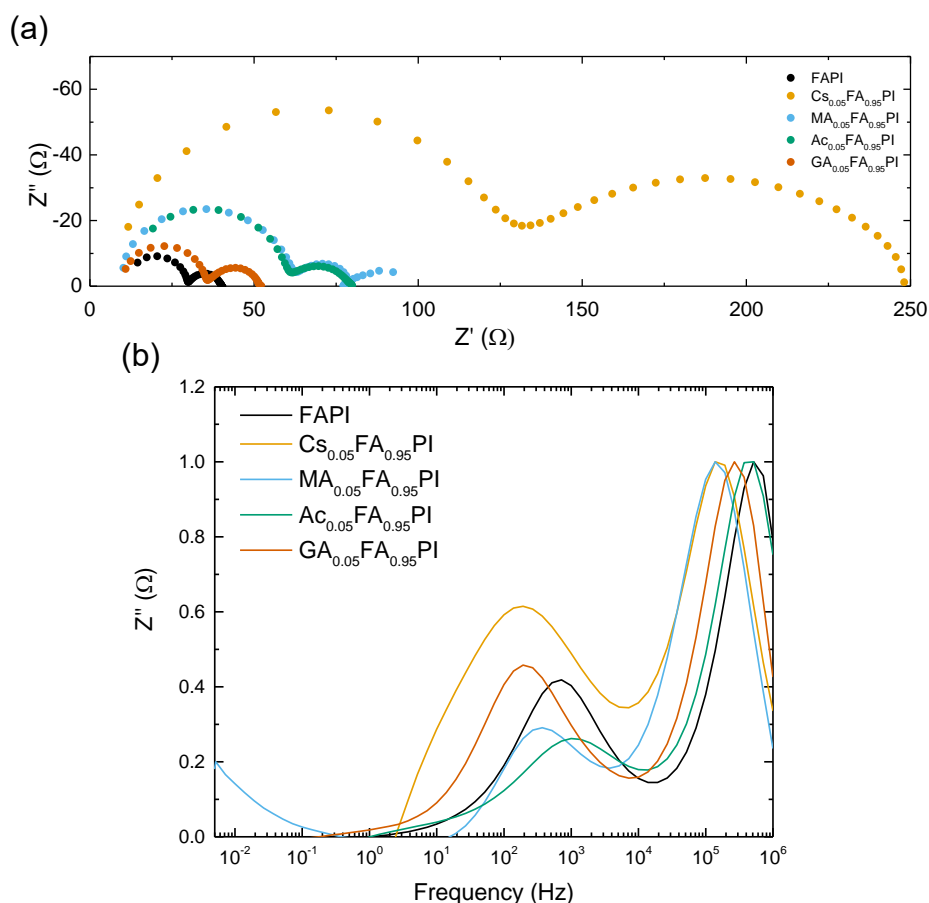
Figure 8.4.3. *Impedance analysis of mixed-cation FAPI perovskites at 25 °C: a) Nyquist plot and b) Cole plot*

The introduction of a low-frequency semicircle is observed in both the perovskites with the addition of smaller cations, yet at very different frequencies, Cs (at around 5-10 Hz) and MA (< 0.1 Hz). With MA the low-frequency semicircle is obvious, however with Cs it appears as a shoulder within the mid-frequency semicircle, making fitting more difficult. As the low-frequency process generally has a higher activation energy than the mid-frequency process, it will be more affected by the change in temperature. Therefore the shoulder apparent at 25 °C in $Cs_{0.05}FA_{0.95}PI$ may become more visible at higher temperatures. Activation energies for the mid-frequency and low-frequency temperature dependent processes were calculated by measuring the impedance over a range of temperatures – these are shown in Figures 8.4.4-8.4.7.
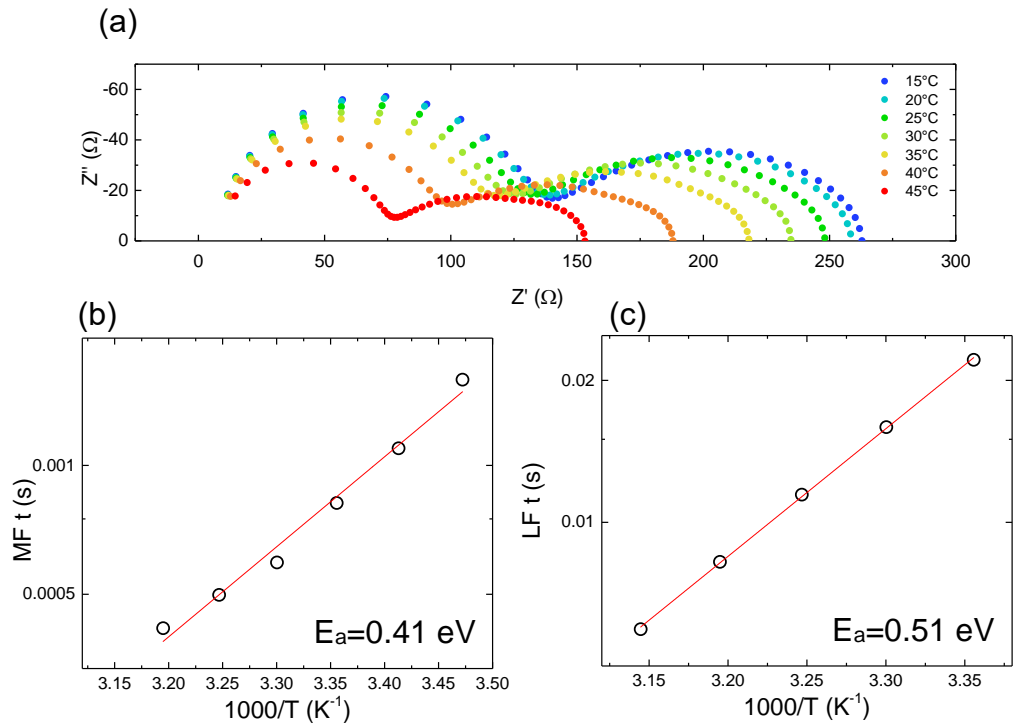
Figure. 8.4.4. *The change in Cs$_{0.05}$FA$_{0.95}$PI impedance with temperature: a) Nyquist plots, b) Arrhenius plot for the mid-frequency feature and c) for the low frequency feature*

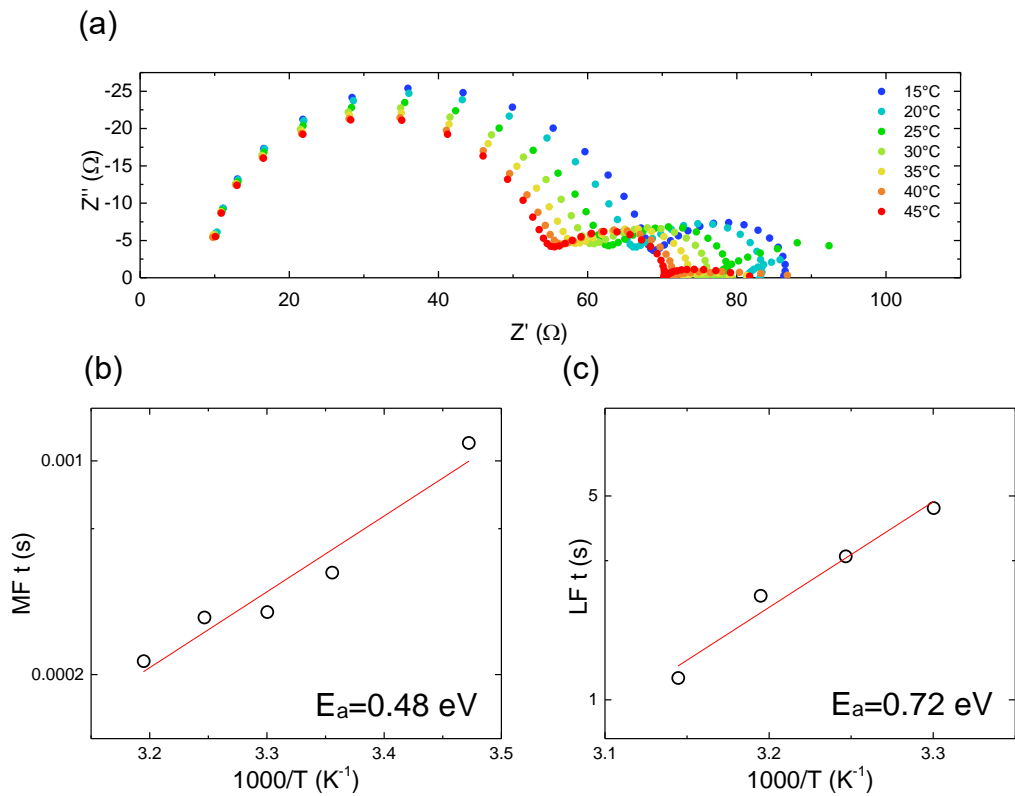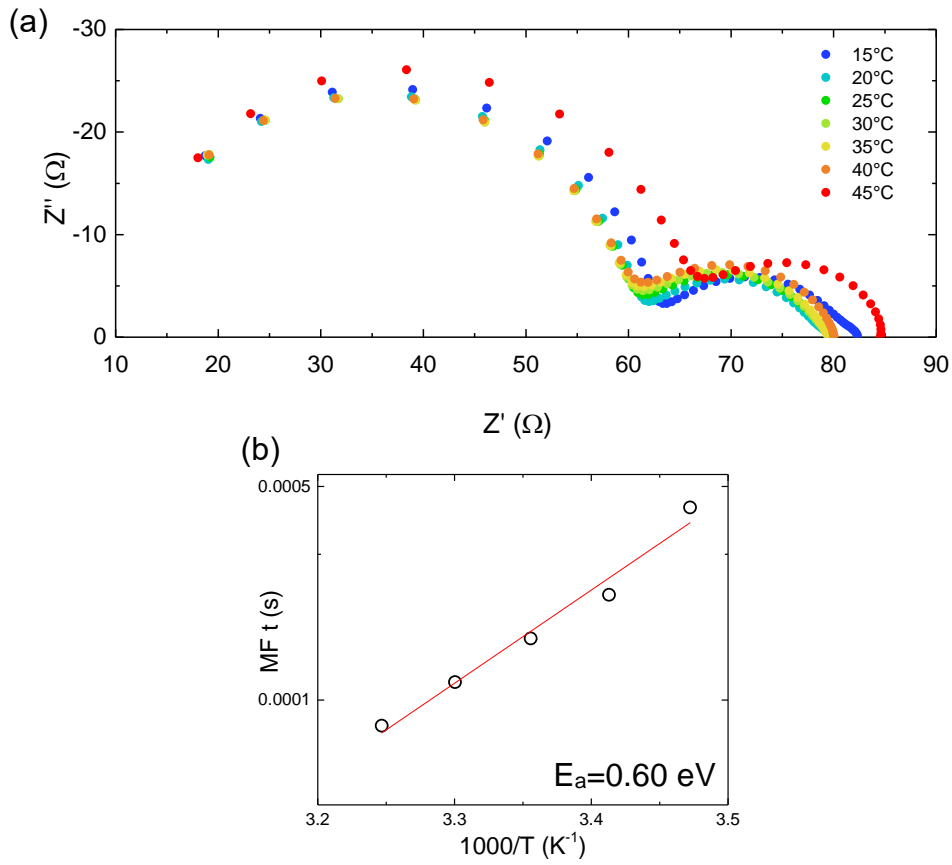***Figure. 8.4.5.*** *The change in MA$_{0.05}$FA$_{0.95}$PI impedance with temperature: a) Nyquist plots, b) Arrhenius plot for the mid-frequency feature and c) for the low frequency feature*

Figure. 8.4.6. *The change in Ac$_{0.05}$FA$_{0.95}$PI impedance with temperature: a) Nyquist plots and b) Arrhenius plot for the mid-frequency feature*
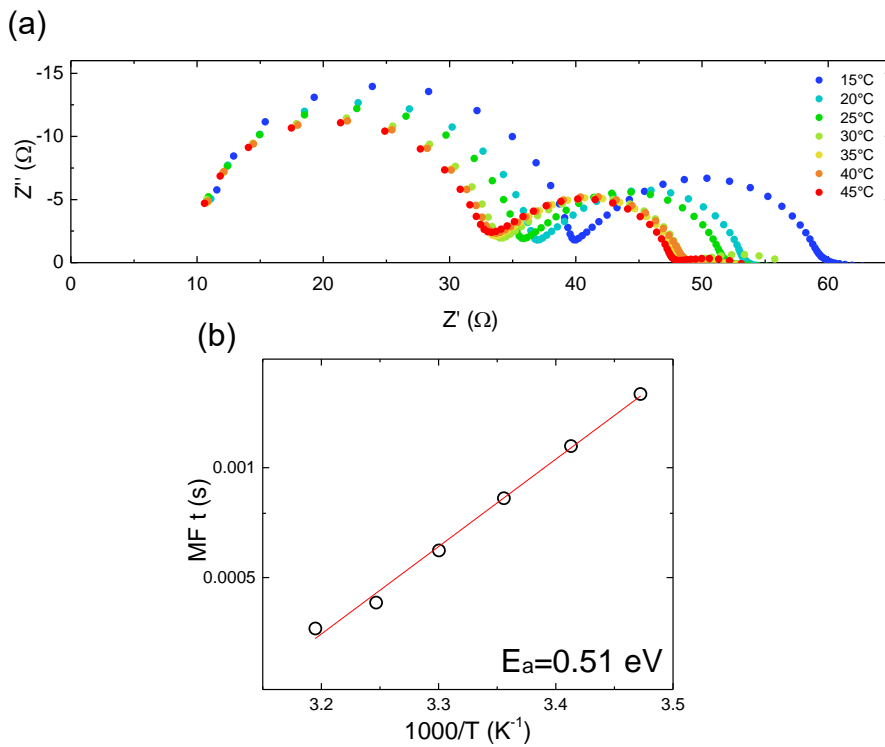

Figure. 8.4.7. *The change in FA$_{0.95}$GA$_{0.05}$PI impedance with temperature: a) Nyquist plots and b) Arrhenius plot for the mid-frequency feature*

196

The activation energies for each perovskite are collated in Table 8.4.1. The values calculated for the low frequency semicircles may demonstrate why this element is not observed in FAPI. The activation energy increases with the additive size from Cs to MA. It could be that as the FAPI lattice is marginally larger than these two that the trend in activation energies continues, the activation energy becoming so large, and the associated process so slow that it is no longer seen on the timescale of the experiment for FAPI, and the perovskites containing Ac and GA.

Table 8.4.1. Activation energies for the mixed-cation perovskites (sorted by the size of the additive)

Perovskite	MF Ea (eV)	LF Ea (eV)
$Cs_{0.05}FA_{0.95}PI$	0.41 ± 0.02	0.51 ± 0.01
$MA_{0.05}FA_{0.95}PI$	0.48 ± 0.07	0.72 ± 0.09
FAPI	**0.37 ± 0.02**	-
$Ac_{0.05}FA_{0.95}PI$	0.60 ± 0.05	**-**
$GA_{0.05}FA_{0.95}PI$	0.51 ± 0.04	**-**

It is difficult to identify a trend in the mid-frequency semi-circle. The value for the activation energy increases with any additive, but there is no trend in relation to cation size.

The results of these experiments have provided an interesting insight into the FAPI perovskite, which is the parent structure for the triple cation/highest efficiency perovskite. In the context of the results of the experiments on MAPI in chapter 7; the local distortions in the perovskite lattice increase the barrier to the low frequency iodide diffusion mode. Mobile iodide ions can change the R_{recomb} value, and the mid-frequency and low-frequency semi-circles in MAPI could be two different iodide diffusion modes with different time constants, e.g. axial-to-equatorial and equatorial-to-equatorial; or bulk iodide diffusion and diffusion along interfaces/grain boundaries. For FAPI, in which only the mid-frequency semi-circle is visible, a distortion in the lattice with the substitution of smaller cations appears to firstly make the low-frequency semi-circle visible, and decreasing the size of the additive from MA to Cs lowers the activation energy required for iodide diffusion.

In the next sections EIS will be measured for the record efficiency perovskite, with a composition of $Cs_{0.05}(FA_{0.83}MA_{0.17}P(I_{0.83}Br_{0.17})_3)$.

8.5) The cationic additives, Methylammonium and Caesium

To start the investigation into the top efficiency $Cs_{0.05}(FA_{0.83}MA_{0.17}Pb(I_{0.83}Br_{0.17})_3)$ cells, the cations were first added separately, before being added together, to the FAPI lattice.

Both $Cs_{0.05}FA_{0.95}PI$ and $FA_{0.83}MA_{0.17}PI$ were synthesised, and originally annealed at 100 °C to determine if either of the cations enabled less energy-intensive fabrication. Thin film XRD shows that although with 17 mol% MA the dominant peak is the cubic FAPI peak, with 5 mol% Cs the δ-FAPI and PbI_2 peaks are the largest. Annealing $Cs_{0.05}FA_{0.95}PI$ at 150 °C removes the impure phases and leaves only cubic FAPI (from this point onward only $Cs_{0.05}FA_{0.95}PI$ annealed at 150 °C will be used).
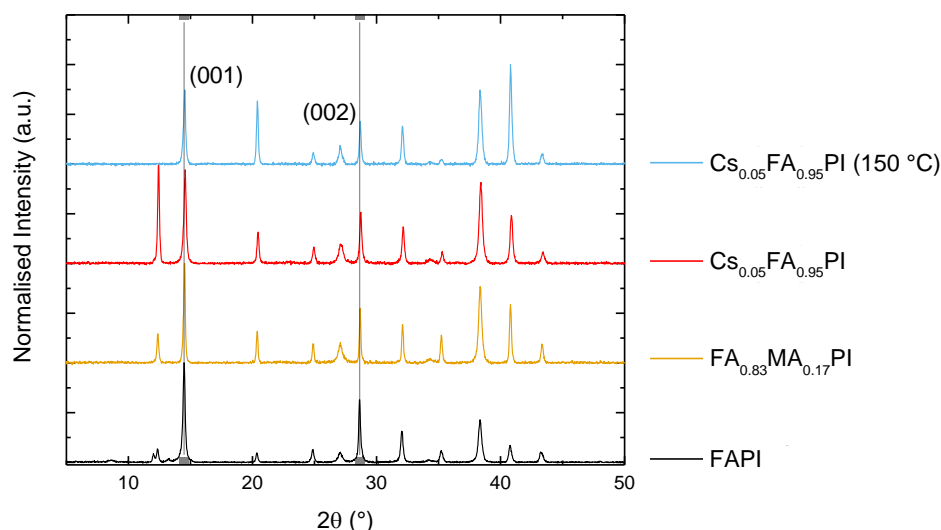

Figure 8.5.1. Thin Film XRD analysis of FAPI with the inclusion of the cationic additives, with lines representing the (001) and (002) peaks in FAPI

There is some distortion of the lattice with the substitution of the Cs and MA cations. The 001 and 002 peaks in every case are shifted to slightly higher 2θ values. Shifting the peak to higher angles suggests a contraction of the unit cell. This is to be expected, as MA and Cs are both smaller than FA, so replacing some of the FA cations with either will lead to local contraction of the lattice – which is sometimes referred to as locking in the structure.[19]
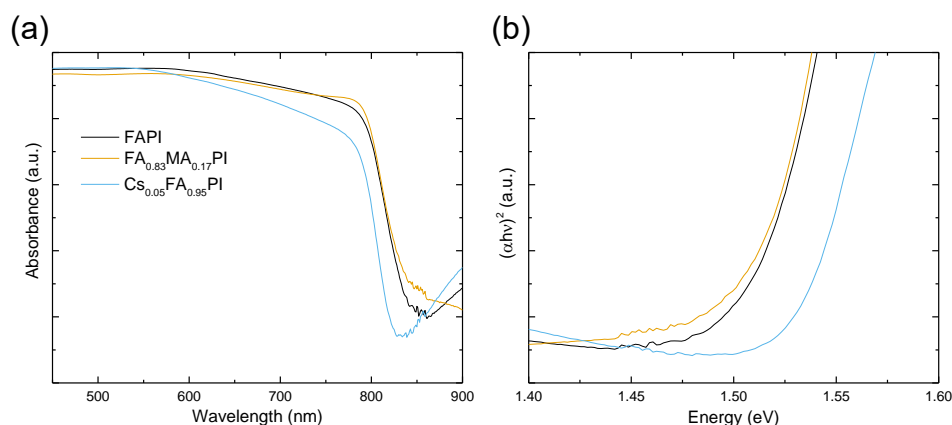
Figure 8.5.2. *a) UV/Vis spectroscopy of FAPI + cationic additives and b) Tauc transformation for band gap determination*

Formamidinium and methylammonium are completely phase miscible, and exhibit a range of band gaps with different ratios of the two cations, however there is no discernible change in the band gap of the material on the addition of 17 mol% MA (Figure 8.5.2), and a small blue shift for the absorption onset of $Cs_{0.05}FA_{0.95}PI$.[28]

17 mol% MA seems to decrease the uniformity of the crystallites in the AFM image, as can be seen in Figure 8.5.3. With the addition of Cs (Figure 8.5.3b), the crystallites become larger with some reaching almost 1 micron in size (compared to 200 nm in pure FAPI). There are still very few pinholes in the film, which should cause a high shunt resistance, and enable good interfacial contact allowing for effective charge extraction.
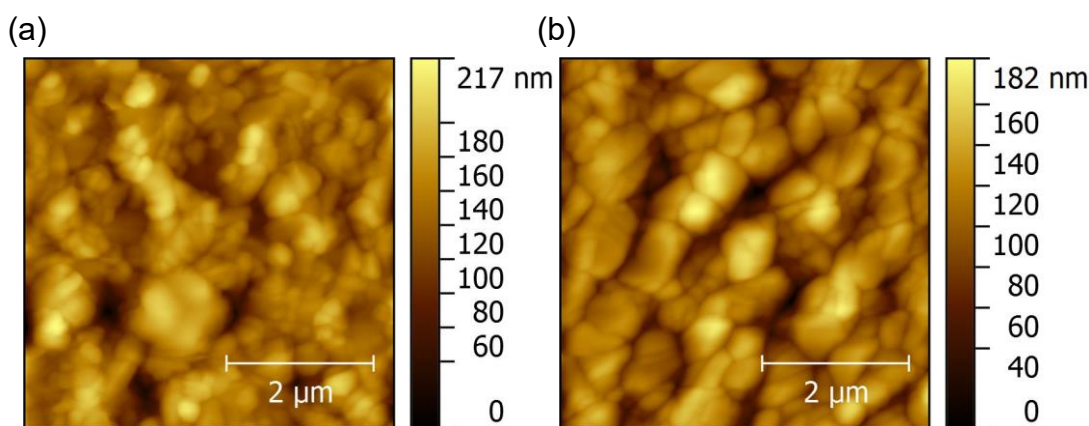
Figure 8.5.3. *AFM image of (a) $FA_{0.83}MA_{0.17}PI$ and (b) $Cs_{0.05}FA_{0.95}PI$ (taken over 5 μm in phase contrast mode)*

Cells made using these solutions showed some interesting trends. In Figure 8.4.4 and the accompanying Table 8.4.1 show that both cations are having distinct effects.
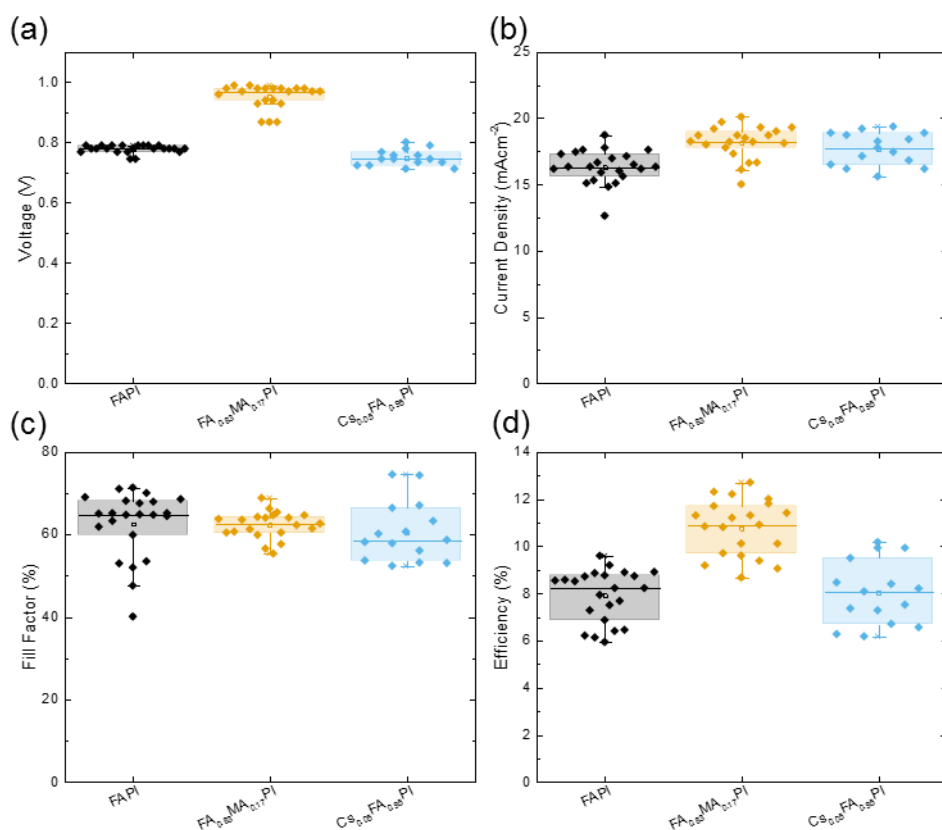
199

Figure 8.5.4. *Solar cell parameters for **FAPI**, **FA$_{0.83}$MA$_{0.17}$PI** and **Cs$_{0.05}$FA$_{0.95}$PI**: a) Open-circuit voltage, b) short-circuit current density, c) Fill Factor and d) Efficiency*

Table 8.5.1. Average Solar cell parameters for **FAPI, FA$_{0.83}$MA$_{0.17}$PI** and **Cs$_{0.05}$FA$_{0.95}$PI** with standard deviation

Perovskite	V_{OC} (V)	J_{SC} (mAcm^{-2})	FF (%)	Efficiency (%)
FAPI	0.78 (±0.013)	16.31 (±1.24)	60.96 (±12.16)	7.90 (±1.08)
FA$_{0.83}$MA$_{0.17}$PI	0.95 (±0.039)	18.15 (±1.22)	62.23 (±3.18)	10.76 (±1.15)
Cs$_{0.05}$FA$_{0.95}$PI	0.75 (±0.026)	17.68 (±1.20)	59.59 (±6.16)	8.02 (±1.32)

Although there is an efficiency improvement with each cation, it is the cause of this that may be significant. For MA, it is largely due to a 170 mV average increase in the open-circuit voltage. For Cs, a 1.4 mAcm^{-2} improvement in short-circuit current density. V_{OC} is usually determined by band-gap, however there was no apparent change of this in the UV/Vis spectroscopy of FA$_{0.83}$MA$_{0.17}$PI, so the improvement is likely to be caused by improved band edge alignment with the contact layers. The improvement of short-circuit current density in Cs$_{0.05}$FA$_{0.95}$PI could be attributed to the improvement in crystallinity (Figure 8.4.3b) facilitating effective charge extraction.

The next stage was to investigate for any synergistic effects of the two cations, by creating a triple cation perovskite (without bromide), $Cs_{0.05}(FA_{0.83}MA_{0.17}PI)$. Analysis of this material is shown in Figure 8.5.5. X-ray Diffractometry (Figure 8.5.5a) shows that the triple cation perovskite has only one peak within the range of 10-15 °, suggesting that it is purely the cubic FAPI phase with no δ-phase or PbI_2 impurities, even when annealed at 100 °C. There is now a greater shift in the 001 and 002 peaks – as two cations are added the distortion becomes even greater. Nevertheless it is still not a large distortion, and the optical properties remain very similar (Figures 8.5.5 b and c).
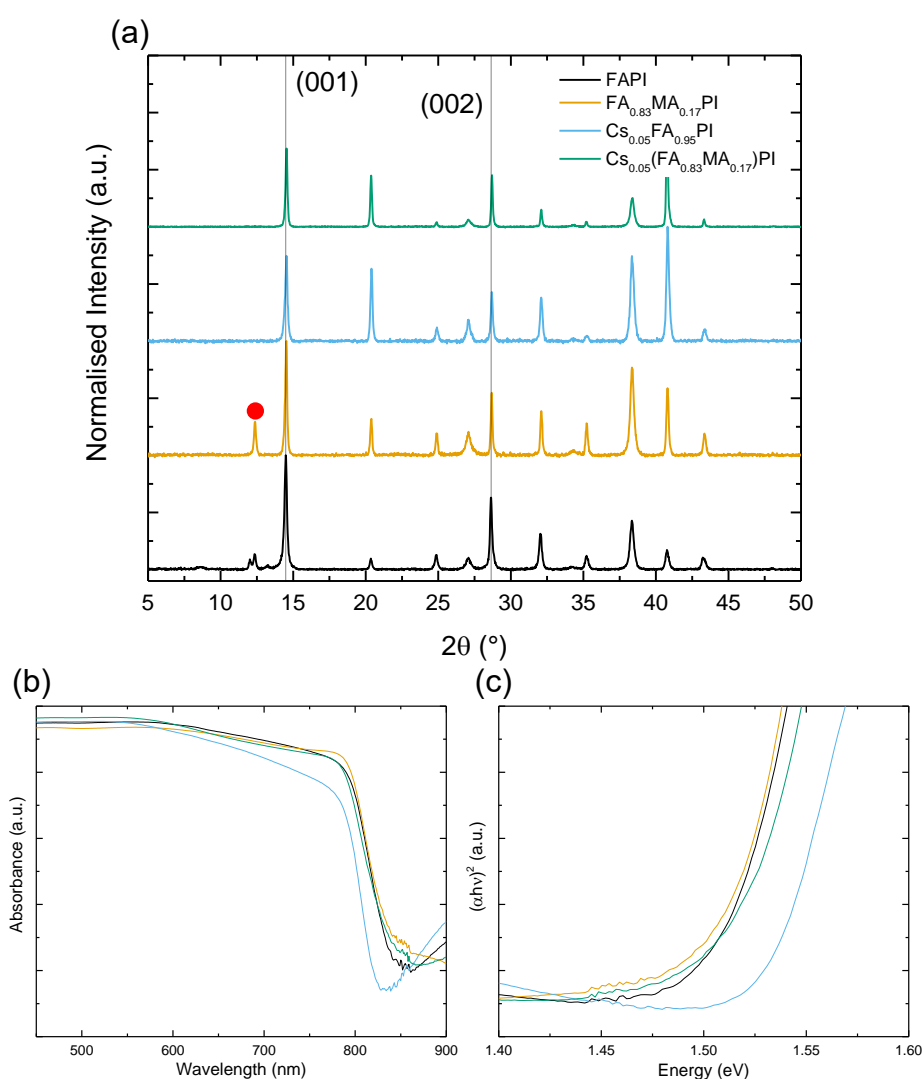

Figure 8.5.5. *Triple cation film: a) Thin film XRD with lines representing the 001 and 002 cubic FAPI peaks and a red mark showing the position of the characteristic δ-FAPI peak, b) UV/Vis Spectroscopy and c) Tauc plot*

When both cations are included the overall performance of the cells does not change greatly. There is a V_{OC} enhancement compared to FAPI, but a reduction in the Fill

Factor means that this does not benefit the efficiency of the $Cs_{0.05}(FA_{0.83}MA_{0.17}PI)$ cells, which have an average efficiency of 8.54 ± 0.88 %, compared to 7.9 % in pure FAPI.
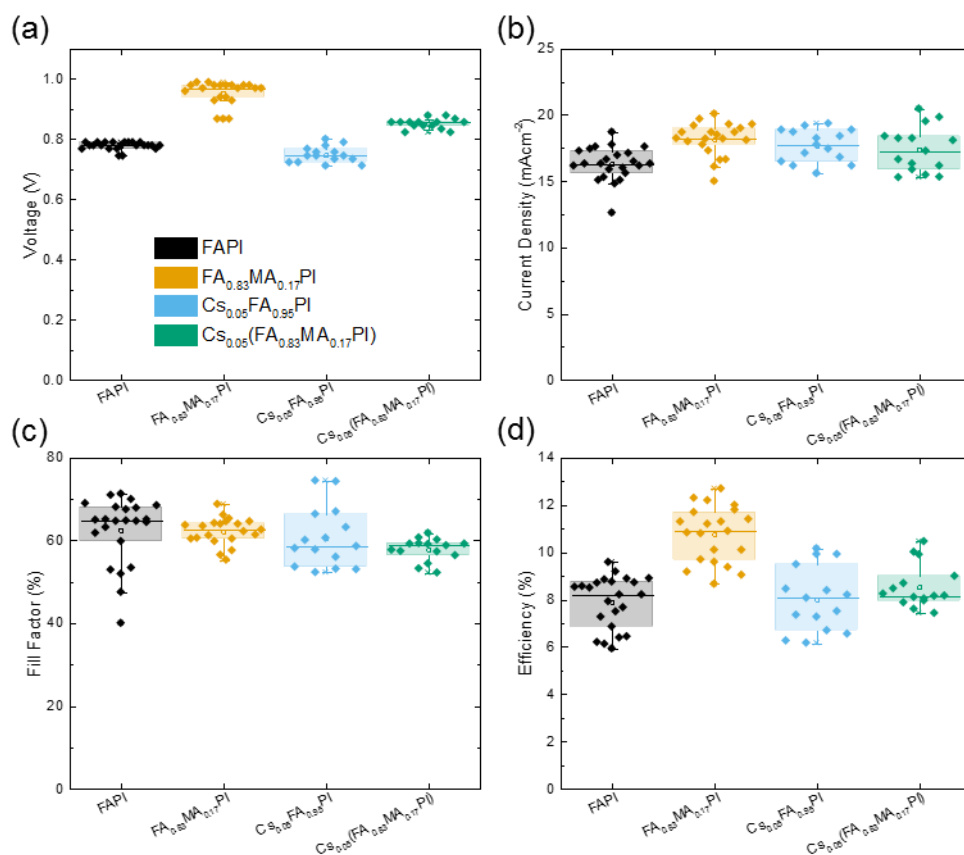

Figure 8.5.6. *Solar cell parameters for **FAPI, FA$_{0.83}$MA$_{0.17}$PI, Cs$_{0.05}$FA$_{0.95}$PI** and **Cs$_{0.05}$(FA$_{0.83}$MA$_{0.17}$PI)**: a) Open-circuit voltage, b) short-circuit current density, c) Fill Factor and d) Efficiency*

The crystallinity of this film seems to be more like that of the 17 mol% MA sample, as it is fairly non-uniform, and does not possess the same large crystallite sizes as the 5 mol% Cs sample does – suggesting that the greater proportion of MA to Cs in the perovskite is determining the surface morphology in this case.
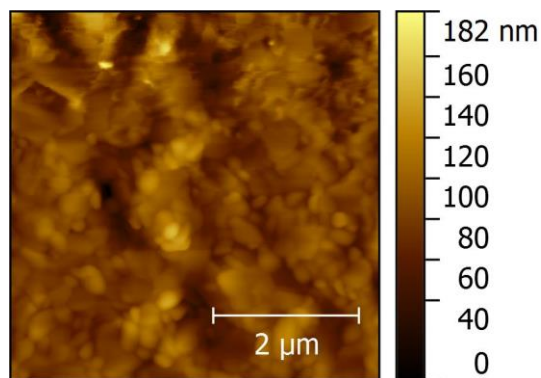
Figure 8.5.7. *AFM image of Cs$_{0.05}$(FA$_{0.83}$MA$_{0.17}$PI) (taken over 5 µm in phase contrast mode)*

EIS was performed on a cell made using each perovskite film to primarily assess for any effect on ion diffusion the cation inclusion may have had. In the previous section it was established that lattice distortions caused by adding in a smaller cation allowed for the observation of the low frequency semicircle that has been attributed to iodide diffusion. In this case all the cations added have reduced the size, therefore it should be the case that it is observable in all the following mixtures. The sample with 5 mol% Cs has been discussed in section 8.4 (Figure 8.4.4), and as such the temperature dependent Nyquist plots and Arrhenius plots will not be displayed again.

A comparison of the Nyquist plots at 25 °C is displayed in Figure 8.5.8. It appears that the inclusion of MA at ratios above 5 mol% also does not increase R$_{ct}$ by a large amount, with a value of less than 40 Ω (values for all cells are shown in Table 8.5.2). With the Cs$_{0.05}$(FA$_{0.83}$MA$_{0.17}$PI) perovskite the R$_{ct}$ is reduced with respect to FAPI, perhaps as V$_{OC}$ of the measured cell was greater (a higher V$_{OC}$ means that R$_{recomb}$ is lower).
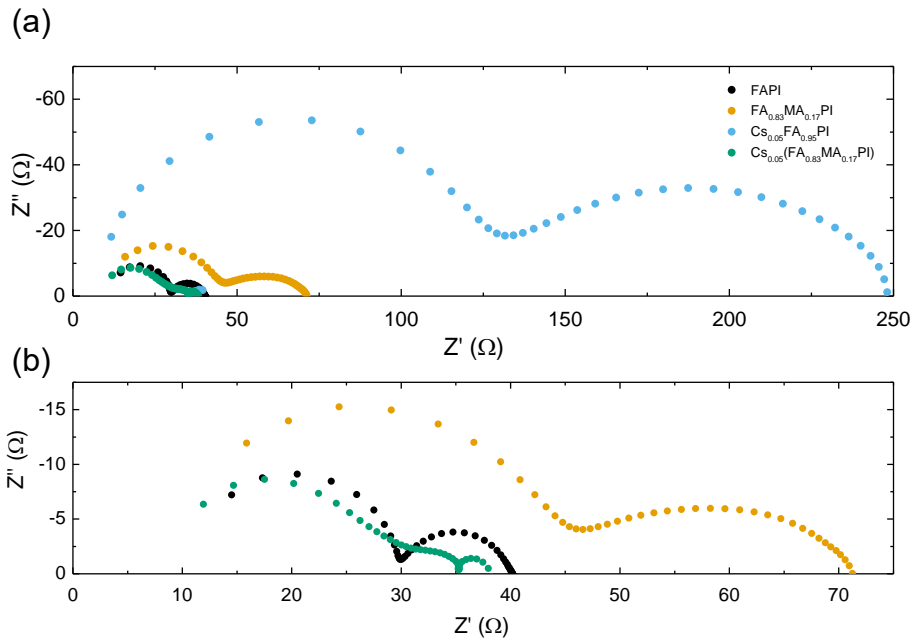
Figure 8.5.8. *a) Nyquist plots for each of the perovskite mixtures at 25 °C and b) zoomed in image of FAPI, FA$_{0.83}$MA$_{0.17}$PI, and Cs$_{0.05}$(FA$_{0.83}$MA$_{0.17}$PI)*

It is also in the Cs$_{0.05}$(FA$_{0.83}$MA$_{0.17}$PI) perovskite that the three semicircles are most distinct; in the samples with MA and Cs separately the low frequency response appears as shoulders in the mid-frequency semicircle. When the data is displayed in the form of a Cole plot (Figure 8.5.9) these features become clearer.

Figure 8.5.9. *Cole plots for each of the perovskite mixtures at 25 °C*

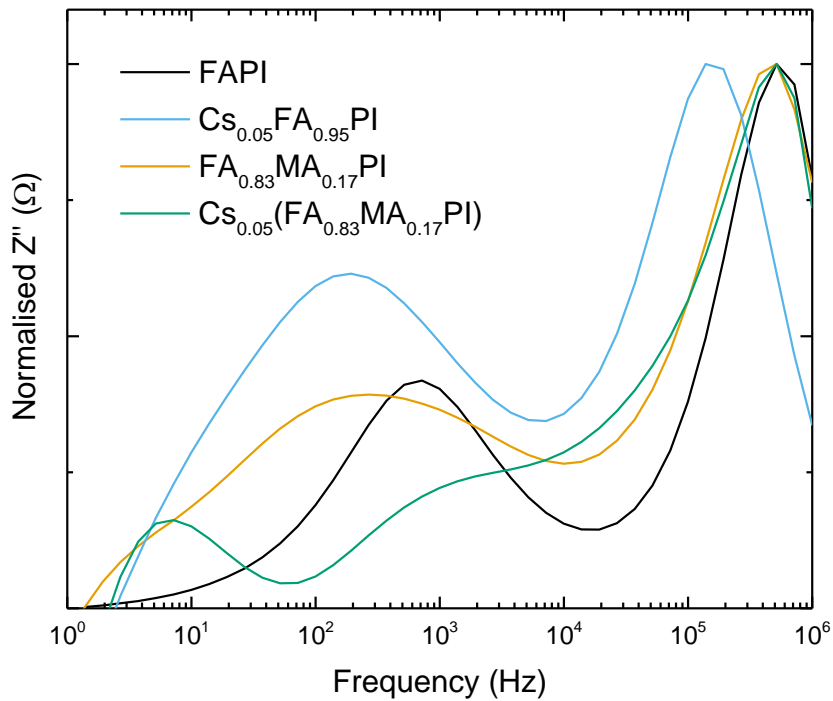The 17 mol% MA sample provides a typical response when measured over a range of temperatures, the Nyquist and Arrhenius plots are shown in Figure 8.5.10. The low frequency semicircle is distinct at higher temperatures, and gradually drops in intensity and visibility. The calculated activation energies are 0.37 eV for the mid-frequency process and 0.53 for the low-frequency process. It has been consistent throughout the cation substitution experiments that the mid-frequency element shows very little trend for changes in the cations, and these results conform to this observation. The low frequency result is very interesting – with an increased amount of MA the activation energy drops from 0.72 with 5 mol% to 0.53 with 17 mol% MA. As the activation energy calculated for MAPI in the previous chapter was 0.4 eV, it could be the case that there is a linear relationship between MA:FA ratio and activation energy.

Figure 8.5.10. The change in $FA_{0.83}MA_{0.17}PI$ impedance with temperature: a) Nyquist plots, b) Arrhenius plot for the mid-frequency feature and c) for the low frequency feature.

The appearance of the $Cs_{0.05}(FAs_{0.83}MA_{0.17}PI)$ response (Figure 8.5.11) is quite different. The low frequency semicircle is easily identifiable at all temperatures, and it is the mid-frequency process that blends in, this time with the high-frequency semicircle (recombination resistance and geometric capacitance). In this case the activation energy for the mid-frequency process is 0.53 eV. If the mid-frequency

element of the spectrum is related to ion diffusion at the interfaces/grain boundaries, it may be random from cell to cell based on synthesis conditions, explaining why there has been no obvious trend in the data up to this point. The value obtained from the low-frequency semi-circle is 0.21 eV. This follows the trend that as smaller cations are added to FAPI, or as the proportion of these smaller cations is increased, that the activation energy for the low-frequency process is decreasing. The results for low amounts of cation substitution in FAPI seem to be complementary to the trends seen with MAPI, where the additions of larger cations increased the activation energy.
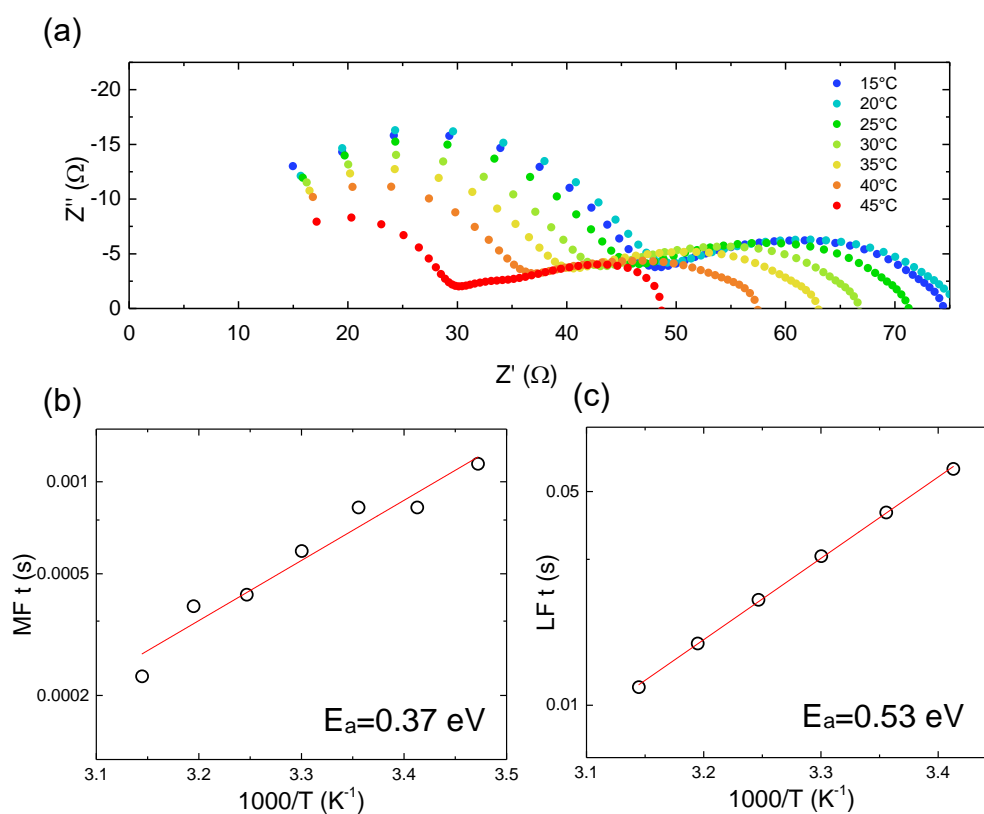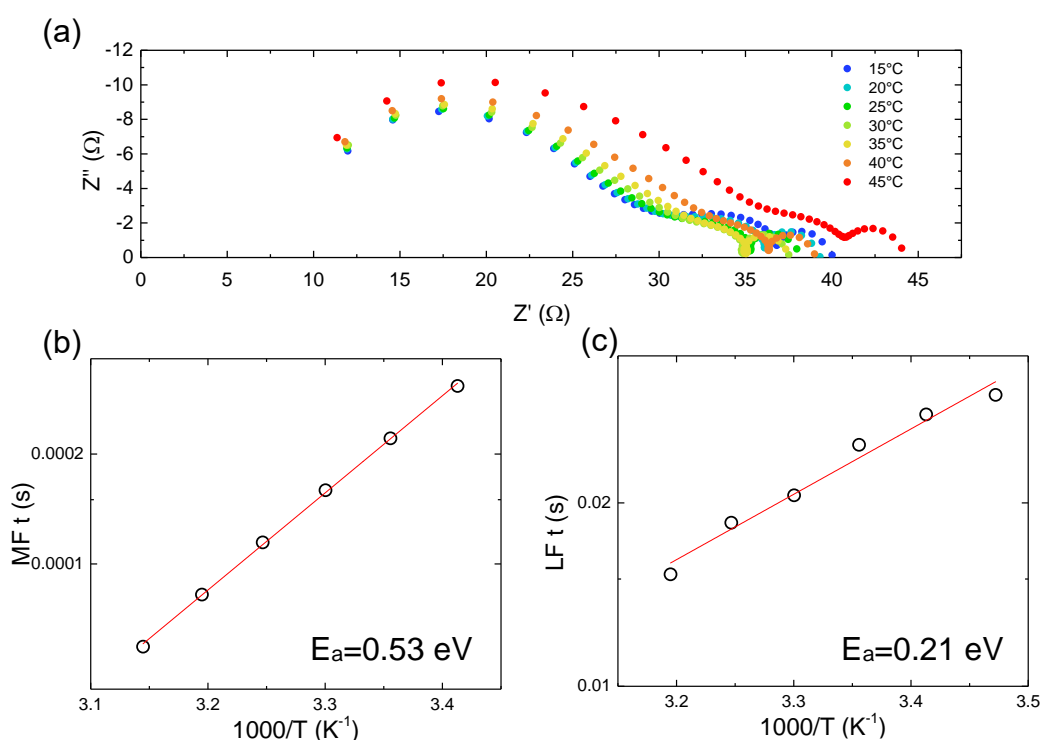

Figure 8.5.11. *The change in $Cs_{0.05}(FA_{0.83}MA_{0.17}PI)$ impedance with temperature: a) Nyquist plots, b) Arrhenius plot for the mid-frequency feature and c) for the low frequency feature.*

Table 8.5.2. Parameters calculated by EIS

Perovskite	R_{ct} at 25 °C (Ω)	C_{dl} at 25 °C (nF)	MF Ea (eV)	LF Ea (eV)
FAPI	38.0	9.4	0.37 ± 0.02	-
$Cs_{0.05}FA_{0.95}PI$	108.3	5.3	0.41 ± 0.02	0.51 ± 0.01
$FA_{0.83}MA_{0.17}PI$	18.75	22.8	0.37 ± 0.03	0.53 ± 0.01
$Cs_{0.05}(FA_{0.83}MA_{0.17}PI)$	17.70	18.0	0.53 ± 0.01	0.21 ± 0.02

To summarise this subsection the effect of each cation on different aspects of the FAPI based PSC is shown below in table 8.5.3. The main impacts of the cations seem to be in the crystallinity – and the facilitation of annealing at lower temperatures than FAPI is an advantageous characteristic. The effect on the perovskite structure translates into the impedance spectra, as in the low frequency semi-circle the activation energy for iodide diffusion is decreased as the proportion of MA and Cs (two cations smaller than FA) is increased in the perovskite film.

Table 8.5.3. The effect of cation addition on Formamidinium Lead Iodide

Additive	Ratio	XRD	UV/Vis	AFM	Cells	Impedance
MA	0.17	Promotes crystallisation at lower temperatures	Very little change (≤ 0.01 eV)	Non-uniform, reduced surface roughness	Increased V_{OC} and J_{SC}	Low-frequency semicircle visible, activation energy 0.53 eV
Cs	0.05	Some shift to larger 2θ values. Although some black phase is formed at 100 °C, the δ-FAPI phase is not removed until 150 °C – but then it is completely removed.	Change of 0.03 eV.	Improved coverage/uniformity, larger crystallites.	Increased J_{SC}	Low-frequency semicircle visible, activation energy 0.51 eV
Cs + MA	0.05 + 0.17	The δ-FAPI phase is completely removed, even at 100 °C	Very little change (≤ 0.01 eV)	Tended towards the MA sample traits	Increased V_{OC} and J_{SC}	Low-frequency semicircle visible, activation energy 0.21 eV

8.6) The addition of Bromide

So far in this chapter (and thesis as a whole) only substitution on the A-site has been investigated. X-site substitution is another very important factor in perovskite solar cells, and is used to tune band gaps and improve stability.[29,30] In the record efficiency triple-cation perovskite, bromide ions are included at a molar proportion of 17 %.[31] Bromide ions have an ionic radius of 186 pm, and will be replacing iodide ions, which have an ionic radius of 206 pm, on the inorganic backbone. In this section the impact of X-site substitution on the frequency dependent response of perovskite solar cells will be explored.

Adding 17 % bromide to pure FAPI has a significant effect on the structure. Although the cubic FAPI peaks are still present in the X-ray diffractogram, they are now dwarfed by a PbI_2 peak at 12.5 ° (Figure 8.6.1.). There are a few peaks in the 12-15 ° range, suggesting that there is phase separation in this perovskite.

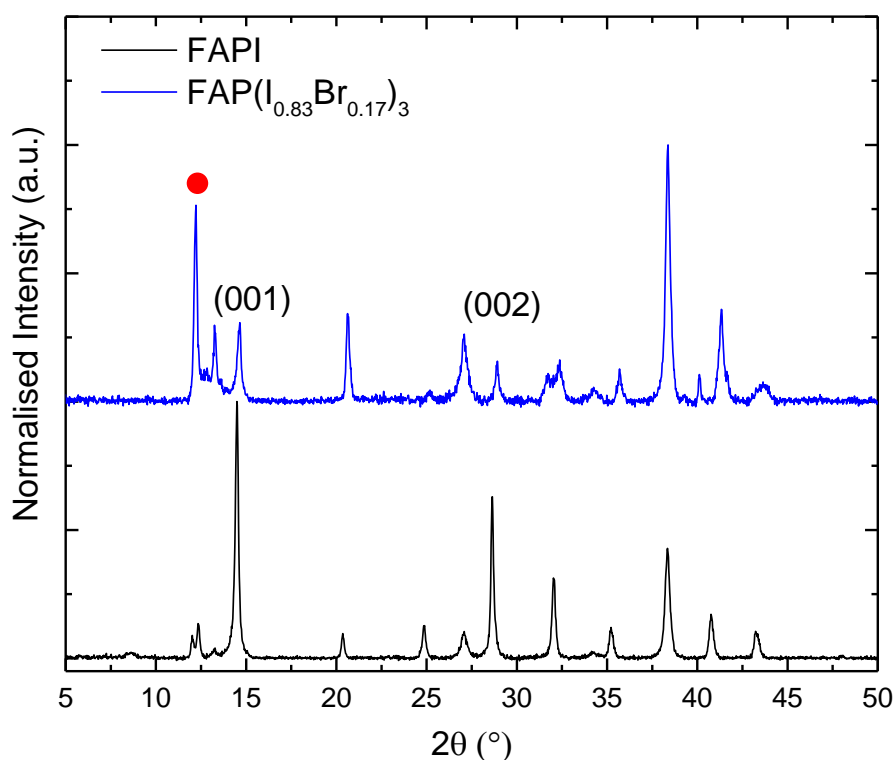***Figure 8.6.1.*** *Thin Film X-ray Diffractogram of FAPI and FAPI$_{0.83}$Br$_{0.17}$, with the (001) and (002) peaks labelled, and the δ-phase peak/PbI$_2$ peak marked with a red circle – the response was normalised to the FTO substrate*

Phase separation is also evident in the optical spectroscopy performed on FAPI$_{0.83}$Br$_{0.17}$, shown in Figure 8.6.2a as multiple onset in the absorbance.

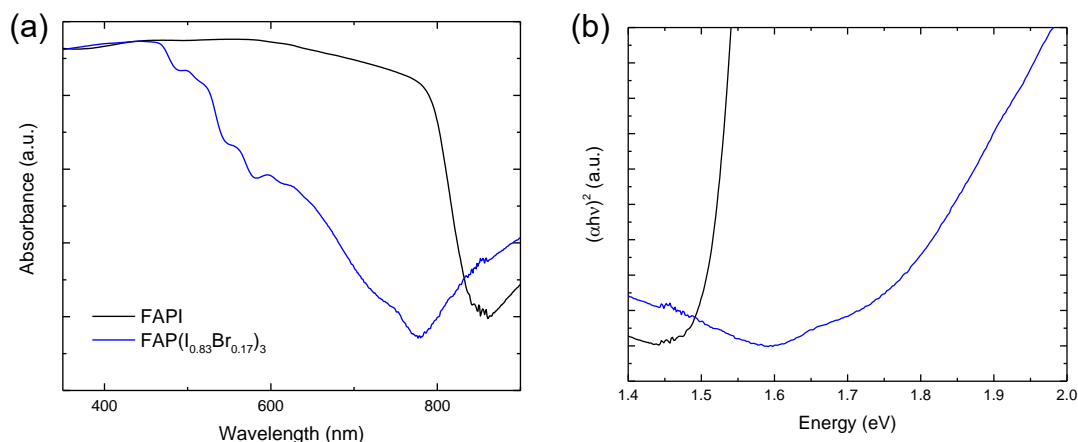***Figure 8.6.2.*** *a) UV/Vis spectroscopy of FAPI and FAPI$_{0.83}$Br$_{0.17}$ and b) Tauc plot*

The film itself is an orange-brown colour (even when annealed at 150 °C), however there is no clear single band gap in either of the graphs produced from UV/Vis spectroscopy. Even the lowest energy onset (at around 780 nm) is significantly blue-shifted from that of FAPI. As such the cells fabricated using FAPI$_{0.83}$Br$_{0.17}$ show a higher V$_{OC}$ (Figure 8.6.3a) and a lower J$_{SC}$ (Figure 8.6.3b) than the pure iodide analogue, as is to be expected for a wider band gap material. The resulting cells had an efficiency of 5.04 ± 0.52 %, which considering the champion cell of the similarly coloured Azetidinium Lead Iodide (AzPI) was only 1.10 % is quite high. An efficiency difference of almost 4 % demonstrates how important the cubic perovskite structure is for charge transfer throughout the material, as the J$_{SC}$ for these cells is much higher than those for the non-3D perovskite AzPI.
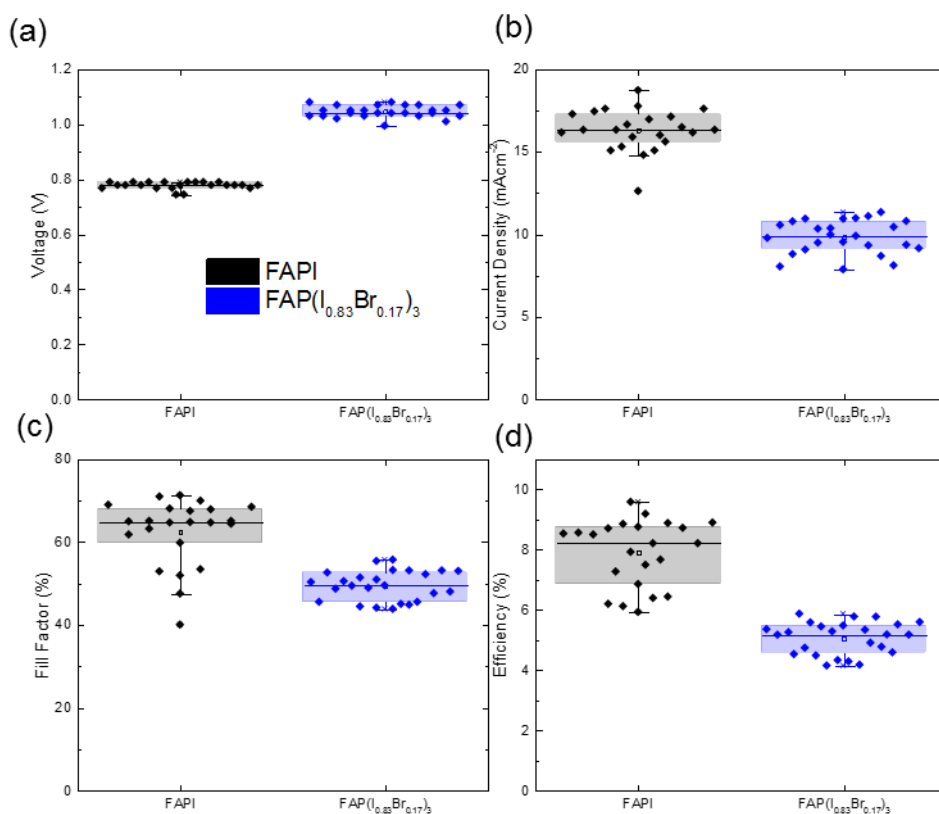
Figure 8.6.3. *Solar cell parameters for **FAPI** and **FAP(I$_{0.83}$Br$_{0.17}$)$_3$**: a) Open-circuit voltage, b) short-circuit current density, c) Fill Factor and d) Efficiency*

To see if there were also any changes in surface morphology, an AFM image was taken of the bromide film (Figure 8.6.4). Bromide addition to FAPI increases the overall crystallite size and uniformity of the perovskite film.
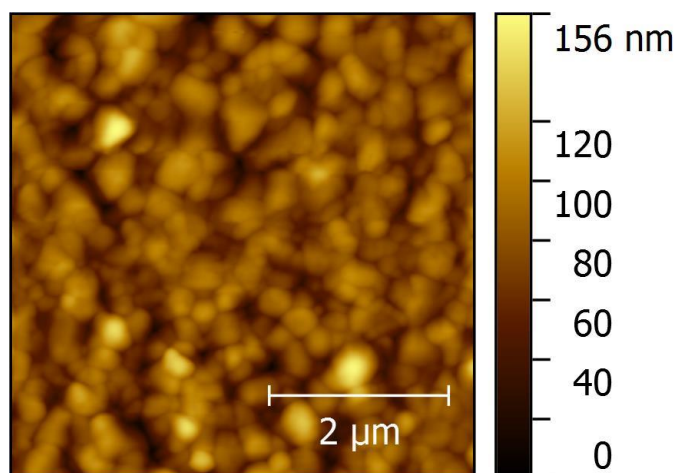

Figure 8.6.4. *AFM image of a FAP(I$_{0.83}$Br$_{0.17}$)$_3$ thin film (taken over 5 μm in phase contrast mode)*

The transformation of $FA_{0.83}MA_{0.17}PI$ to $FA_{0.83}MA_{0.17}P(I_{0.83}Br_{0.17})_3$ yields another significant change in the perovskite, however less severe than for the non-MA containing perovskite. Although there is still a δ-FAPI peak at 13 ° in the XRD spectrum shown in Figure 8.6.5 of the dual-cation dual-anion perovskite, the 001 peak of α-FAPI is now much stronger than that of $FAPI_{0.83}Br_{0.17}$. This could be as distortions to the lattice caused by substitution of a smaller cation at the A-site facilitates the formation of a bromide containing phase of FAPI.
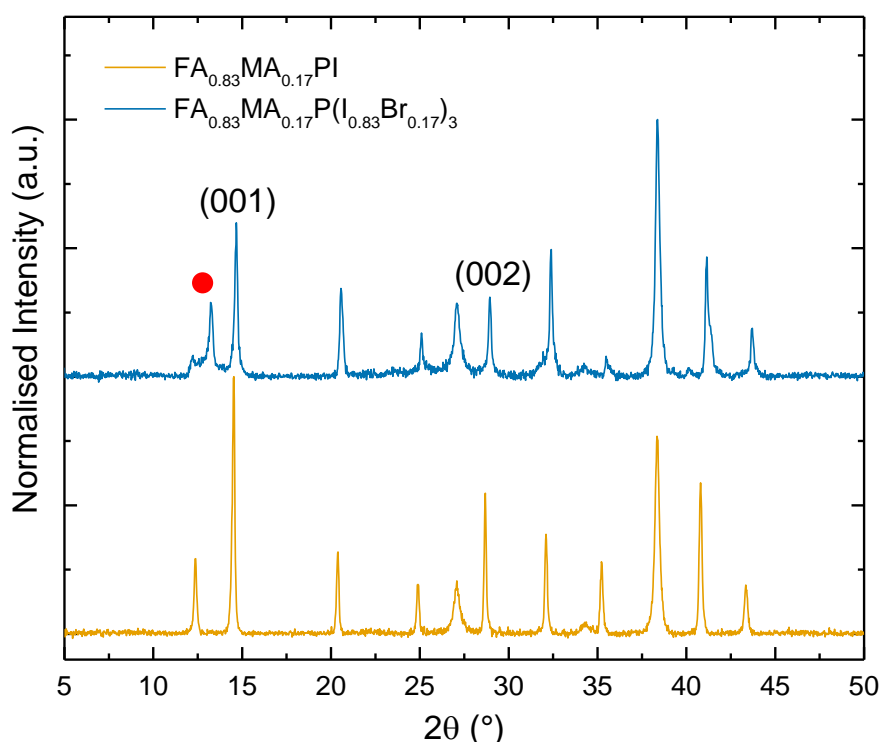
Figure 8.6.5. *Thin Film X-ray Diffractogram of $FA_{0.83}MA_{0.17}PI$ and $FA_{0.83}MA_{0.17}PI_{0.83}Br_{0.17}$, with the (001) and (002) peaks labelled, and the δ-phase peak/PbI_2 peak marked with a red circle – the response was normalised to the FTO substrate*

In the case of the UV/Vis spectroscopy, shown in Figure 8.6.6, there is a blue shift of the band gap, with a greater deviation from FAPI than with any of the other cations (either individually or together). The blue shift is a demonstration of the band-gap engineering effect that can be used by controlling the halide composition to choose the optical band-gap (and colour).[29]
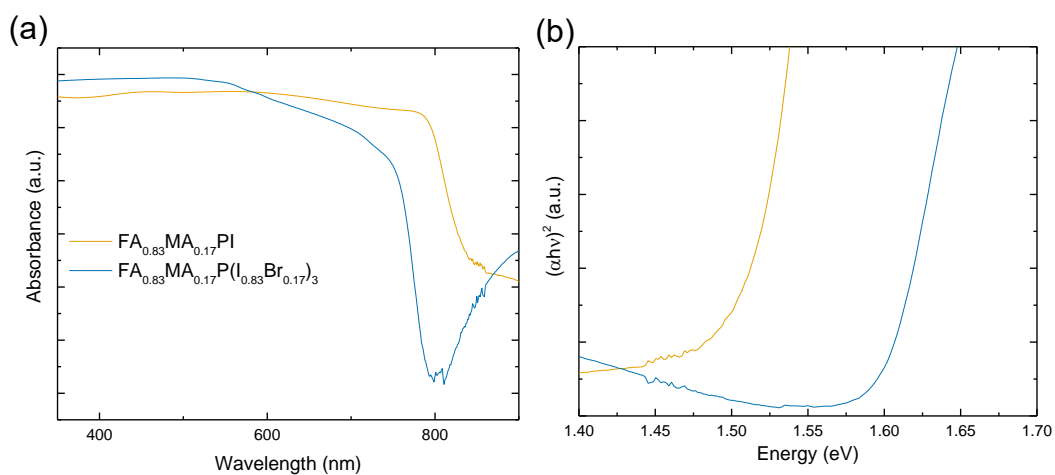
Figure 8.6.6. *a) UV/Vis spectroscopy of FA$_{0.83}$MA$_{0.17}$PI and FA$_{0.83}$MA$_{0.17}$PI$_{0.83}$Br$_{0.17}$ and b) Tauc plot*

The result for the cell performance (Figure 8.6.7) is a small (0.05 V) change in the average voltage of the cell to over 1.0 V. There is also a much higher J$_{SC}$ in FA$_{0.83}$MA$_{0.17}$PI$_{0.83}$Br$_{0.17}$ (16 mAcm^{-2}) in the material as compared to FAPI$_{0.83}$Br$_{0.17}$ (10 mAcm^{-2}). This is due to two reasons: the band gap is not blue shifted to the same extent, so a large proportion of the visible spectrum is still being absorbed, and there is a lower degree of phase separation in the perovskite. Despite these improvements the Fill Factor of FA$_{0.83}$MA$_{0.17}$PI$_{0.83}$Br$_{0.17}$ is around 10 % lower than that of FA$_{0.83}$MA$_{0.17}$PI, resulting in a lower average efficiency.
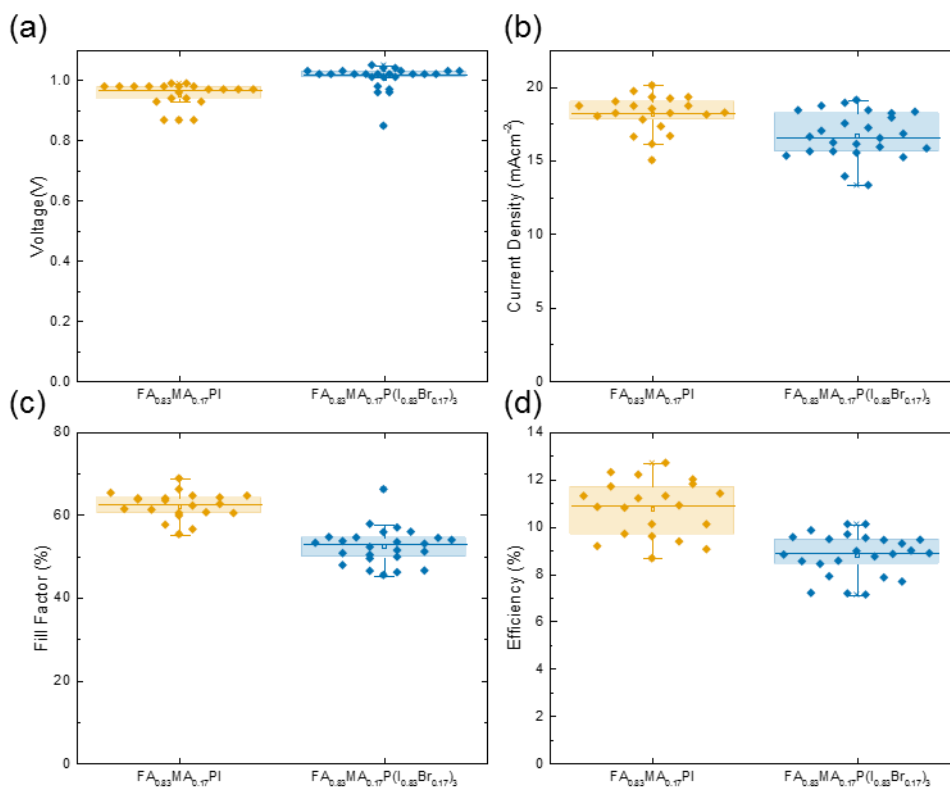
Figure 8.6.7. *Solar cell parameters for **FA$_{0.83}$MA$_{0.17}$PI** and **FA$_{0.83}$MA$_{0.17}$PI$_{0.83}$Br$_{0.17}$**: a) Open-circuit voltage, b) short-circuit current density, c) Fill Factor and d) Efficiency*
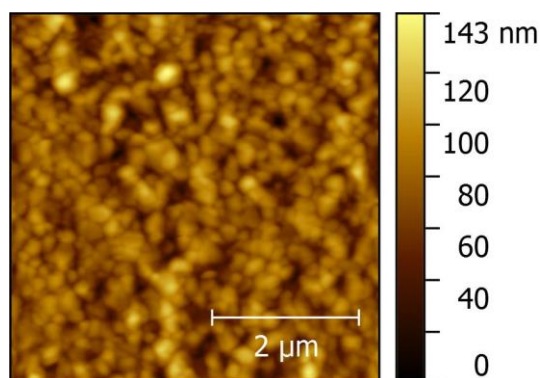
Figure 8.6.8. *AFM image of a FA$_{0.83}$MA$_{0.17}$P(I$_{0.83}$Br$_{0.17}$)$_3$ thin film (taken over 5 μm in phase contrast mode)*

The surface morphology of the double cation/double anion perovskite is shown in Figure 8.6.8. The surface coverage and uniformity of the perovskite is greatly improved, and as with the other bromide perovskite the crystallite size is much smaller than the iodide analogue.

The final perovskite that will be examined in this chapter is Cs$_{0.05}$(FA$_{0.83}$MA$_{0.17}$Pb(I$_{0.83}$Br$_{0.17}$)$_3$), the triple-cation perovskite that allows for the

production of PSC with efficiencies over 23%.[9] It will be assessed as a development from FAPI, $Cs_{0.05}(FA_{0.83}MA_{0.17}PI)$ and $FA_{0.83}MA_{0.17}Pb(I_{0.83}Br_{0.17})_3$ to try to better understand the changes as more components are substituted in.
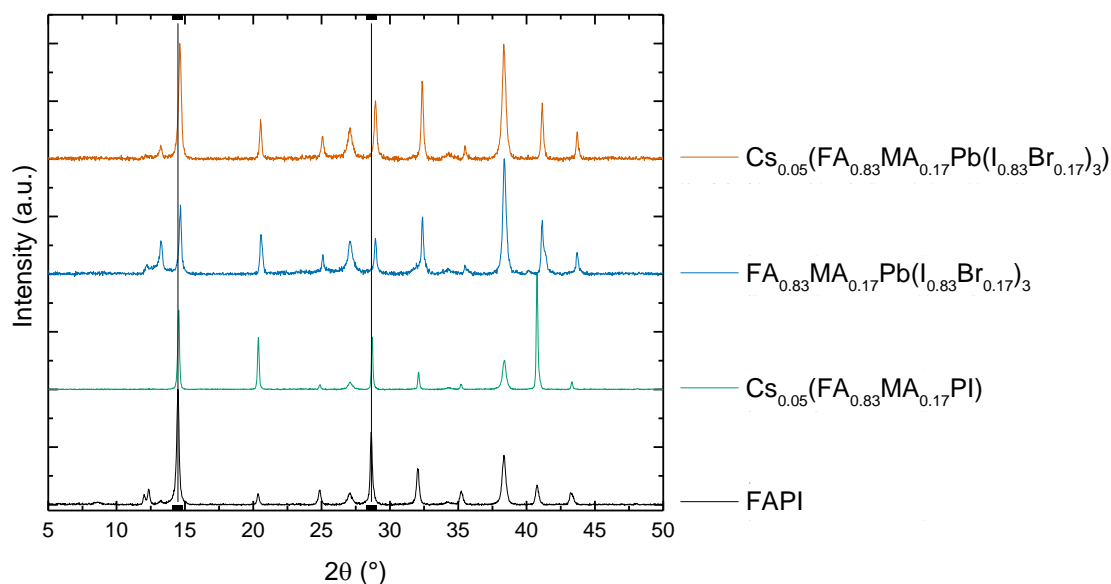
Figure 8.6.9. *Thin Film X-ray Diffractogram for the triple cation based perovskites, with the (001) and (002) peaks labelled– the response was normalised to the FTO substrate*

As with the previous examples in this subsection, the addition of bromide leads to the biggest change in the structure, as can be seen in the XRD from Figure 8.6.9. The diffractogram for the triple cation/double anion perovskite is shifted with respect to FAPI, showing an almost identical pattern to $FA_{0.83}MA_{0.17}Pb(I_{0.83}Br_{0.17})_3$. From this data it seems apparent that whilst the A-site additives promote formation of the cubic phase, bromide substitution on the X-site allows for the formation of impurities. In $FA_{0.83}MA_{0.17}Pb(I_{0.83}Br_{0.17})_3$, there are multiple peaks in the 12-13 ° region suggesting that both δ-FAPI and PbI_2 are formed as impurities. In $Cs_{0.05}FA_{0.83}MA_{0.17}Pb(I_{0.83}Br_{0.17})_3$ only the PbI_2 impurity peak remains.

The UV/Vis spectra of the bromide containing perovskites show very similar blue-shifted absorption profiles (Figure 8.6.10). The change in band gap in turn affects the V_{OC} of the resulting cells, as the values for the bromide-containing triple cation perovskite more strongly match those of the other bromide-containing perovskite in the set. The average efficiency of these cells is only marginally greater than for the others, which although unfortunate as it would be better to have a clearer trend, will allow for better comparison of the impedance later.
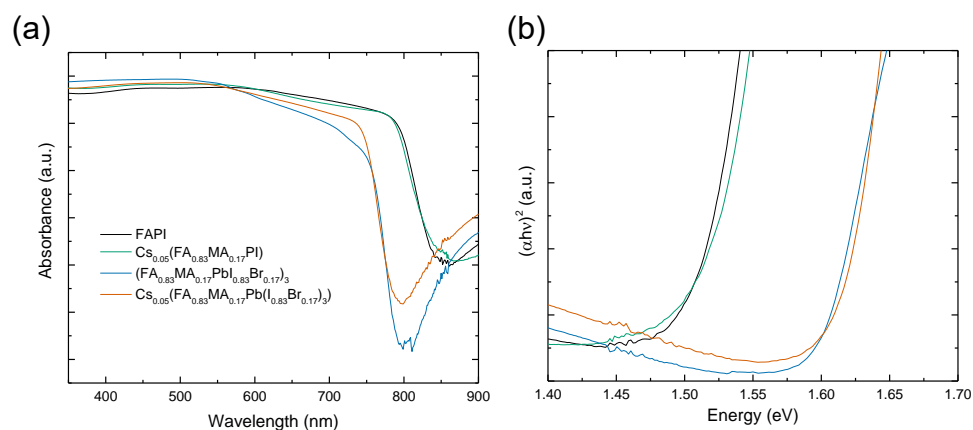
Figure 8.6.10. *a) UV/Vis spectroscopy of triple cation based perovskites and b) Tauc plot*
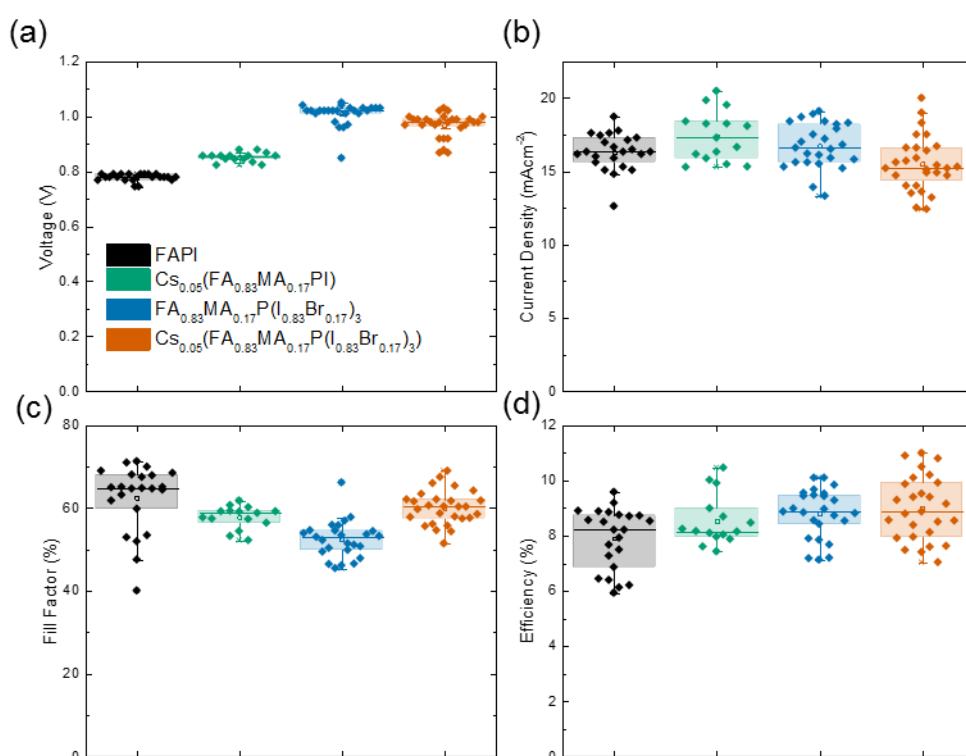
Figure 8.6.11. *Solar cell parameters for triple-cation based perovskites a) Open-circuit voltage, b) short-circuit current density, c) Fill Factor and d) Efficiency*

An AFM image of the triple-cation perovskite shows a larger crystallite size and reduced surface roughness compared to the other bromide perovskites, however there are still some pinholes in the film. From this it would appear that the addition of Cs to the perovskite increases the size of the grains, as was the case in both the iodide and mixed iodide/bromide sets.
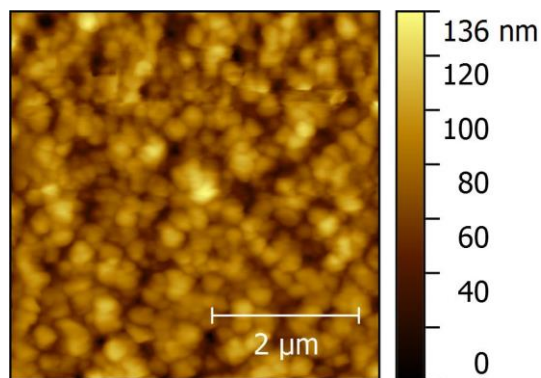
Figure 8.6.12. *AFM image $Cs_{0.05}(FA_{0.83}MA_{0.17}P(I_{0.83}Br_{0.17})_3)$ thin film (taken over 5 μm in phase contrast mode)*

The first impression when looking at the Nyquist plots in Figure 8.6.13 is that the introduction of bromide anions into the perovskite has dramatically increased the resistance. R_{recomb} rises over tenfold from $38\,\Omega$ in FAPI to $240\,\Omega$ in $FA_{0.83}MA_{0.17}P(I_{0.83}Br_{0.17})_3$. All the bromide-containing perovskites exhibit a higher V_{OC} than the pure iodide analogues, so the significant resistance increase cannot be attributed to changes in the voltage. As the capacitance does not change much (all around 10-20 nF), this increased resistance leads to the slowing of the time constants, visible in the Cole plots as a leftward shift in the peaks.
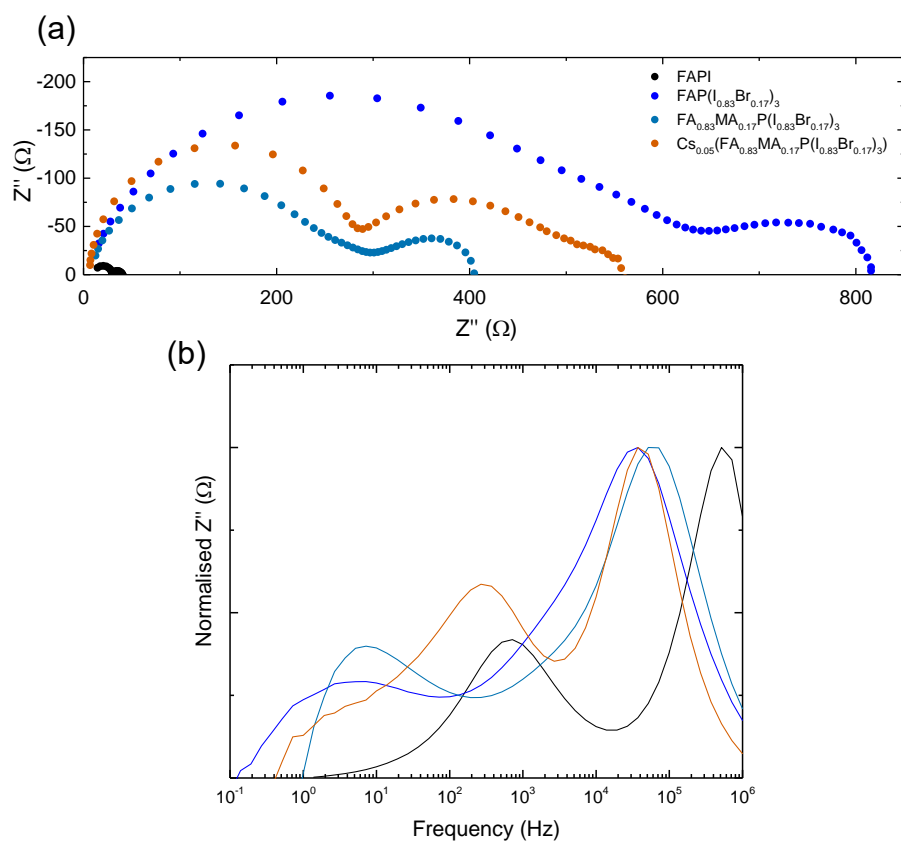
Figure 8.6.13. *a) Nyquist plots for each of the perovskite mixtures at 25 °C and b) Cole plots*

The impedance response of $FAPI_{0.83}Br_{0.17}$ is shown in Figure 8.6.14. The Nyquist plot appears to be a typical response, *i.e.* a semi-circle at higher frequency and one at lower frequency. At higher temperatures (35 °C – 45 °C) there is a more-visible middle frequency semi-circle that becomes less clear as the temperature drops. The shift in the position of the high-frequency peak appears to be covering it at lower temperatures. Despite the presence of mid-frequency and low-frequency semi-circles neither show a linear trend when displayed on an Arrhenius plot (hence a Cole plot is displayed with the Nyquist plots instead). It is very difficult to compare $FAPI_{0.83}Br_{0.17}$ to any of the other perovskite films measured so far, as it has a significantly different band gap and a much-reduced performance (5 % in $FAPI_{0.83}Br_{0.17}$ compared to 8 % in FAPI). As a first observation of the effect of bromide ions on the impedance response of perovskite cells, it would appear the main trend is an increase in recombination resistance leading to a slowing of the time constants for high and low-frequency semi-circles.

218
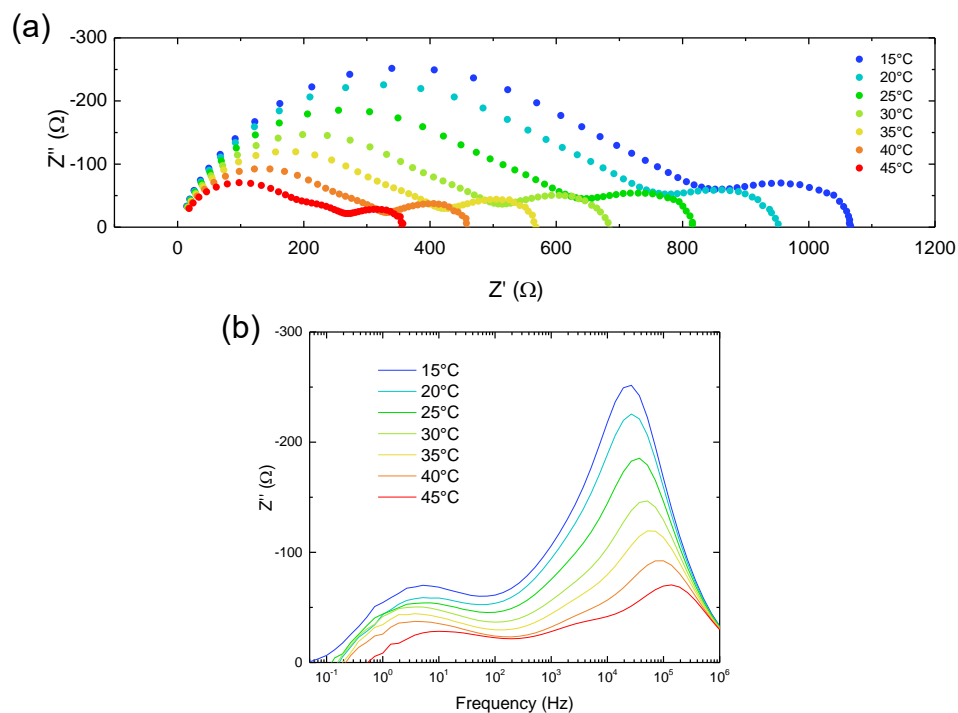
Figure 8.6.14. *The change in FAP(I$_{0.83}$Br$_{0.17}$)$_3$ impedance with temperature: a) Nyquist plots and b) Cole plots*

The feature at 1-10 kHz is still apparent and not fittable once 17 mol% MA is introduced (Figure 8.6.15a and c). The low-frequency semicircle does now behave in a linear manner with temperature, with an activation energy of 0.38 eV. This is similar to the values calculated from FAPI and FA$_{0.83}$MA$_{0.17}$PI (both 0.37 eV), suggesting that X-site substitution is having very little impact on the low-frequency semi-circle.
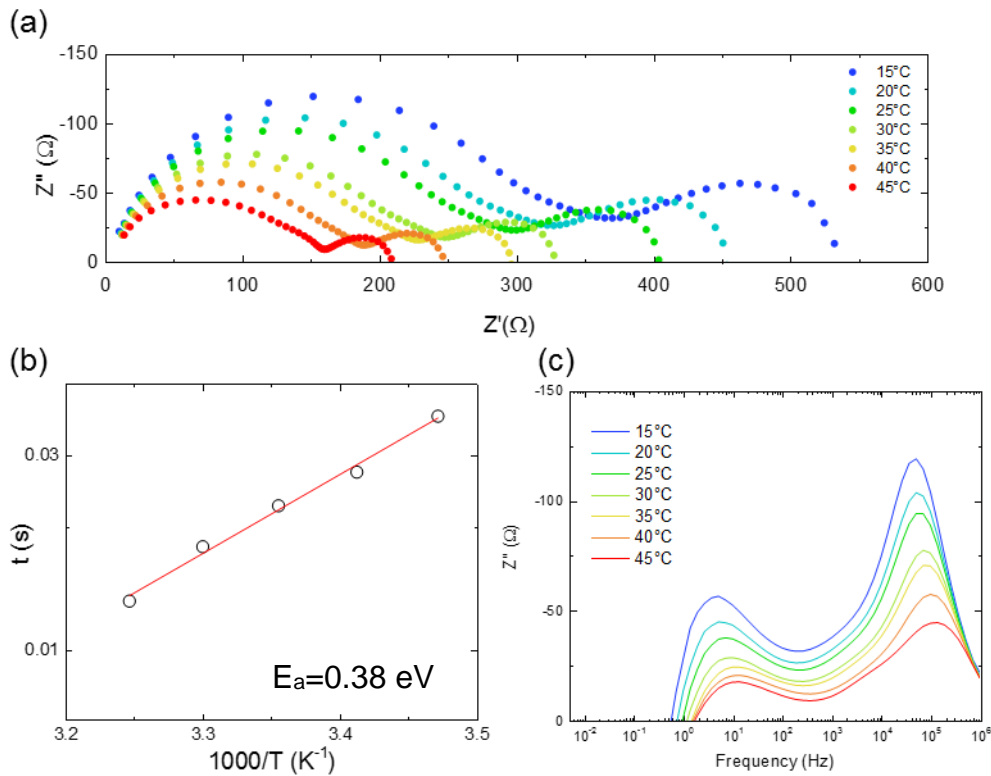
Figure 8.6.15. *The change in* $FA_{0.83}MA_{0.17}P(I_{0.83}Br_{0.17})_3$ *impedance with temperature: a) Nyquist plots, b) Arrhenius plot for the low frequency semicircle and c) Cole plot*

For the $Cs_{0.05}(FA_{0.83}MA_{0.17}P(I_{0.83}Br_{0.17})_3)$ perovskite, there appears to be three semi-circles in the Nyquist plots of Figure 8.6.16a, the mid-frequency semicircle becoming more distinct. The low-frequency semi-circle is also less neat than for all the other perovskite films measured, but it is unclear what the cause is. Activation energies for the mid-frequency and low-frequency processes are 0.45 and 0.81 eV respectively. Throughout the chapter (and thesis) the mid-frequency has shown no real trend with A or X-site substitution and has maintained a value of 0.35-0.5 eV. For the low-frequency semi-circle, partial anion substitution in this case causes the activation energy to increase greatly, from 0.21 eV to 0.80 eV from $Cs_{0.05}(FA_{0.83}MA_{0.17}PI)$ to $Cs_{0.05}(FA_{0.83}MA_{0.17}P(I_{0.83}Br_{0.17})_3)$.
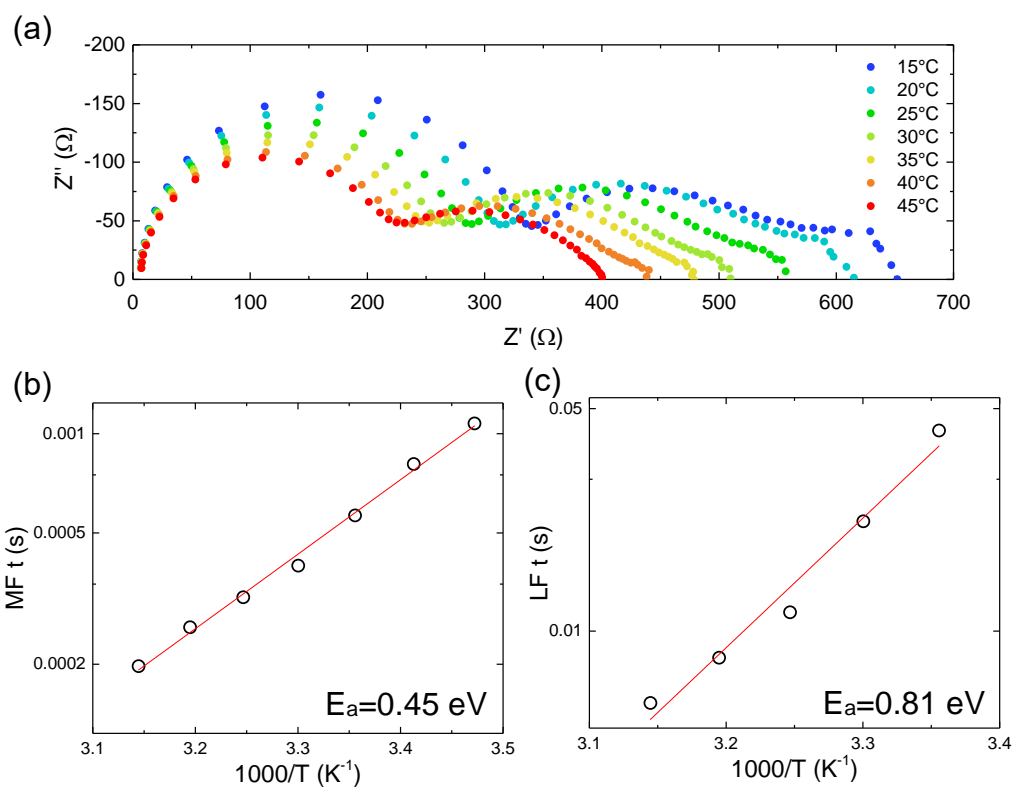
Figure 8.6.16. *The change in Cs$_{0.05}$(FA$_{0.83}$MA$_{0.17}$P(I$_{0.83}$Br$_{0.17}$)$_3$) impedance with temperature: a) Nyquist plots and b) Arrhenius plot for the low frequency semicircle*

A short summary of the main impedance results obtained in this chapter is shown in Table 8.6.1, emphasising the effect of bromide addition to R$_{ct}$.

Table 8.6.1. A summary of selected impedance results of the triple-cation perovskite and its derivatives

Cation	R$_{ct}$ (Ω) (at RT)	C$_{geo}$ (nF) (at RT)	E$_a$ (MF) (eV)	E$_a$ (LF) (eV)
FAPI	18.8	22.7	0.37 ± 0.02	-
Cs$_{0.05}$FA$_{0.95}$PI	135	7.4	0.41 ± 0.02	0.51 ± 0.01
FA$_{0.83}$MA$_{0.17}$PI	38	9.4	0.37 ± 0.04	0.53 ± 0.01
Cs$_{0.05}$(FA$_{0.83}$MA$_{0.17}$PI)	17.7	18.0	0.53 ± 0.01	0.21 ± 0.02
FA$_{0.83}$MA$_{0.17}$P(I$_{0.83}$Br$_{0.17}$)$_3$	241	10.5	0.38 ± 0.03	-
Cs$_{0.05}$(FA$_{0.83}$MA$_{0.17}$P(I$_{0.83}$Br$_{0.17}$)$_3$)	282	14.0	0.45 ± 0.02	0.81 ± 0.07

The impedance response of the mid-frequency and low-frequency response in the cation and anion substituted FAPI-based perovskites is more complex than the

relatively simple trend identified from A-site substitution on MAPI, *i.e.* local distortions in the lattice are increasing the barrier to iodide diffusion. In the MAPI based perovskites the characteristic frequencies for the high-frequency, mid-frequency, or low-frequency process were well defined within the trend. That is that the high-frequency semi-circle was visible in the 10 kHz to 1 MHz region, the mid-frequency from 100-1000 Hz and the low-frequency semi-circle below 100 Hz.

It is difficult to compare the time constants from cell-to-cell, which is why a comparison of the activation energy is a preferred method, as this is based over several measurements. However the frequency range is interesting to discuss. For example, FAPI, $FA_{0.83}MA_{0.17}PI$ and $FA_{0.83}MA_{0.17}P(I_{0.83}Br_{0.17})_3$ all have a process which has an activation energy value of 0.37-0.38 eV. The Cole plots for these cells are shown below in Figure 8.6.17.
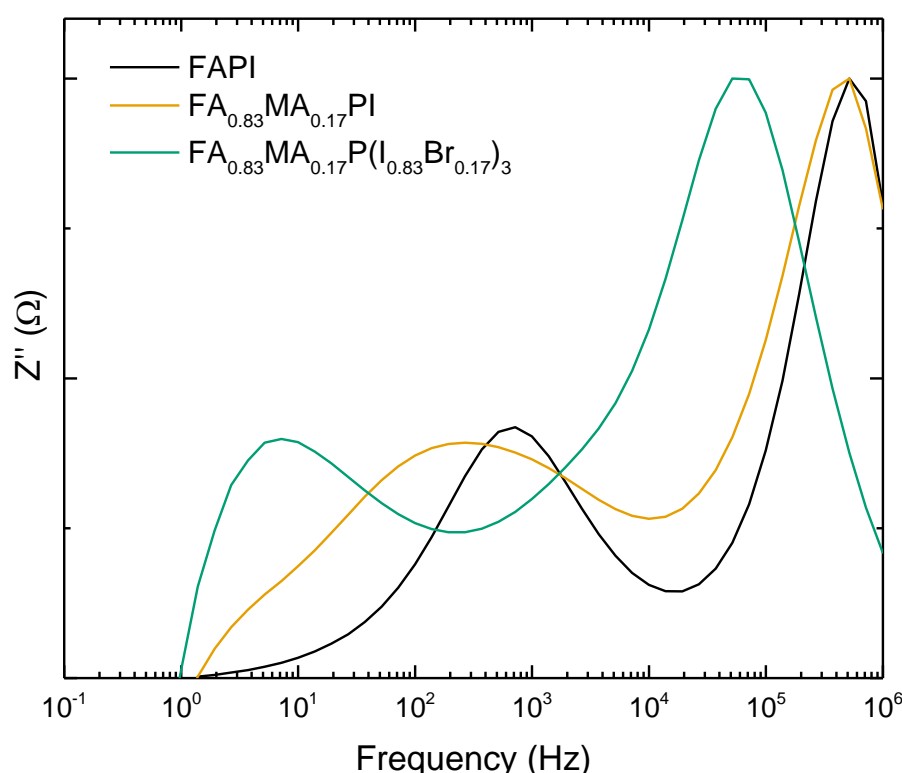
Figure 8.6.17. *Cole plots for FAPI, $FA_{0.83}MA_{0.17}PI$ and $FA_{0.83}MA_{0.17}P(I_{0.83}Br_{0.17})_3$ at 25 °C*

For FAPI and $FA_{0.83}MA_{0.17}PI$, this process is within the 100-1000 Hz range, but for $FA_{0.83}MA_{0.17}P(I_{0.83}Br_{0.17})_3$ the semi-circle that contributes to the 0.38 eV activation energy is closer to 5-10 Hz (and the lower frequency semi-circle for $FA_{0.83}MA_{0.17}PI$). The shift in the peaks makes it difficult to categorically state whether the $FA_{0.83}MA_{0.17}P(I_{0.83}Br_{0.17})_3$ process at 0.38 eV is the mid-frequency process or the low-

frequency process, as it lines up with the low-frequency semicircle in $FA_{0.83}MA_{0.17}PI$ (which had an associated activation energy of 0.53 eV).

There are two possible explanations for the appearance of these impedance plots, both related to the shift in the ω_{max} values for the high-frequency semi-circle. Firstly, that as this process is slowed, *all* processes are slowed hence the appearance of the mid-frequency semi-circle at lower frequencies. The second possible explanation is that the mid-frequency process is less affected by X-site substitution and the mid-frequency semi-circle is merging with the high-frequency semi-circle.

As the change in the recombination resistance with time is larger in the bromide-containing perovskites (visible in the Nyquist plots of 8.6.13a), it follows that the associated ω_{max} values would be lower. Based on this and the fact that they share identical activation energies, it would seem that in the case of $FA_{0.83}MA_{0.17}P(I_{0.83}Br_{0.17})_3$ it is the 'mid-frequency' semi-circle being measured. The slowing of processes caused by X-site substitution could also be a potential cause of the loss of the lower-frequency semi-circle, as it is shifted to timescales not visible in the frequency range of the experiment.

With the record efficiency $Cs_{0.05}(FA_{0.83}MA_{0.17}P(I_{0.83}Br_{0.17})_3)$ perovskite, the mid-frequency process appears at the expected frequency range of 10-100 Hz. In section 8.4 it was established that the addition of smaller cations to FAPI reduced the activation barrier for the low-frequency process. It could be the case that as the bromide-substitution is hindering the mid/low-frequency processes, the introduction of caesium is facilitating it, and the effects of the two are balanced against each other.

Unfortunately the mechanism of how A and X-site substitution affects ion movement in FAPI is not known, and would require computational simulations to help build a picture.

8.7) Conclusions

The aim of this chapter was to investigate the top efficiency triple-cation perovskite $Cs_{0.05}(FA_{0.83}MA_{0.17}Pb(I_{0.83}Br_{0.17})_3)$ in terms of how the different components of this complex perovskite affected its behaviour. There was to be a particular focus on the bulk iodide diffusion as measured by impedance spectroscopy. In the parent perovskite for this material, cubic FAPI, the impedance response showed only two semi-circles (as opposed to three in MAPI). The loss of the low-frequency semi-circle (as observed in MAPI) could be attributed to the activation barrier being increased to a value that means it is no longer observable by this experiment. It could also be the cubic perovskite only has one iodide position in the lead iodide octahedra, hence there being only one iodide diffusion mechanism compared to two in tetragonal MAPI.

Further experiments on low amounts of A-site substitution revealed that the incorporation of smaller cations into FAPI enabled three semi-circles to be visible in the EIS measurements, whereas larger cations had no effect on the impedance. Again there are two possible causes of this. One possibility is that the findings here show a trend complementary to that of the previous chapter, *i.e.* instead of increasing the activation energy by local distortions of the lattice, the reduction of it using smaller cations lowers the activation energy to a point that it is visible. Contraction of the lattice was not visible when ammonium, rubidium and caesium were included in MAPI (all increased the activation energy), but the effect of the small cations on the overall larger FAPI lattice may be different – thorough computational analysis would be useful to fully characterise what is happening here.

Interrupting the lead iodide backbone with bromide anions made a significant impact on the overall resistance of the cell. A further result is that this creates unequal sites in the lattice, meaning iodide diffusion is likely to be more difficult in these perovskites. In $FA_{0.83}MA_{0.17}Pb(I_{0.83}Br_{0.17})_3$ and $Cs_{0.05}(FA_{0.83}MA_{0.17}P(I_{0.83}Br_{0.17})_3)$ there are two and three semicircles respectively. The appearance of these spectra is likely to result from the use of both A-site and X-site additives are having antagonistic effects, bromide increasing the activation energy of the lowest frequency semicircle, and the A-site additives reducing it to the point where it is visible again.

8.8) References

1   A. Pockett, G. E. Eperon, T. Peltola, H. J. Snaith, A. Walker, L. M. Peter and P. J. Cameron, *J. Phys. Chem. C*, 2015, **119**, 3456–3465.

2   A. Pockett, G. E. Eperon, N. Sakai, H. J. Snaith, L. M. Peter and P. J. Cameron, *Phys. Chem. Chem. Phys.*, 2017, **19**, 5959–5970.

3   C. Eames, J. M. Frost, P. R. F. Barnes, B. C. O'Regan, A. Walsh and M. S. Islam, *Nat. Commun.*, 2015, **6**, 7497.

4   A. Baumann, S. Väth, P. Rieder, M. C. Heiber, K. Tvingstedt and V. Dyakonov, *J. Phys. Chem. Lett.*, 2015, **6**, 2350–2354.

5   O. Almora, I. Zarazua, E. Mas-Marza, I. Mora-Sero, J. Bisquert and G. Garcia-Belmonte, *J. Phys. Chem. Lett.*, 2015, **6**, 1645–1652.

6   J. Haruyama, K. Sodeyama, L. Han and Y. Tateyama, *J. Am. Chem. Soc.*, 2015, **137**, 10048–10051.

7   S. Meloni, T. Moehl, W. Tress, M. Franckevičius, M. Saliba, Y. H. Lee, P. Gao, M. K. Nazeeruddin, S. M. Zakeeruddin, U. Rothlisberger and M. Graetzel, *Nat. Commun.*, 2016, **7**, 10334.

8   C. Li, S. Tscheuschner, F. Paulus, P. E. Hopkinson, J. Kießling, A. Köhler, Y. Vaynzof and S. Huettner, *Adv. Mater.*, 2016, **28**, 2446–2454.

9   M. Saliba, T. Matsui, J.-Y. Seo, K. Domanski, J.-P. Correa-Baena, N. Mohammad K., S. M. Zakeeruddin, W. Tress, A. Abate, A. Hagfeldt and M. Grätzel, *Energy Environ. Sci.*, 2016, **9**, 1989–1997.

10   M. T. Weller, O. J. Weber, P. F. Henry, A. M. Di Pumpo and T. C. Hansen, *Chem. Commun.*, 2015, **51**, 4180–4183.

11   M. T. Weller, O. J. Weber, J. M. Frost and A. Walsh, *J. Phys. Chem Lett.*, 2015, **6**, 3209–3212.

12   S. Pang, H. Hu, J. Zhang, S. Lv, Y. Yu, F. Wei, T. Qin, H. Xu, Z. Liu and G. Cui, *Chem. Mater.*, 2014, **26**, 1485–1491.

13   A. Kojima, K. Teshima, Y. Shirai and T. Miyasaka, *J. Am. Chem. Soc.*, 2009,

131, 6050–6051.

14   W. Shockley and H. J. Queisser, *J. Appl. Phys.*, 1961, **32**, 510–519.

15   O. J. Weber, D. Ghosh, S. Gaines, P. F. Henry, A. B. Walker, M. S. Islam and M. T. Weller, *Chem. Mater.*, 2018.

16   N. J. Jeon, J. H. Noh, W. S. Yang, Y. C. Kim, S. Ryu, J. Seo and S. Il Seok, *Nature*, 2015, **517**, 476–480.

17   C. Yi, J. Luo, S. Meloni, A. Boziki, N. Ashari-Astani, C. Grätzel, S. M. Zakeeruddin, U. Rothlisberger and M. Grätzel, *Energy Environ. Sci.*, 2015.

18   M. Salado, S. Kazim and S. Ahmad, *Chem. Pap.*, 2018, **72**, 1645–1650.

19   D. Ghosh, P. Walsh Atkins, M. S. Islam, A. B. Walker and C. Eames, *ACS Energy Lett.*, 2017, **2**, 2424–2429.

20   G. Grancini, C. Roldán-Carmona, I. Zimmermann, E. Mosconi, X. Lee, D. Martineau, S. Narbey, F. Oswald, F. De Angelis, M. Graetzel and M. K. Nazeeruddin, 2017, **8**, 15684.

21   M. Saliba, M. Saliba, T. Matsui, K. Domanski, J.-Y. Seo and A. Ummadisingu, *Science (80-.).*, 2016, **354**, 206–209.

22   O. Almora, K. T. Cho, S. Aghazada, I. Zimmermann, G. J. Matt, C. J. Brabec, M. K. Nazeeruddin and G. Garcia-Belmonte, *Nano Energy*, 2018, **48**, 63–72.

23   P. Wang, M. Ulfa and T. Pauporte, *J. Phys. Chem. C*, 2018.

24   G. E. Eperon, S. D. Stranks, C. Menelaou, M. B. Johnston, L. M. Herz and H. J. Snaith, *Energy Environ. Sci.*, 2014, **7**, 982.

25   J. Burschka, N. Pellet, S.-J. Moon, R. Humphry-Baker, P. Gao, M. K. Nazeeruddin and M. Grätzel, *Nature*, 2013, **499**, 316–319.

26   F. Xie, C.-C. Chen, Y. Wu, X. Li, M. Cai, X. Liu, X. Yang and L. Han, *Energy Environ. Sci.*, 2017, **10**, 1942–1949.

27   G. Richardson, S. O'Kane, R. G. Niemann, T. A. Peltola, J. M. Foster, P. J. Cameron, A. Walker, S. E. J. O'Kane, R. G. Niemann, T. A. Peltola, J. M. Foster, P. J. Cameron and A. B.Walker, *Energy Environ. Sci.*, 2016, **9**, 1476–

1485.

28   O. J. Weber, B. Charles and M. T. Weller, *J. Mater. Chem. A*, 2016, **4**, 15375–15382.

29   J. H. Noh, S. H. Im, J. H. Heo, T. N. Mandal and S. Il Seok, *Nano Lett.*, 2013, **13**, 1764–1769.

30   J. H. Heo and S. H. Im, *Nanoscale*, 2016.

31   M. Saliba, T. Matsui, J.-Y. Seo, K. Domanski, J.-P. Correa-Baena, N. Mohammad K., S. M. Zakeeruddin, W. Tress, A. Abate, A. Hagfeldt and M. Grätzel, *Energy Environ. Sci.*, 2016, **9**, 1989.

9: Conclusions & Outlook

9.1 Conclusions

Since their invention (and indeed since the start of this work) perovskite solar cells have risen to prominence in the field due to an unprecedented rise in the efficiencies, from 3 % in 2009 to over 23 % in 2018. The main cause of is a shift in the standard perovskite absorber used, from methylammonium lead iodide ($MAPbI_3$, MAPI) to $Cs_{0.05}(FA_{0.83}MA_{0.17}Pb(I_{0.83}Br_{0.17})_3)$. The use and effect of multiple components in the ABX_3 perovskite absorber has been a focus of this thesis.

A new cation for hybrid inorganic-organic perovskites was introduced. The azetidinium cation had been identified by computational studies as a potential A-site cation for making 3D perovskites. However when azetidinium lead iodide (AzPI) was synthesised, the structure of the new material was unclear, as single-crystal X-ray diffraction was inconclusive. Based on the PbI_2 skeleton, a possible 2.5 D structure was proposed, in which groups of 3 lead iodide octahedra were joined at the corner to form a semi-continuous block throughout the lattice. Simulations of thin film XRD based on the computational prediction showed a good match to the experimental thin film data obtained. AzPI was also determined to be more stable to extreme exposure to water than MAPI, and maintained its structure despite being submerged entirely.

AzPI was discovered to be a bright orange material with a corresponding optical band gap of 2.15 eV. As a result PSC made using AzPI as the absorber had low efficiencies, with a maximum of 1.1 %. This was the first recorded example of a 2.5 D perovskite solar cell.

Following the studies on pure AzPI, the effect of cation-mixing was investigated, as there had been many reported instances of efficiency improvement by this method. Small percentages (< 5 mol%) of Az^+ improved the overall efficiency and stability of MAPI based perovskites, producing a champion cell of 13 % efficiency with greatly reduced hysteresis.

Due to these results and those of studies involving different A-site cations in the literature, a vast study was devised to account for the observed effects. These were chiefly a reduction in the hysteresis and improvement in stability – both of which at

the time had been attributed in part to reduced iodide anion diffusion throughout the perovskite lattice. The principal method chosen for this purpose was Electrochemical Impedance Spectroscopy taken over a range of temperatures.

To obtain more reliable results a more stable cell configuration was required. Reports had shown that using an inverted cell structure of HTL-Perovskite-ETL as opposed to ETL-Perovskite-HTL prolonged the lifetime of the cell. Cells using NiO_x and PCBM as the HTL and ETL respectively were compared to the standard architecture which used TiO_2 as the ETL, and Spiro-OMeTAD as the HTL. The NiO_x cells were found to be more stable with a decreased spread in V_{OC} and efficiency, which would enable better comparison of the mixed-cation cells later. Further advantages of using the inverted cell architecture were the reduced cost of production; inverted cells were nearly 1/3 the cost of TiO_2 based cells. The overwhelming cause of this was that silver could be used as the top contact instead of gold.

With a new standard in place eight A-site cations were chosen to be used as additives in a MAPI parent structure. These ranged from smaller cations such as ammonium and rubidium, to larger cations including azetidinium and guanidinium. The molar percentage of each cation was fixed at 5 mol% to ensure the perovskite maintained a 3D structure (it was found that using a one-step solution azetidinium did not undergo phase separation at 5 mol% as it had previously). Thin Film XRD analysis of the materials showed that the overall structure was largely the same throughout, with some shifts in the diffractogram (in all additives) suggesting an increase in overall lattice size. Fortunately the efficiencies and voltages of all the resulting PSC were similar (with the exception of the ammonium based sample) allowing for accurate comparison by EIS.

The effect on iodide diffusion of cation substitution was apparent in the calculated activation energies for the process, taken from the low frequency semicircle in the impedance spectrum over a range of temperatures from 45 °C to -12 °C. A value of 0.40 eV was obtained for MAPI. An increase in the activation energy was observed no matter what the cation used for substitution was. As the size difference with the MA^+ cation increased, so did the increase in the activation barrier for bulk iodide diffusion. The two largest cations involved in the study, acetamidinium and guanidinium, increased the activation barrier of this process to such an extent that it was no longer

visible on the timescale of the experiment. The suppression of ion diffusion correlated with literature reports that guanidinium inclusion greatly improved PSC stability. The changes in activation barrier were attributed to distortions in the perovskite lattice hindering the diffusion of iodide anions. Hence the distortion with cations of a greater size disparity to MA^+ being larger, thus the observed increase in activation energy.

The final work extended this study to the current top efficiency perovskite, $Cs_{0.05}(FA_{0.83}MA_{0.17}Pb(I_{0.83}Br_{0.17})_3)$. The triple-cation perovskite was broken down into its constituent parts, starting with the parent FAPI perovskite to determine the effect of each additive, again with a focus on the bulk iodide diffusion as calculated by EIS.

FAPI is a cubic perovskite, as opposed to the tetragonal MAPI, which complicated matters, as in the FAPI impedance spectrum only two semicircles were observed, compared to three in MAPI. The mid-frequency semicircle in MAPI had shown little trend with the cation substitution, and it was thought that it could be because this was due to the iodide diffusion at grain boundaries or interfaces. This could still be the case with FAPI, as the bulk iodide diffusion may be too slow/barrier too high to observe. However it could also be the case that in a cubic perovskite there is only one possible diffusion mode.

A similar study to that which was conducted with MAPI was performed briefly with FAPI. It was found that with smaller cation additives the third semicircle was brought into the impedance spectrum, and with larger cations compared to FA^+ there was no change in the response. It could therefore be proposed that distorting the FAPI lattice to a smaller size facilitates bulk iodide diffusion. This trend continued as the cations were used in the molar ratios appropriate to the triple cation perovskite. Interestingly the activation energy of bulk iodide diffusion decreased from 0.7 to 0.5 eV with increasing MA^+ mol%, and then further to 0.2 eV when 5 mol% Cs^+ was added to the $FA_{0.83}MA_{0.17}$ mixture. The decrease was attributed to a contraction of the lattice reducing the barrier to iodide diffusion.

X-site substitution had a vast effect on all facets of the PSC. First and foremost the main FAPI peaks in the XRD were shifted to higher angles, suggesting a reduction in lattice size. The band gap was also blue-shifted by 0.1 eV. The cells however maintained a similar efficiency to the others in this chapter. The impedance response of cells containing 17 mol% Br^- revealed that interruption of the lead iodide backbone

(the part of the perovskite responsible for charge transfer) greatly increased the charge transfer resistance in the cell. As perhaps may be expected X-site substitution removed the semicircle attributed to bulk iodide diffusion in the impedance of $FA_{0.83}MA_{0.17}Pb(I_{0.83}Br_{0.17})_3$ as compared to $FA_{0.83}MA_{0.17}PbI_3$. This is because the lead iodide skeleton is no longer as regular as it would be in the pure iodide perovskite, hindering the diffusion of iodide anions. In the triple-cation perovskite this third semicircle was observed again with an activation energy of 0.8 eV. It was suggested that this could be the smaller cation Cs^+ counteracting the effects of bromide substitution.

In general this work has attempted to explain the reasons behind the benefits of mixed component perovskites for use in solar cells. The improvement in stability recorded in literature has been associated with increasing the bulk iodide diffusion barrier. A possible cause of this is whether the chosen A-site cation distorts the perovskite lattice by increasing or decreasing the size. X-site substitution interrupts the lead iodide skeleton and thus has a similar effect in increasing the energy required to facilitate bulk iodide diffusion.

9.2 Outlook

The rapid efficiency enhancement in PSC has meant that understanding them is still attempting to catch up. Following this work there are still some unanswered questions with respect to the AC response. Further studies are required to correctly identify the mid-frequency semicircle as either interface iodide diffusion or separate movement modes based on either axial or equatorial positions. Herein the phase miscibility of cubic FAPI and tetragonal MAPI may prove useful. By performing a full range study of $FA_{1-x}MA_xPI$ the impedance response may be able to be attributed to the perovskite structure.

With the global dominance of silicon photovoltaic technology, it is likely that perovskite absorber materials will play a support role in the form of top cells for multijunction devices. As such new materials with more appropriate band gaps still need to be produced. The other option is to take advantage of the simple deposition methods needed for PSC production and to use them in applications that do not require the same efficiency as rooftop or solar farm panels.